Reduced order control of infinite dimensional port Hamiltonian systems: Application to smart material based soft actuators

Yongxin Wu

Habilitation à diriger des recherches
de l'Université Bourgogne Franche-Comté

présentée par

Yongxin WU
Docteur en automatique de l'Université Claude Bernard Lyon 1
Maître de Conférences, Section 61
SUPMICROTECH-ENSMM, Institut FEMTO-ST, UMR 6174

Reduced order control of infinite dimensional port Hamiltonian systems: Application to smart material based soft actuators

soutenue le 14 mars 2024

JURY

Christophe Prieur	Directeur de Recherche, CNRS	Rapporteur
Thomas Meurer	Professeur, Karlsruhe Institute of Technology	Rapporteur
Didier Georges	Professeur des universités, Université Grenoble-Alpes	Rapporteur
Bao-Zhu Guo	Professeur, Chinese Academy of Sciences	Examinateur
Bernhard Maschke	Professeur des universités, University Claude Bernard Lyon 1	Examinateur
Yann Le Gorrec	Professeur des universités, Supmicrotech-ENSMM	Examinateur

Acknowledgment

I finally have the time to complete my HDR thesis, which summarizes my research work since I became a Maître de Conférences at SupMicroTech-ENSMM. It wasn't easy, but I'm grateful for the support and companionship of many people who helped me throughout this journey.

There are so many people to thank, and I'd like to start by expressing my gratitude to the members of my HDR defense committee. I extend my heartfelt thanks to Prof. Thomas Meureur, Prof. Didier Georges, and Dr. Christophe Prieur for accepting the invitation to review my thesis. Your valuable suggestions significantly improved my work.

I would like to express my heartfelt thanks to Prof. Bao-Zhu Guo for attending my defense and for your ongoing support. I am also sincerely grateful to Prof. Bernhard Maschke for chairing the defense committee; it is a privilege to share this important milestone in my academic journey with my esteemed doctoral supervisor. My deepest gratitude goes to Prof. Yann Le Gorrec. From the beginning of my doctoral studies, specially after my arrive at SupMicroTech-ENSMM, your unwavering support has been a constant source of encouragement, guiding me forward every step of the way.

I would also like to thank Dr. Ning Liu, Dr. Jesus Toledo, Dr. Andrea Mattioni, Mr. Nelson Cisneros, Mr. Cristobal Ponce, Ms. Jingyi Zhao for the honor of conducting research with you and being part of your doctoral work. I have learned so much from working with each of you. I couldn't have completed this HDR thesis without your contributions and support.

I would like to express my sincere gratitude to my colleagues at AS2M: Abdenbi, Aude, Zeina, Kanty, Guillaume, Redwan, Cédric, Nadine, Emmanuel, Sounkalo, Jean-Marc, Jean-Julien, Antoine, Christophe, Nourddine, Joël, Jean-Yves, Alexis, Wissem, Hugo, François, Pierre, Noura, Patrick, Moncef, and everyone else. Thanks to all of you, we have a wonderful atmosphere in the department, which I truly enjoy and appreciate. I would like to deeply thank Isabelle and Estelle, who have always been there to help me and have made all the administrative procedures so much easier for me.

I would also like to extend my thanks to my dear colleagues from China: Prof. Yuhu Wu, Prof. Yi Cheng, Prof. Kai-Ning Wu, Prof. Zhenhua Wang, Prof. Zehao Wu, and Prof. Weijun Zhou. Our collaboration has been immensely valuable, and I have greatly benefited from your insights and contributions.

At last but not least, I would like to express my deepest acknowledgement to my dear family. Thank you to my parents and in-laws for your selfless support, which has allowed me to focus on my work. I am also deeply grateful to my two little angels, Sophia and Victoria, who have brought endless joy into my life. Finally, I want to express my deepest gratitude to my beloved wife, Li Na. Your unwavering love and support have been instrumental in helping me complete my HDR thesis. This accomplishment is as much yours as it is mine.

I want to conclude by apologizing to all persons who supported me during my research career, but are not mentioned here. Thanks to all of you.

Yongxin Wu
22 August 2024, Besançon

Contents

List of Figures

Chapter 1

General introduction

1.1. Motivation and previous work

This manuscript presents my research activities as a "Maître de Conférences" at the Engineering school "Supmicrotech-ENSMM" and a member of FEMTO-ST Institute since 2016. It is divided into two main parts, each of them corresponding to my main research activities over the last 7 years: Control of infinite-dimensional systems governed by partial differential equations (PDEs) and Modeling and control of smart material-based soft actuators. The central methodology employed in both research themes is the port Hamiltonian (PH) approach, a framework based on energy principles that enables the modeling and control of intricate, multi-physical dynamic systems. The use of the PH approach is motivated by its fundamental reliance on the energy and its generality to represent any type of physical system. This approach offers several advantages in the context of modeling and control of complex dynamic system. By expressing the systems in terms of energy variables, it becomes possible to obtain a clear and intuitive representation of the underlying dynamics and interconnections. Additionally, the PH framework ensures that the models derived in such way preserve essential the physical properties of the considered systems, such as energy conservation, passivity, and stability.

My research on control of infinite dimensional systems governed by PDEs started with my master thesis supervised by Dr. Valerie Dos Santos Martins and Dr. Mickael Rodrigues at the University Claude Bernard Lyon 1 using the conventional propositional integral control method and a multi-model approach (Dos Santos Martins et al., 2014). The use of PH system has started during Ph.D thesis with prof. Bernhard Mashcke, prof. Yann Le Gorrec and Dr. Boussad Hamroun at the University Claude Bernard Lyon 1 in Lyon (Wu, 2015). During my Ph.D., I elaborated on passivity and structure preserving model and controller reduction for PHS. The reduced order passive LQG control for finite dimensional PHS governed by ordinary differential equations (ODEs) (Wu et al., 2018) and for in-domain controlled infinite dimensional PHS (Wu et al., 2020) have been proposed. It was the starting point of my first research theme: Control design for PDEs using the PHS framework.

After my Ph.D. thesis, I pursued my scientific career as maître de Conférences at Supmicrotech-ENSMM in Besançon. I am continuing my work on control design for PDEs using PHS framework. This work has been done through two Ph.D. thesis co-supervised with prof. Yann Le Gorrec. The first Ph.D. thesis of Jesus Toledo studied the reduced order observer based controller design for boundary controlled PHS (Toledo Zucco, 2021; Toledo et al., 2020, 2022). The second Ph. D. thesis of Ning Liu investigated on the in-domain reduced order distributed control of infinite dimensional PHS via Energy shaping (Liu, 2020; Liu et al., 2021c, 2024). At the same time, I co-supervised the Ph.D. thesis of Andrea Mattioni with prof. Yann Le Gorrec. During this thesis, we studied how to exponentially stabilize mixed ODEs-PDEs PHS using strong dissipation control (Mattioni, 2021; Mattioni et al., 2022).

Regarding the second aspect of my research activities, I have been driven to delve into smart material-based soft actuators in collaboration with Prof. Yann Le Gorrec and Dr. Kanty Rabenorosoa. This collaboration was initiated following my recruitment at Supmicrotech-ENSMM and FEMTO-ST. This work started with the co-supervision of the Ph.D. thesis of Ning Liu which has investigated on the multi scale modeling of a type of Electro-active polymer based actuator, Ionic polymer–metal composites (IPMC) (Liu et al., 2021b). The use of IPMC actuators for the control of the flexible structure has been the topic of the Master internship of Andrea Mattioni (Mattioni et al., 2020). Since 2021, my research efforts have been dedicated to the exploration of a novel class of artificial muscle-like actuators known as Hydraulically Amplified Self-healing ELectrostatic (HASEL) actuators. In this study, we have made significant progress in the modeling and control aspects of HASEL actuators. Notably, these preliminary results are documented in the ongoing Ph.D. thesis of Nelson Cisneros (Yeh et al., 2022), which is being co-supervised by Prof. Yann Le Gorrec and Dr. Kanty Rabenorosoa. All my publications and Ph.D supervisions are summarized in Fig. 1.1.

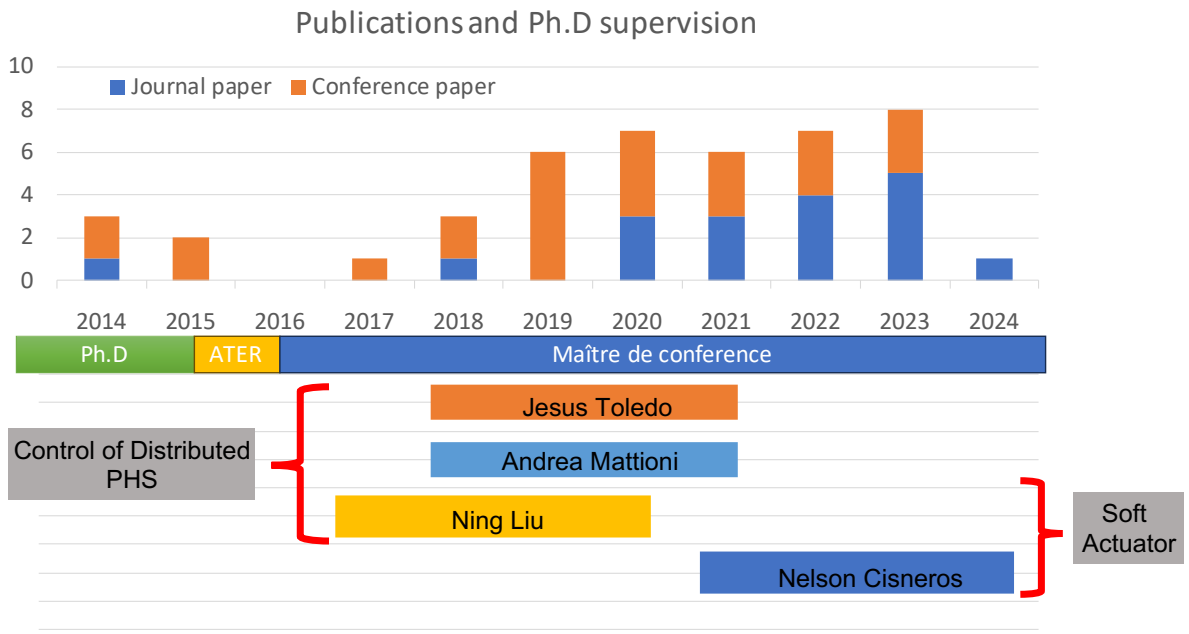

Figure 1.1: Publications and supervision summary.

This manuscript provides a summary of the research activities I have carried out since my recruitment at Supmicrotech-ENSMM and FEMTO-ST in 2016. It gives an in-depth and impartial overview of the research areas to which I have contributed.

1.2. Organization of the manuscript

The manuscript is divided into two independent parts, each corresponding to one of my main research activities. The first part (Part I) focuses on the control of infinite-dimensional PHS. It begins with Introduction 2, which motivates the proposed works while providing some preliminary notions of PHS. Chapter 3 presents the reduced observer-based control methods for boundary-controlled PHS (Toledo et al., 2020, 2022) that we have developed. Chapter 4 provides a presentation of the reduced order in-domain distributed control through energy shaping for infinite-dimensional PHS (Liu et al., 2024). Chapter 5 demonstrates the stabilization of mixed PDEs-ODEs PHS using strong dissipation control on the ODEs part of the mixed systems (Mattioni et al., 2022). Part I ends with Conclusion 6.

Part II addresses the second research line of my activities, which involves modeling and control of smart material-based soft actuators. This part begins with an Introduction 7, providing motivation and a literature review. Chapter 8 presents the modeling of IPMC using multi-scale PHS, building upon the work of (Liu et al., 2021b). The use of IPMC actuators for controlling flexible structures is discussed in Chapter 9, which is based on the work of (Mattioni et al., 2020). Chapter 10 presents preliminary works on modeling and control of HASEL actuators, relying on the research of (Yeh et al., 2022). Part II ends with Conclusion 11.

The manuscript is concluded by a section gathering some final remarks and perspectives on future work.

Part I

Control design for infinite dimensional port Hamiltonian systems

Chapter 2

Introduction of Part I

2.1. Context and contribution

Over the past few decades, there has been significant interest in controlling distributed parameter systems (DPSs) governed by Partial Differential Equations (PDEs). This heightened attention is primarily due to the increasing use of compliant structures, information networks within systems, smart materials and structures, and the growing prevalence of multi-scale and multi-physics systems in engineering applications. Port Hamiltonian (PH) formulations, which expand upon Hamiltonian formulations to encompass open multi-physics systems, have demonstrated their exceptional suitability for modeling and controlling nonlinear lumped parameter (finite dimensional systems governed by Ordinary Differential Equations (ODEs)) (Maschke and van der Schaft, 1992; Maschke et al., 1992; Duindam et al., 2009). The PH formulation has been extended to DPSs or systems described by PDEs in (van der Schaft and Maschke, 2002) using differential geometry and in (Le Gorrec et al., 2005; Jacob and Zwart, 2012) in the case of one dimensional linear systems using functional analysis. This approach has shown in a period of twenty years to be a successful approach for the modeling, analysis, and control design of DPSs Rashad et al. (2020).

A PH system is characterized by its energy and the exchange of power among different components within the system and with the surrounding environment, including controllers, perturbations, or other systems. This provides different advantages for the modeling and control of multi-physic systems. This approach has shown to be efficient to prove existence of solutions (Le Gorrec et al., 2005; Jacob and Zwart, 2012). It has also been shown that this approach can be employed to achieve asymptotic or exponential stabilizing of the system in two scenarios: when the actuators are positioned at the boundary of its spatial domain (Villegas et al., 2009; Ramirez et al., 2014; Macchelli et al., 2017, 2020) and when they are located within its spatial domain (Wu et al., 2014a, 2020; Malzer et al., 2020a,b).

The objective of my research is to develop implementable control laws for distributed parameter systems through the PH framework. To design controllers for DPSs, there are typically two approaches: the late-lumping approach and the early-lumping approach. In the late-lumping approach, the controller is designed directly on the DPSs, resulting in a controller structure that is typically infinite dimensional. The main challenge that arises from the infinite dimensional aspect of the controller is that it needs to be reduced for practical and real-time implementation. In the early-lumping approach, the system is first approximated and a finite-dimensional controller is designed on this reduced order system. However, the main drawback is the introduction of the spillover effect caused by the use of a reduced order controller on the infinite dimensional system. This spillover effect can lead to the destabilization of high-frequency mode of the infinite dimensional systems. (Bontsema and Curtain, 1988).

From the practical point view, the early-lumping provides the easiest implementable controller for DPSs because they have a finite dimensional structure. Using the passive properties inherent to PH systems, we can ensure stability when implementing the finite dimensional controller in the

DPSs. Keeping this idea in mind, two control scenarios have been considered: when the actuator is situated at the boundary of the spatial domain, leading to a boundary control system (BCS) and when actuators and sensors are located within the spatial domain. In the first case, a reduced order observer based control design is studied, which can help mitigating the controller initialization issue arising when using the Control by Interconnection method (Macchelli et al., 2017). In the in-domain control case, we investigate how dynamic extensions and structural invariants can be employed to modify the internal properties of the system when it is under full actuation and how it can be done in an approximate way when the system is actuated using piece-wise continuous actuators, which results from the application of patches.

The PH theory provides a modular modeling approach to model the mixed ODEs-PDEs system in a structural manner. This class of systems is also widely used to model multi-physic system such as rotating and/or translating beams (Aoues et al., 2017; Banavar and Dey, 2010), controlled nanotweezer used for DNA manipulation (Ramirez et al., 2014) as well as electric transmission lines with load (Macchelli and Melchiorri, 2005). My research is also dedicated to the design of control laws for mixed ODEs-PDEs PH system when the actuation is on the ODEs part. To this end, the concept of combined strong dissipation and position control is developed. In this context, we propose a Lyapunov argument to show the asymptotic stability of the closed-loop system.

Before presenting the aforementioned control design strategies, we first recall the finite dimensional and infinite dimensional PH system as well as its discretization.

2.2. Finite dimensional PH systems

The general formulation of a finite dimensional port Hamiltonian system in the input-state-output form with dissipation is given by:

$$\dot{x} = (J(x) - R(x)) \frac{\partial H}{\partial x}(x) + B(x)u, \tag{2.1a}$$

$$y = B(x)^T \frac{\partial H}{\partial x}(x), \tag{2.1b}$$

where $R(x) \in \mathbb{R}^{n\times n}$ is positive semidefinite and $B(x) \in \mathbb{R}^{n\times m}$ is the input matrix. $u \in \mathbb{R}^m$ denotes the input and $y \in \mathbb{R}^m$ gives the power conjugated output. The Hamiltonian (energy) of the system is denoted by $H(x)$. In the linear case, the Hamiltonian is defined in the quadratic form as:

$$H(x) = \frac{1}{2} x^T Q x. \tag{2.2}$$

The time derivative of the Hamiltonian is computed as:

$$\begin{aligned}
\frac{\mathrm{d}H}{\mathrm{d}t} &= \frac{\partial H}{\partial x}(x)^T \dot{x} \\
&= \frac{\partial^T H}{\partial x}(x)^T \left(J(x) - R(x)\right) \frac{\partial H}{\partial x}(x) + \frac{\partial H}{\partial x}(x)^T B(x)u \\
&= -\frac{\partial H}{\partial x}(x)^T R \frac{\partial H}{\partial x}(x) + y^T u \qquad (2.3) \\
&\leq y^T u, \qquad (2.4)
\end{aligned}$$

which implies that the time variation of the energy is equal to the difference between the power exchanged power with the environment and the dissipated power. If the Hamiltonian H is bounded from below, we can say that the system (2.1) is **passive**.

2.3. Infinite dimensional PH systems

we consider partitioned PH systems defined on a one dimensional spatial domain $\zeta \in [0, L]$ with distributed and boundary control and observation of the form:

$$\frac{\partial}{\partial t}\begin{bmatrix} x_1(\zeta,t) \\ x_2(\zeta,t) \end{bmatrix} = \begin{bmatrix} 0 & \mathcal{G} \\ -\mathcal{G}^* & -R \end{bmatrix} \begin{bmatrix} \mathcal{L}_1(\zeta)x_1(\zeta,t) \\ \mathcal{L}_2(\zeta)x_2(\zeta,t) \end{bmatrix} + \begin{bmatrix} 0 \\ B_0 \end{bmatrix} u_d(\zeta,t) \tag{2.5}$$

$$y_d(\zeta,t) = \begin{bmatrix} 0 & B_0^* \end{bmatrix} \begin{bmatrix} \mathcal{L}_1(\zeta)x_1(\zeta,t) \\ \mathcal{L}_2(\zeta)x_2(\zeta,t) \end{bmatrix} \tag{2.6}$$

$$u_b = \mathcal{B}\begin{bmatrix} \mathcal{L}_1(\zeta)x_1(\zeta,t) \\ \mathcal{L}_2(\zeta)x_2(\zeta,t) \end{bmatrix},\ y_b = \mathcal{C}\begin{bmatrix} \mathcal{L}_1(\zeta)x_1(\zeta,t) \\ \mathcal{L}_2(\zeta)x_2(\zeta,t) \end{bmatrix} \tag{2.7}$$

where $x = [x_1^T, x_2^T]^T \in X := L^2([a,b], \mathbb{R}^n) \times L^2([a,b], \mathbb{R}^n)$, $\mathcal{L} = \text{diag}(\mathcal{L}_1, \mathcal{L}_2)$ is a bounded and Lipschitz continuous matrix-valued function such that $\mathcal{L}(\zeta) = \mathcal{L}^T(\zeta)$ and $\mathcal{L}(\zeta) \geq \eta$ with $\eta > 0$ for all $\zeta \in [a,b]$, $R \in \mathbb{R}^{(n,n)}, R = R^T > 0$, $\mathcal{B}(\cdot)$ and $\mathcal{C}(\cdot)$ are some boundary input and boundary output mapping operators that will be defined later. The distributed input operator B_0 is formulated as:

$$B_0 = \begin{cases} 1 & \text{for } n = 1, \\ \begin{bmatrix} 0 \\ 1 \end{bmatrix} & \text{for } n = 2. \end{cases}$$

$X \ni x$ is the space of energy variables and $\mathcal{L}x$ denotes the co-energy variable associated to the energy variable x. The total energy of the system is given by

$$H(x_1, x_2) = \frac{1}{2}\int_a^b \left(x_1^T \mathcal{L}_1 x_1 + x_2^T \mathcal{L}_2 x_2\right) d\zeta. \tag{2.8}$$

The operator $\mathcal{G}$ is defined as:

$$\mathcal{G} = G_0 + G_1 \frac{\partial}{\partial \zeta}, \tag{2.9}$$

with $G_0, G_1 \in \mathbb{R}^{n \times n}$ and G_1 full rank. $\mathcal{G}^*$ is the formal adjoint of $\mathcal{G}$ *i.e.*

$$\mathcal{G}^* = G_0^T - G_1^T \frac{\partial}{\partial \zeta}.$$

The dissipation operator R is bounded, symmetric ($R^* = R$) and coercive ($\langle z, Rz \rangle_{L_2} > a\|z\|_{L_2}$, $\forall z \in L_2([0,L], \mathbb{R}^n)$ and $a > 0$). u_d and y_d denote the distributed input and output, respectively. The system (2.5) with (2.9) stems from the modeling of wavelike systems like elastic strings, Timoshenko beams or waves and beams organised in networks. The proposed approach is easy to extend to second order operators defining Euler-Bernouilli beam equation for example.

By defining $P_1 = \begin{bmatrix} 0 & G_1 \\ G_1^T & 0 \end{bmatrix}$, $P_1 = \begin{bmatrix} 0 & G_0 \\ -G_0^T & 0 \end{bmatrix}$ and $\mathcal{R} = \begin{bmatrix} 0 & 0 \\ 0 & R \end{bmatrix}$, the formulation (2.5) can be recasted into the general PH formulation:

$$\frac{\partial x}{\partial t}(\zeta,t) = \left(P_1 \frac{\partial}{\partial \zeta} + P_0 - \mathcal{R}\right)\mathcal{L}(\zeta)x(\zeta,t) + \begin{bmatrix} 0 \\ B_0 \end{bmatrix} u_d(\zeta,t) \tag{2.10}$$

$$y_d(\zeta,t) = \begin{bmatrix} 0 & B_0^* \end{bmatrix} \mathcal{L}(\zeta)x(\zeta,t) \tag{2.11}$$

$$u_b = \mathcal{B}\mathcal{L}(\zeta)x(\zeta,t),\ y_b = \mathcal{C}\mathcal{L}(\zeta)x(\zeta,t) \tag{2.12}$$

Definition 2.3.1. *The boundary port variables associated to the system* (2.5) *are defined by:*

$$\begin{bmatrix} f_\partial \\ e_\partial \end{bmatrix} = \underbrace{\frac{1}{\sqrt{2}} \begin{bmatrix} P_1 & -P_1 \\ I & I \end{bmatrix}}_{R_{ext}} \begin{bmatrix} \mathcal{L}x(L) \\ \mathcal{L}x(0) \end{bmatrix}. \tag{2.13}$$

◊

By definition the boundary port variables are such that:

$$\frac{\mathrm{d}H}{\mathrm{d}t} = \int_0^L y_d^T u_d \mathrm{d}\zeta + f_\partial^T e_\partial - \int_0^L (\mathcal{L}_2 x_2)^T R(\mathcal{L}_2 x_2) d\zeta. \tag{2.14}$$

The boundary inputs and outputs are defined by:

$$u_b = W \begin{bmatrix} f_\partial^T & e_\partial^T \end{bmatrix}^T, \quad y_b = \tilde{W} \begin{bmatrix} f_\partial^T & e_\partial^T \end{bmatrix}^T, \tag{2.15}$$

with $\tilde{W}$ full rank and $\begin{bmatrix} W^T, & \tilde{W}^T \end{bmatrix}^T$ invertible.
The existence of the solution of (2.5) has been investigated in (Le Gorrec et al., 2005) as stated in Theorem 2.3.1.

Theorem 2.3.1. *Let W be a $2n \times 4n$ matrix. If W has full rank and satisfies $W\Sigma W^T \geq 0$, where $\Sigma = \begin{bmatrix} 0 & I \\ I & 0 \end{bmatrix}$, then the system operator*

$$\mathcal{A} = (\mathcal{J} - \mathcal{R})\,\mathcal{L}$$

where

$$\mathcal{J} = \begin{bmatrix} 0 & \mathcal{G} \\ -\mathcal{G}^* & 0 \end{bmatrix} \quad \textit{and} \quad \mathcal{R} = \begin{bmatrix} 0 & 0 \\ 0 & R \end{bmatrix}$$

with domain

$$D(\mathcal{A}) = \left\{ x \in H^N\left([0, L], \mathbb{R}^{2n}\right) \mid \begin{bmatrix} f_\partial \\ e_\partial \end{bmatrix} \in ker(W) \right\}$$

generates a contraction semigroup. Furthermore, the system (2.10) - (2.12) *and* (2.15) *defines a boundary control PH system (BC-PHS).* ◊

Proof. The proof follows Theorem 4.1 in (Le Gorrec et al., 2005). □

2.4. Discretization of infinite dimensional PH systems

In this manuscript, we consider the early lumping approach for the controller design. Hence, the first step is to spatially discretize the system (2.5). The discretization needs to preserve the structure and the passivity of the system to take advantage of the PHS properties. Therefore we apply the mixed finite element method (Golo et al., 2004) as shown in Fig. 2.1 and the approximated system of (2.5) is again a PH system with p elements.

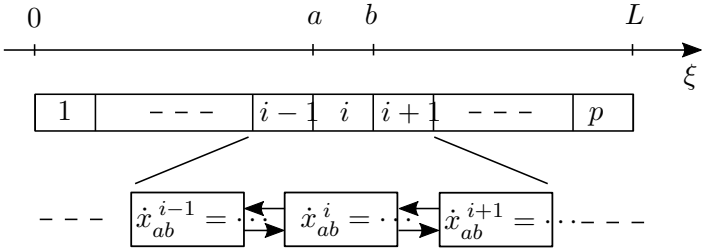

Figure 2.1: Discretization scheme with the mixed finite element method

$$\begin{bmatrix} \dot{x}_{1d} \\ \dot{x}_{2d} \end{bmatrix} = (J_n - R_n) \begin{bmatrix} Q_1 x_{1d} \\ Q_2 x_{2d} \end{bmatrix} + B_d u_b + \begin{bmatrix} 0 \\ B_{0d} \end{bmatrix} \mathbf{u}_d, \tag{2.16a}$$

$$y_b = B_d^T \begin{bmatrix} Q_1 x_{1d} \\ Q_2 x_{2d} \end{bmatrix} + D_b u_b, \tag{2.16b}$$

$$\mathbf{y}_d = \begin{bmatrix} 0 & B_{0d}^T \end{bmatrix} \begin{bmatrix} Q_1 x_{1d} \\ Q_2 x_{2d} \end{bmatrix}, \tag{2.16c}$$

where $x_{id} = \begin{bmatrix} x_i^1 & \cdots & x_i^p \end{bmatrix}^T$ for $i \in \{1, \cdots, 2n\}$, $\mathbf{u}_d \in \mathbb{R}^p$, $\mathbf{y}_d \in \mathbb{R}^p$,

$$J_n = \begin{bmatrix} 0 & J_i \\ -J_i^T & 0 \end{bmatrix} \text{ and } R_n = \begin{bmatrix} 0 & 0 \\ 0 & R_d \end{bmatrix}, \tag{2.17}$$

are the discretized matrices of the operators $\mathcal{J}$ and $\mathcal{R}$ with J_i and R_d the discretized matrices of the operators $\mathcal{G}$ and R. $Q_1 \in \mathbb{R}^{np \times np}$ and $Q_2 \in \mathbb{R}^{np \times np}$ are the discretized matrices of $\mathcal{L}_1$ and $\mathcal{L}_2$, respectively. B_d is the discretized matrix of the boundary input operator $\mathcal{B}$. B_{0d} is the discretized matrix of B_0 and writes:

$$B_{0d} = \begin{cases} I_p & \text{for } n = 1, \\ \begin{bmatrix} I_p \\ 0_p \end{bmatrix} & \text{for } n = 2, \end{cases}$$

where I_p and 0_p denote the identify matrix and the zeros matrix of dimension $p \times p$, respectively. For the sake the simplification, we denote $x_d = \begin{bmatrix} x_{1d} \\ x_{2d} \end{bmatrix} \in \mathbb{R}^{n_d}$ with $n_d = 2np$ and $Q_d = \text{diag}[Q_1, Q_2] \in \mathbb{R}^{n_d \times n_d}$. We take $A_d = (J_d - R_d) Q_d$ The input u_b denotes the boundary input which corresponds to the boundary actuation or/and conditions.
The Hamiltonian of the discretized model (2.16) writes:

$$H_d(x_{1d}, x_{2d}) = \frac{1}{2} \left(x_{1d}^T Q_1 x_{1d} + x_{2d}^T Q_2 x_{2d} \right). \tag{2.18}$$

It is important to notice that in what follows the choice of the structure-preserving discretization method is not unique. One could have alternatively used other discretization methods such as (Kotyczka et al., 2018; Moulla et al., 2012) that also guarantee the existence of PH structure and structural invariants suitable for control design purposes.

2.5. Organization of Part I

Part I composes of three main chapters. In Chapter 3, we consider the reduced order observer based boundary control for infinite dimensional PH systems (2.5) (BC-PHS). Chapter 4 presents the in-

domain distributed control of the infinite dimensional PH via energy shaping using the early lumping approach. In Chapter 5, the strong dissipation feedback for the mixed finite and infinite dimensional PH systems will be discussed.

Chapter 3

Boundary control design based on the reduced order observer

3.1. Introduction

In this chapter, we stabilize the Boundary Controlled Port Hamiltonian Systems (BC-PHS) by using *observer-based state feedback* (OBSF) controllers. To this end, we employ an *early-lumping approach*. The BC-PHS is first discretized to a Linear Time invariant (LTI) system (2.16) using the structure preserving discretization method. Then, the synthesis of the OBSF gains is based on the discretized LTI system. Finally, the OBSF controller has to guarantee the closed-loop stability when it is applied to the BC-PHS.

One of the main advantages of using an *early-lumping approach* is the number of tools available in the literature for designing the OBSF gains of LTI systems Kalman et al. (1969); Luenberger (1964). These techniques are, for instance, the *linear quadratic regulator* (LQR) Anderson and Moore (2007), the pole-placement Brasch and Pearson (1970), and more recently, the *control by interconnection* using *Casimirs* Ortega et al. (2008), and the *interconnection and damping assignment passivity based control* (IDA-PBC) Ortega et al. (2002); Prajna et al. (2002). However, since the design is based on the discretized model (LTI system) and not on the BC-PHS, the closed-loop stability is not guaranteed when applying the OBSF controller to the BC-PHS. We use an example to show this issue. We design some OBSF gains using classical control techniques for LTI systems. Then, we show that when applying the OBSF controller to the BC-PHS, the closed-loop system becomes unstable. This phenomenon is known as spillover effect Balas (1978, 1982) and it occurs when some high-frequency modes that are not considered for the design destabilize the closed-loop system. To overcome this effect and to guarantee closed-loop stability (when applying the OBSF controller to the BC-PHS), the classical control techniques have to be adapted.

In this chapter, we impose a passive structure on the OBSF controller. This structure guarantees the closed-loop stability when the OBSF controller is applied to the BC-PHS. We convert the classical OBSF representation into an equivalent dynamic output feedback representation Villegas et al. (2005); Villegas (2007); Wu et al. (2018). If the dynamic output feedback controller (or equivalently the OBSF controller) is *strictly positive real* (SPR), the closed-loop between the infinite-dimensional system (BC-PHS) and the OBSF controller is asymptotically stable Morgül (1994); Morgul (1998); Yang et al. (2005); Villegas (2007). To achieve this structure, we propose two methodologies for the synthesis of the OBSF gains. In the first method, the state feedback gain is freely designed by using classical control techniques. Then, the observer gain is designed (through the resolution of an algebraic Riccati equation) such that the OBSF controller is SPR. In the second method, the observer gain is freely designed and the state feedback gain is designed (through the resolution of a set of linear matrix inequalities) such that the OBSF is SPR. In both cases, it is not completely free the design of one of the two gains. The benefit of using these constraints is that we can guarantee

closed-loop stability when applying the OBSF controller to the BC-PHS. We use the vibrating string and the Timoshenko beam as application examples.
This chapter is organized as follows. In Section 3.2, we recall the classic OBSF controller for LTI systems and show in a counterexample that if we implement the classical finite dimensional OBSF to the BC-PHS, the closed-loop stability can not be guaranteed. In Section 3.3, we impose a passive structure to the OBSF controller such that when applying it to the BC-PHS and the asymptotic stability is showed when applying the OBSF controller to the BC-PHS in Section 3.4. In Section 3.5 and Section 3.6, two methodologies are proposed for designing the controller and observer gains. These methodologies is numerically illustrated using the vibrating string and the Timoshenko beam models to show their effectiveness. Finally, some conclusions are presented in Summary 3.7.

3.2. Luenberger observer based state feedback and motivation example

State feedback allows to assign the overall closed-loop eigenvalues and may also be used to assign a part of the closed-loop eigenstructure (Kalman et al., 1969; Andry et al., 1983; Jiang, 1994). For example, state feedback may be used to assign settling time, rise time, damping ratio or overshoot. The main drawback of this control strategy is that it requires the measurement of the overall state. To overcome this, the state is reconstructed using observers. An observer is a dynamical system that uses the dynamical model of the system and the measurement of the input and output to reconstruct the state variables (Luenberger, 1964).

Definition 3.2.1. *A full observer-based state feedback controller for the system* (2.16) *is defined as follows:*

$$u(t) = -K\hat{x}(t) + r(t) \tag{3.1a}$$

$$\dot{\hat{x}}(t) = A_d\hat{x}(t) + B_d u(t) + L(y(t) - C_d\hat{x}(t)), \quad \hat{x}(0) = \hat{x}_0, \tag{3.1b}$$

where (3.1a) *is the observed state feedback and* (3.1b) *is a Luenberger observer.* $K \in \mathbb{R}^{n\times n_d}$ *and* $L \in \mathbb{R}^{n_d\times n}$ *are the controller and the observer gains, respectively. These gains are designed such that* $A_d - B_dK$ *and* $A_d - LC_d$ *are Hurwitz matrices.* $\hat{x}(t) \in \mathbb{R}^{n_d}$ *is the observed state with initial condition* $\hat{x}_0$*, and* $r(t) \in \mathbb{R}^n$ *is an external input.* ◊

The system (2.16) is assumed to be observable and controllable. Then, the synthesis of the state feedback and observer gains can be designed using classical control tools. However, several issues can occur when applying the OBSF controller to the BC-PHS (2.10)-(2.12). The most critical one is the instability in closed-loop caused by the spillover effect. In this case, the high frequency modes that have not been taken into account during the design are destabilized when the OBSF controller is applied to the BC-PHS. This effect is shown in the following example.

Example 3.2.1. *Consider the one-dimensional wave equation with unitary parameters and Neumann boundary control at both sides, i.e. with force actuators at both sides. The system can be written as a BC-PHS* (2.10)-(2.12) *with*

$$P_1 = \begin{bmatrix} 0 & 1 \\ 1 & 0 \end{bmatrix}, \quad P_0 = 0, \quad \mathcal{H} = I_2.$$

This model is discretized by using finite differences on staggered grids in order to preserve the structure of the system (Trenchant et al., 2018). Consider $p = 59$ *elements for the discretization. All the eigenvalues of* A_d *are on the imaginary axis as shown in Figure 3.1 (a).* (A_d, B_d) *is controllable and* (A_d, C_d) *is observable, hence* K *and* L *can be designed such that* $A_K = A_d - B_dK$ *and* $A_L = A_d - LC_d$ *are Hurwitz matrices. Using for instance the LQR method, the closed-loop eigenvalues can be assigned as shown in Figure 3.1 (a).*

The question that naturally arises is if the same OBSF controller, i.e. the same choice of matrices K and L, preserves the stability when applying it to the infinite-dimensional system. The answer is in general no. In this particular case for instance, when applying the designed OBSF controller (with $n_d = 59$ states) to a more precise discretized model that uses for example $n_d = 67$ states, the closed-loop system turns unstable as shown in Figure 3.1 (b). ◊

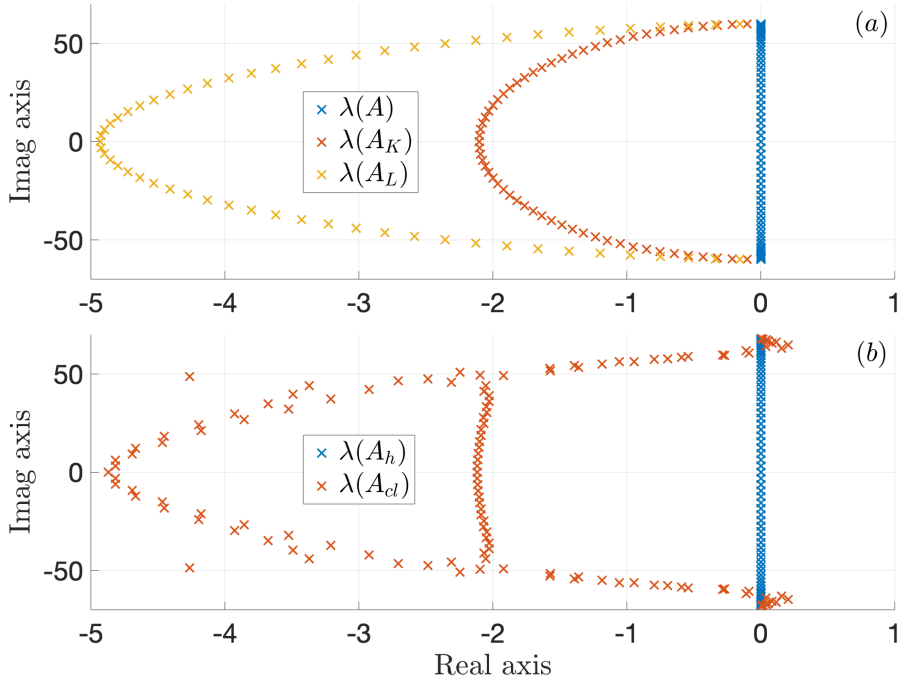

Figure 3.1: (a): $\lambda(A)$: Eigenvalues of A_d with $n_d = 59$, $\lambda(A_K)$: $A_d - B_d K$ eigenvalues and $\lambda(A_L)$: $A_d - LC_d$ eigenvalues. (b): $\lambda(A_h)$: discretized model eigenvalues with $n_d = 67$, $\lambda(A_{cl})$: closed-loop eigenvalues.

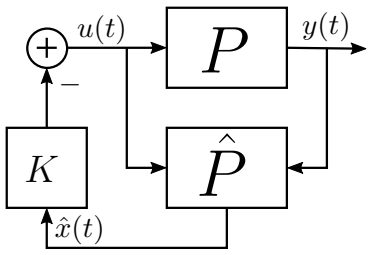

Figure 3.2: Observer-based state feedback diagram block

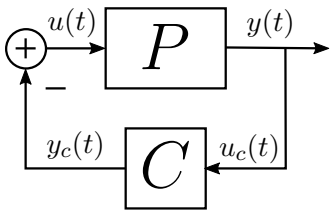

Figure 3.3: Passive observer-based state feedback diagram block.

In Example 3.2.1, we have shown that the classical control tools have to be adapted to guarantee closed-loop stability when applying the OBSF controller to the BC-PHS. In the following section, we convert the classical closed-loop structure between (2.16) and (3.1), represented in Figure 3.2 with $r(t) = 0$, into an equivalent closed-loop structure represented in Figure 3.3, where C represents the OBSF controller. By imposing a passive structure to the dynamic controller C (or the OBSF controller), we can guarantee closed-loop stability when applying the OBSF controller to the BC-PHS. Then, the matrices K and L are restricted to obtain a passive OBSF controller. In the following section, we present the conditions to have a passive OBSF controller and in Sections 3.5 and 3.6, we propose two methods for the synthesis of the OBSF gains.

3.3. Passive observer-based state feedback structure

In this section, we adapt the OBSF scheme of Figure 3.2 into an equivalent closed-loop scheme as shown in Figure 3.3, where C is a passive dynamic controller with input $u_c(t)$ and output $y_c(t)$. To this end, we replace (3.1a) in (3.1b)

$$\dot{\hat{x}}(t) = (A_d - B_dK - LC_d)\hat{x}(t) + Ly(t) + B_dr(t). \tag{3.2}$$

Then, the synthesis of the matrices K and L are chosen such that the dynamical system (3.2) is a finite-dimensional port-Hamiltonian system with inputs $y(t)$ and $r(t)$. To do that, the matrices K and L have to be chosen such that

$$A_d - LC_d - B_dK = (J_c - R_c)Q_c \tag{3.3}$$

is satisfied for some $n_c \times n_c$ matrices $J_c = -J_c^T$, $R_c = R_c^T \geq 0$, $Q_c = Q_c^\top > 0$, (A_d, B_d, C_d) defined in (2.16), and n_c the size of the controller given by the discretized model used for design. If (3.3) is satisfied we can write (3.2) as a finite-dimensional port-Hamiltonian system as follows:

$$C\begin{cases} \dot{\hat{x}}(t) = (J_c - R_c)Q_c\hat{x}(t) + B_cu_c(t) + B_dr(t), \quad \hat{x}(0) = \hat{x}_0, \\ y_c(t) = B_c^\top Q_c\hat{x}(t), \\ y_r(t) = B_d^\top Q_c\hat{x}(t). \end{cases} \tag{3.4}$$

with $B_c = L$ and $u_c(t) = y(t)$. The inputs of this system are $u_c(t)$ and $r(t)$ with conjugated outputs $y_c(t)$ and $y_r(t)$, respectively. Then, the closed-loop dynamics when using *control by interconnection* with the passive interconnection

$$\begin{pmatrix} u(t) \\ u_c(t) \end{pmatrix} = \begin{pmatrix} 0 & -1 \\ 1 & 0 \end{pmatrix} \begin{pmatrix} y(t) \\ y_c(t) \end{pmatrix} + \begin{pmatrix} 1 \\ 0 \end{pmatrix} r(t) \tag{3.5}$$

between (2.16) and (3.4) is equivalent to the closed-loop dynamics between (3.1) and (2.16). In the following proposition, the matching conditions (3.3) guaranteeing the equivalence between the scheme of Figure 3.2 and the scheme of Figure 3.3 are made explicit.

Proposition 1. *The original OBSF controller* (3.1) *applied to* (2.16) *using the scheme of Figure 3.2 is equivalent to the control by interconnection between* (2.16) *and* (3.4) *through* (3.5) *as shown in Figure 3.3 if the following matching conditions are satisfied*

$$\begin{aligned} (J_c - R_c)Q_c &= A_d - B_dK - LC_d, \\ B_c^TQ_c &= K, \\ B_c &= L. \end{aligned} \tag{3.6}$$

Proof. *The matching equations* (3.6) *are directly obtained replacing* (3.1a) *in* (3.1b) *and identifying with* (3.4) *in order to get a passive and collocated dynamic controller. The first matching condition in* (3.6) *is obtained from* (3.3)*, the second matching condition in* (3.6) *is such that* $y_c(t)$ *is a conjugated output of* $u_c(t)$*. The last condition in* (3.6) *is obtained such that* $y(t)$ *is an input of the controller* (3.4). ■

Then, solving the algebraic equation (3.6) of Proposition 1 and imposing $R_c > 0$ to the controller, we can show the asymptotic stability of the closed-loop system between the discretized model (2.16) and the OBSF controller (3.4) through the passive interconnection (3.5) (Figure 3.3).

Theorem 3.3.1. *The interconnection* (3.5) *between* (2.16) *and* (3.4) *is asymptotically stable and converges to zero if* $R_c = R_c^T > 0$ *and* $r(t) = 0$. ◊

Proof. *Consider the total energy as Lyapunov function*

$$V(x_d, \hat{x}) = \frac{1}{2} x_d^T Q_d x_d + \frac{1}{2} \hat{x}^T Q_c \hat{x}$$

Then from (2.16) *and* (3.4) *we have*

$$\dot{V}(x_d, \hat{x}) = -{x_d}^T Q_d R_d Q_d x_d - \hat{x}^T Q_c R_c Q_c \hat{x},$$

with $R_d \geq 0$ *and* $R_c > 0$. *From Lasalle's invariance principle the system converges to the invariant set corresponding to* $\dot{V}(x_d, \hat{x}) = 0$, *i.e.* $\hat{x} = 0$ *(since* $R_c > 0$*). In this case,* $\hat{x} = 0$ *implies* $\dot{\hat{x}} = 0$, *which implies* $B_c u_c = 0$ *(from* (3.4) *and* $r = 0$*). The controller being controllable implies* $u_c = 0$ *and* $\hat{x} = 0$ *implies* $y_c = 0$ *(from* (3.4)*). From the interconnection* (3.5) $y = u_c = 0$ *and* $u = -y_c = 0$ *(since* $r = 0$*). The system* (2.16) *being observable implies that the only equilibrium point is* $x_d = 0$.

■

In Theorem 3.3.1 we show that the OBSF controller (3.4) stabilizes asymptotically the discretized model (2.16). In the following section we show that the same OBSF controller stabilizes asymptotically the BC-PHS (2.10)-(2.12).

3.4. Asymptotic stability analysis

Now, we apply the OBSF controller (3.4) to the BC-PHS (2.10)-(2.12) in a power preserving way as it is shown in Figure 3.4, where $\mathcal{P}$ refers to the BC-PHS (2.10)-(2.12) and C refers to the OBSF controller (3.4). In the following theorem, we show that the controller (3.4), being *strictly positive real*, stabilizes asymptotically the BC-PHS (2.10)-(2.12).

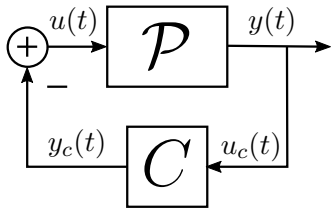

Figure 3.4: Closed-loop system between a BC-PHS and a finite-dimensional controller

Theorem 3.4.1. *Consider the closed-loop system obtained from the passive interconnection* (3.5) *between the BC-PHS* (2.10)-(2.12) *and the OBSF controller* (3.4) *with* $r(t) = 0$ *as shown in Figure 3.4. If the matrix* R_c *from the OBSF controller* (3.4) *is strictly positive definite, then the followings results hold*

(i) The closed-loop system is well-posed.

(ii) The closed-loop system is asymptotically stable.

◊

Proof. *The controller* (3.4) *is strictly positive real (SPR) if* R_c *is strictly positive definite. Then, the proof follows the same line of (Villegas, 2007, Chapter 5.1.2), with the only difference coming from the controller output* $y_c(t) = C_c \hat{x}(t)$, *with* $C_c = B_c^T Q_c$, *which does not depend on the controller input* $u_c(t)$ *as in the case of (Villegas, 2007, Chapter 5.1.2). Then, the result* (i) *of Theorem 3.4.1 is a direct application of (Villegas, 2007, Theorem 5.8).*

The result (ii) of Theorem 3.4.1 is shown using LaSalle's invariance principle extended to infinite-dimensional systems. First, the precompactness of the solution trajectories of the closed-loop system are guaranteed in (Villegas, 2007, Theorem 5.9). Then, we define the total energy as a Lyapunov function

(3.7)

Using (2.10)-(2.12), (3.4), *and* (3.5) *we obtain*

$$\dot{E}_c(t) = -\hat{x}(t)^T Q_c R_c Q_c \hat{x}(t). \tag{3.8}$$

From LaSalle's invariance principle ((Luo et al., 2012, Theorem 3.64)), it follows that the solutions of the closed-loop system tend to the maximal invariant set of

$$\vartheta_c = \{x \in L_2([a,b],\mathbb{R}^n),\ \hat{x} \in \mathbb{R}^{n_c} \mid \dot{E}_c(t) = 0\}. \tag{3.9}$$

We define the largest invariant subset of ϑ_c as $\mathcal{I}$, and then, we show that $\mathcal{I}$ only contains the zero state, i.e. $\mathcal{I} = \{x(\zeta,t) = 0,\ \hat{x}(t) = 0\}$. From (3.8), *$\dot{E}_c = 0$ implies $\hat{x}(t) = 0$ and that implies $\dot{\hat{x}}(t) = 0$. Since $r(t) = 0$,* (3.4) *implies $y_c(t) = 0$ and $B_c u_c(t) = 0$. Since the controller* (3.4) *is controlable, $\hat{x}(t) = 0$ and $y_c(t) = 0$ implies $u_c(t) = 0$. Finally, the interconnection* (3.5) *implies $u(t) = 0$ and $y(t) = 0$. Then, since the invariant solution of the closed-loop system, subject to $\dot{E}_c = 0$, corresponds to the solution of the PDE with all the boundary variables set to zero, hence from Holmgren's Theorem (See (John, 1949)) the only solution is $x(\zeta,t) = 0$. Thus, the asymptotic stability of the closed-loop is guaranteed.* ■

Theorem 3.4.1 uses the passive interconnection (3.5) considering that the full inputs and outputs are available for the interconnection between the BC-PHS and the OBSF controller. However, this is not always possible and some times only some parts of the inputs and outputs are used for the interconnection as shown in Figure 3.5. This is for instance, the case of the string attached at one side and actuated at the other side. In these cases, we have to assume that the BC-PHS is *approximately observable* with respect to the interconnected output (as for example the output $y_1(t)$ from Figure 3.5). *Approximate observability* (Curtain and Zwart, 2012, Corollary 4.1.14) states that if the output of a system with homogenous input is zero for a period of time, then the state of the system is zero as well. Using this property, similarly to Theorem 3.4.1, we can use LaSalle's invariance principle to show that the closed-loop system is asymptotically stable.

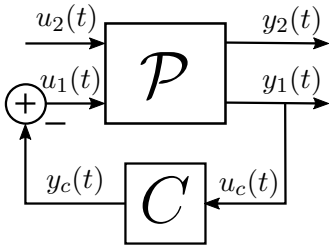

Figure 3.5: Closed-loop system between a BC-PHS and a finite-dimensional controller by partial interconnection

Corollary 3.4.1. *Consider the closed-loop scheme of Figure 3.5, where $\mathcal{P}$ is the impedance energy preserving BC-PHS* (2.10)-(2.12) *with*

$$u(t) = \begin{pmatrix} u_1(t) \\ u_2(t) \end{pmatrix} \quad \textit{and} \quad y(t) = \begin{pmatrix} y_1(t) \\ y_2(t) \end{pmatrix},$$

and C is the OBSF controller (3.4) *with $r(t) = 0$. Provided that the closed-loop system is well-posed and that the solution trajectories are precompact, If the matrix $R_c > 0$, $u_2(t) = 0$, and*

(2.10)-(2.12) *is approximately observable with respect to the output* $y_1(t)$*, then the closed-loop system is asymptotically stable.* ◊

Proof. *We consider the following as a Lyapunov function:*

$$V(t) = \frac{1}{2}\int_a^b x(\zeta,t)^T \mathcal{H}(\zeta) x(\zeta,t) d\zeta + \frac{1}{2}\hat{x}(t)^T Q_c \hat{x}(t).$$

It follows from LaSalle's invariance principle (See (Luo et al., 2012, Theorem 3.64)) that all solutions of the closed-loop system tend to the maximal invariant set of

$$\vartheta_c = \{x \in L_2([a,b],\mathbb{R}^n),\ \hat{x} \in \mathbb{R}^{n_c} \mid \dot{V}(t) = 0\}. \tag{3.10}$$

We define the maximal invariant subset of ϑ_c *as* $\mathcal{I}$*, and we show that* $\mathcal{I}$ *only contains the zero state, i.e.* $\mathcal{I} = \{x(\zeta,t) = 0,\ \hat{x}(t) = 0\}$*. From* (2.10)-(2.12)*,* (3.4)*, and* $r(t) = 0$*, we obtain the following balance for the Lyapunov function:*

$$\dot{V}(t) = -\hat{x}(t)^T Q_c R_c Q_c \hat{x}(t). \tag{3.11}$$

Since $R_c > 0$*,* $\dot{V}(t) = 0$ *implies* $\hat{x}(t) = 0$*, which implies* $\dot{\hat{x}}(t) = 0$*. Then, from* (3.4) $B_c u_c(t) = 0$*. Since the controller is controllable,* $u_c(t) = 0$*. Since* $\hat{x}(t) = 0$*, from* (3.4) $y_c(t) = 0$*. Since* $u_c(t) = y_c(t) = 0$*, from the interconnection (Figure 3.5)*

$$\begin{pmatrix} u_1(t) \\ u_c(t) \end{pmatrix} = \begin{pmatrix} 0 & -1 \\ 1 & 0 \end{pmatrix} \begin{pmatrix} y_1(t) \\ y_c(t) \end{pmatrix},$$

we can conclude $y_1(t) = u_1(t) = 0$*. Then, the maximal invariant set* $\mathcal{I}$ *contains* $\hat{x} = 0$ *and the solution of the following BC-PHS:*

$$\begin{cases} \dfrac{\partial x}{\partial t}(\zeta,t) = P_1 \dfrac{\partial}{\partial \zeta}(\mathcal{H}(\zeta)x(\zeta,t)) + P_0 \mathcal{H}(\zeta)x(\zeta,t), \quad x(\zeta,0) = x_0(\zeta), \\ W_{\mathcal{B}} \begin{pmatrix} f_\partial(t) \\ e_\partial(t) \end{pmatrix} = \begin{pmatrix} u_1(t) \\ u_2(t) \end{pmatrix} = \begin{pmatrix} 0 \\ 0 \end{pmatrix}, \\ y(t) = W_{\mathcal{C}} \begin{pmatrix} f_\partial(t) \\ e_\partial(t) \end{pmatrix} = \begin{pmatrix} y_1(t) \\ y_2(t) \end{pmatrix} = \begin{pmatrix} 0 \\ y_2(t) \end{pmatrix}. \end{cases}$$

By definition, the latter is approximately observable with respect to $y_1(t)$*. This implies that if* $y_1(t) = 0$ *for an interval of* t*, then the state is such that* $x(\zeta,t) = 0$ *(See (Curtain and Zwart, 2012, Corollary 4.1.14)). Then, the maximal invariant set* $\mathcal{I}$ *only contains the states* $x(\zeta,t) =$ *and* $\hat{x}(t) = 0$*. Thus, by LaSalle's invariance principle, the asymptotic stability of the closed-loop system is guaranteed.* ■

In the following two sections, two methods are provided for the synthesis of the matrices K and L such that the OBSF controller is on the form (3.4) with $R_c > 0$. Then, the asymptotic stability is preserved when applying it to the BC-PHS (2.10)-(2.12) (Figure 3.4 or Figure 3.5). In the first method, the gain K is freely designed using classical control tools and the gain L is designed such that the OBSF controller is passive. In the second method, the gain L is freely designed using classical control tools and the gain K is designed such that the OBSF controller is passive.

3.5. Observer design for a specific state feedback

In this section, the state feedback gain K is first designed using an approach like *LQR* (Anderson and Moore, 2007), pole-placement (Brasch and Pearson, 1970), *control by interconnection* using *Casimirs* (Ortega et al., 2008), or IDA-PBC (Ortega et al., 2002; Prajna et al., 2002). Then, by solving an *algebraic Riccati equation* (ARE), the observer gain L is designed in order to satisfy the matching conditions of Proposition 1. This section is organized as follows. First, the methodology is proposed, and then, the vibrating string and the Timoshenko beam are used as examples.

3.5.1. Design method

The gains K and L are designed on the discretized model (A_d, B_d, C_d) from (2.16). The discretized model is an approximation of the BC-PHS (2.10)-(2.12). Then, we have to choose n_d (from (2.16)) large enough to have similar performances when applying the OBSF controller to the discretized model than when applying it to the BC-PHS. Since the pair (A_d, B_d) is controllable, the matrix K is chosen with classical control tools such that the following assumption is satisfied.

Assumption 3.5.1. *The gain K is designed such that $A_d - B_d K$ is Hurwitz.* ◊

Remark 3.5.1. *In this case, the design of the state feedback is free and it can be achieved by using traditional methods such as LQR, pole-placement or the LMI passivity based control proposed in (Prajna et al., 2002).* ◊

After designing the gain K such that $A_d - B_d K$ is Hurwitz, we have to design the gain L such that the OBSF controller is passive. To this end, we fix the matrix R_c and we obtain the matrices J_c, Q_c and L such that the matching conditions of Proposition 1 are satisfied. To this end, we have to chose $R_c > 0$ in such a way that there exists a solution for the matching conditions (3.6).

Assumption 3.5.2. *The matrix R_c is chosen positive definite such that the following matrix*

$$H_M = \begin{pmatrix} A_K & 2R_c \\ -C_K & -A_K^T \end{pmatrix} \tag{3.12}$$

with

$$A_K = A_d - B_d K, \quad C_K = -(K^T C_d + C_d^T K), \tag{3.13}$$

has no pure imaginary eigenvalues. ◊

The matrix H_M in (3.12) is known as the Hamiltonian matrix related to the *algebraic Riccati equation* (ARE) (3.14). If the H_M has no pure imaginary eigenvalues, then there exists a solution $Q_c = Q_c^T > 0$ for the ARE (3.14). A simple choice to have solution is the choice of $R_c = \alpha I_{n_c}$ for some $\alpha > 0$ small enough such that the matrix (3.12) has no pure imaginary eigenvalues. Finally, using the following proposition, we can complete the design and obtain the gain L such that the matching conditions (3.6) are satisfied.

Proposition 2. *Let Assumptions 3.5.1 and 3.5.2 be satisfied. There exists a matrix $Q_c = Q_c^T > 0$, solution of the algebraic Riccati equation (ARE)*

$$A_K^T Q_c + Q_c A_K + 2Q_c R_c Q_c + C_K = 0, \tag{3.14}$$

such that the matching equations (3.6) are satisfied with

$$\begin{aligned} J_c &= \frac{1}{2}\left[A_K Q_c^{-1} - Q_c^{-1} A_K^T - Q_c^{-1}(K^T C_d - C_d^T K) Q_c^{-1}\right], \\ B_c &= Q_c^{-1} K^T, \\ L &= B_c. \end{aligned} \tag{3.15}$$

Furthermore, the matrix $A_d - LC_d$ is Hurwitz.

Proof. *From (Kosmidou, 2007) it is known that if the Hamiltonian matrix (3.12) has no pure imaginary eigenvalues then there exists a solution $Q_c = Q_c^T > 0$ for (3.14). Hence we only need to prove that (3.14) is compatible with the matching equation (3.6) for J_c and L as in (3.15). Since Q_c is invertible and solution of (3.14) we have*

$$\begin{aligned} R_c &= -\frac{1}{2}\left[Q_c^{-1} A_K^T + A_K Q_c^{-1} + Q_c^{-1} C_K Q_c^{-1}\right] \\ &= -\frac{1}{2}\left[Q_c^{-1} A_K^T + A_K Q_c^{-1} - Q_c^{-1}(K^T C_d + C_d^T K) Q_c^{-1}\right]. \end{aligned} \tag{3.16}$$

Then, using (3.15) and (3.16) we have

$$\begin{aligned}(J_c - R_c)Q_c &= \frac{1}{2}(2A_K Q_c^{-1} - 2Q_c^{-1}K^T C Q_c^{-1})Q_c \\ &= A_K - Q_c^{-1}K^T C \\ &= A_K - LC \\ &= A_d - B_d K - LC_d\end{aligned} \tag{3.17}$$

which corresponds to (3.6). From Theorem 3.3.1 the closed-loop system

$$\frac{d}{dt}\begin{pmatrix} x_d \\ \hat{x}\end{pmatrix} = \begin{pmatrix} A_d & -B_d K \\ B_c C_d & (J_c - R_c)Q_c\end{pmatrix}\begin{pmatrix} x_d \\ \hat{x}\end{pmatrix} + \begin{pmatrix} B_d \\ B_d\end{pmatrix} r \tag{3.18}$$

is asymptotically stable. Applying the following transformation

$$\begin{pmatrix} x_d \\ \tilde{x}\end{pmatrix} = \begin{pmatrix} I & 0 \\ I & -I\end{pmatrix}\begin{pmatrix} x_d \\ \hat{x}\end{pmatrix},$$

the closed-loop system (3.18) can be written

$$\frac{d}{dt}\begin{pmatrix} x_d \\ \tilde{x}\end{pmatrix} = \begin{pmatrix} A_K & B_d K \\ A_K - B_c C_d - A_c & A_c + B_d K\end{pmatrix}\begin{pmatrix} x_d \\ \tilde{x}\end{pmatrix} + \begin{pmatrix} B_d \\ B_d\end{pmatrix} r \tag{3.19}$$

with $A_K = A_d - B_d K$, $B_c = L$ and $A_c = (J_c - R_c)Q_c = A_d - B_d K - LC_d$ or equivalently

$$\frac{d}{dt}\begin{pmatrix} x_d \\ \tilde{x}\end{pmatrix} = \begin{pmatrix} A_d - B_d K & B_d K \\ 0 & A_d - LC_d\end{pmatrix}\begin{pmatrix} x_d \\ \tilde{x}\end{pmatrix} + \begin{pmatrix} B_d \\ 0\end{pmatrix} r \tag{3.20}$$

Since A_K is Hurwitz, and the closed-loop system asymptotically stable, $A_d - LC_d$ is also Hurwitz. ■

Note that, using Proposition 2 the design of the matrix L depends on the matrix K, and then, the separation principle is not satisfied using this methodology. However, an important benefit of using this approach is that the controller (3.1) can stabilize not only the discretized model (2.16) but also the BC-PHS (2.10)-(2.12).

Theorem 3.5.1. *Consider the BC-PHS (2.10)-(2.12) controlled by (3.1) with K and L designed using Proposition 2. The closed-loop system converges asymptotically to zero for $r(t) = 0$.* ◊

Proof. *The proof is a direct application of Theorem 3.4.1. By Proposition 2, since R_c is positive definite, the controller is SPR and then, from Theorem 3.4.1, the closed-loop is asymptotically stable.* ■

In the following, we present a summary of the design procedure of the OBSF controller proposed in this section. Then, the procedure is exemplified in the following sections using the vibrating string and the Timoshenko beam as examples.

Procedure 3.5.1. *The design procedure is summarized as follows:*

Step 1: Represent the BC-PHS as in (2.10)-(2.12).

Step 2: Derive a structure-preserving finite-dimensional approximation P as in (2.16).

Step 3: Design K such that $A_d - B_d K$ is Hurwitz.

Step 4: Choose a matrix $R_c > 0$ such that H_M in (3.12) has no pure imaginary eigenvalues. For example $R_c = \alpha I_{n_c}$ with $\alpha > 0$.

Step 5: Solve the ARE (3.14) to find Q_c.

Step 6: Implement the OBSF controller with $L = Q_c^{-1} K^T$.

$\Diamond$

3.5.2. Application examples

In this section, we use the vibrating string example to show the design procedure proposed in Procedure 3.5.1.

Example 3.5.1. *We consider the vibrating string with normalized mass density and Young's modules $\rho(\zeta) = T(\zeta) = 1$, and $\zeta \in [a, b] = [0, 1]$. The string is attached at $\zeta = 0$ and it is controlled with a force actuator at $\zeta = 1$. By only measuring the velocity at $\zeta = 1$, we aim to apply a state feedback control law obtained using energy shaping and damping injection.*
Now, we follow the Procedure 3.5.1 to design the OBSF controller.
Step 1. The dynamical system is represented as a BC-PHS

$$\frac{\partial}{\partial t}\begin{pmatrix} q(\zeta,t) \\ p(\zeta,t) \end{pmatrix} = \begin{pmatrix} 0 & 1 \\ 1 & 0 \end{pmatrix} \frac{\partial}{\partial \zeta}\begin{pmatrix} q(\zeta,t) \\ p(\zeta,t) \end{pmatrix}, \quad \begin{pmatrix} q(\zeta,0) \\ p(\zeta,0) \end{pmatrix} = \begin{pmatrix} q_0(\zeta) \\ p_0(\zeta) \end{pmatrix},$$
$$p(0,t) = 0,$$
$$q(1,t) = u(t),$$
$$y(t) = p(1,t),$$

where $q(\zeta,t)$ and $p(\zeta,t)$ are the displacement and the momentum of the string, respectively. $u(t)$ and $y(t)$ are respectively, the force and the velocity at the right side of the string. In this case, the vibrating string has no internal dissipation. This makes more difficult the stabilization than the case in which internal dissipation is included.
Step 2. The finite-dimensional approximation of the BC-PHS is obtained using the method as shown in Section 2.4 with $n_d = 8$, that corresponds to 4 elements for the force and 4 elements for the velocity. The discretized model is represented as (2.16) with

$$x_d(t) = \begin{bmatrix} q_d(t) \\ p_d(t) \end{bmatrix}, \quad u(t) = q(1,t), \quad y(t) = p_4(t).$$

$$q_d(t) = \begin{bmatrix} q_1(t) \\ \vdots \\ q_4(t) \end{bmatrix}, \qquad p_d(t) = \begin{bmatrix} p_1(t) \\ \vdots \\ p_4(t) \end{bmatrix},$$

where $q_i(t)$ and $p_i(t)$ with $i = \{1, 2, 3, 4\}$ are respectively, the approximation of the strain (force) and the momentum (velocity) along ζ. The matrices of the discretized model (2.16) are

$$J_d = \begin{bmatrix} 0_4 & D \\ -D^T & 0_4 \end{bmatrix}, \quad R_d = \begin{bmatrix} 0_4 & 0_4 \\ 0_4 & 0_4 \end{bmatrix}, \quad Q_d = h\begin{bmatrix} I_4 & 0_4 \\ 0_4 & I_4 \end{bmatrix}, \quad B_d = \begin{bmatrix} 0_{4\times 1} \\ b_b \end{bmatrix}$$

$$D = \frac{1}{h^2}\begin{bmatrix} 1 & 0 & 0 & 0 \\ -1 & 1 & 0 & 0 \\ 0 & -1 & 1 & 0 \\ 0 & 0 & -1 & 1 \end{bmatrix}, \quad b_b = \frac{1}{h}\begin{bmatrix} 0 \\ 0 \\ 0 \\ 1 \end{bmatrix}$$

where $h = \frac{2}{9}$ *is the spatial distance between two consecutive variables as for example* $h = \zeta_q^2 - \zeta_q^1 = \zeta_p^2 - \zeta_1^1$.

Step 3. The control law is obtained by using energy shaping and damping injection (Macchelli et al., 2020). The control law ends in the following state feedback:

$$u(t) = -\int_0^1 q(\zeta, t)d\zeta - p(1, t),$$

that it is approximated in terms of the discretized model as follows

$$u(t) = -h\sum_{i=1}^{4} q_i(t) - p_4(t),$$

or equivalently as

$$u(t) = -Kx_d(t)$$

with

$$K = \begin{bmatrix} h & h & h & h & 0 & 0 & 0 & 1 \end{bmatrix}.$$

The closed-loop matrix $A_K = A_d - B_d K$ *is Hurwitz, since all its eigenvalues have negative real part as shown in Figure 3.6.*

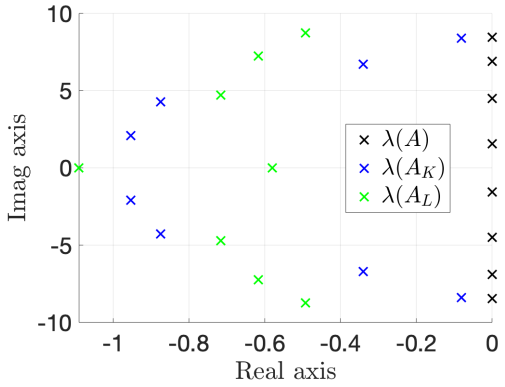

Figure 3.6: Plant eigenvalues $\lambda(A)$, controller eigenvalues $\lambda(A_K)$, and observer eigenvalues $\lambda(A_L)$.

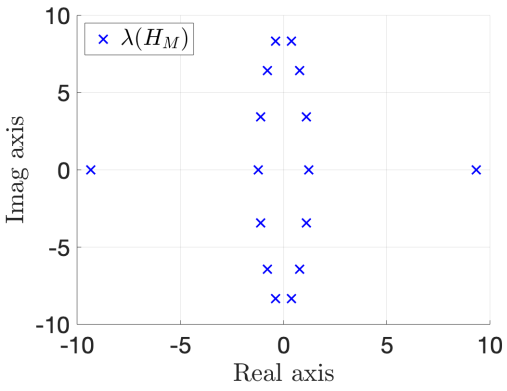

Figure 3.7: Hamiltonian matrix eigenvalues $\lambda(H_M)$.

Step 4. For simplicity, we chose a matrix R_c as a diagonal matrix such that

$$R_c = \begin{pmatrix} 10 & \cdots & 0 & 0 \\ \vdots & \ddots & \vdots & \vdots \\ 0 & \cdots & 10 & 0 \\ 0 & \cdots & 0 & 20 \end{pmatrix}.$$

The matrix H_M has no eigenvalues on the imaginary axis as shown in Figure 3.7. Note that, the last element of the diagonal of R_c is chosen bigger than the other ones since the last state variable of the observer is the one related to the available sensor $y(t) = p(1,t)$.
Step 5. We solve the algebraic Riccati equation (3.14) using the numerical method proposed in (Lanzon et al., 2008). The eigenvalues of the matrix Q_c are all pure real and positive define as we show in Figure 3.8.
Step 6. We compute $L = Q_c^{-1}K$. The eigenvalues of $A_L = A_d - LC_d$ are shown in Figure 3.6.

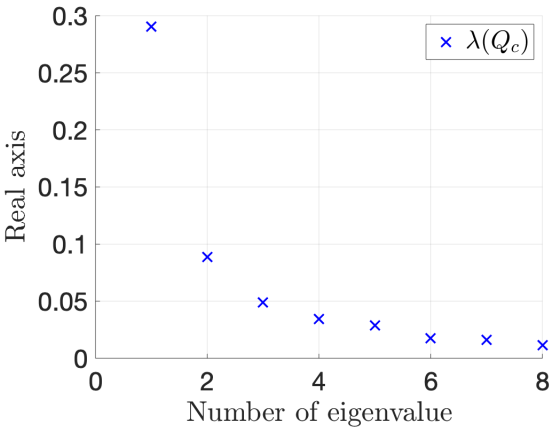

Figure 3.8: Eigenvalues of Q_c $\lambda(Q_c)$

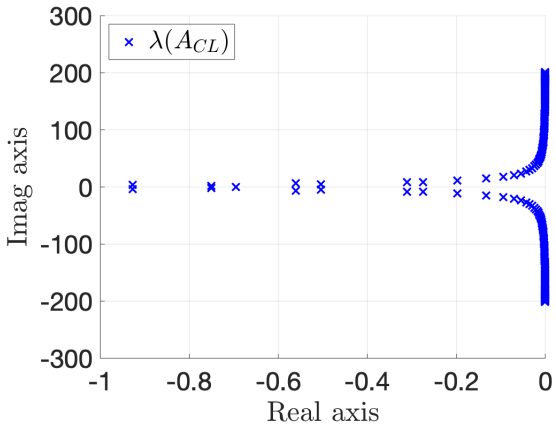

Figure 3.9: Closed-loop eigenvalues $\lambda(A_{CL})$

Finally, we simulate the closed-loop system between the designed OBSF controller and a new discretized model (2.16) that uses $n_d = 200$, i.e. a more precise model of the BC-PHS (2.10)-(2.12). In this case, the closed-loop system is composed by 208 states and all the closed-loop eigenvalues are in the left hand side of the imaginary axis as Figure 3.9 shows. Note that, the stability is preserved when applying the OBSF controller to a new model that it has not been used for the design. This is due to the structure imposed to the OBSF controller and not in the model used for design.
We simulate the closed-loop system with initial conditions $w_0(\zeta) = 0.1\zeta$, $q_0(\zeta) = 0.1$, $p_0(\zeta) = 0$, and $\hat{x}_0 = 0$. Figure 3.10 shows the string deformation in closed-loop, and Figure 3.11 shows the estimated one. Note that, since the size of the model used for the design is $n_d = 8$, some high frequency modes are not considered for the OBSF design. Then, the oscillations due to these frequency modes are not controlled as we can see in Figures 3.10 and 3.11. To reduce these oscillations, a more precise model has to be used for the design. In the following, we repeat the design from Step 2 using a more precise discretized model for the design.
Step 2. If we chose $n_d = 80$, the discretized model is represented as (2.16) with the same structure as before.
Step 3. Similarly as before, the state feedback matrix is obtained as follows:

$$K = \begin{bmatrix} h & \cdots & h & 0 & \cdots & 0 & 1 \end{bmatrix}_{40\times 1}.$$

The closed-loop matrix $A_K = A_d - B_d K$ is Hurwitz and its eigenvalues are shown in Figure 3.12.

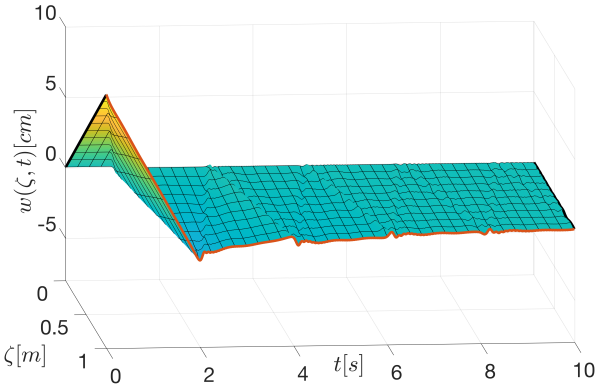

Figure 3.10: Deformation.

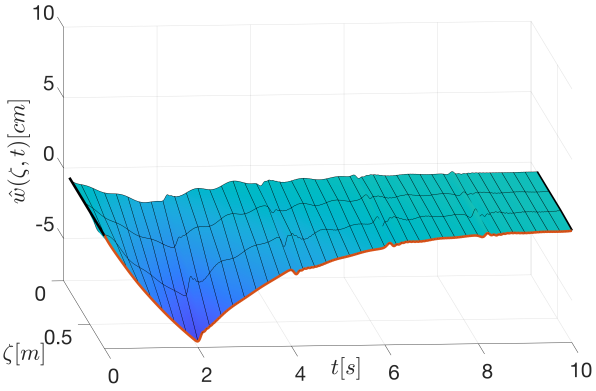

Figure 3.11: Observed deformation.

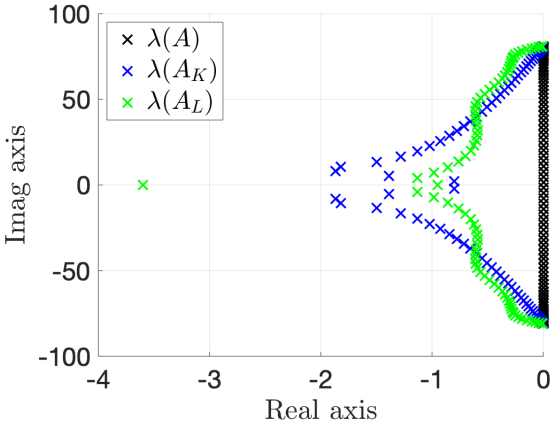

Figure 3.12: Plant eigenvalues $\lambda(A)$, controller eigenvalues $\lambda(A_K)$, and observer eigenvalues $\lambda(A_L)$.

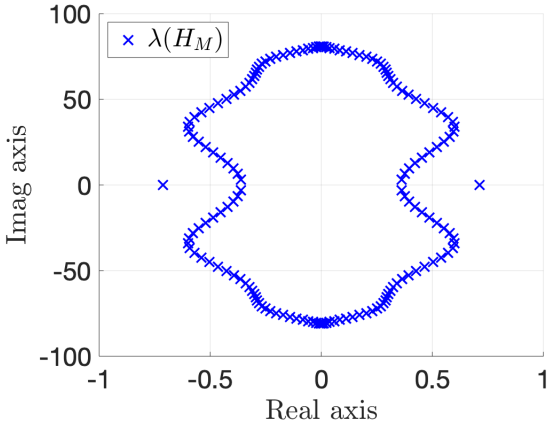

Figure 3.13: Hamiltonian matrix eigenvalues $\lambda(H_M)$.

Step 4. In this case, we chose a matrix R_c as a diagonal matrix such that

$$R_c = \begin{pmatrix} 1 & \cdots & 0 & 0 & 0 & 0 \\ \vdots & \ddots & \vdots & \vdots & \vdots & \vdots \\ 0 & \cdots & 1 & 0 & 0 & 0 \\ 0 & \cdots & 0 & 500 & 0 & 0 \\ 0 & \cdots & 0 & 0 & 500 & 0 \\ 0 & \cdots & 0 & 0 & 0 & 2500 \end{pmatrix}.$$

The matrix H_M has no eigenvalues on the imaginary axis as Figure 3.13.
Step 5. We solve the algebraic Riccati (3.14) *with the numerical method proposed in (Lanzon et al., 2008). The eigenvalues of the matrix Q_c are all pure real and they are shown in Figure 3.14.*
Step 6. We compute $L = Q_c^{-1}K$. The eigenvalues of $A_L = A_d - LC_d$ are shown in Figure 3.12. Finally, we simulate the closed-loop system between the obtained observer-based state feedback controller and a new discretized model (2.16) *that uses $n_d = 200$, i.e. a more precise model of the BC-PHS* (2.10)-(2.12). *In this case, the closed-loop system is composed by* 280 *states and all the closed-loop eigenvalues are in the left hand side of the imaginary axis as Figure 3.15*

shows. Hence, the stability is preserved when applied the observer-based controller to a more precise discretized model of the BC-PHS.

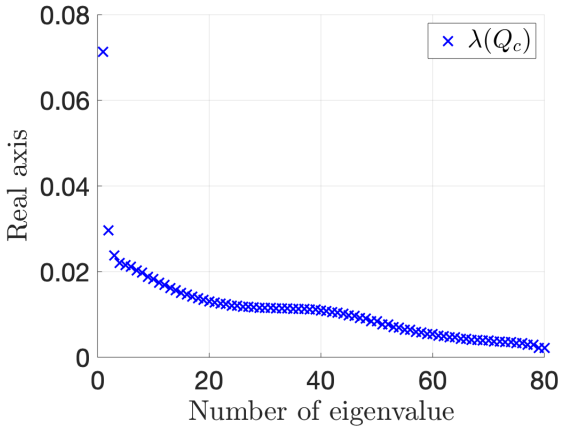

Figure 3.14: Eigenvalues of Q_c $\lambda(Q_c)$.

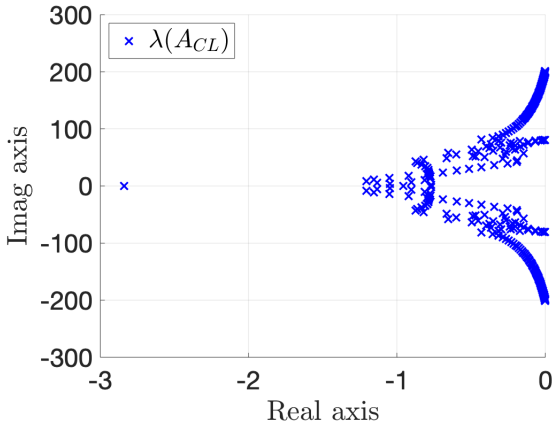

Figure 3.15: Closed-loop eigenvalues $\lambda(A_{CL})$

The initial conditions are $w_0(\zeta) = 0.1\zeta$, $q_0(\zeta) = 0.1$, $p_0(\zeta) = 0$, *and* $\hat{x}_0 = 0$. *Figure 3.16 shows the string deformation in closed-loop, and Figure 3.17 shows the estimated one. Different to the previous simulation (Figure 3.10 and Figure 3.11), now the oscillations are reduced. This is mainly due to the fact that more frequency modes are taken into account for the observer-based state feedback controller.*

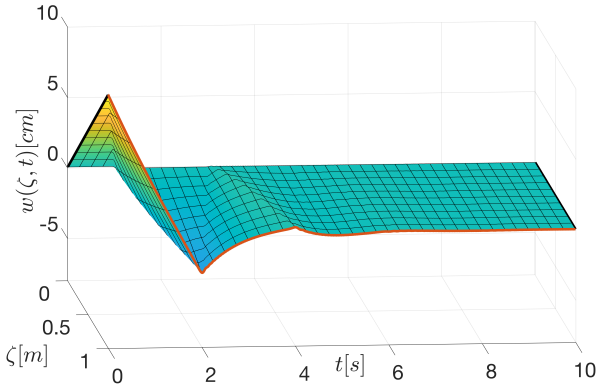

Figure 3.16: Deformation.

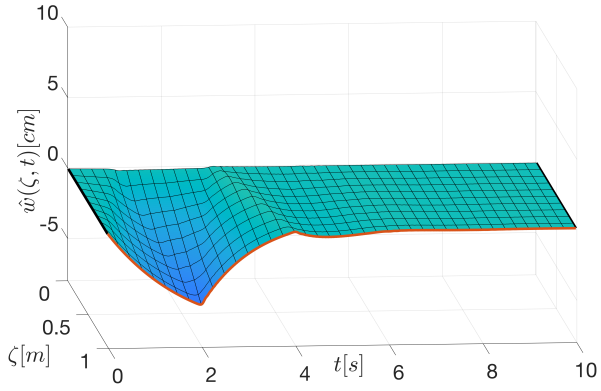

Figure 3.17: Observed deformation.

◊

3.6. State feedback design for a specific observer

Different to the previous section, the methodology proposed in this section allows to design the observer gain L (as a dual problem of designing K) with different approaches like LQR (Anderson and Moore, 2007), pole-placement (Brasch and Pearson, 1970), *control by interconnection* using *Casimirs* (Ortega et al., 2008), or IDA-PBC (Ortega et al., 2002; Prajna et al., 2002). Then, by solving a set of *linear matrix inequalities* (LMIs), we perform the state feedback gain K in order to satisfy the matching conditions of Proposition 1. This section is organized as follows. First, the methodology is proposed, and then, the Timoshenko beam is used as example.

3.6.1. Design method

Since the pair (A_d, C_d) is observable, the gain L of the observer is chosen with classical control tools such that the following assumption is satisfied.

Assumption 3.6.1. *The gain L is designed such that $A_d - LC_d$ is Hurwitz.* ◊

Remark 3.6.1. *In this case, the design of the observer gain is free and it can be achieved by using traditional methods such as LQR design, pole-placement or the LMI proposed in (Prajna et al., 2002).* ◊

After the gain L is designed such that Assumption 3.6.1 is satisfied, we design the feedback gain K such that the matching conditions (3.6) are satisfied. The degrees of freedom of this methodology are related to the lower and upper bounds of the matrices R_c and Q_c from the OBSF controller (3.4). In the following proposition, the design of the state feedback gain K is achieved by tuning the lower and upper bounds of the matrices R_c and Q_c.

Proposition 3. *Consider the finite-dimensional port-Hamiltonian system (2.16) and the matrix L such that $A_L := A_d - LC_d$ is Hurwitz, if the following LMIs:*

$$\begin{aligned} 2\Gamma_1 - B_d L^\top - L B_d^\top + A_L \mathbf{X} + \mathbf{X} A_L^\top &\leq 0, \\ -2\Gamma_2 + B_d L^\top + L B_d^\top - A_L \mathbf{X} - \mathbf{X} A_L^\top &\leq 0, \\ -\Delta_1^{-1} + \mathbf{X} &\leq 0, \\ \Delta_2^{-1} - \mathbf{X} &\leq 0, \end{aligned} \tag{3.21}$$

have a solution in the unknown matrix $\mathbf{X} = \mathbf{X}^\top$, for some $n_d \times n_d$ symmetric matrices Γ_1, Γ_2, Δ_1 and Δ_2 such that $0 \leq \Gamma_1 < \Gamma_2$ and $0 < \Delta_1 < \Delta_2$, then with the interconnection (3.5) between (2.16) and (3.4) and matrices

$$\begin{aligned} S_c &= A_L \mathbf{X} - B_d L^\top, & J_c &= \tfrac{1}{2}(S_c - S_c^\top), \\ R_c &= -\tfrac{1}{2}(S_c + S_c^\top), & Q_c &= \mathbf{X}^{-1}, \\ B_c &= L, & K &= B_c^\top Q_c, \end{aligned} \tag{3.22}$$

the following results hold:

(i) $\lim_{t\to\infty}(x_d(t) - \hat{x}(t)) = 0$ *with the performances given by the matrix A_L;*

(ii) Matrices R_c and Q_c satisfy

- *(a)* $\Gamma_1 \leq R_c \leq \Gamma_2$;
- *(b)* $\Delta_1 \leq Q_c \leq \Delta_2$;

(iii) The controller (3.4) is a finite-dimensional port-Hamiltonian system. Moreover, if $\Gamma_1 > 0$, it is SPR.

Proof. *Since the error is given by $\tilde{x}(t) = x(t) - \hat{x}(t)$, the result (i) in Proposition 3 is equivalent to prove that the error $\tilde{x}(t)$ converges asymptotically to zero. The error dynamic $\dot{\tilde{x}}(t)$ is obtained from (2.16) and (3.4). Then, replacing the interconnection (3.5) and matrices (3.22) the error dynamic becomes $\dot{\tilde{x}}(t) = (A_d - LC_d)\tilde{x}(t)$. Since $A_L = A_d - LC_d$ is Hurwitz, the error converge asymptotically to zero. For the result (ii), we check from the LMI (3.21) that*

$$\begin{aligned} 2\Gamma_1 \leq B_d L^\top + L B_d^\top - A_L \mathbf{X} - \mathbf{X} A_L^\top \leq 2\Gamma_2 \\ {\Delta_2}^{-1} \leq \mathbf{X} \leq {\Delta_1}^{-1} \end{aligned}$$

Replacing $\mathbf{X}$, S_c *and* $S_c^\top$ *from (3.22) and inverting the second inequality we obtain*

$$2\Gamma_1 \leq -(S_c + S_c^\top) \leq 2\Gamma_2$$
$$\Delta_1 \leq Q_c \leq \Delta_2$$

then, replacing R_c *from (3.22) we can conclude the result (ii). The controller* (3.4) *is a port-Hamiltonian system since* $J_c = -J_c^\top$, $R_c = R_c^\top \geq 0$ *and* $Q_c = Q_c^\top > 0$ *are satisfied from (3.22) and (ii). Finally, by Kalman-Yakubovich-Popov KYP-Lemma, the controller* (3.4) *is SPR if* $R_c > 0$. *The matrix* R_c *is strictly positive definite if the matrix* Γ_1 *so is.* ■

Remark 3.6.2. *The simplest choice for* Γ_1, Γ_2, Δ_1 *and* Δ_2 *is to consider an identity matrix multiplied by a scalar.* ◊

Remark 3.6.3. *Although, the design parameters related to the matrix* R_c *are* Γ_1 *and* Γ_2, *when they are modified, the obtained matrix* Q_c *is also. Similar for the design paramenters* Δ_1 *and* Δ_2 *that are related to the matrix* Q_c. ◊

The design is completed by using Proposition 3. Then, we apply the OBSF controller (3.1) to the BC-PHS (2.10)-(2.12). The closed-loop stability between the BC-PHS and the OBSF controller is guaranteed due to the structure imposed to the OBSF controller. Since, it is SPR the closed-loop system between the BC-PHS and the OBSF controller is asymptotically stable.

Theorem 3.6.1. *Consider the BC-PHS* (2.10)-(2.12) *and the control law* (3.1) *with* K *and* L *designed using Proposition 3. If* $\Gamma_1 > 0$, *the closed-loop system converges asymptotically to zero for* $r(t) = 0$. ◊

Proof. *The proof is a direct application of Theorem 3.4.1. By Proposition 3,* $\Gamma_1 > 0$ *implies* $R_c > 0$. *Since* R_c *is positive definite, the controller is SPR.* ■

In the following, we present a procedure for the design of the observer-based state feedback controller proposed in this section.

Procedure 3.6.1. *The design procedure is summarized as follows:*

Step 1: Represent the BC-PHS as in (2.10)-(2.12).

Step 2: Derive a finite-dimensional approximation P *as in* (2.16).

Step 3: Design L *such that* $A_d - LC_d$ *is Hurwitz.*

Step 4: Choose matrices Γ_1, Γ_2, Δ_1 *and* Δ_2. *For example, the identity by a positive constant.*

Step 5: Solve the LMI (3.21) *to find* Q_c.

Step 6: Implement the OBSF controller with $K = L^T Q_c$.

◊

3.6.2. Application example

In this subsection, the Timoshenko beam is considered to apply the Procedure 3.6.1.

Example 3.6.1. *We consider the Timoshenko beam clamped at the left side and actuated at the right side with force and torque actuators. We consider that the transverse velocity and angular*

velocity are measured. For simplicity, we use unitary parameters as in Table 3.1. Step 1. The Timoshenko beam is represented as a BC-PHS

$$\frac{\partial}{\partial t}\begin{pmatrix} x_1 \\ x_2 \\ x_3 \\ x_4 \end{pmatrix} = \begin{pmatrix} 0 & 1 & 0 & 0 \\ 1 & 0 & 0 & 0 \\ 0 & 0 & 0 & 1 \\ 0 & 0 & 1 & 0 \end{pmatrix} \frac{\partial}{\partial \zeta}\begin{pmatrix} Tx_1 \\ \frac{1}{\rho}x_2 \\ EIx_3 \\ \frac{1}{I_\rho}x_4 \end{pmatrix} + \begin{pmatrix} 0 & 0 & 0 & -1 \\ 0 & 0 & 0 & 0 \\ 0 & 0 & 0 & 0 \\ 1 & 0 & 0 & 0 \end{pmatrix}\begin{pmatrix} Tx_1 \\ \frac{1}{\rho}x_2 \\ EIx_3 \\ \frac{1}{I_\rho}x_4 \end{pmatrix}, \quad x(\zeta,0) = x_0(\zeta),$$

$$\frac{1}{\rho}x_2(a,t) = \frac{1}{I_\rho}x_4(a,t) = 0$$
$$\begin{pmatrix} Tx_1(b,t) \\ EIx_3(b,t) \end{pmatrix} = u(t), \quad y(t) = \begin{pmatrix} \frac{1}{\rho}x_2(b,t) \\ \frac{1}{I_\rho}x_4(b,t) \end{pmatrix}$$

where $u(t)$ contains the force and torque at the right side and $y(t)$ contains the transverse velocity and the angular velocity at the right side.

Table 3.1: Plant Parameters.

	Value	Measurement unit
T	1	Pa
ρ	1	$kg.m^{-1}$
EI	1	$Pa.m^4$
I_ρ	1	$Kg.m^2$
$[a,b]$	$[0,1]$	m

Step 2. The finite-dimensional approximation of the BC-PHS is obtained using the method as shown in Section 2.4 with $n_d = 16$.

The discretized model used for the design is on the form (2.16) *with the following variables:*

$$x_d(t) = \begin{bmatrix} x_1^d(t) \\ x_2^d(t) \\ x_3^d(t) \\ x_4^d(t) \end{bmatrix}, u(t) = \begin{bmatrix} Tx_1(b,t) \\ EIx_3(b,t) \end{bmatrix},$$

$$x_1^d(t) = \begin{bmatrix} x_1^1(t) \\ \vdots \\ x_1^4(t) \end{bmatrix}, \quad x_2^d(t) = \begin{bmatrix} x_2^1(t) \\ \vdots \\ x_2^4(t) \end{bmatrix}, \quad x_3^d(t) = \begin{bmatrix} x_3^1(t) \\ \vdots \\ x_3^4(t) \end{bmatrix}, \quad x_4^d(t) = \begin{bmatrix} x_4^1(t) \\ \vdots \\ x_4^4(t) \end{bmatrix}.$$

The matrices of the discretized model (2.16) *are given by*

$$J_d = \begin{bmatrix} 0_4 & D & 0_4 & -F \\ -D^T & 0_4 & 0_4 & 0_4 \\ 0_4 & 0_4 & 0_4 & D \\ F^T & 0_4 & -D^T & 0_4 \end{bmatrix}, \qquad R_d = \begin{bmatrix} 0_4 & 0_4 & 0_4 & 0_4 \\ 0_4 & 0_4 & 0_4 & 0_4 \\ 0_4 & 0_4 & 0_4 & 0_4 \\ 0_4 & 0_4 & 0_4 & 0_4 \end{bmatrix},$$
$$Q_d = h \begin{bmatrix} TI_4 & 0_4 & 0_4 & 0_4 \\ 0_4 & \frac{1}{\rho} I_4 & 0_4 & 0_4 \\ 0_4 & 0_4 & EII_4 & 0_4 \\ 0_4 & 0_4 & 0_4 & \frac{1}{I_\rho} 4 \end{bmatrix}, \quad B_d = \begin{bmatrix} 0_{4\times 1} & 0_{4\times 1} \\ b_{44} & 0_{4\times 1} \\ 0_{4\times 1} & 0_{4\times 1} \\ b_{43} & b_{44} \end{bmatrix}, \tag{3.23}$$

with

$$D = \frac{1}{h^2} \begin{bmatrix} 1 & 0 & \cdots & 0 \\ -1 & 1 & \ddots & 0 \\ \vdots & \ddots & \ddots & \ddots \\ 0 & 0 & \cdots & 1 \end{bmatrix}_{4\times 4}, \; F = \frac{1}{2h} \begin{bmatrix} 1 & 0 & \cdots & 0 \\ 1 & 1 & \ddots & 0 \\ \vdots & \ddots & \ddots & \ddots \\ 0 & 0 & \cdots & 1 \end{bmatrix}_{4\times 4},$$

$$b_{44} = \frac{1}{h} \begin{bmatrix} 0_{3\times 1} \\ 1 \end{bmatrix}, \quad b_{43} = \frac{1}{2} \begin{bmatrix} 0_{3\times 1} \\ 1 \end{bmatrix},$$

and $h = \frac{2}{9}$. *Note that,* n_d *is a design parameter and it has to be chosen multiple of* 4 *in this case. In order to show the structure of the discretized model, we have considered* $n_d = 16$. *However, for the design we chose different values of* n_d. *We show that increasing the precision of the model used for design, the performances are improved. Note that, when changing* n_d, *the model* (2.16) *preserves the same matrices* (3.23) *with appropriated dimensions and* $h = \frac{2(b-a)}{0.5n_d+1}$.

Step 3. The observer gain L *is designed using IDA-PBC method proposed in (Prajna et al., 2002). This method uses linear matrix inequalities (LMIs) for solving the IDA-PBC problem for LTI systems. It is worth stressing that the gain* L *can be designed using classical approaches like LQR or pole placement. In this example, we use this approach to have a complete design based on LMIs. Note that, due to the duality of the observer and control design, we have to replace* A_d *by* A_d^T, B_d *by* C_d^T *and* F *by* $-L^T$ *in order to obtain the matrix* L.

Three different OBSF controllers are developed. The observer gains are designed using the method proposed in (Prajna et al., 2002) with the design parameters of Table 3.2. Note that, for the observer, designs 1 and 2 are equivalent and the design 3 uses a more precise model for the synthesis. The matrices $A_L = A_d - LC_d$ *are all Hurwitz, we show the eigenvalues of the matrix* A_L *for design 3).*

Step 4. For simplicity, we chose the matrices Γ_1, Γ_2, Δ_1, *and* Δ_2 *as shown in Table 3.3 for the state feedback design. Note that,* $\Gamma_1 > 0$ *in every case, and we only change the design parameters related to the energy matrix* Q_c.

Step 5. The LMI from Proposition 3 is solved using the Matlab@ Robust Control Toolbox. Note that, in every case $\Delta_1 < Q_c < \Delta_2$ *and* $\Gamma_1 < R_c < \Gamma_2$.

Step 6. We compute $K = L^T Q_c$. *The matrix* $A_K = A_d - B_d K$ *is Hurwitz. For the design 3, in Figure 3.18, we show the obtained eigenvalues for the matrices* A_K *and* A_L.

Finally, we simulate the closed-loop system obtained using the OBSF state feedback controllers and a new discretized model (2.16) *that uses* $n_d = 200$, *(a more precise model of the BC-PHS* (2.10)-(2.12)*). For the designs 1 and 2, the closed-loop system is composed by* 220 *states, while*

Table 3.2: Observer design parameters.

	Design1	Design 2	Design 3
Λ_1	$0.1I_{20}$	$0.1I_{20}$	$0.1I_{40}$
Λ_2	$5000I_{20}$	$5000I_{20}$	$5000I_{40}$
Ξ_1	$1I_{18}$	$1I_{18}$	$1I_{38}$
Ξ_2	$1000I_{18}$	$1000I_{18}$	$1000I_{38}$
γ	10	10	10
n_d	5	5	10

Table 3.3: Controller design parameters

Matrix	Design 1	Design 2	Design 3
Γ_1	I_{20}	I_{20}	I_{40}
Γ_2	$1000I_{20}$	$1000I_{20}$	$1000I_{40}$
Δ_1	$0.005I_{20}$	$0.015I_{20}$	$0.015I_{40}$
Δ_2	$1I_{20}$	$1I_{20}$	$0.1I_{40}$
n_d	5	5	10

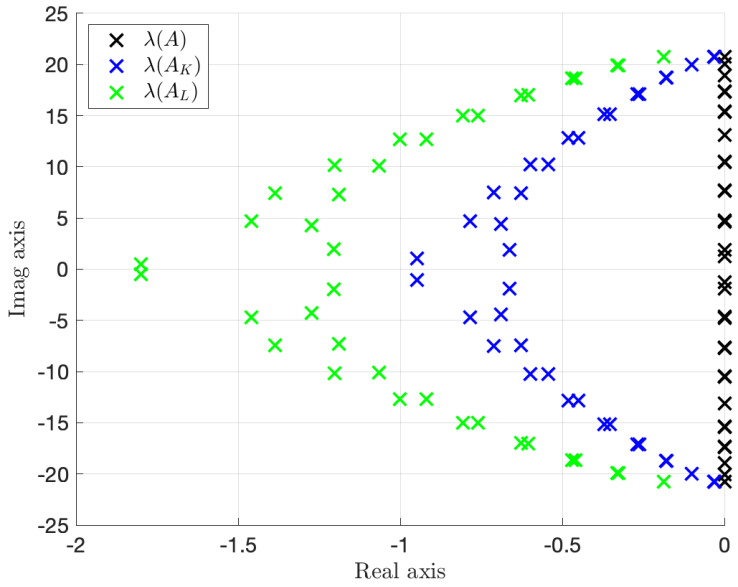

Figure 3.18: Plant $\lambda(A)$, controller $\lambda(A_K)$, and observer eigenvalues $\lambda(A_L)$ (design 3)

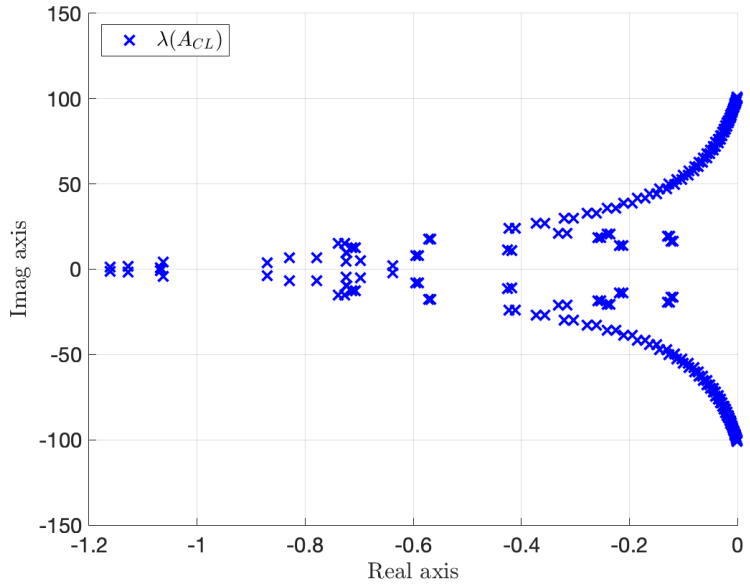

Figure 3.19: Closed-loop eigenvalues $\lambda(A_{CL})$ (design 3)

for the design 3 the closed-loop system is composed by 240 states. For the design 3, the closed-loop eigenvalues are shown in Figure 3.19. The simulation starts from the initial condition

$$
\begin{aligned}
x_1(\zeta, 0) &= 0.01, \\
x_2(\zeta, 0) &= 0, \\
x_3(\zeta, 0) &= -0.01(\zeta - 1), \\
x_4(\zeta, 0) &= 0,
\end{aligned}
$$

corresponding to the equilibrium position associated to a force of $0.01N$ *applied at the end tip of the beam. The initial condition for the observer is* $\hat{x}(0) = 0$.

In Figure 3.20, we show the end-tip displacement of the beam for the three different designs. We can notice that the settling time of design 2 is faster than the one of design 1. This is because the design parameter Δ_1 *is bigger in design 2 than in design 1. This implies a matrix* Q_c *with bigger eigenvalues for design 2 than design 1. Finally, using design 3, we can notice that high-frequency oscillations are attenuated. This is because the model used in design 3 is more precise than the one used for design 2.*

In Figure 3.21 and Figure 3.22, we show the beam deformation along the space and the time for design 1. The settling time is improved using design 2 as shown in Figure 3.23 and Figure 3.24. We can notice that the beam reaches the equilibrium approximately at $t = 6\,s$. *For* $t > 6\,s$, *some high-frequency oscillations remain unattenuated. However, due to the structure imposed on the OBSF controller, these oscillations do not destabilize the closed-loop system.*

Finally, in Figure 3.25 and Figure 3.26, we show the beam deformation along the space and time for design 3. The main difference with design 2 is that in design 3, the OBSF controller contains a more accurate model of the infinite-dimensional system. By increasing n_d *(see Table 3.2 and Table 3.3), some higher frequency oscillations can also be attenuated.*

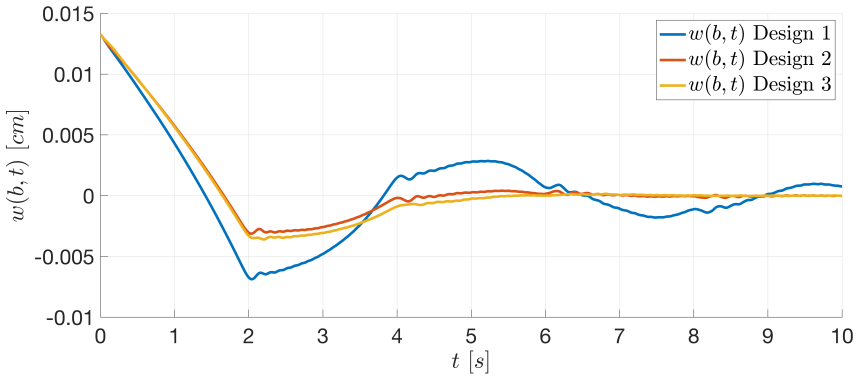

Figure 3.20: End tip deformation

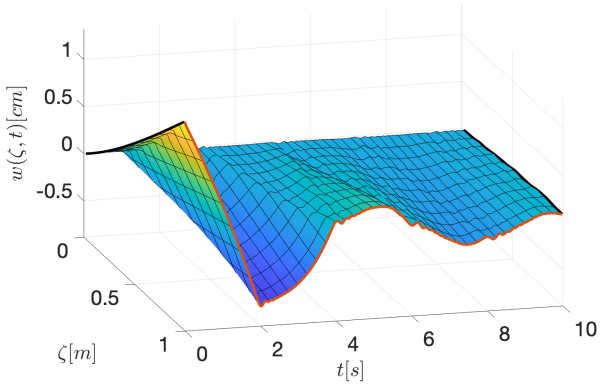

Figure 3.21: Beam deformation

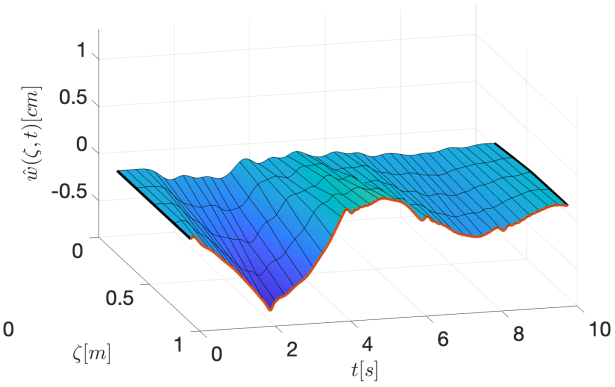

Figure 3.22: Observed deformation

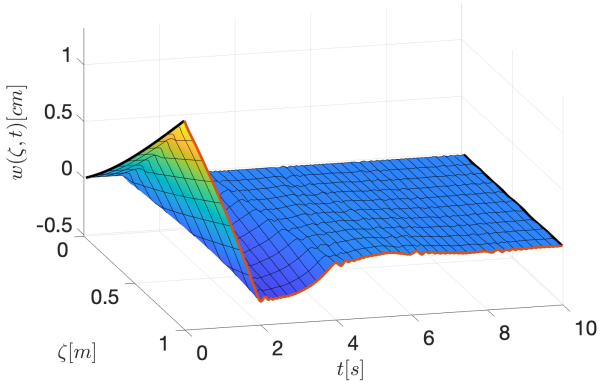

Figure 3.23: Beam deformation

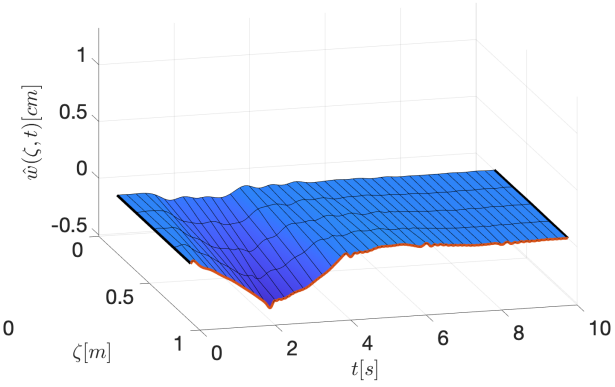

Figure 3.24: Observed deformation

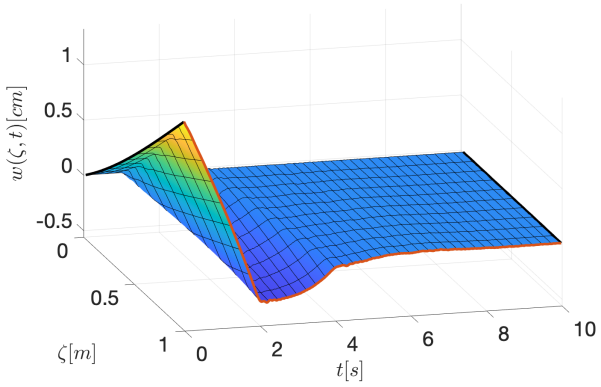

Figure 3.25: Beam deformation

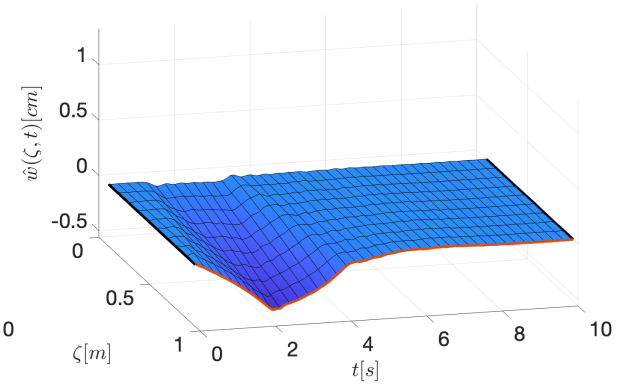

Figure 3.26: Observed deformation

◊

3.7. Summary

In this chapter, we have used the *early-lumping approach* to design OBSF controllers for the stabilization of BC-PHSs. Using this approach, the BC-PHS is first discretized and the synthesis of the OBSF gains is based on the discretized model. To guarantee the closed-loop stability, we have imposed a passive structure on the OBSF controller. We have shown that using this structure, the OBSF controller stabilizes the BC-PHS. Then, we have proposed two methodologies for the synthesis of the OBSF gains.

In the first method, the state feedback gain is freely designed by using classical control techniques, for instance, *linear quadratic regulator* or *pole placement*. Then, the observer gain is designed such that either the OBSF controller achieves a passive structure and some performances are assigned to the observer. In the second method, the observer gain is freely designed and the state feedback gain is designed such that either the OBSF controller achieves the desired structure and some performances are assigned to the state feedback gain. In both cases, the design of one of the two gains (K or L) is not completely free. This is the price to pay to achieve closed-loop stability when applying the OBSF controller to the BC-PHS. To exemplify these methodologies, we have used the vibrating string and the Timoshenko beam models.

Chapter 4

Reduced order distributed control design via energy shaping

4.1. Introduction

In this chapter, we consider the in-domain control of the distributed port Hamiltonian (PH) systems where the actuators and sensors are located within the spatial domain. To deal with this problem, the *early lumped approach* is also employed for in-domain control design of the distributed PH systems. Then the Control by Interconnection (CbI) method is used to design the energy shaping controller for the finite dimensional discretization of the distributed PH systems. The first result on CbI for distributed parameter PHSs with in-domain distributed control can be found in Trenchant et al. (2017) where a positive feedback, late lumping approach and full actuation are investigated. Later on, Malzer et al. (2019) has applied the same late lumping approach, but with negative feedback and jet bundle formalism to design a finite dimensional PH controller for piezo-actuated Euler-Bernoulli beam. The initial conditions have been estimated by an observer proposed in Malzer et al. (2020c). This controller has been extended to a 2D Kirchhoff–Love plate in Malzer et al. (2020b). The Casimir functions proposed in both Malzer et al. (2019) and in Malzer et al. (2020b) establish a relation between the state variables of the plant and those of the controller. Part of the controller state variables are used for energy shaping, whereas the others are for damping injection. Because the jet bundle method focuses more on the geometric properties, the stability of the closed-loop system has not been investigated yet.

Different from existing work presented before, we consider here the CbI of distributed PHS using a negative feedback, an early-lumping approach and a limited number of actuators. The controller design takes all the information of the discretized plant into account to achieve both energy shaping and damping injection at the same time. In this chapter, we present an in-domain CbI control design methodology for the distributed PH system (2.5) with early lumped approach. By using the semigroup theory and passivity properties, we establish the asymptotic stability of the closed-loop system, even when applying the obtained finite-dimensional controller to the infinite-dimensional plant. This successfully eliminates the well-known spillover effect, as documented in Balas (1978, 1982). Furthermore, in addition to achieving asymptotic stabilization of the closed-loop system, our controller can change the dynamic performance of the system over a predefined range of frequencies. It accomplishes this by accelerating the system while minimizing oscillations and overshoot.

Two different cases are investigated for the dynamic performances improvement: the ideal *fully-actuated case* where the control input works independently on each element of the discretized model and the *under-actuated case* where the input acts identically on sets of elements, providing less degrees of freedom. This latter case is closer to the real implementation because the control is usually carried out through actuator patches that act similarly over spatial elements. It is shown

how to change the closed-loop energetic properties of the discretized system in a perfect way when the system is fully-actuated and in an *optimal way* when the system is under-actuated.
This chapter is organized as follows: in Section 4.2, the CbI and energy shaping methods are investigated for both *fully-actuated case* and *under-actuated case* as well as the closed loop stability analysis when the finite dimensional controller is implemented in the distributed PH systems. Section 4.3 provides some simulation results with a comparison between the fully- and under-actuated cases using a vibrating string example. Section 4.4 ends up with conclusions and perspectives.

4.2. Control by interconnection and energy shaping

In this part, we extend the CbI method to the in-domain distributed input and output case. The main difference with CbI for finite dimensional PHSs (van der Schaft, 2000; Ortega et al., 2001) is that the controller uses the overall information of the plant into consideration, as depicted in Fig. 4.1 for an ideal interconnection case. The arrow in Fig. 4.1 represents the signal of both input and output. $\mathbf{u}_d$ and $\mathbf{y}_d$ represent the power conjugated distributed input and output of system (2.16). u_c and y_c are power conjugated input and output of the controller (4.1). These two pairs of input and output are interconnected in a power-preserving way as formulated in (4.2). As a result, one can shape the distributed Hamiltonian function all over the system with an appropriate parametrization of the controller and the use of structural invariants *i.e.* Casimir functions (Duindam et al., 2009). The main objective of the proposed CbI method is to improve the closed-loop performances over a given frequency range while guaranteeing the overall closed-loop stability (v.s. neglected dynamics during the synthesis). One can also modify the equilibrium point by changing the minima of the energy function.

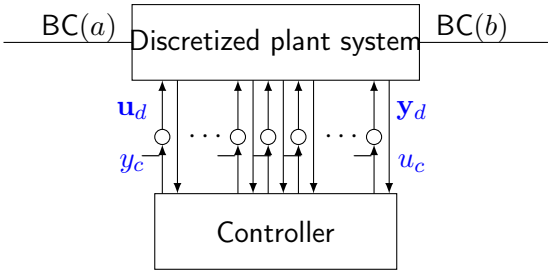

Figure 4.1: Distributed control by interconnection strategy.

The controller in Fig. 4.1 is designed to be a finite dimensional PHS, which is expressed as follows:

$$\begin{aligned} \dot{x}_c &= [J_c - R_c]\, Q_c x_c + B_c u_c, \\ y_c &= B_c^T Q_c x_c + D_c u_c, \end{aligned} \tag{4.1}$$

where $x_c \in \mathbb{R}^m$, $J_c = -J_c^T \in \mathbb{R}^{m\times m}$, $R_c = R_c^T \geq 0$ and $Q_c = Q_c^T \geq 0$, $B_c \in \mathbb{R}^{m\times m}$, $\mathbb{R}^{m\times m} \ni D_c > 0$, $u_c \in \mathbb{R}^m$ and $y_c \in \mathbb{R}^m$. Matrices Q_c and D_c are used for energy shaping and damping injection/diffusion, respectively.
Without considering external signals, the interconnection between the discretized plant system (2.16) and the controller (4.1) is given by

$$\begin{bmatrix} \mathbf{u}_d \\ u_c \end{bmatrix} = \begin{bmatrix} 0 & -M \\ M^T & 0 \end{bmatrix} \begin{bmatrix} \mathbf{y}_d \\ y_c \end{bmatrix}, \tag{4.2}$$

where $\mathbb{R}^{p\times m} \ni M = I_m \otimes \mathbf{1}_k$, with I_m the identity matrix of dimension m, $\mathbf{1}_k$ a ones vector of dimension $k \times 1$, and $\otimes$ denoting the Kronecker product. k is the number of elements covered by one actuator. The relation among m, k and p gives

$$p = mk.$$

The passive interconnection (4.2) guarantees the passivity of the closed-loop system. It results in a new PHS in closed-loop:

$$\dot{x}_{cl} = [J_{cl} - R_{cl}]\, Q_{cl} x_{cl}, \tag{4.3}$$

where $x_{cl} = \begin{bmatrix} x_{1d}^T, & x_{2d}^T, & x_c^T \end{bmatrix}^T$, $Q_{cl} = \text{diag}\begin{bmatrix} Q_1, & Q_2, & Q_c \end{bmatrix}$,

$$J_{cl} = \begin{bmatrix} 0 & J_i & 0 \\ -J_i^T & 0 & -B_{0d} M B_c^T \\ 0 & B_c M^T B_{0d}^T & J_c \end{bmatrix},$$

$$R_{cl} = \begin{bmatrix} 0 & 0 & 0 \\ 0 & R_d + B_{0d} M D_c M^T B_{0d}^T & 0 \\ 0 & 0 & R_c \end{bmatrix}.$$

The Hamiltonian of the controller (4.1) is:

$$H_c(x_c) = \frac{1}{2} x_c^T Q_c x_c. \tag{4.4}$$

Therefore, the closed-loop Hamiltonian function reads:

$$H_{cld}(x_{1d}, x_{2d}, x_c) = H_d(x_{1d}, x_{2d}) + H_c(x_c). \tag{4.5}$$

The next step is to design the controller matrices J_c, R_c, B_c, Q_c, and D_c in order to shape the closed-loop Hamiltonian (4.5). In Proposition 4 we first show how the controller states can be related to the plant states using structural invariants.

Proposition 4. *Assigning $J_c = 0$, and $R_c = 0$, the closed-loop system (4.3) admits the Casimir function $C(x_{1d}, x_c)$ defined by:*

$$C(x_{1d}, x_c) = B_c M^T B_{0d}^T J_i^{-1} x_{1d} - x_c \tag{4.6}$$

as structural invariant, i.e. $\dot{C}(x_{1d}, x_c) = 0$ along the closed-loop trajectories. If the initial conditions of $x_{1d}(0)$ and $x_c(0)$ satisfy $C(x_{1d}(0), x_c(0)) = 0$, the controller is a proportional-integral control, and the control law (4.1)-(4.2) is equivalent to the state feedback:

$$\begin{aligned} y_c &= B_c^T Q_c B_c M^T B_{0d}^T J_i^{-1} x_{1d} + D_c M^T B_{0d}^T Q_2 x_{2d}, \\ \mathbf{u}_d &= -M y_c. \end{aligned} \tag{4.7}$$

Therefore, the closed-loop system yields:

$$\begin{bmatrix} \dot{x}_{1d} \\ \dot{x}_{2d} \end{bmatrix} = \begin{bmatrix} 0 & J_i \\ -J_i^T & -\tilde{R}_d \end{bmatrix} \begin{bmatrix} \tilde{Q}_1 x_{1d} \\ Q_2 x_{2d} \end{bmatrix}, \tag{4.8}$$

where

$$\tilde{R}_d = \left[R_d + B_{0d} M D_c M^T B_{0d}^T \right], \tag{4.9}$$

$$\tilde{Q}_1 = Q_1 + J_i^{-T} B_{0d} M B_c^T Q_c B_c M^T B_{0d}^T J_i^{-1} \tag{4.10}$$

are the new closed-loop dissipation matrix and energy matrix associated to x_{1d}.

Proof. We consider here Casimir functions of the form:

$$C(x_{1d}, x_{2d}, x_c) = F(x_{1d}, x_{2d}) - x_c. \tag{4.11}$$

The time derivative of C is given by

$$\begin{aligned} \frac{\mathrm{d}C}{\mathrm{d}t} &= \frac{\partial^T C}{\partial x_{cl}} \frac{\partial x_{cl}}{\partial t} \\ &= \left[\frac{\partial^T F}{\partial x_{1d}}, \quad \frac{\partial^T F}{\partial x_{2d}}, \quad -I \right] (J_{cl} - R_{cl})\, e_{cl}, \end{aligned} \tag{4.12}$$

where $e_{cl} = \frac{\partial H_{cld}}{\partial x_{cl}} = Q_{cl} x_{cl}$. The Casimir functions are dynamic invariants, i.e. $\dot{C} = 0$ that do not depend on the trajectories of the system *i.e.* on the Hamiltonian. Therefore, (4.12) with $\dot{C} = 0$ gives rise to the following matching equations:

$$\frac{\partial^T F}{\partial x_{2d}} \left(-J_i^T\right) = 0, \tag{4.13a}$$

$$\frac{\partial^T F}{\partial x_{1d}} J_i - \frac{\partial^T F}{\partial x_{2d}} \tilde{R}_d - B_c M^T B_{0d}^T = 0, \tag{4.13b}$$

$$\frac{\partial^T F}{\partial x_{2d}} \left(-B_{0d} M B_c^T\right) - (J_c - R_c) = 0. \tag{4.13c}$$

Solving (4.13a), one gets $\partial F / \partial x_{2d} = 0$, which indicates that x_c does not depend on x_{2d}. Therefore, with $J_c = -J_c^T$ and $R_c = R_c^T \geq 0$, (4.13c) indicates that J_c and R_c equal zero. Since J_i is full rank, from (4.13b) one gets (4.6) as a structural invariant as soon as the initial condition $x_c(0)$ is chosen properly. Taking the initial conditions $x_{1d}(0)$ and $x_c(0)$ such that $C(x_{1d}(0), x_c(0)) = 0$, (4.6) becomes

$$B_c M^T B_{0d}^T J_i^{-1} x_{1d}(t) - x_c(t) = 0, \tag{4.14}$$

which allows to link the state of the controller with the state of the plant. Replacing x_c in (4.3) by (4.14), the control law (4.1) becomes a state feedback as formulated in (4.7). Therefore the closed-loop system (4.3) becomes (4.8). □

Remark 4.2.1. *The choice of Casimir function* (4.11) *is not unique, which can be either linear or nonlinear. We have chosen a particular linear case in this work.* ◊

From Proposition 4, the closed-loop Hamiltonian function (4.5) is now only a function of the discretized plant state variables :

$$H_{cld}(x_{1d}, x_{2d}) = \frac{1}{2} \left(x_{1d}^T \tilde{Q}_1 x_{1d} + x_{2d}^T Q_2 x_{2d} \right), \tag{4.15}$$

with its time derivative being:

$$\frac{\mathrm{d}H_{cld}}{\mathrm{d}t} = -x_{2d}^T Q_2 \left(R_d + B_{0d} M D_c M^T B_{0d}^T \right) Q_2 x_{2d} \leq 0. \tag{4.16}$$

From a physical point of view, (4.15) implies that with the dynamic controller (4.1) equivalent to the state feedback (4.7), it is possible to change, at least partially (depending on p and the range of B_{0d}), the energy matrix related to x_{1d}. Actually, one can only shape the energy matrix related to the first p elements of x_{1d}, i.e. $\left(\tilde{Q}_1\right)_{p \times p}$. For a given number of distributed input m, the objectives of the energy shaping is to look for matrices B_c and Q_c such that the norm of the difference (considered here in the Frobenius norm, see Definition 6.4 of (Shores, 2007)) between the desired energy matrix $\tilde{Q}_{1d}$ and the closed-loop one $\tilde{Q}_1$ is minimal:

$$\min_{B_c^T Q_c B_c} \| J_i^{-T} B_{0d} M B_c^T Q_c B_c M^T B_{0d}^T J_i^{-1} + Q_1 - \tilde{Q}_{1d} \|_F. \tag{4.17}$$

If we consider p elements and eliminate B_{0d}, (4.17) is equivalent to:

$$\min_{B_c^T Q_c B_c} \|(J_i)_{p\times p}^{-T} M B_c^T Q_c B_c M^T (J_i)_{p\times p}^{-1} - Q_m\|_F, \tag{4.18}$$

where the $(J_i)_{p\times p}$ are the first p lines p columns of J_i and $Q_m = \left(\tilde{Q}_{1d} - Q_1\right)_{p\times p} \geq 0$. Furthermore, (4.18) can be formalized by the optimization Problem 4.2.1.

Problem 4.2.1. *The closed loop energy function related to the first p elements of x_{1d} is shaped in an optimal way if and only if $X = B_c^T Q_c B_c \in SR_0^{m\times m}$ minimizes the criterion*

$$f(X) = \|AXA^T - Q_m\|_F, \tag{4.19}$$

where $A = (J_i)_{p\times p}^{-T} M \in \mathbb{R}^{p\times m}$ and $SR_0^{m\times m}$ represents the set of symmetric and positive semi-definite matrices. ◊ The solution to Problem 4.2.1 depends on the independent number of distributed input that are available. We consider two different cases: the *ideal* fully-actuated case ($m = p$) and the under-actuated case ($m < p$).

4.2.1. Fully-actuated case

We first consider the fully-actuated case where each discretized element of the plant is controlled by an independent input, *i.e.* $u_d \in \mathbb{R}^m$ and $m = p$, as illustrated in Fig. 4.2. The input matrix

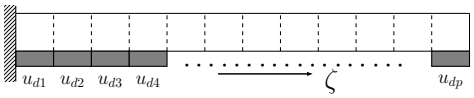

Figure 4.2: Fully-actuated case illustration.

$M = I \in \mathbb{R}^{p\times p}$. Therefore, the optimization Problem 4.2.1 admits an exact solution that is given in Proposition 5.

Proposition 5. *In the fully-actuated case, i.e. $m = p$ the optimization Problem 4.2.1 has an exact analytical solution $\hat{X} = M^{-1} (J_i)_{p\times p}^T Q_m (J_i)_{p\times p} M^{-T}$ leading to $f(X) = 0$. The controller matrices B_c and Q_c can be chosen as:*

$$B_c = (J_i)_{p\times p}, \quad Q_c = Q_m. \tag{4.20}$$

Proof. The matrix A is invertible, therefore, (4.19) admits a minimum in 0 when

$$\begin{aligned} \hat{X} &= A^{-1} Q_m A^{-T} = M^{-1} (J_i)_{p\times p}^T Q_m (J_i)_{p\times p} M^{-T} \\ &= (J_i)_{p\times p}^T Q_m (J_i)_{p\times p}. \end{aligned} \tag{4.21}$$

From the expression of X, one can choose B_c and Q_c as in (4.20) to satisfy (4.21). □

Remark 4.2.2. *The choice $B_c = (J_i)_{p\times p}$ can be regarded as the numerical approximation of the operator $\frac{\partial}{\partial\zeta}$, which has also been used in the late lumping control design approach in (Trenchant et al., 2017).* ◊

4.2.2. Under-actuated case

We study now the more realistic case where the same control input is applied to a set of elements, as shown in Fig. 4.3, where k denotes the number of elements sharing the same input. The number of distributed inputs m is less than the number of discretized elements, and follows $m = p/k$.
In this case the controller has less degree of freedom than in the fully actuated case, hence the matrix A in (4.19) is not invertible and the optimization Problem 4.2.1 is ill-conditioned. The solution of the optimization Problem 4.2.1 is given in Proposition 6.

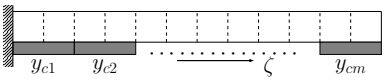

Figure 4.3: Under-actuated case with $k = 2$.

Proposition 6. *$f(X)$ defined in (4.19) is convex and the minimization of $f(X)$ is equivalent to the minimization of $f^2(X)$, which has a unique minimum given for $\hat{X} = V\Sigma_0^{-1}U_1^T Q_m U_1 \Sigma_0^{-1} V^T$, with V, Σ_0 and U_1 the matrices of the singular value decomposition (SVD) of the matrix A i.e.*

$$A = U\Sigma V^T = \begin{bmatrix} U_1 & U_2 \end{bmatrix} \begin{bmatrix} \Sigma_0 \\ 0 \end{bmatrix} V^T, \tag{4.22}$$

where $U \in \mathbb{R}^{p\times p}$ and $V \in \mathbb{R}^{m\times m}$ are unitary matrices, $U_1 \in \mathbb{R}^{p\times m}$, $U_2 \in \mathbb{R}^{p\times q}$, $q = p - m$, and $\Sigma_0 = \Sigma_0^T \geq 0$ is the diagonal matrix of singular values of A.

Proof. The proof of Proposition 6 is similar to that of Proposition 3 in (Liu et al., 2021c). Substituting (4.22) into $f^2(X)$, one gets:

$$\begin{aligned} &\min_{X\in SR_0^{m\times m}} f^2(X) \\ &= \min_{X\in SR_0^{m\times m}} \|U\Sigma V^T X V \Sigma^T U^T - Q_m\|_F^2 \\ &= \min_{X\in SR_0^{m\times m}} \left(\|\Sigma_0 V^T X V \Sigma_0^T - T_1\|_F^2 + 2\|T_2\|_F^2 + \|T_3\|_F^2\right), \end{aligned} \tag{4.23}$$

where $T_1 = U_1^T Q_m U_1$, $T_2 = U_1^T Q_m U_2$, and $T_3 = U_2^T Q_m U_2$. Since $\|T_2\|_F^2$ and $\|T_3\|_F^2$ are given once the matrices A and Q_m are defined, the minimization of (4.23) is equivalent to:

$$\min_{\bar{X}\in SR_0^{m\times m}} \|\bar{X} - T_1\|_F^2, \text{ with } \bar{X} = \Sigma_0 V^T X V \Sigma_0^T. \tag{4.24}$$

According to Theorem 2.1 in (Higham, 1988), $T_1 \in SR_0^{m\times m}$, and (4.24) admits a unique solution $\hat{\bar{X}} = T_1$. Therefore, (4.23) has the minimum when:

$$\hat{X} = V\Sigma_0^{-1}\hat{\bar{X}}\Sigma_0^{-1}V^T = V\Sigma_0^{-1}U_1^T Q_m U_1 \Sigma_0^{-1} V^T. \tag{4.25}$$

□

The choice of controller matrices B_c and Q_c is not unique, as long as they satisfy the condition (4.25). We will present a possible choice in Subsection 4.3.2.

Remark 4.2.3. *We have investigated the choices of controller matrices B_c and Q_c under two different cases in Proposition 5 and 6, respectively. The objective is to shape the closed-loop Hamiltonian H_{cld} with the modification of part of the potential energy matrix. The choice of the controller matrix D_c follows the similar procedure, with the optimization of the difference between (4.16) and the desired one.* ◊

4.2.3. Closed-loop stability

In this subsection we consider the closed-loop stability of the infinite-dimensional system (2.5) controlled by the finite-dimensional controller (4.1) derived from the early lumping approach. The power-preserving interconnection between (2.5) and (4.1) is formulated as:

$$\begin{bmatrix} u_d \\ u_c \end{bmatrix} = \begin{bmatrix} 0 & -\mathbf{1}_\zeta \\ \mathbf{1}_\zeta^* & 0 \end{bmatrix} \begin{bmatrix} y_d \\ y_c \end{bmatrix}, \tag{4.26}$$

with

$$\mathbf{1}_\zeta : \mathbb{R}^m \to L_2, \qquad \mathbf{1}_\zeta^* : L_2 \to \mathbb{R}^m. \tag{4.27}$$

$\mathbf{1}_\zeta$ is the characteristic function that distributes the point-wise value of the controller in $\mathbb{R}^m$ space to the sub-interval L_2 space, as illustrated in Fig. 4.4.

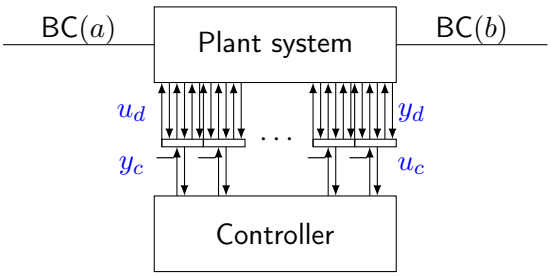

Figure 4.4: Distributed control by interconnection strategy.

Lemma 4.2.1. *The interconnection* (4.26) *generates a Dirac structure with the following power conservation:*

$$\int_0^L y_d^* \mathbf{1}_\zeta y_c \mathrm{d}\zeta = y_c^T \mathbf{1}_\zeta^* y_d. \tag{4.28}$$

$\Diamond$ The closed-loop system is equivalent to:

$$\dot{\mathcal{X}} = \underbrace{\begin{bmatrix} 0 & \mathcal{G} & 0 \\ -\mathcal{G}^* & -\mathcal{R}_{cl} & -B_0 \mathbf{1}_\zeta B_c^T \\ 0 & B_c \mathbf{1}_\zeta^* B_0^* & 0 \end{bmatrix}}_{\mathcal{A}_{cl}} \mathcal{L}_{cl}\, \mathcal{X}, \tag{4.29}$$

where $\mathcal{X} = \begin{bmatrix} x \\ x_c \end{bmatrix} \in X_s$ is the state defined on the state space $X_s = L_2\left([a,b], \mathbb{R}^{2n}\right) \times \mathbb{R}^m$, $\mathcal{R}_{cl} = R + B_0 \mathbf{1}_\zeta D_c \mathbf{1}_\zeta^* B_0^*$ and $\mathcal{L}_{cl} = \mathrm{diag}\left(\mathcal{L}_1, \mathcal{L}_2, Q_c\right)$. The domain of $\mathcal{A}_{cl}$ is defined as:

$$D\left(\mathcal{A}_{cl}\right) = \left\{ \mathcal{X} \in X_s \mid \begin{bmatrix} x \\ x_c \end{bmatrix} \in H^1\left([a,b], \mathbb{R}^{2n}\right) \times \mathbb{R}^m, \mathcal{B}\left(\mathcal{L}x\right) = 0 \right\}.$$

The Hamiltonian of (4.29) is:

$$H_{cl} = \frac{1}{2} \int_a^b \left(\mathcal{L}_1(\zeta) x_1^2(\zeta, t) + \mathcal{L}_2(\zeta) x_2^2(\zeta, t) \right) \mathrm{d}\zeta + \frac{1}{2} x_c^T Q_c x_c \tag{4.30}$$

with

$$\begin{aligned} \frac{\mathrm{d}H_{cl}}{\mathrm{d}t} &= \int_0^L y_d^* u_d \mathrm{d}\zeta + y_c^T u_c - \int_0^L (\mathcal{L}_2 x_2)^* \mathcal{R}_{cl} (\mathcal{L}_2 x_2) d\zeta \\ &= - \int_0^L (\mathcal{L}_2 x_2)^* \mathcal{R}_{cl} (\mathcal{L}_2 x_2) d\zeta. \end{aligned} \tag{4.31}$$

The last step of (4.31) is derived considering (4.28).
In order to prove stability of the closed-loop system using Lyapunov arguments and LaSalle's invariance principle we first state the following theorems.

Theorem 4.2.1. *The linear operator $\mathcal{A}_{cl}$ defined in* (4.29) *generates a contraction semigroup on X_s.* ◊

Proof. To prove that the closed-loop operator $\mathcal{A}_{cl}$ generates a contraction semigroup, we apply Lumer-Phillips Theorem (Theorem 1.2.3 in (Liu and Zheng, 1999)). The proof is done in two steps: first, we show that the operator $\mathcal{A}_{cl}$ is dissipative. Second, we show that

$$\text{range}\,(\lambda I - \mathcal{A}_{cl}) \in X_s, \text{ for } \lambda > 0. \tag{4.32}$$

According to Definition 6.1.4 in (Jacob and Zwart, 2012), $\mathcal{A}_{cl}$ is dissipative if $\text{Re}\langle \mathcal{A}_{cl}\mathcal{X}, \mathcal{X}\rangle \leq 0$, which is equivalent to $\langle \mathcal{A}_{cl}\mathcal{X}, \mathcal{X}\rangle + \langle \mathcal{X}, \mathcal{A}_{cl}\mathcal{X}\rangle \leq 0$. For the sake of clarity and without any restriction, we take $\mathcal{L}_1 = \mathcal{L}_2 = 1$ and $Q_c = I$ in the rest of this section. From (4.29), one has:

$$\begin{aligned}
&\langle \mathcal{A}_{cl}\mathcal{X}, \mathcal{X}\rangle + \langle \mathcal{X}, \mathcal{A}_{cl}\mathcal{X}\rangle \\
=&\langle \mathcal{G}x_2, x_1\rangle_{L_2} + \langle -\mathcal{G}^* x_1 - \mathcal{R}_{cl}x_2, x_2\rangle_{L_2} \\
&+ \langle -B_0 \mathbf{1}_\zeta B_c^T x_c, x_2\rangle_{L_2} + \langle B_c \mathbf{1}_\zeta^* B_0^* x_2, x_c\rangle_{\mathbb{R}^m} \\
&+ \langle x_1, \mathcal{G}x_2\rangle_{L_2} + \langle x_2, -\mathcal{G}^* x_1 - \mathcal{R}_{cl}x_2\rangle_{L_2} \\
&+ \langle x_2, -B_0 \mathbf{1}_\zeta B_c^T x_c\rangle_{L_2} + \langle x_c, B_c \mathbf{1}_\zeta^* B_0^* x_2\rangle_{\mathbb{R}^m}.
\end{aligned} \tag{4.33}$$

According to (4.28), we get

$$\begin{aligned}
\langle B_0 \mathbf{1}_\zeta B_c^T x_c, x_2\rangle_{L_2} &= \langle B_c \mathbf{1}_\zeta^* B_0^* x_2, x_c\rangle_{\mathbb{R}^m}, \\
\langle x_2, -B_0 \mathbf{1}_\zeta B_c^T x_c\rangle_{L_2} &= \langle x_c, B_c \mathbf{1}_\zeta^* B_0^* x_2\rangle_{\mathbb{R}^m}.
\end{aligned} \tag{4.34}$$

Substituting (4.34) into (4.33), we have:

$$\begin{aligned}
&\langle \mathcal{A}_{cl}\mathcal{X}, \mathcal{X}\rangle + \langle \mathcal{X}, \mathcal{A}_{cl}\mathcal{X}\rangle \\
=&\langle \mathcal{G}x_2, x_1\rangle_{L_2} + \langle -\mathcal{G}^* x_1, x_2\rangle_{L_2} - \langle \mathcal{R}_{cl}x_2, x_2\rangle_{L_2} \\
&+ \langle x_1, \mathcal{G}x_2\rangle_{L_2} + \langle x_2, -\mathcal{G}^* x_1\rangle_{L_2} - \langle x_2, -\mathcal{R}_{cl}x_2\rangle_{L_2} \\
=&- \langle \mathcal{R}_{cl}x_2, x_2\rangle_{L_2} - \langle x_2, -\mathcal{R}_{cl}x_2\rangle_{L_2} \leq 0,
\end{aligned}$$

where the last step is obtained according to the boundary conditions. Therefore, the operator $\mathcal{A}_{cl}$ is dissipative.
To show (4.32), we apply the proof of Theorem 3.3.6 in (Augner, 2018) with adjustment dedicated to our in-domain control. For the sake of simplicity, we choose $\lambda = 1$. Taking an arbitrary function

$$f = \begin{bmatrix} \tilde{x} \\ \tilde{x}_c \end{bmatrix} \in X_s,$$

(4.32) is then equivalent to the problem:

$$\text{find } \mathcal{X} \in X_s : (I - \mathcal{A}_{cl})\,\mathcal{X} = f, \tag{4.35}$$

which is again equivalent to:

$$x_1 - \mathcal{G}x_2 = \tilde{x}_1, \tag{4.36a}$$

$$\mathcal{G}^* x_1 + (I + \mathcal{R}_{cl})\,x_2 + B_0 \mathbf{1}_\zeta B_c^T x_c = \tilde{x}_2, \tag{4.36b}$$

$$-B_c \mathbf{1}_\zeta^* B_0^* x_2 + x_c = \tilde{x}_c. \tag{4.36c}$$

Substituting (4.36c) into (4.36b), one gets:

$$\mathcal{G}^* x_1 + (I + \mathcal{M})\,x_2 = \tilde{x}_2 - B_0 \mathbf{1}_\zeta B_c^T \tilde{x}_c, \tag{4.37}$$

with $\mathcal{M} = \mathcal{R}_{cl} + B_0 \mathbf{1}_\zeta B_c^T \mathbf{1}_\zeta^* B_0^*$.
According to the definition of $\mathcal{G}$ and $\mathcal{G}^*$, (4.36a) and (4.37) become:

$$x_1 - \sum_{k=0}^{1} G_k \frac{\partial^k}{\partial \zeta^k} x_2 = \tilde{x}_1, \tag{4.38}$$

$$\sum_{k=0}^{1} (-1)^k G_k^T \frac{\partial^k}{\partial \zeta^k} x_1 + (I + \mathcal{M})\, x_2 = \tilde{x}_f, \tag{4.39}$$

with $\tilde{x}_f = \tilde{x}_2 - B_0 \mathbf{1}_\zeta B_c^T \tilde{x}_c$. Thus one gets:

$$\frac{\partial^N x_1}{\partial \zeta^N} = (-1)^{N+1} G_N^{-T} \left[\sum_{k=0}^{N-1} (-1)^k G_k^T \frac{\partial^k x_1}{\partial \zeta^k} + (I + \mathcal{M})\, x_2 - \tilde{x}_f \right], \tag{4.40}$$

$$\frac{\partial^N x_2}{\partial \zeta^N} = G_N^{-1} \left[x_1 - \sum_{k=0}^{N-1} G_k \frac{\partial^k x_2}{\partial \zeta^k} - \tilde{x}_1 \right]. \tag{4.41}$$

Define:

$$h = \begin{bmatrix} x_1 \\ x_2 \end{bmatrix}. \tag{4.42}$$

According to (4.40) and (4.41), one can derive the following relation:

$$\frac{\partial h}{\partial \zeta} = B_h h + g_h. \tag{4.43}$$

For $N = 1$,

$$B_h = \begin{bmatrix} G_1^{-T} \begin{bmatrix} G_0^T, & I + \mathcal{M} \end{bmatrix} \\ G_1^{-1} \begin{bmatrix} 1, & -G_0 \end{bmatrix} \end{bmatrix}, \qquad g_h = \begin{bmatrix} -G_1^{-T} \tilde{x}_f \\ -G_1^{-1} \tilde{x}_1 \end{bmatrix}.$$

The solution of the function (4.43) is derived as:

$$h(\zeta) = e^{B_h \zeta} h(a) + q(\zeta), \tag{4.44}$$

with $q(\zeta) = \int_a^\zeta e^{\zeta - s} B_h g_h \mathrm{d}s$.
Therefore, to solve the problem (4.35), one needs to find the solution of $h(\zeta)$, and eventually the solution of $h(a)$. According to the boundary condition in Theorem 1, we have:

$$W R_{\text{ext}} \begin{bmatrix} h(b) \\ h(a) \end{bmatrix} = W R_{\text{ext}} \begin{bmatrix} e^{B_h} h(a) + q(b) \\ h(a) \end{bmatrix} = \begin{bmatrix} 0 \\ 0 \end{bmatrix}.$$

By calculation, $W R_{\text{ext}} \begin{bmatrix} e^{B_h} \\ I \end{bmatrix}$ has full rank. Hence, one can get the solution of $h(a)$ as:

$$h(a) = - \left(W R_{\text{ext}} \begin{bmatrix} e^{B_h} \\ I \end{bmatrix} \right)^{-1} W R_{\text{ext}} \begin{bmatrix} q(b) \\ 0 \end{bmatrix}.$$

Therefore $h(\zeta)$ is obtained from (4.44). One then has the solution of $x = \begin{bmatrix} 1 & 0 & \cdots & 0 \end{bmatrix} h(\zeta)$. Substituting x into (4.36b), one obtains x_c. As a result, the problem (4.35) is solved. According to the Lumer-Phillips theorem, the operator $\mathcal{A}_{cl}$ generates a contraction semigroup that concludes the proof. □

Theorem 4.2.2. *The operator $\mathcal{A}_{cl}$ has a compact resolvent.* ◊

Proof. According to the Definition A.4.24 in (Curtain and Zwart, 2012), we need to prove that the operator $(\lambda I - \mathcal{A}_{cl})^{-1}$ is compact for some $\lambda \in \rho(\mathcal{A}_{cl})$, with $\rho(\mathcal{A}_{cl})$ denoting the resolvent set of $\mathcal{A}_{cl}$. This proof follows from Garding's inequality (Theorem 7.6.4 in (Naylor and Sell, 1971)) and the proof of Theorem 2.26 in (Villegas, 2007).
Define $\mathcal{T} = \lambda I - \mathcal{A}_{cl}$. From the previous Theorem 4.2.1, $\mathcal{A}_{cl}$ generates a contraction semigroup, thus $\lambda > 0$ is in the resolvent set of $\mathcal{A}_{cl}$. $\mathcal{T}$ is boundedly invertible and satisfies $\|\mathcal{T}\mathcal{X}\|_{L_2} \geq \|\mathcal{X}\|_{H^1}$. Therefore, $\mathcal{T}^{-1}$ is compact which concludes the proof. □

Due to Theorem 4.2.1 and Theorem 4.2.2, the trajectory of the closed-loop system is pre-compact and its asymptotic stability can be proven by Lyapunov arguments and LaSalle's invariance principle (Theorem 3.64 of (Luo et al., 2012)) as shown in Theorem 4.2.3.

Theorem 4.2.3. *For any $\mathcal{X}(0) \in L_2\left([a,b], \mathbb{R}^{2n}\right) \times \mathbb{R}^m$, the unique solution of (4.29) tends to zero asymptotically, and the closed-loop system (4.29) is globally asymptotically stable.* ◊

Proof. We choose the energy of the closed-loop system as Lyapunov function. From (4.31), the time derivation of the Lyapunov function is semi-negative definite:

$$\frac{\mathrm{d}H_{cl}}{\mathrm{d}t} = -\int_a^b (\mathcal{L}_2 x_2)^* \mathcal{R}_{cl} (\mathcal{L}_2 x_2) d\zeta \leq 0. \tag{4.45}$$

Using LaSalle's invariance principle, it remains to show that the only solutions associated with $\frac{\mathrm{d}H_{cl}}{\mathrm{d}t}$ is 0 i.e the only solutions associated with $\mathcal{L}_2 x_2 = 0$ is $x_2 = 0$. From (2.5), one obtains $\dot{x}_2 = 0$, which implies that $-\mathcal{G}^* x_1 = 0$, and that x_1 is independent of the space. From the clamped-free boundary condition, we conclude $x_1 = 0$. Therefore, only solution associated with this problem is the origin. The controller being a simple integrator, if well initialized it also converges to $x_c = 0$ as the state of the system converges to $x = 0$. □

4.3. Numerical simulations

As illustrative example we consider a vibrating string of length $L = 2$ m, modulus of elasticity $T = 1.4 \times 10^6$ N density $\rho = 1.225$ kg/m and dissipation coefficient $R = 10^{-3}$. The dynamic model of the string can be written:

$$\begin{bmatrix} \dot{x}_1 \\ \dot{x}_2 \end{bmatrix} = \begin{bmatrix} 0 & \frac{\partial}{\partial \zeta} \\ \frac{\partial}{\partial \zeta} & -R \end{bmatrix} \begin{bmatrix} \mathcal{L}_1 x_1 \\ \mathcal{L}_2 x_2 \end{bmatrix} + \begin{bmatrix} 0 \\ 1 \end{bmatrix} u_d \tag{4.46}$$

with $x_1(\zeta, t) = \frac{\partial \omega}{\partial \zeta}(\zeta, t)$, and $x_2(\zeta, t) = \rho(\zeta) \frac{\partial \omega}{\partial t}(\zeta, t)$. $\omega(\zeta, t)$ is the longitudinal displacement over the spatial domain with the state space $x = \in L_2([0, L], \mathbb{R}^2)$. $\mathcal{L}_1 = T$ and $\mathcal{L}_2 = \frac{1}{\rho}$. The dissipation term is chosen to be very small $R = 10^{-3}$. The distributed input u_d is the force density. From Definition 2.3.1:

$$Q = \begin{bmatrix} P_1 & P_2 \\ -P_2 & 0 \end{bmatrix}, \text{ with } \quad P_1 = \begin{bmatrix} 0 & 1 \\ 1 & 0 \end{bmatrix}, \text{ and } \quad P_2 = \begin{bmatrix} 0 & 0 \\ 0 & 0 \end{bmatrix}.$$

Taking the full rank matrix

$$M_0 = \begin{bmatrix} 1 & 0 & 0 & 0 \\ 0 & 1 & 0 & 0 \end{bmatrix}^T,$$

one can compute $Q_M = P_1$ and $M_Q = M_0^T$. Then the boundary port variables give:

$$\begin{bmatrix} f_\partial \\ e_\partial \end{bmatrix} = \frac{1}{\sqrt{2}} \begin{bmatrix} \mathcal{L}_2 x_2(L) - \mathcal{L}_2 x_2(0) \\ -\mathcal{L}_1 x_1(L) + \mathcal{L}_1 x_1(0) \\ \mathcal{L}_1 x_1(L) + \mathcal{L}_1 x_1(0) \\ \mathcal{L}_2 x_2(L) + \mathcal{L}_2 x_2(0) \end{bmatrix}.$$

We consider a clamped-free scenario with in-domain control. Hence, we define the boundary input formulated in (2.15) with:

$$W = \frac{\sqrt{2}}{2} \begin{bmatrix} 0 & 1 & 1 & 0 \\ -1 & 0 & 0 & 1 \end{bmatrix}, \quad \text{and } W\Sigma W^T \geq 0.$$

The clamped-free boundary condition implies $u_b = 0$. The discretization model is derived through the application of the mixed finite element method, as detailed in Section 2.4, and is expressed in the form of (2.16). Initial conditions are set to a spatial distribution $x_1(\zeta, 0) \sim \mathcal{N}(1.5, 0.113)$ for the strain distribution and to zero for the velocity distribution *i.e.*, $x_2(\zeta, 0) = 0$. The string is discretized into 50 elements. We consider a time step of 5×10^{-5}s and mid-point time discretization method[1] for simulations. The open loop evolution of the string deformation ω is given in Fig. 4.5.

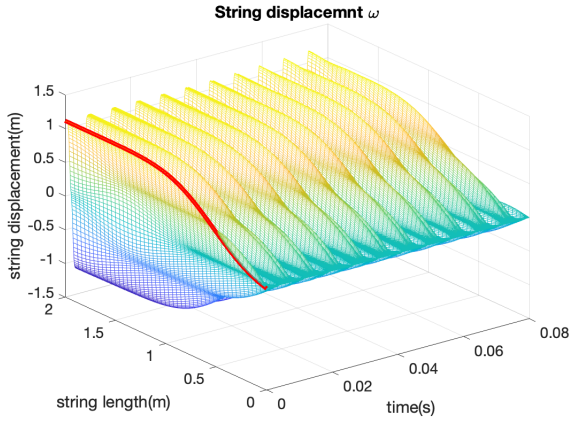

Figure 4.5: Open loop deformation of the vibrating string.

Next we investigate the numerical simulations of the closed-loop system considering both fully-actuated and under-actuated cases.

4.3.1. Fully-actuated case

Following Proposition 4 and Proposition 5, we choose $B_c = J_i$ in order to guarantee the existence of structural invariants, and the initial conditions of the controller such that $C = 0$. In this case (4.6) becomes: $x_c = x_{1d}$, and the closed-loop system (4.8) reads:

$$\begin{bmatrix} \dot{x}_{1d} \\ \dot{x}_{2d} \end{bmatrix} = \begin{bmatrix} 0 & J_i \\ -J_i^T & -(R_d + D_c) \end{bmatrix} \begin{bmatrix} \tilde{Q}_1 x_{1d} \\ Q_2 x_{2d} \end{bmatrix}, \tag{4.47}$$

[1] Implicit midpoint rule is known to be a structure preserving time integrator for PHSs (Aoues et al., 2013). It is a particular case in the family of symplectic collocation methods for time integration which is investigated in (Kotyczka et al., 2018).

One can see that *the equivalent* closed-loop stiffness $\tilde{Q}_1$ can be shaped through the choice of Q_c. We first consider the pure damping injection case, *i.e.* varying D_c with $Q_c = 0$. We consider $D_c = \text{diag}\,(\alpha L_{ab})$ with α denoting the damping coefficient. In Fig. 4.6(a) we can see that this degree of freedom allows to damp the vibrations of the string to the detriment of the time response. Next we fix $\alpha = 4000$ corresponding to the slightly over-damped case in order to illustrate the effect of the energy shaping on the achievable performances. For that we use the control by energy shaping.We can see in Fig. 4.6(b) that we can speed up the closed-loop system by increasing the closed-loop stiffness via energy shaping, without introducing any overshoot. The energy matrix of the controller $Q_c = \text{diag}\left(\frac{\beta}{L_{ab}}\right)$, with β denoting the energy shaping parameter. A good dynamic performance is achieved when $\beta = 5 \times 10^6$, which relates to an equivalent string stiffness of $\tilde{T} = 6.4 \times 10^6$ N.

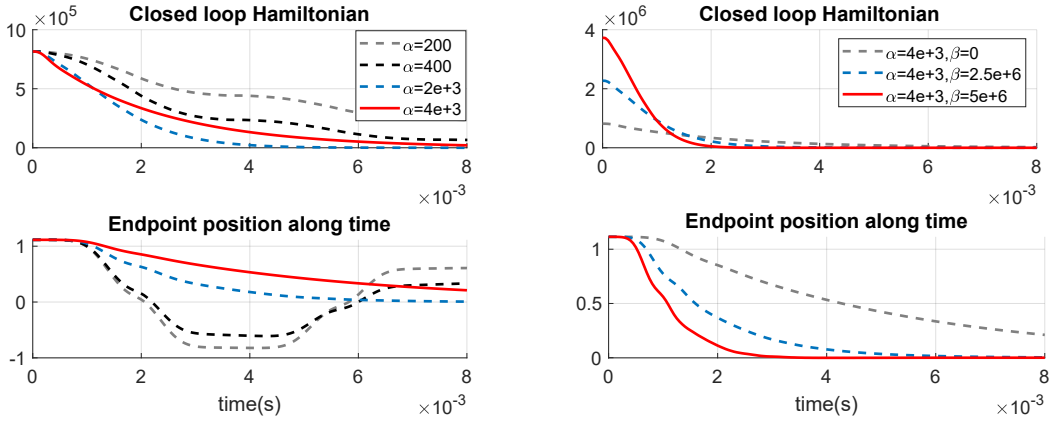

Figure 4.6: Closed-loop Hamiltonian function and endpoint position in the fully-actuated case with (a) pure damping injection and with (b) energy shaping plus damping injection.

The evolution of the distributed input and of the string deformation along time with damping injection and energy shaping are given in Fig. 4.7(a) and (b) respectively. We can see in Fig. 4.7(a) that the control remains smooth. Fig. 4.7(b) shows that the closed-loop stabilization time is about $3 \times 10^{-3}s$ which is much faster than $8 \times 10^{-3}s$ resulting from the pure damping injection case.

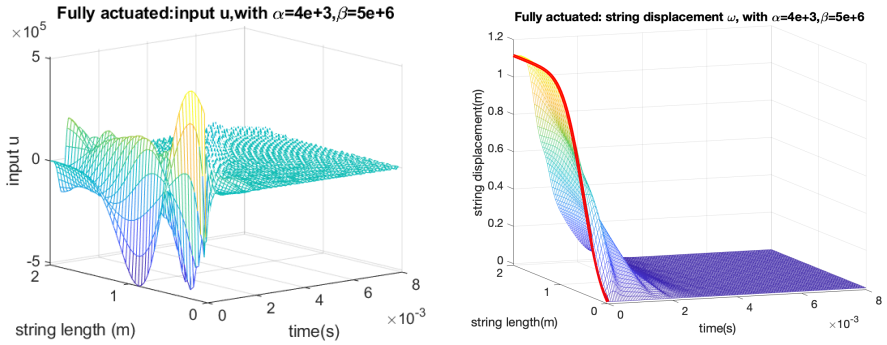

Figure 4.7: (a) Evolution of the closed-loop input signal and (b) deformation in the energy shaping and damping injection case with full actuation, $\alpha = 4 \times 10^3$, $\beta = 5 \times 10^6$.

4.3.2. Under-actuated case

We now consider that the control is achieved using m patches as depicted in Fig. 4.3. The aim of the control design is to modify as far as possible the internal elasticity $\tilde{T}$ of the string to get similar performances as in the fully-actuated case. We choose the controller matrix $B_c = J_m$

with $J_m \in \mathbb{R}^{m\times m}$ stemming from the discretization of $\frac{\partial}{\partial\varsigma}$. According to (4.25) in Proposition 6, $Q_c = J_m^{-T} V \Sigma_0^{-1} U_1^T Q_m U_1 \Sigma_0^{-1} V^T J_m^{-1}$.

D_c is chosen according to Remark 4.2.3, with desired time derivative of the Hamiltonian formulated in (4.16) being the fully-actuated case, *i.e.* in order to satisfy $\min_{D_c\in\mathbb{R}^{m\times m}} \|MD_cM^T - \text{diag}\,(\alpha L_{ab})\|_F$. As a results, the optimal D_c is given by $\hat{D}_c = \text{diag}\left(\frac{\alpha L_{ab}}{k}\right)$.

We first consider the case with 10 patches, *i.e.* $p = 50$, $m = 10$ and $k = 5$. The evolution of the string deformation as depicted in Fig. 4.8(a) is quite similar to that obtained in the fully-actuated case in Fig. 4.7(b). This indicates that if the controller matrices B_c, Q_c and D_c are adequately selected, the achievable performances in the under-actuated case can be optimized in order to be close to the ones obtained in the fully-actuated case. When the number of patches is reduced to 5, these performances are slightly deteriorated at high frequencies as shown in Fig. 4.8(b).

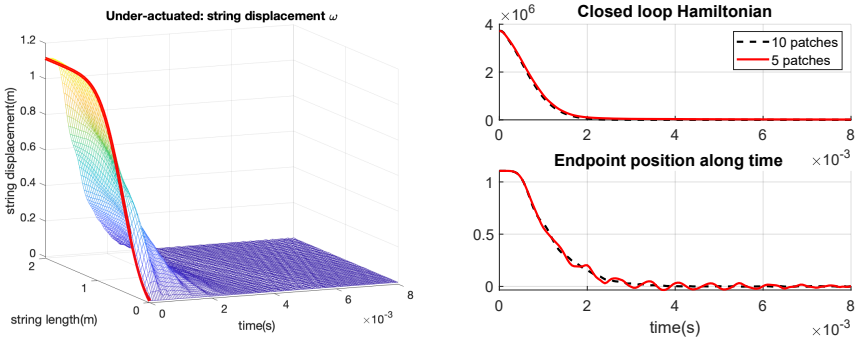

Figure 4.8: (a) Closed-loop evolution of the deformation, (b) Hamiltonian function and endpoint position in the under-actuated case for $k = 5$, and $k = 10$.

In order to illustrate the effect of the neglected dynamics on the achievable performances, we implement the controller designed considering 10 patches on the discretized system with $p = 50$, to a more precise model of the string derived using $p = 200$. In Fig. 4.9 we can see that, due to the damping injection and the associated closed-loop bandwidth, the neglected dynamics does not impact significantly the closed-loop response of the system to the considered initial condition. An example of in-domain controller design on Timoshenko beam model has been investigated in (Liu et al., 2021c; Le Gorrec et al., 2022).

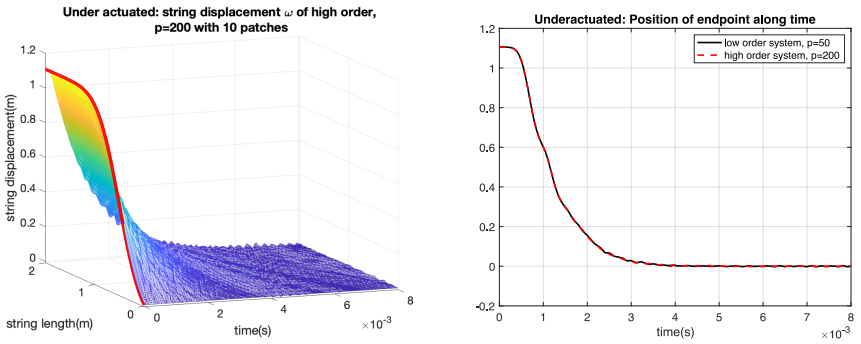

Figure 4.9: Closed-loop evolution of the deformation of the high order system, and comparison of the endpoint position of the low order and high order systems using the same controller.

4.4. Summary

In this chapter, we focus on the in-domain distributed control of the infinite dimensional PH systems using an early lumping approach. For the sake of clarity and compactness, the plant system is formulated with the example of a dissipative vibrating string. For control design purposes, we extend the Control by Interconnection method to the use of controllers distributed in space. The distributed structural invariants, $i.e.$ the Casimir functions, are employed to interconnect the state variables of the discretized plant system and the state variables of the controller. This structure invariants allows to modify the closed loop potential energy of the system, $e.g.$ the stiffness of the vibrating string example.

Two different cases of the controller design are investigated due to the independent number of inputs. The first case pertains to the ideal scenario in which the system is fully-actuated. The second case, referred to as the under-actuated case, involves achieving control through the use of piecewise homogeneous inputs. In this latter case, the controller is derived through an optimization method.

As for the early lumping approach, we study the stability of the closed loop between the infinite dimensional system and the finite dimensional controller. The closed loop system is asymptotically stable since the proposed controller has PHS structure and the control by interconnection maintain the passivity.

Simulations of both fully-actuated and under-actuated cases show that the damping injection renders the system asymptotically stable, while the energy shaping improves the dynamic performances of the closed loop system. Comparisons of the two cases also indicate that with an appropriate choice of the controller parameters, one can achieve similar performances for the under and fully-actuated cases over a given range of frequencies.

Chapter 5

Control of Mixed port Hamiltonian systems

5.1. Introduction

In this chapter, we investigate the stabilization of the Mixed ODE-PDE (m-ODE-PDE) with the actuation on the ODE part using the port Hamiltonian (PH) approach. The control design and the stabilization problem of m-ODE-PDE have been successfully tackled in different control scenarios using backstepping techniques. In particular, the stabilization problem for sandwiched parabolic m-PDE-ODE systems with control on the PDE boundaries and on the set of ODE has been solved on (Deutscher, 2015; Wang and Krstic, 2019), respectively. Moreover, backstepping control design has been applied to obtain the exponential stabilization of a class of heterodirectional hyperbolic m-ODE-PDE with actuation on the PDE boundaries (Meglio et al., 2018). Further, this result has been extended firstly to the same class of systems with space dependent parameters (Deutscher et al., 2019), and secondly for a class of heterodirectional m-ODE-PDE-ODE systems with actuation on one set of ODE (Deutscher et al., 2018). In this latter work, exponential stability is achieved trough a control law that, to be implementable, needs the use of an observer. In this work, we propose an asymptotically stabilizing static control strategy for a different class of hyperbolic m-ODE-PDE systems, that in most applications does not need the implementation of a dynamical controller.
It has been proven that linear operator equations of the form

$$\begin{aligned} \dot{x} &= Ax + Bu \quad x(0) = x_0 \\ y &= Cx \end{aligned} \tag{5.1}$$

with A generator of a bounded group (*i.e.* $\sup_{t\in\mathbb{R}} ||T(t)|| < \infty$) on a infinite dimensional state space X, and input matrix $B \in \mathcal{L}(\mathbb{R}^n, X)$, are not exponentially stabilizable with classical bounded linear feedback $u = -Fx$ with $F \in \mathcal{L}(X, \mathbb{R}^n)$(see in Lemma 8.4.1 of (Curtain and Zwart, 2020)). However, it has been shown that it is possible to use a "strong dissipation" feedback term $u = K_p \frac{\partial}{\partial t}(Cx)$ instead of the classical dissipation term. This type of feedback has already been applied and studied for specific sets of mixed ODE-PDE. In fact, the *strong dissipation* feedback has been used in (Morgül et al., 1994) to exponentially stabilize a wave equation with dynamic boundary conditions or in (Conrad and Morgül, 1998) for an Euler Bernoulli beam with a tip mass (see also (de Queiroz et al., 1999, 1997) for other examples). Compared to the these previous works that use the *strong dissipation* feedback (Rao, 1995), we extend the class of linear systems that could be interconnected at the boundary, allowing the presence of a position control or, equivalently, the presence of a spring. The combined *strong dissipation* and position control has already been obtained using backstepping techniques in (d' Andréa-Novel and Coron, 2000) for the specific case of a wave equation with dynamic boundary conditions. In (d' Andréa-Novel and Coron, 2000), the authors

carried out the analysis without position control term, concluding exponential stability of the closed-loop system. Besides, the *strong dissipation* with position control applied to a translating and rotating Timoshenko's beam in contact scenario has already been studied in (Endo et al., 2017), where exponential stability has been proved.
In this chapter, the considered m-PDE-ODE system is presented in Section 5.2. Then we investigate on the *strong dissipation* control for the m-PDE-ODE that encloses a variety of practical applications. First the strong *strong dissipation* without position control is considered in Section 5.3. With the use of Lyapunov argument and the help of PH structure of closed loop system, we show the wellposedness and the exponential stability of the closed-loop system. A Vibrating string with tip mass is used to show the effectiveness of the proposed *strong dissipation* control law. Secondly, we generalize the concept of combined *strong dissipation* and position control for the considered m-PH systems in Section 5.4. In this case, we propose a Lyapunov argument to show the asymptotic stability of the closed-loop system. The stability proof makes use of the properties of infinite dimensional PH systems. The effectiveness of the proposed control law is shown via the application on a Rotating translating flexible beam on the free side, together with a simulation comparison with a simple PD control law.

5.2. Mixed PH systems

In this section we would like to design different stabilizing control laws for a class of m-PH systems. Let $z \in L_2([0,L],\mathbb{R}^n)$, $p \in \mathbb{R}^m$ and consider the following m-PH system, as depicted in Figure 5.1

$$\begin{aligned} \begin{bmatrix} \dot{z} \\ \dot{p} \end{bmatrix} &= \begin{bmatrix} P_1 \frac{\partial}{\partial \xi}(\mathcal{H}z) + P_0(\mathcal{H}z) \\ -y_z + u \end{bmatrix} \\ y &= M^{-1}p \quad u_z = y \end{aligned} \tag{5.2}$$

where $\mathcal{H} \in C^1([0,L];\mathbb{R}^{n\times n})$, $\mathcal{H}(\xi)$ is self adjoint for all $\xi \in [0,L]$ and $cI \leq \mathcal{H}(\xi) \leq CI$ for all $\xi \in [0,L]$ and some $C, c > 0$ independent of ξ, $P_1 \in \mathbb{R}^{n\times n}$ is invertible and self adjoint, $P_0 \in \mathbb{R}^{n\times n}$ is skew adjoint, and with input output operators of the infinite dimensional part defined as

$$\begin{aligned} u_z &= \mathcal{B}_1(\mathcal{H}z) = W_{B,1}\begin{bmatrix} f_\partial \\ e_\partial \end{bmatrix} \quad \mathcal{B}_2(\mathcal{H}z) = W_{B,2}\begin{bmatrix} f_\partial \\ e_\partial \end{bmatrix} \\ y_z &= \mathcal{C}_1(\mathcal{H}z) = W_{C,1}\begin{bmatrix} f_\partial \\ e_\partial \end{bmatrix} \quad \mathcal{C}_2(\mathcal{H}z) = W_{C,2}\begin{bmatrix} f_\partial \\ e_\partial \end{bmatrix} \end{aligned} \tag{5.3}$$

such that $\operatorname{rank}(W_{B,1}) = \operatorname{rank}(W_{C,1}) = m$, and $\operatorname{rank}(W_{B,2}) = \operatorname{rank}(W_{C,2}) = n - m$ and $\left[\begin{smallmatrix} f_\partial \\ e_\partial \end{smallmatrix}\right]$ defined in Definition 2.13. Note that the output $y_z(t)$ has the same dimension as the input $u_z(t)$. We define the complete input and output operators as the composition of the previously defined operators

$$\begin{aligned} \mathcal{B}(\mathcal{H}z) &= \begin{bmatrix} \mathcal{B}_1(\mathcal{H}z) \\ \mathcal{B}_2(\mathcal{H}z) \end{bmatrix} = \begin{bmatrix} W_{B,1} \\ W_{B,2} \end{bmatrix} \begin{bmatrix} f_\partial \\ e_\partial \end{bmatrix} = W_B \begin{bmatrix} f_\partial \\ e_\partial \end{bmatrix} \\ \mathcal{C}(\mathcal{H}z) &= \begin{bmatrix} \mathcal{C}_1(\mathcal{H}z) \\ \mathcal{C}_2(\mathcal{H}z) \end{bmatrix} = \begin{bmatrix} W_{C,1} \\ W_{C,2} \end{bmatrix} \begin{bmatrix} f_\partial \\ e_\partial \end{bmatrix} = W_C \begin{bmatrix} f_\partial \\ e_\partial \end{bmatrix} \end{aligned} \tag{5.4}$$

with boundary flow and effort defined in Definition 2.13.

Remark 5.2.1. *The output operator $\mathcal{C}(\mathcal{H}z)$ is a point evaluation of the state $z(\xi,t)$, therefore it is a bounded operator from the state space Z to the output space $\mathbb{R}^n$, hence an admissible observation operator according to Definition* (5.2.1). ◊

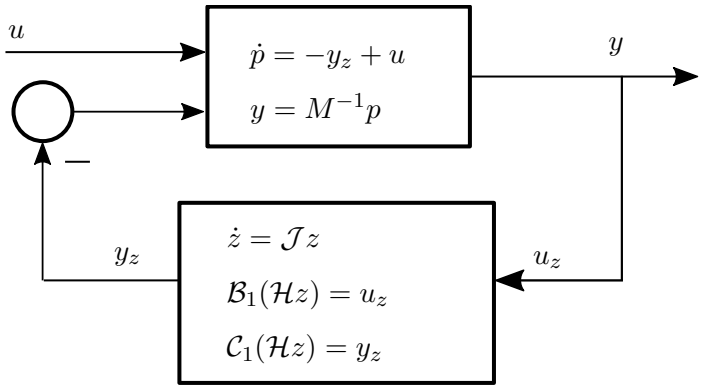

Figure 5.1: Considered class of m-PH systems.

We now recall the conditions for the m-PH system (5.2)-(5.4) and that will be assumed throughout the rest of this chapter.

Assumption 5.2.1. *1. The matrix* $\begin{bmatrix} W_B \\ W_C \end{bmatrix}$ *is invertible;*

2. W_B *and* W_C *are such that*

$$\begin{bmatrix} W_B\Sigma W_B^T & W_B\Sigma W_C^T \\ W_C\Sigma W_B^T & W_C\Sigma W_C^T \end{bmatrix} = \begin{bmatrix} 0 & I \\ I & 0 \end{bmatrix}. \tag{5.5}$$

◊ Before bringing the main results on the control design, we recall the following definition and theorem of approximately observability.

Definition 5.2.1. *Consider the linear system* $\Sigma(A, -, C, -)$*. The operator* $C : X \mapsto Y$ *is called an admissible observation operator for* $T(t)$ *if the estimate*

$$\int_0^\tau ||CT(t)x_0||^2 dt \leq k(\tau)||x_0||^2 \tag{5.6}$$

holds for every $\tau > 0$ *and for every* $x_0 \in \mathbf{D}(A)$*.* ◊

If $C \in \mathcal{L}(X, Y)$ then obviously it is admissible. In the following theorem, we make the connection between the approximate observability concept and the fact that the only solution of a homogeneous boundary control problem with constant output and zero as the only equilibrium position is the zero solution.

Lemma 5.2.1. *For the linear system* $\Sigma(A, -, C, -)$*the following statements are equivalent*

1. If $y(t)$ *is constant, then* $x_0 = 0$*.*

2. $\Sigma(A, -, C, -)$ *is approximately observable and its only equilibrium point is the origin.*

◊

Proof. 1) ⇒ 2) Let x_0 be such that the output $y(t)$ of $\Sigma(A, -, C, -)$ is identically zero. By 1) we see that $x_0 = 0$, and thus $\Sigma(A, -, C, -)$ is approximately observable.
Let x_{eq} be an equilibrium solution, then $0 = Ax_{eq}$, and the corresponding output (corresponding to $x(t) \equiv x_{eq}$) is $y(t) = Cx_{eq}$. This is constant, and so by 1) $x_{eq} = 0$.
2) ⇒ 1) Let $y(t)$ be a constant output of $\Sigma(A, C)$ and let $x(t)$ be the corresponding state trajectories. Define $y_\Delta(t) := y(t + t_1) - y(t) = 0$, $t_1 > 0$. The corresponding state trajectories is $x_\Delta(t) = x(t + t_1) - x(t)$. By approximate observability we have that $x_\Delta(0) = 0$. Thus $x(t_1) - x(0) = 0$. Since t_1 was arbitrary, we have that $x(t) \equiv x(0)$, and thus $x(0)$ is an equilibrium solution. By assumption we conclude that $x(0) = x_0 = 0$. □

This lemma will be applied to the infinite dimensional part of the obtained closed-loop system in order to find the large invariant subspace of the space for which the Lyapunov functional's derivative is zero.
In Lemma 5.2.1 we have shown the relation between the approximate observability property and the fact that a system admits zero as only solution. In the following theorem we give the conditions to obtain approximate observability for the class of 1-D dpH systems present in (5.2)-(5.4).

Theorem 5.2.1. *Consider the equation*

$$\dot{z} = P_1 \frac{\partial}{\partial \xi}(\mathcal{H}z) + P_0(\mathcal{H}z) = \mathcal{J}z \tag{5.7}$$

and boundary input/output operators (5.3)-(5.4)*, with homogeneous boundary conditions* $\mathcal{B}(\mathcal{H}z) = 0$*. Assume that the input/output of the system are chosen such that*

$$\begin{gathered} ||\mathcal{H}z(0,t)||^2 \leq ||u_z(t)||^2 + ||y_z(t)||^2 \\ or \\ ||\mathcal{H}z(L,t)||^2 \leq ||u_z(t)||^2 + ||y_z(t)||^2 \end{gathered} \tag{5.8}$$

then the system is approximately observable with respect to the $y_z = \mathcal{C}_1(\mathcal{H}z)$ *output.* ◊

Proof. We know that $\mathcal{J}$ is a skew-adjoint, therefore its eigenvalues belong to the imaginary axis. Operator (5.7) generates a unitary group if and only if it is a skew-adjoint operator (see Theorem 2.32 in (Luo et al., 2012)) and by Theorem 2.28 in (Villegas, 2007), its resolvent is compact, then we know by Theorem A.4.19 (Curtain and Zwart, 2020), that its eigenvectors forms an orthonormal basis. Since an orthonormal basis is a special case of a Riesz-Basis, operator (5.7) is a Riesz-spectral operator. Consequently, using theorem 6.3.6 of (Curtain and Zwart, 2020), to check that the system is approximately observable we have to show that there exists no eigenvector in the kernel of $\mathcal{C}_1$. To show this, assume by contradiction that there exists an eigenvector v such that $\mathcal{C}_1 v = 0$. We now consider the first inequality of (5.8) to hold. Using the homogeneous boundary conditions together with $y_z = \mathcal{C}_1 v = 0$ in the first inequality of (5.8), we obtain $\mathcal{H}z(0,t) = 0$. We integrate both side of the eigenvalue problem's equation (obtained imposing $z = v(\xi)e^{iwt}$ in (5.7), where v is the eigenvector and iw the corresponding eigenvalue)

$$iwv(\xi) = P_1 \frac{\partial}{\partial \xi}(\mathcal{H}v)(\xi) + P_0(\mathcal{H}v)(\xi) \tag{5.9}$$

to obtain

$$\begin{aligned} iw \int_0^s v(\xi)d\xi = &\quad P_1 \int_0^s \frac{\partial}{\partial \xi}(\mathcal{H}v)(\xi)d\xi + \int_0^s P_0(\mathcal{H}v)(\xi)d\xi \\ \int_0^s (w\mathcal{H}^{-1}(\xi) - P_0)(\mathcal{H}v)(\xi)d\xi = &\quad P_1[(\mathcal{H}v)(s) - (\mathcal{H}v)(0)] \\ \int_0^s (w\mathcal{H}^{-1} - P_0)\mathcal{H}v(\xi)d\xi = &\quad P_1(\mathcal{H}v)(s) \end{aligned} \tag{5.10}$$

With P_1 being full rank, the former equation is equivalent to

$$(\mathcal{H}v)(s) = P_1^{-1} \int_0^s g(\xi)(\mathcal{H}v)(\xi)d\xi, \tag{5.11}$$

with $g(\xi) = (iw\mathcal{H}^{-1}(\xi) - P_0)$. From the former equation we get

$$\begin{aligned} ||(\mathcal{H}v)(s)|| \leq &\quad ||P_1^{-1}|| \int_0^s ||g(\xi)\mathcal{H}v(\xi)||d\xi \\ \leq &\quad ||P_1^{-1}|| \int_0^s ||g(\xi)|| \cdot ||\mathcal{H}v(\xi)||d\xi \\ \leq &\quad K \int_0^s ||\mathcal{H}v(\xi)||d\xi \end{aligned}$$

since both P_1^{-1} and $||g(\xi)||$ are bounded from above. Using the integral form of the Gronwall's Lemma we obtain that

$$||(\mathcal{H}v)(s)|| \leq 0, \tag{5.12}$$

that implies $(\mathcal{H}v)(s) \equiv 0$, which since $\mathcal{H}(\xi) \geq mI$ with $m > 0$ implies $v(s) \equiv 0$, that is a contradiction to the fact that v is an eigenvector. If the second inequality of (5.8) holds instead of the first one, we obtain $\mathcal{H}z(L,t) = 0$. Therefore, we integrate (5.9) from s to L such that

$$iw \int_s^L v(\xi)d\xi = P_1 \int_s^L \frac{\partial}{\partial \xi}(\mathcal{H}v)(\xi)d\xi + \int_s^L P_0(\mathcal{H}v)(\xi)d\xi. \tag{5.13}$$

The rest of the proof follows in a similar manner as before. □

An immediate consequence is that a 1-D dpH system with a sufficient number of inputs and constant boundary output admits zero as only solution if the origin is its only equilibrium point.

Corollary 5.2.1. *Consider the dpH system* (5.7) *with boundary input/output and operators defined in* (5.3)-(5.4). *Assume that the input/output of the system are selected such to fulfil* (5.8), *then if* $y_z(t)$ *is constant and the origin is the only equilibrium point, then* $z(t) \equiv 0$ *for all* $t \geq 0$. ◊

Proof. It is a direct consequence of Lemma 5.2.1 and Theorem 5.2.1. □

In the following, we will present the strong dissipation control applicable to the considered class of m-PH systems. At the end, we present an application of the proposed control law for the clamped-free vibrating string with moving mass attached to the free side. The example are endowed with numerical simulations that have been performed using Matlab®.

5.3. Strong dissipation control of a m-PH system

In this section we propose an (unbounded) linear feedback that allows to exponentially stabilize the considered class of system:

$$u(t) = -R_p M^{-1} p - R_p M^{-1} K_p \mathcal{C}_1(\mathcal{H}z) - K_p \frac{d}{dt}(\mathcal{C}_1(\mathcal{H}z)) \tag{5.14}$$

where $R_p = \text{diag}([r_{p,1} \ \dots \ r_{p,m}]) \in \mathbb{R}^{m\times m}$, $K_p = \text{diag}([k_{p,1} \ \dots \ k_{p,m}]) \in \mathbb{R}^{m\times m}$ and the last term is known in the literature of stabilization of mixed PDEs-ODEs systems as *strong dissipation feedback*. The proposed linear feedback is unbounded because it contains a time derivative of the state: even if the state is bounded, there is no *a priori* assurance that also the control law is bounded.The control law (5.14) uses the output $\mathcal{C}_1(\mathcal{H}z)$ of the distributed parameter part together with the standard output $y = M^{-1}p$ of the system. Since all the variables needed to the application of the control law can be obtained through the use of sensors, we can class the control law (5.14) as *output feedback*. This type of control law has also been used in the stabilization of flexible beams, and it is normally referred to as *strain rate feedback* (Weldegiorgis et al., 2014). In case of application on moving flexible beams, this control input can be computed calculating an approximated and filtrated version of the time derivative of the strain measurement as explained in (de Queiroz et al., 1999). Applying the control law (5.14) to system (5.2), we obtain the closed-loop system depicted in Figure 5.2 of equations

$$\begin{cases} \dot{z} = P_1 \frac{\partial}{\partial \xi}(\mathcal{H}z) + P_0(\mathcal{H}z) \\ \dot{p} = -\mathcal{C}_1(\mathcal{H}z) - R_p M^{-1}(p + K_p \mathcal{C}_1(\mathcal{H}z)) - K_p \frac{d}{dt}(\mathcal{C}_1(\mathcal{H}z)). \end{cases} \tag{5.15}$$

To analyse the resulting closed-loop system we perform the change of variable $\eta = p + K_p\mathcal{C}_1(\mathcal{H}z)$. Therefore, we define $x = [\begin{smallmatrix} z \\ \eta \end{smallmatrix}] \in X = L_2([a,b],\mathbb{R}^n) \times \mathbb{R}^{2m}$ such to write the system as a linear operator equation

$$\dot{x} = Ax = \begin{bmatrix} P_1 \frac{\partial}{\partial \zeta}(\mathcal{H}z) + P_0(\mathcal{H}z) \\ -\mathcal{C}_1(\mathcal{H}z) - R_p M^{-1}\eta \end{bmatrix} \tag{5.16}$$

with domain defined as

$$\begin{aligned} \mathbf{D}(A) = \; & \big\{ x \in X \mid z \in H^1([a,b],R^n), \\ & \mathcal{B}_1(\mathcal{H}z) = M^{-1}(\eta - K_p\mathcal{C}_1(\mathcal{H}z)), \mathcal{B}_2(\mathcal{H}z) = 0 \big\}. \end{aligned} \tag{5.17}$$

We define the inner product

$$\langle x_1, x_2 \rangle_X = \langle z_1, \mathcal{H}z_2 \rangle_{L_2} + \eta_1^T M^{-1} \eta_2 \tag{5.18}$$

and we equip the state space X with the associated norm $||x|| = \sqrt{\langle x, x \rangle_X}$. Since the made change of variables is bounded and invertible, studying the stability of (5.16) is equivalent to studying the stability of (5.15).
To conclude about exponential stability of the closed-loop system (5.16)-(5.17), throughout this section we assume the following assumption on the number of actuated inputs for the infinite dimensional part.

Assumption 5.3.1. *The m input/output of the system are chosen such that*

$$\begin{gathered} ||\mathcal{H}z(0,t)||^2 \leq ||u_z(t)||^2 + ||y_z(t)||^2 \\ or \\ ||\mathcal{H}z(L,t)||^2 \leq ||u_z(t)||^2 + ||y_z(t)||^2. \end{gathered} \tag{5.19}$$

$\Diamond$

In practice, these inequalities require that we have all the boundary controls at least at one side of the spatial domain. We want to remark that these inequalities are the same required also in Theorem 5.2.1, to conclude about approximate observability of a 1-D dpH system. Moreover, these same inequalities are required in (Ramirez et al., 2017) in order to have a 1-D dpH system that is exponentially stabilizable.
We start by showing that the closed-loop operator generates a contraction C_0-semigroup in the defined state space X.

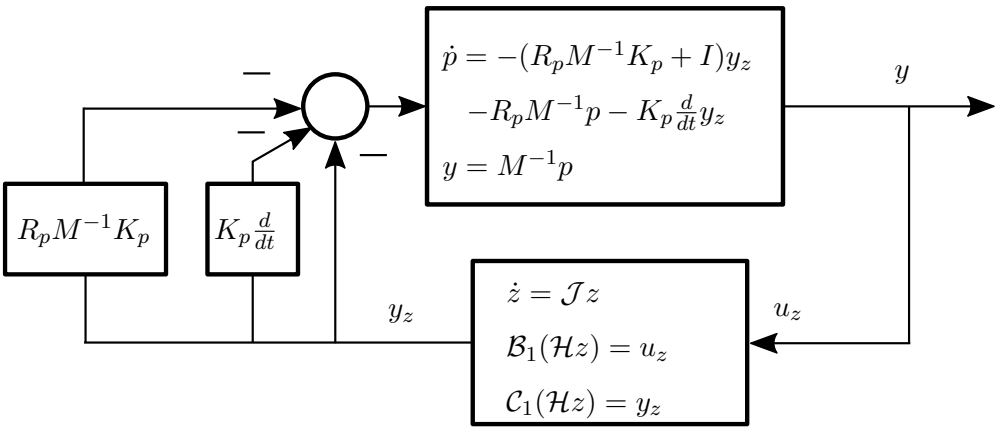

Figure 5.2: m-PH system in closed-loop with a *strong feedback* control law.

Theorem 5.3.1. *Under Assumption 5.2.1, system* (5.16) *with domain defined by* (5.17) *generates a contraction C_0-semigroup in the state space X and has a compact resolvent.* ◊

Proof. Thanks to Theorem 1.3.1 (Mattioni, 2021) we only have to show that the operator A with domain $\mathbf{D}(A)$ is dissipative in the norm associated to the state space X. Therefore, knowing that $y_z = \mathcal{C}_1(\mathcal{H}z)$, we compute

$$\begin{aligned}\langle Ax, x\rangle = &\ \langle \mathcal{J}z, z\rangle_Z + (-\mathcal{C}_1(\mathcal{H}z) - R_pM^{-1}\eta)^TM^{-1}\eta \\ = &\ y_z^Tu_z - \mathcal{C}_1(\mathcal{H}z)^TM^{-1}\eta - (M^{-1}\eta)^TR_p(M^{-1}\eta) \\ = &\ y_z^TM^{-1}(\eta - K_py_z) - y_z^TM^{-1}\eta - (M^{-1}\eta)^TR_p(M^{-1}\eta) \\ = &\ -y_z^TK_pM^{-1}y_z - (M^{-1}\eta)^TR_p(M^{-1}\eta) \leq 0.\end{aligned} \tag{5.20}$$

This shows that the operator A is dissipative in X and therefore that generates a contraction C_0-semigroup in X and has a compact resolvent. □

In the following lemmas we show some inequalities that will be necessary for the exponential stability proof of the closed-loop operator.

Lemma 5.3.1. *Let $x(\zeta, t)$ be a solution generated by* (5.16)-(5.17). *Under Assumption 5.3.1 there exists a constant $\alpha > 0$ such that the state trajectories satisfies*

$$\begin{gathered}\alpha\left(||\mathcal{H}z(0,t)||^2 + ||\eta||^2\right) \leq y_z^TK_pM^{-1}y_z + (M^{-1}\eta)^TR_p(M^{-1}\eta) \\ or \\ \alpha\left(||\mathcal{H}z(L,t)||^2 + ||\eta||^2\right) \leq y_z^TK_pM^{-1}y_z + (M^{-1}\eta)^TR_p(M^{-1}\eta).\end{gathered} \tag{5.21}$$

◊

Proof. Use equation (5.19) and (5.17) to write

$$\begin{aligned}||\mathcal{H}z(0,t)||^2 + ||\eta(t)||^2 \leq &\ ||u_z||^2 + ||y_z||^2 + ||\eta||^2 \\ = &\ ||M^{-1}(\eta + K_py_z)||^2 + y_z^Ty_z + \eta^TM^{-1}\eta\end{aligned} \tag{5.22}$$

that since we are considering the norm associated to the inner product (5.18)

$$\begin{aligned}||\mathcal{H}z(0,t)||^2 + ||\eta(t)||^2 \leq &\ (\eta + K_py_z)^TM^{-2}(\eta + K_py_z) + y_z^Ty_z \\ &+\eta^TM^{-1}\eta \\ = &\ y_z^T(K_p^2M^{-2} + I)y_z + \eta^T(M^{-2} + M^{-1})\eta \\ &+2\eta M^{-2}K_py_z.\end{aligned} \tag{5.23}$$

Then, we use the inequality

$$2\eta M^{-2}K_py_z \leq y_z^TK_p^2M^{-2}y_z + \eta^TM^{-2}\eta \tag{5.24}$$

together with the fact that M and K_p are diagonal matrices, to write

$$\begin{aligned}||\mathcal{H}z(0,t)||^2 + ||\eta(t)||^2 \leq &\ y_z^T(2K_p^2M^{-2} + I)y_z + \eta^T(2M^{-2} + M^{-1})\eta \\ = &\ y_z^TK_p(2K_pM^{-1} + K_p^{-1}M)M^{-1}y_z \\ &+(M^{-1}\eta)^TR_pR_p^{-1}(2I + M))(M^{-1}\eta) \\ \leq &\ \gamma_1y_z^TK_pM^{-1}y_z + \gamma_2(M^{-1}\eta)^TR_p(M^{-1}\eta) \\ \leq &\ \max\{\gamma_1, \gamma_2\}(y_z^TK_pM^{-1}y_z + (M^{-1}\eta)^TR_p(M^{-1}\eta))\end{aligned} \tag{5.25}$$

where γ_1 and γ_2 are the biggest eigenvalues of $2K_pM^{-1}+K_p^{-1}M$ and $R_p^{-1}(2I+M)$, respectively. Finally define

$$\alpha = \frac{1}{\max\{\gamma_1, \gamma_2\}} \tag{5.26}$$

such that equation (5.21) follows. □

Lemma 5.3.2. *Let $x(\zeta, t)$ be a solution generated by the closed-loop system* (5.16) - (5.17)*, then under Assumption 5.2.1 and 5.3.1 the functional*

$$V(x) = \frac{1}{2}\langle x, x\rangle_X = \frac{1}{2}\int_0^L z(\xi,t)^T\mathcal{H}z(\xi,t)d\xi + \frac{1}{2}\eta^T M^{-1}\eta \tag{5.27}$$

is a Lyapunov functional and satisfies for $t > 2\gamma L$, where γ is such that $P_1^{-1} + \gamma\mathcal{H}(\xi)$ and $-P_1^{-1} + \gamma\mathcal{H}(\xi)$ are positive definite,

$$c_1(t)V(x(t)) \leq \int_0^t ||\mathcal{H}z(0,\tau)||^2 d\tau + \int_0^t ||\eta(\tau)||^2 d\tau \tag{5.28}$$

where $c_1(t) = \frac{2(t-2\gamma L)}{\beta_1}$, $\beta_1 = \max\{L, 1\}$ or

$$c_2(t)V(x(t)) \leq \int_0^t ||\mathcal{H}z(L,\tau)||^2 d\tau + \int_0^t ||\eta(\tau)||^2 d\tau \tag{5.29}$$

where $c_2(t) = \frac{2(t-2\gamma L)}{\beta_2}$, $\beta_2 = \max\{Le^{\kappa L}, 1\}$ and κ is such that $\mathcal{H}(\xi)P_0^TP_1^{-1} + P_1^{-1}P_0\mathcal{H}(\xi) + \frac{\partial\mathcal{H}}{\partial\xi}(\xi) \leq \kappa\mathcal{H}(\xi)$. ◊

Proof. We define the function $F : [0, L] \mapsto \mathbb{R}$ by

$$F(\xi) = \int_{\gamma\xi}^{t-\gamma\xi} z^T(\xi,\tau)\mathcal{H}(\xi)z(\xi,\tau)d\tau, \quad \xi \in [0, L], \tag{5.30}$$

where we assume that $\gamma > 0$ and $t > 2\gamma L$. Differentiating the function F with respect to ξ gives

$$\begin{aligned}\frac{dF}{d\xi}(\xi) = \; & \int_{\gamma\xi}^{t-\gamma\xi} z^T(\xi,\tau)\frac{\partial}{\partial\xi}(\mathcal{H}(\xi)z(\xi,\tau))d\tau \\ & + \int_{\gamma\xi}^{t-\gamma\xi}\left(\frac{\partial}{\partial\xi}z(\xi,\tau)\right)^T\mathcal{H}(\xi)z(\xi,\tau)d\tau \\ & -\gamma z^T(\xi,t-\gamma\xi)\mathcal{H}(\xi)z(\xi,t-\gamma\xi) - \gamma z^T(\xi,\gamma\xi)\mathcal{H}(\xi)z(\xi,\gamma\xi).\end{aligned} \tag{5.31}$$

After some similar passages as in the proof of Lemma 9.1.2 in (Jacob and Zwart, 2012) we get

$$\begin{aligned}\frac{dF}{d\xi}(\xi) = \; & -\int_{\gamma\xi}^{t-\gamma\xi} z^T(\xi,\tau)\left(\mathcal{H}(\xi)P_0^TP_1^{-1} + P_1^{-1}P_0\mathcal{H}(\xi) + \frac{\partial\mathcal{H}}{\partial\xi}(\xi)\right)z(\xi,\tau)d\tau \\ & -z^T(\xi,t-\gamma\xi)\left(-P_1^{-1} + \gamma\mathcal{H}(\xi)\right)z(\xi,t-\gamma\xi) \\ & -z^T(\xi,\gamma\xi)\left(P_1^{-1} + \gamma\mathcal{H}(\xi)\right)z(\xi,\gamma\xi).\end{aligned} \tag{5.32}$$

Now we select γ large enough, such that $P_1^{-1} + \gamma\mathcal{H}$ and $-P_1^{-1} + \gamma\mathcal{H}$ are positive definite, such to obtain

$$\frac{dF}{d\xi}(\xi) \leq -\int_{\gamma\xi}^{t-\gamma\xi} z^T(\xi,\tau)\left(\mathcal{H}(\xi)P_0^TP_1^{-1} + P_1^{-1}P_0\mathcal{H}(\xi) + \frac{\partial\mathcal{H}}{\partial\xi}(\xi)\right)z(\xi,\tau)d\tau. \tag{5.33}$$

Since P_1 and P_0 are constant matrices and $\frac{\partial \mathcal{H}}{\partial \xi}(\xi)$ is bounded, there exists a constant $\kappa > 0$ such that for all $\xi \in [0, L]$ we have

$$\mathcal{H}(\xi)P_0^T P_1^{-1} + P_1^{-1}P_0\mathcal{H}(\xi) + \frac{\partial \mathcal{H}}{\partial \xi}(\xi) \geq \kappa_1 \mathcal{H}(\xi) \tag{5.34}$$

and therefore we obtain

$$\frac{dF}{d\xi}(\xi) \leq -\kappa \int_{\gamma\xi}^{t-\gamma\xi} z^T(\xi,\tau)\mathcal{H}(\xi)z(\xi,\tau)d\tau = -\kappa_1 F(\xi). \tag{5.35}$$

The former inequality implies

$$F(\xi) \leq e^{-\kappa\xi}F(0) \quad \text{for } \xi \in [0, L], \tag{5.36}$$

that in turn means $F(\xi) \leq F(0)$. In order to obtain the second inequality (5.29) we select

$$F(\xi) = \int_{\gamma(L-\xi)}^{\tau-\gamma(L-\xi)} z(\xi,t)^T \mathcal{H} z(\xi,t)dt. \tag{5.37}$$

instead of (5.30) and following the same passages as in Lemma 9.1.2 of (Jacob and Zwart, 2012), it is possible to obtain that $F(\xi) \leq e^{\kappa L}F(0)$ where κ is such that

$$\mathcal{H}(\xi)P_0^T P_1^{-1} + P_1^{-1}P_0\mathcal{H}(\xi) + \frac{\partial \mathcal{H}}{\partial \xi}(\xi) \leq \kappa \mathcal{H}(\xi). \tag{5.38}$$

We now compute the time derivative of (5.27) using Assumption 5.2.1 and the A dissipativity

$$\dot{V}_+(x) = \langle x, Ax\rangle_X \leq 0. \tag{5.39}$$

Therefore, the functional V is a Lyapunov functional. For the rest of the proof we proceed similarly to the proof of *Lemma* 4.1 in (Ramirez et al., 2014).
Using the fact that the Lyapunov functional (5.27) is non-increasing along the system's trajectories, it holds

$$\begin{aligned} \int_{\gamma L}^{t-\gamma L} V(x(\tau))d\tau \geq & \quad V(x(t-\gamma L)) \int_{\gamma L}^{t-\gamma L} 1 d\tau \\ = & \quad (t-2\gamma L)V(x(t-\gamma L)). \end{aligned} \tag{5.40}$$

We use again the non-increasing property of the Lyapunov functional to write

$$\begin{aligned} & 2(t-2\gamma L)V(x(t)) \\ \leq & \quad 2(t-2\gamma L)V(x(t-\gamma L)) \\ \leq & \quad 2\int_{\gamma L}^{t-\gamma L} V(x(\tau))d\tau \\ = & \quad \int_0^L \int_{\gamma L}^{t-\gamma L} z^T(\xi,\tau)\mathcal{H}z(\xi,\tau)d\tau d\xi + \int_{\gamma L}^{t-\gamma L} ||\eta(\tau)||^2 d\tau \\ \leq & \quad \int_0^L \int_{\gamma\xi}^{t-\gamma\xi} z^T(\xi,\tau)\mathcal{H}z(\xi,\tau)d\tau d\xi + \int_0^t ||\eta(\tau)||^2 d\tau \end{aligned} \tag{5.41}$$

where, for the last inequality, we have increased the integration time. Use definition (5.30) and increase once again the integration interval of the second term to obtain

$$\begin{aligned} 2(t-2\gamma L)V(x(t)) \leq & \quad \int_0^L F(\xi)d\xi + \int_0^t ||\eta(\tau)||^2 d\tau \\ \leq & \quad LF(0) + \int_0^t ||\eta(\tau)||^2 d\tau \\ = & \quad L\int_0^t z(0,\tau)^T \mathcal{H} z(0,\tau)d\tau + \int_0^t ||\eta(\tau)||^2 d\tau \\ \leq & \quad \beta\left(\int_0^t ||\mathcal{H}z(0,\tau)||^2 d\tau + \int_0^t ||\eta(\tau)||^2 d\tau\right) \end{aligned} \tag{5.42}$$

where $\beta = \max\{L, 1\}$. Hence, we obtain

$$\frac{2(t-2\gamma L)}{\beta} V(x(t)) \leq \int_0^t ||\mathcal{H}z(0,\tau)||^2 d\tau + \int_0^t ||\eta(\tau)||^2 d\tau \tag{5.43}$$

that shows inequality (5.28) with $c(\tau) = \frac{2(t-2\gamma L)}{\beta}$. The other inequality is obtained using $F(\xi) \leq F(L)e^{\kappa L}$ instead of $F(\xi) \leq F(0)$ in (5.42)

$$\begin{aligned} 2(t-2\gamma L)V(x(t)) \leq & \int_0^L F(\xi)d\xi + \int_0^t ||\eta(\tau)||^2 d\tau \\ \leq & LF(0)e^{\kappa L} + \int_0^t ||\eta(\tau)||^2 d\tau \\ = & Le^{\kappa L} \int_0^t z(0,\tau)^T \mathcal{H} z(0,\tau) d\tau + \int_0^t ||\eta(\tau)||^2 d\tau \\ \leq & \beta_2 \left(\int_0^t ||\mathcal{H}z(0,\tau)||^2 d\tau + \int_0^t ||\eta(\tau)||^2 d\tau \right) \end{aligned} \tag{5.44}$$

where $\beta_2 = \max\{Le^{\kappa L}, 1\}$. □

Now we are in position to state the theorem on exponential stability of the origin of the closed-loop operator.

Theorem 5.3.2. *Under Assumption 5.2.1 and Assumption 5.3.1, the origin of the closed-loop system described by equations* (5.16)-(5.17) *is exponentially stable.* ◊

Proof. We use equations (5.20) and (5.39) to obtain

$$\dot{V}_+(x) = -y_z^T K_p M^{-1} y_z - (M^{-1}\eta)^T R (M^{-1}\eta). \tag{5.45}$$

We use inequality (5.21) in the above equation

$$\dot{V}_+(x) \leq -\alpha \left(||\mathcal{H}z(0,t)||^2 + ||\eta||^2 \right) \tag{5.46}$$

and integrating in time between 0 and t both sides of the above equation and using inequality (5.28), we obtain

$$\begin{aligned} V(x(t)) - V(x(0)) \leq & -\alpha \left(\int_0^t ||\mathcal{H}z(0,\tau)||^2 d\tau + \int_0^t ||\eta(\tau)|| d\tau \right) \\ \leq & -\alpha c(t) V(x(t)) \end{aligned} \tag{5.47}$$

which implies,

$$V(x(t)) \leq \frac{1}{1+\alpha c(t)} V(x(0)). \tag{5.48}$$

It is possible to see that the Lyapunov functional V is equivalent to the square norm of the state, hence the above equation implies

$$||x(t)||^2 \leq \frac{1}{1+\alpha c(t)} ||x(0)||^2. \tag{5.49}$$

Let $T(t)$ be the semigroup generated by the operator A. From the latter equation we obtain for all $x_0 \in X$

$$||T(t)x_0||^2 \leq \frac{1}{1+\alpha c(t)} ||x_0||^2 \tag{5.50}$$

that is equivalent to

$$||T(t)||^2 \leq \frac{1}{1+\alpha c(t)}. \tag{5.51}$$

Since $c(t)$ is a positive function such that $c(t) \to \infty$ for $t \to \infty$, there exists a $t^* > 0$ such that $||T(t)|| < 1$ for all $t > t^*$. Consequently $w_0 = \inf_{t>0} \left(\frac{1}{t} \log ||T(t)||\right) < 0$ and by Theorem 5.1.5 (Jacob and Zwart, 2012) we can conclude that there exist constants $M_w > 0$ and $w < 0$ such that $||T(t)|| \leq M_w e^{wt}$ for all $t \geq 0$. □

Remark 5.3.1. *The previous theorem states that the norm of the state $||x(t)||$ can be bounded by an exponential, i.e.*

$$||x(t)|| \leq M_w e^{wt} ||x_0|| \tag{5.52}$$

with $w < 0$ and in general $M_w \leq 0$. The constant M_w is not a priori known and is in general strictly greater than zero. ♢

In the following example we show how to apply the strong dissipation feedback control law to an applicative example, and how it is possible to compute the exponential bound of the system's state norm along time.

Example 5.3.1 (Vibrating string with tip mass and Strong dissipation control)**.** *We study the control problem of the stabilization of a clamped string with tip mass on the other side using a force applied on the tip mass. The model is written as the following form:*

$$\begin{aligned} \dot{z} &= P_1 \tfrac{\partial}{\partial \xi}(\mathcal{H}z) = \mathcal{J}z \\ \dot{p} &= -\mathcal{C}_1(\mathcal{H}z) + f(t), \end{aligned} \tag{5.53}$$

with matrix P_1 and the energy density defined as

$$P_1 = \begin{bmatrix} 0 & 1 \\ 1 & 0 \end{bmatrix} \quad \mathcal{H}(\xi) = \begin{bmatrix} \frac{1}{\rho(\xi)} & 0 \\ 0 & T(\xi) \end{bmatrix}. \tag{5.54}$$

and domain of the $\mathcal{J}$ operator

$$\mathbf{D}(\mathcal{J}) = \left\{ z \in L_2([0,L], \mathbb{R}^2) \mid (\mathcal{H}z) \in H^1([0,L], \mathbb{R}^2), \mathcal{B}_1(\mathcal{H}z) = \frac{1}{m}p,\ \mathcal{B}_2(\mathcal{H}z) = 0 \right\}. \tag{5.55}$$

The energy variable $z = [z_1 \ \ z_2]^T$ and p are defined as:

$$z_1(\xi,t) = \rho(\xi)\frac{\partial w}{\partial t}(\xi,t), \quad z_2(\xi,t) = \frac{\partial w}{\partial \xi}(\xi,t), \quad p(t) = m\frac{dw}{dt}(0,t), \tag{5.56}$$

and we define the input output operators for the string equation

$$\begin{aligned} \mathcal{B}(\mathcal{H}z) &= \begin{bmatrix} \mathcal{B}_1(\mathcal{H}z) \\ \mathcal{B}_2(\mathcal{H}z) \end{bmatrix} = \begin{bmatrix} \frac{1}{\rho(0)} z_1(0,t) \\ \frac{1}{\rho(L)} z_1(L,t) \end{bmatrix}, \\ \mathcal{C}(\mathcal{H}z) &= \begin{bmatrix} \mathcal{C}_1(\mathcal{H}z) \\ \mathcal{C}_2(\mathcal{H}z) \end{bmatrix} = \begin{bmatrix} -T(0) z_2(0,t) \\ T(L) z_2(L,t) \end{bmatrix} \end{aligned}. \tag{5.57}$$

The energy of the vibrating string with a tip mass can be expressed as

$$E(z,p) = \frac{1}{2}\langle z, \mathcal{H}z \rangle_{L_2} + \frac{1}{2m}p^2. \tag{5.58}$$

The control objective is to stabilize the system in the zero state $p = 0$, $z = 0$, as depicted in Figure 5.3. Consider the closed-loop operator (5.16)-(5.17) *with matrices and input-output operators corresponding to the vibrating string with a tip mass introduced in* (5.53)*. The considered*

Table 5.1: Simulation parameters; strong dissipation example

Name	Variable	Value
String's Length	L	$1\ m$
Density	ρ	$1\ \frac{kg}{m}$
Tension	T	1
Tip's mass	m	$1\ kg$

physical parameters are listed in Table 5.1, while the control parameters are selected such that $k_p = 0.7$, $r_p = 5$. *We notice that*

$$\begin{aligned} ||\mathcal{H}z(0,t)||^2 = &\ ||\tfrac{1}{\rho(0)}z_1(0,t)||^2 + ||T(0)z_2(0,t)||^2 \\ = &\ ||u_z(t)||^2 + ||y_z(t)||^2 \end{aligned} \tag{5.59}$$

and therefore, according to Theorem 5.3.2, the origin of the string equation with a tip mass (5.53) *in closed-loop with a strong dissipation feedback* (5.14) *is exponentially stable.*
Therefore, we can compute all the parameters necessary to find the exponential bound of the state's norm. In particular, according to Lemma 5.3.2 we can compute that for a wave equation with varying parameters

$$\gamma > \max_{\xi\in[0,L]} \sqrt{\frac{\rho(\xi)}{T(\xi)}}. \tag{5.60}$$

Then, $\gamma_1 = 2k_p m^{-2} + kp^{-1}$ $\gamma_2 = r_p^{-1}(2m^{-1} + m)$. *Considering the control and the system's parameters in Table 5.1, we find*

$$\gamma = 1 \quad \beta = 1 \quad \gamma_1 = 2.83 \quad \gamma_2 = 0.60 \tag{5.61}$$

and consequently $\alpha = 0.35$.

For the simulation propose, we use the methodology introduced in Section 2.2 of Chapter 2 in (Mattioni, 2021) to discretize the system (5.53). *The initial conditions are set as following* $z_1(\xi,0) = 0$, $z_2(\xi,0) = sin(2\pi\frac{\xi}{L}) - \xi + 1$, $\eta = 0$. *In Figure 5.4 and 5.5a are shown the string deformation and the Energy behaviour along time, respectively. In Figure 5.5b we plot the state's norm together with the exponential bound assured by Theorem 5.3.2. As highlighted in Remark 5.3.1, the system's norm is bounded by an exponential* $||x(t)|| \leq M_w e^{w_0 t}||x_0||$ *for* $t \geq 0$. *The exponential bound has been computed as* $w_0 = \inf_{t>0}\left(\frac{1}{t}\log||T(t)||\right)$ *through Matlab® numerical methods, using the* C_0*-semigroup norm defined in* (5.51), *and it results to be equal to* $w_0 = -0.1099$. *It is worth to remark that the exponential bound in Figure 5.5b has been plotted fixing the parameter* $M_w = 1.03$, *that has been decided only after the state's norm decay was obtained. This to say that in case the parameter* M_w *is needed for any set of initial conditions, a more sharper analysis has to be carried.* ◊

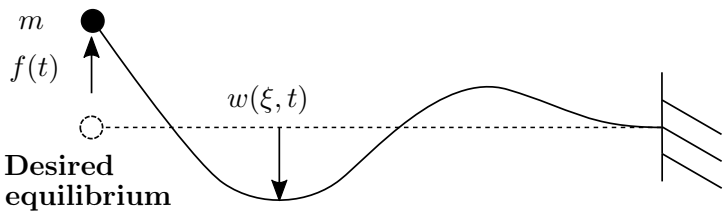

Figure 5.3: String with a tip mass with origin equilibrium point.

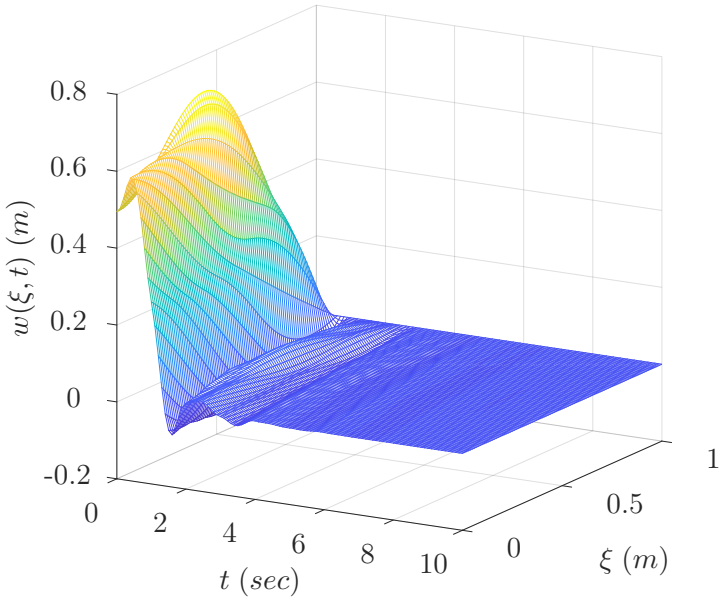

Figure 5.4: String deformation along time.

The control law introduced in this section allows to stabilize the variables z and p without any control on the position of the tip mass. If the control objective is to stabilize the system in a desired position, we are forced to add in the control law a term proportional to the position, that will be investigated in the next section.

5.4. Strong dissipation plus position control of a m-PH system

In this section we add to the control law (5.14) the term corresponding a new state variable q defined as the time integral of the momenta p multiplying the inverse of the mass matrix

$$q(t) = \int_0^t M^{-1}p(\tau)d\tau. \tag{5.62}$$

Since the quantity $M^{-1}p$ physically corresponds to a velocity, its time integral corresponds to a position configuration in case the modelled system corresponds to a mechanical mechanism. Adding this variable in the control-loop means that the controller will be able to steer the mechanism to a desired configuration. In this purpose, we propose the following control law

$$u = -R_pM^{-1}p - Kq + (I - R_pM^{-1}K_p)\mathcal{C}_1(\mathcal{H}z) - K_p\frac{d}{dt}(\mathcal{C}_1(\mathcal{H}z)), \tag{5.63}$$

where $R_p = diag([r_{p,1}\ \dots\ r_{p,m}])$, $K = diag([k_1\ \dots\ k_m])$, $K_p = diag([k_{p,1}\ \dots\ k_{p,m}]) \in \mathbb{R}^{m\times m}$, where $r_{p,i},\ k_i,\ k_{p,i} > 0$ for $i \in \{1,\dots,m\}$. A very similar control law has been obtained in (d' Andréa-Novel and Coron, 2000) using a baskstepping control design. From an intuitive point of view, the first two terms corresponds to a PD controller, the last term corresponds to a *strong dissipation* feedback, while the third term modifies the gain of the restoring force, relating it to the dissipation matrix R_p and the *strong dissipation* matrix K_p. For the same reasons explained in the the previous Section 5.3, we can consider the control law (5.63) as an *output feedback*. The closed-loop system obtained by applying (5.63) to (5.2) is depicted in Figure 5.6 and writes

$$\begin{cases} \dot{z} = P_1\frac{\partial}{\partial\xi}(\mathcal{H}z) + P_0(\mathcal{H}z) \\ \dot{x}_f = (J-R)Qx_f - g_1R_pM^{-1}K_p\mathcal{C}_1(\mathcal{H}z) - g_1K_p\frac{d}{dt}(\mathcal{C}_1(\mathcal{H}z)), \end{cases} \tag{5.64}$$

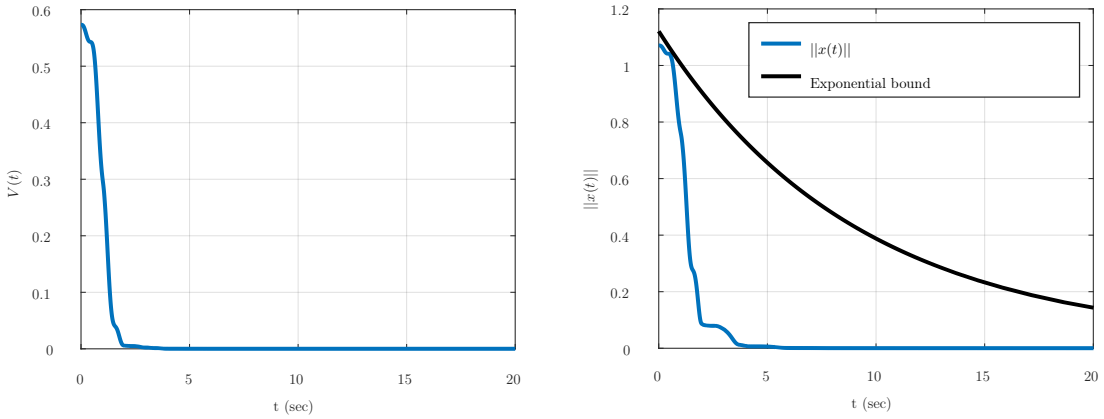

(a) Lyapunov functional evolution along time. (b) State's norm bounded by an exponential.

Figure 5.5: Lyapunov functional and state's norm.

where the finite dimensional state is $x_f = [\begin{smallmatrix} p \\ q \end{smallmatrix}]$, and the matrices are defined as

$$J = \begin{bmatrix} 0 & -I \\ I & 0 \end{bmatrix} \quad R = \begin{bmatrix} R_p & 0 \\ 0 & 0 \end{bmatrix} \quad Q = \begin{bmatrix} M^{-1} & 0 \\ 0 & K \end{bmatrix} \quad g_1 = \begin{bmatrix} I \\ 0 \end{bmatrix}. \tag{5.65}$$

To analyse the obtained closed-loop system we perform the change of variables $\eta = p + K_p \mathcal{C}_1 z$, such to rewrite the system as

$$\begin{cases} \dot{z} = P_1 \frac{\partial}{\partial \xi}(\mathcal{H}z) + P_0(\mathcal{H}z) \\ \dot{v} = (J - R)Qv + g_2 M^{-1} K_p \mathcal{C}_1(\mathcal{H}z), \end{cases} \tag{5.66}$$

where, $g_2 = [\begin{smallmatrix} 0 \\ I \end{smallmatrix}]$ and $v = [\begin{smallmatrix} \eta \\ q \end{smallmatrix}] \in \mathbb{R}^{2m}$. This system can be written as a linear operator equation of the form

$$\dot{x} = Ax = \begin{bmatrix} P_1 \frac{\partial}{\partial \xi}(\mathcal{H}z) + P_0(\mathcal{H}z) \\ -g_2 M^{-1} K_p \mathcal{C}_1(\mathcal{H}z) + (J - R)Qv \end{bmatrix} \tag{5.67}$$

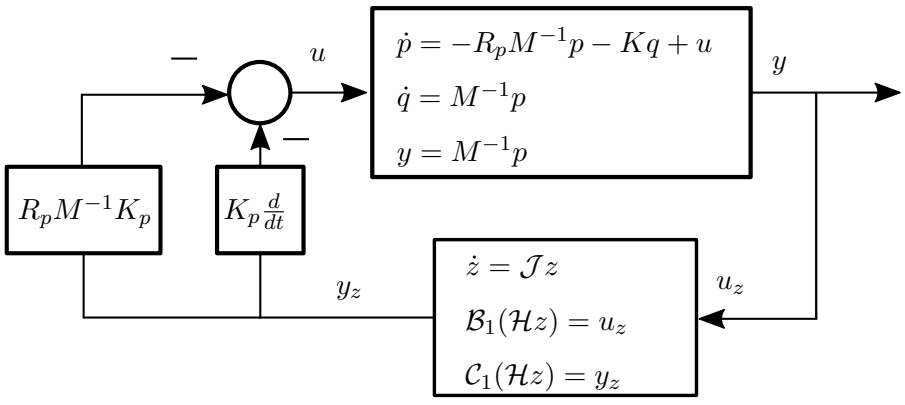

Figure 5.6: m-PH system in closed-loop with a *strong dissipation* feedback plus position control law.

with domain defined as

$$\begin{aligned}\mathbf{D}(A) = \big\{ x \in L_2([a,b],\mathbb{R}^n) \times \mathbb{R}^{2m} \mid \mathcal{H}z \in H^1([a,b],\mathbb{R}^n), \\ \mathcal{B}_1(\mathcal{H}z) = M^{-1}(\eta - K_p\mathcal{C}_1 z), \mathcal{B}_2(\mathcal{H}z) = 0\big\}\end{aligned} \tag{5.68}$$

and state defined as $x = \begin{bmatrix} z \\ v \end{bmatrix}$. The closed-loop operator is defined as the non-power preserving interconnection between an infinite and a finite dimensional linear pH systems. Since the interconnection is not power preserving, it is not possible to show the contraction C_0-semigroup generation in $L_2([a,b],\mathbb{R}^n)\times\mathbb{R}^{2m}$ equipped with the energy norm, as in classical interconnected m-PH systems (Villegas, 2007). Hence, in the next theorem we show that the closed-loop operator generates a contraction C_0-semigroup in $L_2([a,b],\mathbb{R}^n) \times \mathbb{R}^{2m}$ equipped with a special (energy-like) weighted norm.

Theorem 5.4.1. *Under Assumption 5.2.1, there exists a weighted $L_2([a,b],\mathbb{R}^n) \times \mathbb{R}^{2m}$ space such that the closed-loop operator* (5.67) *with domain defined by* (5.68) *generates a contraction C_0-semigroup on this space, provided that $r_i^2 \geq m_i k_i$ for all $i \in \{1,\dots,m\}$. Moreover the operator A has a compact resolvent.* ◊

Proof. Using Theorem 1.3.1 in (Mattioni, 2021), we only have to show that there exists a space on which the operator A is dissipative. We define a new space $\Gamma = L_2([a,b],\mathbb{R}^n) \times \mathbb{R}^{2m}$ with inner product

$$\langle x_1, x_2\rangle_\Gamma = \langle z_1, z_2\rangle_Z + v_1^T M_v v_2 \tag{5.69}$$

where

$$M_v = \begin{bmatrix} K^{-1}M^{-1}R_pK_p^{-1} & K_p^{-1} \\ K_p^{-1} & 2KMR_p^{-1}K_p^{-1} \end{bmatrix} = \begin{bmatrix} A_{11} & A_{12} \\ A_{21} & A_{22} \end{bmatrix}. \tag{5.70}$$

To check the positive definitiveness of M_v we use the Schur complements. In fact, since all the matrices in (5.70) are strictly positive definite, A_{22} and $A_{11} - A_{12}A_{22}^{-1}A_{21}$ are strictly positive definite matrices, from which it follows the positive definitiveness of M_v. We now check the dissipativity of the operator A in the new space Γ, considering Lemma 1.2.1 in (Mattioni, 2021) and taking into account that $\mathcal{C}_1 z = y_z$,

$$\begin{aligned}\langle Ax, x\rangle_\Gamma = \; & \langle \mathcal{J}z, z\rangle_Z + ((J-R)Qv - g_2M^{-1}K_py_z)^T M_v v \\ = \; & u_z^T y_z - \eta^T K^{-1}M^{-2}R_p^2K_p^{-1}\eta - 2\eta^T M^{-1}R_pK_p^{-1}q + \eta^T K_p^{-1}M^{-1}\eta \\ & -q^T K_pKq + 2q^T KR_p^{-1}K_p^{-1}\eta - \eta^T M^{-1}y_z - 2q^T KR_p^{-1}y_z \\ = \; & -y_zK_pM^{-1}y_z - \eta^T K^{-1}M^{-2}R_p^2K_p^{-1}\eta - 2\eta^T M^{-1}R_pK_p^{-1}q \\ & +\eta^T K_p^{-1}M^{-1}\eta - q^T K_pKq + 2q^T KR_p^{-1}K_p^{-1}\eta - 2q^T KR_p^{-1}y_z.\end{aligned} \tag{5.71}$$

Since all the matrices are diagonal, the previous inequality can be rewritten as

$$\begin{aligned}\langle Ax, x\rangle_\Gamma = \; & -y_zK_pM^{-1}y_z - \eta^T(K^{-1}M^{-2}R_p^2K_p^{-1} - K_p^{-1}M^{-1})\eta \\ & 2\eta^T(M^{-1}R_pK_p^{-1} - KR_p^{-1}K_p^{-1})q - 2q^T KR_p^{-1}y_z - q^T K_p^{-1}Kq \\ = \; & -y_zK_pM^{-1}y_z - \eta^T K^{-1}M^{-2}R_p^2K_p^{-1}(I - KMR_p^{-2})\eta \\ & 2\eta^T K_p^{-1}R_pM^{-1}(I - KMR_p^{-2})q - 2q^T KR_p^{-1}y_z - q^T K_p^{-1}Kq.\end{aligned} \tag{5.72}$$

We define $\Lambda = KMR_p^{-2}$ and we rewrite the former equality as

$$\begin{aligned}\langle Ax, x\rangle_\Gamma = & -y_z K_p M^{-1} y_z - 2q^T K R_p^{-1} y_z - q^T (K_p^{-1} K - M^{-1} K_p^{-1}(I-\Lambda)\Lambda R_p^2))q \\ & -(\Lambda^{-\frac{1}{2}}\eta + R_p\Lambda^{\frac{1}{2}}q)^T M^{-1} K_p^{-1}(I-\Lambda)(\Lambda^{-\frac{1}{2}}\eta + R_p\Lambda^{\frac{1}{2}}q) \\ = & -y_z K_p M^{-1} y_z - 2q^T K R_p^{-1} y_z - q^T K^2 M R_p^{-2} K_p^{-1} q \\ & -(\Lambda^{-\frac{1}{2}}\eta + R_p\Lambda^{\frac{1}{2}}q)^T M^{-1} K_p^{-1}(I-\Lambda)(\Lambda^{-\frac{1}{2}}\eta + R_p\Lambda^{\frac{1}{2}}q) \\ = & -(K_p^{\frac{1}{2}} y_z + KMR_p^{-1}K_p^{-\frac{1}{2}}q)^T M^{-1}(K_p^{\frac{1}{2}} y_z + KMR_p^{-1}K_p^{-\frac{1}{2}}q) \\ & -(\Lambda^{-\frac{1}{2}}\eta + R_p\Lambda^{\frac{1}{2}}q)^T M^{-1} K_p^{-1}(I-\Lambda)(\Lambda^{-\frac{1}{2}}\eta + R_p\Lambda^{\frac{1}{2}}q).\end{aligned} \tag{5.73}$$

The assumption that $r_i^2 > m_i k_i$ for all $i \in \{1, \dots, m\}$ implies that the matrix $(I - \Lambda)$ is strictly positive definite. Therefore we obtain that $\langle Ax, x\rangle_\Gamma \leq 0$, and by means of Theorem 1.3.1 in (Mattioni, 2021), we can conclude that the operator A generates a contraction C_0-semigroup in the space Γ and has a compact resolvent. □

It is well known that if an operator is the infinitesimal generator of a C_0-semigroup in a space equipped with a certain norm, then it generates a C_0-semigroup in all the spaces equipped with equivalent norms. In the next corollary we show that the norm defined through (5.69) is equivalent to the standard norm in $L_2([a,b],\mathbb{R}^n) \times \mathbb{R}^{2m}$. Hence, this directly implies that the closed-loop operator (5.67)-(5.68) generates a C_0-semigroup in $L_2([a,b],\mathbb{R}^n) \times \mathbb{R}^{2m}$ equipped with the standard norm.

Corollary 5.4.1. *Under Assumption 5.2.1, the closed-loop operator* (5.67)-(5.68) *generates a C_0-semigroup in $L_2([0,L],\mathbb{R}^n) \times \mathbb{R}^{2m}$ equipped with the standard norm*

$$||x|| = \sqrt{\langle z, z\rangle_{L_2} + v^T v}. \tag{5.74}$$

◊

Proof. It is sufficient to show that the norm associated to the inner product (5.69)

$$||x||_\Gamma = \sqrt{\langle z, \mathcal{H}z\rangle_{L_2} + v^T M_v v}, \tag{5.75}$$

is equivalent to the standard norm, *i.e.* that there exist $C > c \in \mathbb{R}^+$ such that

$$c||x|| \leq ||x||_\Gamma \leq C||x||. \tag{5.76}$$

The first inequality of (5.76) can be rewritten as

$$c\sqrt{\langle z, z\rangle_{L_2} + v^T v} \leq \sqrt{\langle z, \mathcal{H}z\rangle_{L_2} + v^T M_v v}, \tag{5.77}$$

that is equivalent to

$$c^2\left(\langle z, z\rangle_{L_2} + v^T v\right) \leq \langle z, \mathcal{H}z\rangle_{L_2} + v^T M_v v. \tag{5.78}$$

The last inequality is fulfilled if

$$\langle z, (c^2 I - \mathcal{H})z\rangle \leq 0, \quad v^T(c^2 I - M_v)v \leq 0. \tag{5.79}$$

Since $\mathcal{H}$ and M_v are strictly positive definite, it exists a constant $c \in \mathbb{R}$ such that both inequalities hold. The second inequality in (5.76) can be rewritten as

$$\sqrt{\langle z, \mathcal{H}z\rangle_{L_2} + v^T M_v v} \leq C\sqrt{\langle z, z\rangle_{L_2} + v^T v}, \tag{5.80}$$

and it holds if

$$\langle z, (\mathcal{H} - C^2 I)z\rangle \leq 0, \quad v^T(M_v - C^2 I)v \leq 0. \tag{5.81}$$

Since the entries of both $\mathcal{H}$ and M_v are always finite, it exists a $C \in \mathbb{R}$ such that both these inequalities are fulfilled. We therefore conclude that (5.75) is equivalent to the standard norm in $L_2([0,L],\mathbb{R}^n) \times \mathbb{R}^{2m}$. As a consequence, since the closed-loop operator (5.67)-(5.68) generates a contraction C_0-semigroup in $L_2([0,L],\mathbb{R}^n) \times \mathbb{R}^{2m}$ equipped with the norm (5.75), it also generates a C_0-semigroup in the same space equipped with the standard norm. □

Since by Theorem 5.4.1 the operator A generates a contraction C_0-semigroup $T(t)$ in $L_2([0,L],\mathbb{R}^n)\times \mathbb{R}^{2m}$ equipped with the norm (5.75), we have that

$$||T(t)||_\Gamma \leq 1. \tag{5.82}$$

Using (5.76), it is possible to obtain the bound of the C_0-semigroup generated by the operator A in $L_2([0,L],\mathbb{R}^n) \times \mathbb{R}^{2m}$ equipped with the standard norm (5.74)

$$||T(t)|| \leq \frac{C}{c}. \tag{5.83}$$

The asymptotic stability of the system described by equation (5.67) - (5.68) is equivalent to show the asymptotic stability of system (5.66). To show asymptotic stability we consider the state space $X = L_2([a,b],\mathbb{R}^n) \times \mathbb{R}^{2m}$ with inner product $\langle x_1, x_2\rangle_X = \langle z_1, z_2\rangle_{L_2} + v_1^T v_2$ and associated norm (5.74). We now prove that with the proper choice of control parameters the closed-loop system is asymptotically stable.

Theorem 5.4.2. *Consider the closed-loop system* (5.67)-(5.68). *Assume that the distributed parameter part of the system with homogeneous boundary conditions is approximately observable with respect to the output y_z and $z_{eq} = 0$ is its only equilibrium point. Under Assumption 5.2.1, if the control gains $k_{p,i}, r_i, k_i$ with $i = \{1,..,m\}$ are chosen such that*

$$r_i^2 > 2m_i k_i, \quad k_{p,i} > 0 \tag{5.84}$$

then the origin $x_{eq} = 0$ is an asymptotically stable equilibrium. ◊

Proof. We define the candidate Lyapunov functional

$$V(x) = \frac{1}{2}\langle x, x\rangle_\Gamma \tag{5.85}$$

with inner-product defined in (5.69). The time derivative of the Lyapunov functional can be computed as

$$\begin{aligned} \dot{V}_+(x) = &\ \langle x, Ax\rangle_\Gamma \\ = &\ \langle z, \mathcal{J}z\rangle_Z + v^T M_v((J-R)Qv - g_2 M^{-1}K_p y_z) \end{aligned} \tag{5.86}$$

that, because of Lemma 1.2.1 in (Mattioni, 2021) and equations (5.71)-(5.73), can be rewritten as

$$\begin{aligned} \dot{V}_+(x) = &\ \langle \mathcal{J}z, z\rangle_Z + ((J-R)Qv - g_2 M^{-1}K_p y_z)^T M_v v \\ = &\ -(K_p^{\frac{1}{2}} y_z + KMR_p^{-1}K_p^{-\frac{1}{2}} q)^T M^{-1}(K_p^{\frac{1}{2}} y_z + KMR_p^{-1}K_p^{-\frac{1}{2}} q) \\ &-(\Lambda^{-\frac{1}{2}}\eta + R_p\Lambda^{\frac{1}{2}} q)^T M^{-1}K_p^{-1}(I-\Lambda)(\Lambda^{-\frac{1}{2}}\eta + R_p\Lambda^{\frac{1}{2}} q) \end{aligned} \tag{5.87}$$

where $\Lambda = KMR_p^{-2}$. To use the LaSalle's invariance principle, we show that the largest invariant subset $\mathbf{S}$ of $\mathbf{S}_0 = \{x_0 \in X \mid \dot{V}(x) = 0\}$ consists of only the origin of the state space. To do so, we characterize the set for which the Lyapunov functional's time derivative is equal to zero:

$$\begin{aligned} \mathbf{S}_0 = &\ \left\{x_0 \in X \mid \eta = -KMR_p^{-1}q, y_z = -KMR_p^{-1}K_p^{-1}q\right\} \\ = &\ \left\{x_0 \in X \mid \eta = -KMR_p^{-1}q, y_z = K_p^{-1}\eta\right\}. \end{aligned} \tag{5.88}$$

Then, substitute the former relations in the closed-loop dynamic (5.67)-(5.68) to obtain

$$\begin{cases} \dot{z} = \mathcal{J}z \\ \dot{\eta} = 0 \\ \dot{q} = 0 \end{cases} \tag{5.89}$$

with domain

$$\mathbf{D}(\mathcal{J}) = \left\{ x \in X | z \in H^1([a,b], \mathbb{R}^n), \mathcal{B}(\mathcal{H}z) = 0 \right\}, \tag{5.90}$$

$\mathcal{C}_2 z(\mathcal{H}z)(\xi,t) = \tilde{y}(t)$, and the other part of the output

$$\mathcal{C}_1 z(\mathcal{H}z)(\xi,t) = y_z(t) = -KMR_p^{-1}K_p^{-1}q(t). \tag{5.91}$$

System (5.89) implies that η and q must be constant along time, i.e. $\eta(t) = \eta^*$ $q(t) = q^*$. Hence, $x_0 \in E$ should verify

$$\begin{aligned} &\dot{z}(t) = \mathcal{J}z(t) \\ &\mathcal{B}(\mathcal{H}z) = 0 \quad \mathcal{C}_1(\mathcal{H}z) = -KMR_p^{-1}K_p^{-1}q^*. \end{aligned} \tag{5.92}$$

Using the approximate observability of the infinite dimensional part of system together with Lemma 5.2.1, we know that the only solution of (5.92) is $z = 0$, which in turn implies $y_z = 0$ and consequently $q^* = \eta^* = 0$ using the relations in (5.88). Thus the largest invariant set $\mathbf{S} \subset \mathbf{S}_0$ corresponds to $\mathbf{S} = \{0\}$. Since by Theorem 1.3.1 in (Mattioni, 2021) we know that the resolvent of A is compact , we apply Corollary 3.1.1 in (Mattioni, 2021) to obtain that the trajectories set is pre-compact in the space X. Then we can conclude by the LaSalle's invariance principle that the solution converges asymptotically to the origin. □

Example 5.4.1 (Rotating translating flexible beam with strong dissipation plus position control)**.** *In this example, we want to stabilize the translating rotating flexible beam model in the zero state $z = 0$, $p = q = 0$, as depicted in Figure 5.7.The model is written as following form:*

$$\begin{aligned} &\dot{z} = P_1 \tfrac{\partial}{\partial \xi}(\mathcal{H}z) + P_0(\mathcal{H}z) = \mathcal{J}z \\ &\dot{p} = -\mathcal{C}_1(\mathcal{H}z) + u(t), \end{aligned} \tag{5.93}$$

where $u(t) = [f(t)\ \tau(t)]^T$ and P_0, P_1 are defined as:

$$P_1 = \begin{bmatrix} 0 & 0 & 1 & 0 \\ 0 & 0 & 0 & 1 \\ 1 & 0 & 0 & 0 \\ 0 & 1 & 0 & 0 \end{bmatrix} \qquad P_0 = \begin{bmatrix} 0 & 0 & 0 & 0 \\ 0 & 0 & 1 & 0 \\ 0 & -1 & 0 & 0 \\ 0 & 0 & 0 & 0 \end{bmatrix}. \tag{5.94}$$

The energy variables are defined by

$$\begin{gathered} z_1 = \rho(\dot{w} + \xi\dot{\theta} + \dot{s}) \quad z_2 = I_\rho(\dot{\phi} + \dot{\theta}) \quad z_3 = \tfrac{\partial w}{\partial \xi} - \phi \quad z_4 = \tfrac{\partial \phi}{\partial \xi} \\ p_1 = m\dot{s} \quad p_2 = J\dot{\theta} \end{gathered} \tag{5.95}$$

and $z = [z_1\ z_2\ z_3\ z_4]^T$ is the flexible beam's state, and $p = [p_1\ p_2]^T$ is the state related to the hub's motion. The domain of the $\mathcal{J}$ operator is defined as

$$\mathbf{D}(\mathcal{J}) = \{z \in L_2([0,L], \mathbb{R}^4) \mid z \in H^1([0,L], \mathbb{R}^2) \mathcal{B}_1(\mathcal{H}z) = Qp,\ \mathcal{B}_2(\mathcal{H}z) = 0\} \tag{5.96}$$

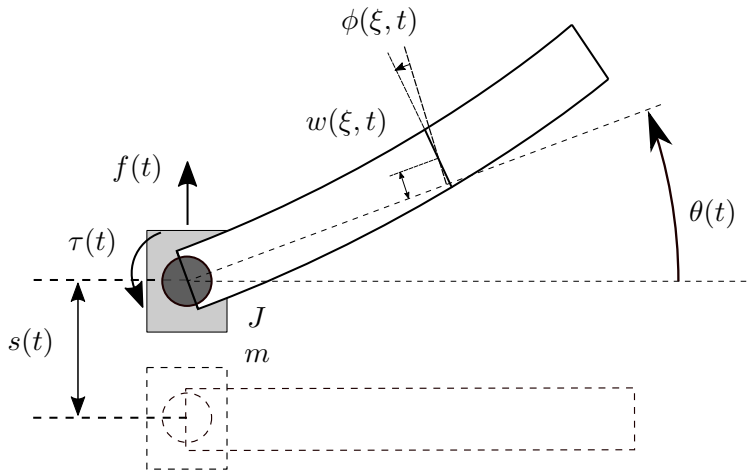

Figure 5.7: Rotating translating beam with desired equilibrium point.

Table 5.2: Simulation parameters; PD controller example

Name	Variable	Value
Beam's Length	L	$1\ m$
Beam's Width	L_w	$0.1\ m$
Beam's Thickness	L_t	$0.02\ m$
Density	ρ	$1.9\ \frac{kg}{m}$
Young's modulus	E	$8 \times 10^8\ \frac{N}{m^2}$
Bulk's modulus	K	$1.7 \times 10^9\ \frac{N}{m^2}$
Hub's inertia	J	$1\ kg \cdot m^2$

where $Q = diag[m^{-1}, J^{-1}]$ *and* $\mathcal{H}(\xi) = diag[\rho^{-1}(\xi), I_\rho^{-1}(\xi), K(\xi), EI(\xi)]$. *The energy of the overall mechanism can be expressed as:*

$$E = \frac{1}{2}\langle z, \mathcal{H}z\rangle_{L_2} + \frac{1}{2}p^T Q p. \tag{5.97}$$

The input and output operators are defined as

$$\begin{aligned} \mathcal{B}_1(\mathcal{H}z) &= \begin{bmatrix} \frac{1}{\rho(0)} z_1(0,t) \\ \frac{1}{I_\rho(0)} z_2(0,t)) \end{bmatrix} \quad \mathcal{C}_1(\mathcal{H}z) = -\begin{bmatrix} K(0) z_3(0,t) \\ EI(0) z_4(0,t) \end{bmatrix} \\ \mathcal{B}_2(\mathcal{H}z) &= \begin{bmatrix} K(L) z_3(L,t) \\ EI(L) z_4(L,t) \end{bmatrix} \quad \mathcal{C}_2(\mathcal{H}z) = \begin{bmatrix} \frac{1}{\rho(L)} z_1(L,t) \\ \frac{1}{I_\rho(L)} z_2(L,t) \end{bmatrix} \end{aligned} . \tag{5.98}$$

under the operator form of (5.67)-(5.68).
The considered physical parameters are listed in Table 5.2, together with the hub's mass $m = 1\ kg$. *We begin by computing*

$$\begin{aligned} ||\mathcal{H}z(0,t)||^2 = &\ ||\tfrac{1}{\rho(0)} z_1(0,t)||^2 + ||\tfrac{1}{I_\rho(0)} z_2(0,t)||^2 + ||K(0) z_3(0,t)||^2 \\ &+ ||EI(0) z_4(0,t)||^2 \\ = &\ ||u_z||^2 + ||y_z||^2 \end{aligned} \tag{5.99}$$

that because of Theorem 5.2.1, implies that the distributed parameter part of the system is approximately observable. It is possible to show that $z_{eq} = 0$ is the only equilibrium position of the distributed parameter part of the system. We select the control parameters in a way that the inequalities in (5.84) are respected: $r_{p,1} = r_{p,2} = 50$, $k_1 = k_2 = 500$, $k_{p,1} = k_{p,2} = 2$. Then, to perform the numerical simulation, we apply the discretization procedure introduced

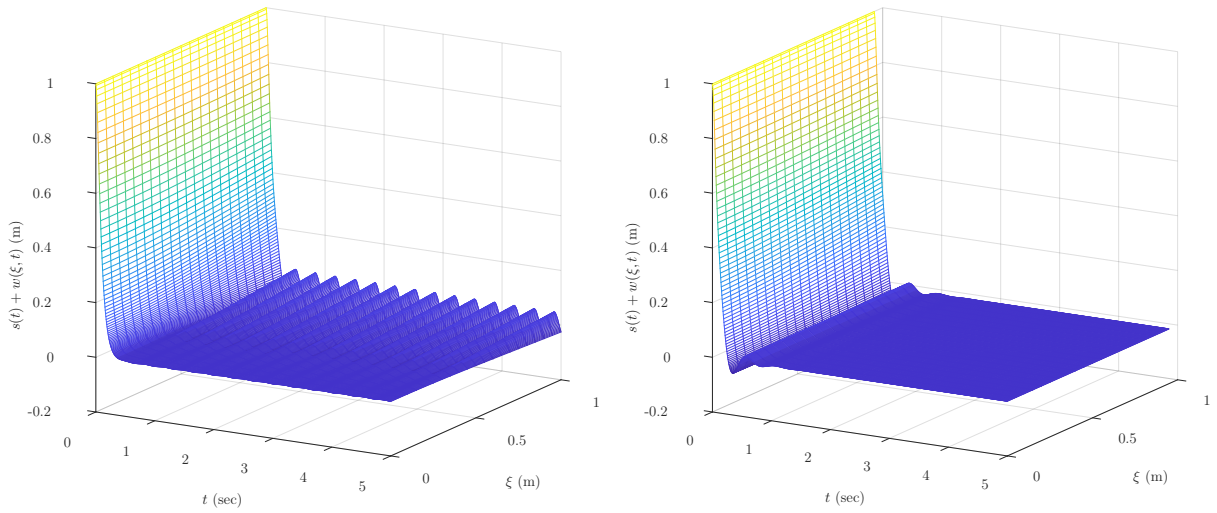

(a) PD control action.

(b) PD plus strong dissipation control action.

Figure 5.8: Beam's Deformation plus displacement along time.

in Section 2.2 of Chapter 2 in (Mattioni, 2021). The initial conditions are set to be $z_0 = 0$, $p = 0$, $q_0 = [\frac{1}{0}]$. Figure 5.8 compares the displacement plus deformation behaviour along time

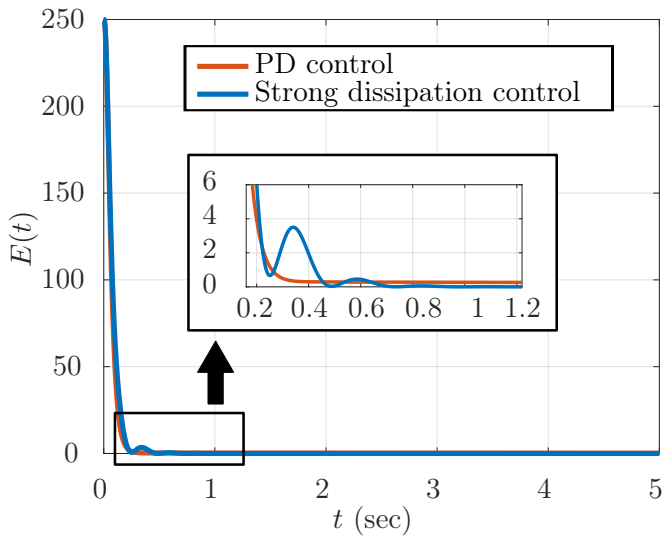

Figure 5.9: closed-loop energy evolution in time.

in case the system is controlled with a PD or with a PD plus strong dissipation control action, respectively. We can appreciate that in case of a strong dissipation control law, the vibration are suppressed much faster than with a PD control law. Figure 5.9 shows the closed-loop energy evolution in case PD control and PD plus strong dissipation control. We can observe that the closed-loop energy in case of application of PD plus strong dissipation control is not decreasing along the system's trajectories. This is the reason why it can not be used as Lyapunov functional

to show the asymptotic stability of the closed-loop system. We remark that in this example we stabilize the system to the origin, but if we want to stabilize it around a different configuration s^*, θ^**, it suffices to define a translated position variable* $q = \left[\begin{smallmatrix} s-s^* \\ \theta-\theta^* \end{smallmatrix}\right]$. ◊

5.5. Summary

In this chapter, we develop a control strategy that stabilizes a class of mixed ODE-PDE systems with the actuation on the ODE part. The closed-loop operator has been obtained after an appropriate change of coordinates, and it has been shown to generate a contraction C_0-semigroup in an appropriate space equipped with a weighted inner product. Further, a Lyapunov based stability proof has been used to show the exponentially/asymptotic stability of the closed-loop system. This analysis takes advantage of the pH structure of the system to be controlled. Finally, the control law has been applied to a clamped vibrating string with a tip mass in the free side and control action on the mass' dynamic. Simulation results have been given such to validate the theoretical development.

Chapter 6

Conclusion of Part I

This part presents my contributions to the control design for distributed PH systems, focusing on three specific cases.
Firstly, in Chapter 3, the control design for distributed PH systems with the actuation at the boundary is presented. In this research, the observer based controller has been investigated using the early lumped approach. The reduced order (finite dimensional) controller is derived through the discretization of the distributed PH systems. Two strategies have been proposed such that the obtained reduced order controllers are SPR. With the SPR property of these controllers, we can guarantee the stability of the closed-loop system when implementing them on the distributed PH systems.
Secondly, in Chapter 4, I introduce the control design for distributed PH systems with the actuation within the spatial domain using the early lumped approach. In this work, the Control by Interconnection method, along with the use of the structural invariants, is employed to design the controller. This method allows us to modify the potential energy of the system in the closed loop. Through this proposed method, reduced order controllers can be derived while maintaining the PH structure. With the power preserving interconnection between the reduced order control and the distributed PH plant, the PH structure is preserved within the closed loop system which ensures the asymptotic stability of the closed loop system and avoids the spillover effect.
In the third case, I address the control design for the m-PDE-ODE PH system with the actuation in the ODE part, as presented in Chapter 5. In this research, the derivative plus $strong\ dissipative$ feedback control is derived to exponentially stabilize the m-PDE-ODE systems. Meanwhile, A PD control plus $strong\ dissipative$ feedback is explored to position the system in the desired equilibrium and asymptotically stabilize the closed-loop system. Throughout these investigations, the well-posedness and stability results for each control law are provided, along with practical applications demonstrated through examples involving a flexible mechanism and associated numerical simulations.

Publication list

1. Jesus Toledo, **Yongxin Wu**, Hector Ramirez, Yann Le Gorrec, *Observer-based Boundary Control of Distributed Port Hamiltonian Systems*, Automatica, Volume 120, October 2020. https://doi.org/10.1016/j.automatica.2020.109130.

2. Jesus Toledo, **Yongxin Wu**, Hector Ramirez, Yann Le Gorrec, *Linear Matrix Inequality Design of Observer-Based Controllers for port Hamiltonian systems*, IEEE Transactions on Automatic Control, DOI: 10.1109/TAC.2022.3227927.

3. Andrea Mattioni, **Yongxin Wu**, Yann Le Gorrec, Hans Zwart, *Stabilization of a Class of Mixed ODE-PDE port-Hamiltonian Systems with Strong Dissipation Feedback*, Automatica, Volume 142, August 2022, 110284 DOI: 10.1016/j.automatica.2022.110284.

4. Ning Liu, **Yongxin Wu**, Yann Le Gorrec, Laurent Lefèvre, Hector Ramirez. *Reduced order in domain control of distributed parameter port-Hamiltonian systems via energy shaping*. Automatica, Accepted.

Part II

Modeling and control of smart materiel based soft actuators

Chapter 7

Introduction of Part II

Traditional robots have been made using hard materials such as steel or aluminum. These programmable robots can be used for accomplishing repetitive and precise tasks which are difficult to be handled by humans. However, because of their rigidity and limited adaptability, they are usually used for simple tasks that does not require care with respect to the environment. Due to the raise of health-cares, manipulation of delicate objects (food, soft matter, bio-material etc.), and human interactions, it is necessary to develop robots that are safe and able to adapt themselves to unknown environments.

Due to the recent technological progresses in material sciences and also inspired by nature, soft robots based on active materials have raised a particular attention over the last decades. Unlike the traditional rigid robots, soft robots can provide high compliance and adaptability similar to natural creatures and can emerge the gap between human interaction and robotic environments (Tolley et al., 2014; Seok et al., 2013; Majidi, 2014; Rus and Tolley, 2015)

Soft actuators are an essential component in a soft robot, which provide the system with a deformable body and allows it to interact with the environment to achieve a desired actuation pattern (El-Atab et al., 2020; Pan et al., 2022). Different actuation mechanisms can classify soft actuators into the following categories: first, electro-active polymers such as ionic polymer-metal composites (IPMCs) (Shahinpoor, 2016), dielectric elastomer actuators (DEAs) (Gu et al., 2017; Pelrine et al., 2000); second, shape-memory materials (SMAs) (Committee, 1990) and shape memory polymers (SMPs) (Liu et al., 2007); third, the pressure-driven actuators such as pneumatic or hydraulic (Pagoli et al., 2021) and finally, the hybrid actuation, for instance, the Hydraulically Amplified Self-healing Electrostatic (HASEL) actuators (Acome et al., 2018) which combine the electro-activation and hydraulic driven. The advantages and limitations of different actuators are listed in Table 7.1.

In this Part, we focus on the modeling and control application of two specific soft actuators. Firstly, we investigate on the IPMCs actuators for the flexible structure control purpose. The advantages as large deformation and bio-compatible of IPMC actuator make it very attractive in biomedical and micro- or macro-mechatronic systems (Shahinpoor and Kim, 2004). In (Chikhaoui et al., 2014) at FEMTO-ST institute, the IPMC actuators are used to drive the micro-endoscope with 4.5 mm diameter. Motivated by this application, we investigate on the modeling of IPMC actuators and the control design of the flexible structure using such kind of actuators. Moreover, we study a new class of hybrid soft actuator, HASEL actuators (Acome et al., 2018). HASEL actuators use an electrohydraulic mechanism to enable all-soft-matter hydraulic systems. They combine the versatility of soft fluidic actuators with the muscle-like performance and self-sensing capabilities of dielectric elastomer (DE) actuators (Rothemund et al., 2020a). This class of actuators takes the advantage of both fluidic actuators (generation of large force) and DE actuators (fast responses, large stroke). Meanwhile it overcomes the limitations of both types of actuators, for instance, it does not need an external pumps system and have self healing ability to avoid the material damage caused by high voltage.

Actuator type	Power supply	Avantages	Challenges
Ionic polymer-metal composites (IPMCs)	Electric	Bending in both directions Variable stiffness Large bending Low actuation voltage Biocompatible Self-sensing	Slow response Low produced force
Dielectric elastomer actuators (DEAs)	Electric	Large actuation strokes Fast response time Self-sensing Small currents	High applied voltage Easy to damage Difficult fabrication procedure for complex geometry
Shape memory alloys (SMAs)	Electric/thermal	High active stress High elastic modulus Self-sensing	Slow response and speed Hysteresis High power consumption
Shape memory polymers (SMPs)	Electric/thermal	Variable stiffness capability Biodegradable Low density Highly elastic deformable	Low produced force Rigid components to recover the original shape
Pressure driven (Fluidic)	Pneumatic hydraulic	High force generation Large stroke bending	External pumps bulky and heavy
Hybrid driven (HASEL)	Electric	Large deformation Fast response time Self-healing Low power consumption Low cost Self-sensing	High applied voltage

Table 7.1: Different type of soft actuators

While the aforementioned soft actuators are extensively employed in the development of soft robotic applications, their inherent multi-physical properties and non-linear characteristics, including large deformations, hysteresis, drift behavior, state depended parameter variation, and more, have made modeling and controlling these actuators a persistent and significant research challenge. To overcome these constraints, my research investigates on the dynamic modeling and control design of several soft actuators using port Hamiltonian (PH) approach. As mentioned in the previous part of this manuscript, PH modeling is based on the characterization of energy exchanges between the different components of the system (Maschke and van der Schaft, 1992). This approach is particularly adapted for the modular modeling of multi-physical systems (Maschke et al., 1992; Duindam et al., 2009). On the other hand, the PH approach is well suited passivity based control design with clear physical interpretation for nonlinear and distributed parameter systems (Ortega et al., 2002; Ortega and Garcia-Canseco, 2004; Ortega et al., 2008).
In this part, a detailed modeling of IPMCs is presented in Chapter 8, which takes account different physical phenomena of the actuator. Furthermore, in Chapter 9, we employ IPMCs to control the motion of a flexible structure. With reasonable assumptions, we simplify the IPMCs model to interconnected with the flexible structure and propose a passivity-based controller for the system. Chapter 10 delves into the investigation of the HASEL actuator. We provide a dynamic model that encompasses the primary behaviors of the HASEL actuator, and we propose a position control design based on the IDA-PBC control strategy. A few concluding remarks of this part will be provided in Chapter 11.

Chapter 8

Modeling of Ionic polymer–metal composites

8.1. Introduction

In this Chapter, we investigate at the modeling of Ionic polymer metal composites (IPMCs) actuators. IPMCs are widely used as actuators or/and sensors in biomedical and industrial domains (Shahinpoor and Kim, 2004; Wang et al., 2017), due to their advantages of low-cost voltage, large deformation, as well as broad bandwidth in comparison with piezoelectric materials.

IPMCs are composed of an electroactive polymer (poly-electrolyte gel) whose surfaces are coated with a conductor such as gold. The working principle is the following: cations and solvent molecules in the gel transport to the cathode side of the electrode when an electrical potential difference is imposed across the two boundaries of the double layer. As a consequence, the cathode side swells and the anode side shrinks, entailing a bending effect to the anode side (Park et al., 2010).

Based on the aforementioned physical structure and working principle, various models of such actuators have been proposed in the literature, mainly sorted into three subclasses: black box models, white box models and grey box models.

As initially proposed in (Xiao and Bhattacharya, 2001; Newbury and Leo, 2002), the black box model, which is purely empirical and which focuses only on the relation between specific inputs and outputs (e.g. voltage and tip displacement of the IPMC), is simple to establish(Khawwaf et al., 2019). However, as it is based on strong assumptions, it cannot be applied to all types of IPMC, nor to different boundary or experimental conditions. In contrast to the previous one, the white box model is established via principles of physics and chemistry at the molecular level (Shahinpoor, 1995; Nemat-Nasser and Li, 2000; Branco and Dente, 2006), resulting in a set of partial differential equations (PDEs). The complexity of such model makes it difficult to handle from a numerical point of view and difficult to be validated experimentally.

Different from the two previous models, the grey box model has been investigated in (Kanno et al., 1995; Newbury and Leo, 2003; Chen and Tan, 2008). It is formulated according to physical principles in conjunction with simplified assumptions and parameter identifications. It is proven that this kind of model presents a higher accuracy and wider universality than the black box model. Meanwhile, it is more preferable than its white counterpart in terms of the numerical implementation and the experimental validation. According to the composition of IPMCs, the model is derived considering three subsystems: the interface between the gel and the electrode, the polymer and the mechanical structure. In (Chen and Tan, 2008) a control-oriented and physical-based model of an IPMC actuator using an infinite dimensional transfer function between the input voltage and the output endpoint displacement of the actuator is proposed. The mechanical dynamics is approximated by a second-order system, which is valid only at low frequencies. With the model reduction of the infinite

dimensional transfer function, an H_∞ controller is implemented. This work focuses on the modeling and control design of a single actuator in a given range of frequencies.

The proposed approach is different as it aims at providing a model of IMPC patches suitable for distributed control of flexible structures. The proposed model has then to cope with higher frequency modes and to be easy to interconnect with both elastic beams and thin shell models, the control design being derived using energy based control design methods in order to have a better physical interpretation for the controller. Recently, a new type of grey box model has been proposed in (Nishida et al., 2011b) within the framework of port Hamiltonian (PH) systems. This port based modeling expresses the dynamics of the system through energy exchanges between its subcomponents. As a result, it is particularly well suited for the modeling of complex, multiphysical and multiscale systems via power preserving interconnections. Yet, due to the considered assumptions, the model proposed in (Nishida et al., 2011b) presents some important limitations. In (Nishida et al., 2011b) a local homogeneity assumption is considered for the polymer deformation. The multiscale coupling of the gel with the mechanical structure is done through the bending moment, locally defined for the polymer gel, and the structure deformation, globally defined for the mechanical structure. Furthermore the polymer action is seen as modifying the internal properties of the mechanical structure. As a consequence singularities may appear when the mechanical deformation is homogeneous. In this case, due to the considered assumptions, the bending moment provided by the polymer gel is homogeneous and without any effect on the distributed mechanical structure. On the other hand, the coupling between the mechanical properties of the gel (considered as quasi-static) and the mechanical properties of the actuator structure in (Nishida et al., 2011b) is implicit, with conflicting causalities in the proposed Bond Graph. In this work we make the quasi-static behavior of the gel explicit and express the algebraic constraint arising from the coupling between the gel and the mechanical structure of the actuator with a Lagrange multiplier. We also consider the action of the polymer gel on the mechanical structure as an external distributed bending moment, avoiding singularities associated with homogeneous deformations. The discretization of the proposed IPMC model is structure preserving, such that our discretized model is again a PH system.

The Chapter is organized as follows. Section 8.2 establishes the energy based model of the IPMC as a modular composition of three subsystems and their multiscale coupling under the PH framework. The overall structure of the system and the associated energy balance are made explicit. In Section 8.3, the finite difference method on staggered grids is applied to discretize the IPMC model in a structure preserving way. Meanwhile, the Lagrange multipliers are eliminated by projection. Comparisons between simulated and experimental results are given in Section 8.4. We summarize this chapter in Section 8.5.

8.2. Modeling of the IPMC actuator

The IPMC patch under investigation is of length L, width b and thickness h. Its shape and structure are depicted in Fig. 8.1.

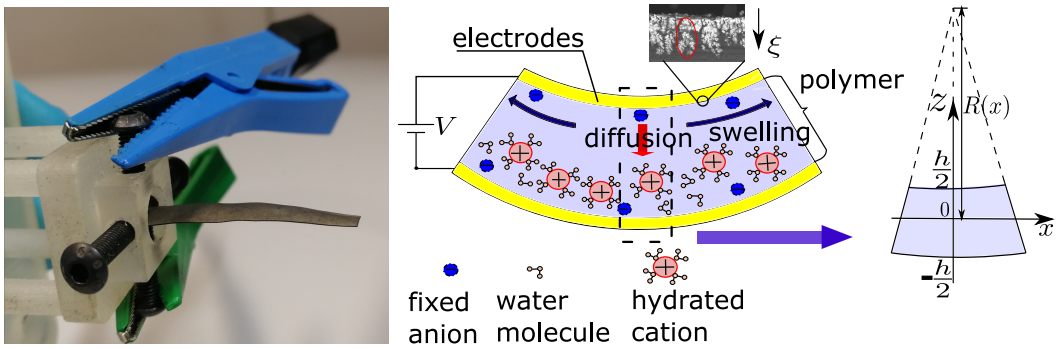

(a) IPMC patch. (b) IPMC structure(Shahinpoor, 2016).

Figure 8.1: Shape and structure of an IPMC actuator patch.

This IPMC model is composed of three subsystems: the electrical system stemming from the modeling of the electrode/polymer interface, the electro-stress diffusion system stemming from the modeling of the polymer, and the mechanical system stemming from the modeling of the overall mechanical structure deformation, which are at scales of nanometer, micrometer and centimeter (Nishida et al., 2011b), respectively. In this section, the different subsystems and the way they are coupled are discussed. The main differences with the model proposed in (Nishida et al., 2011b) lie in the electro-stress diffusion and mechanical models and the way they are interconnected (cf. subsections B, C, D).

8.2.1. Electrical system

Starting with the electrical part, we assume that the voltage V is uniformly distributed on the double layers. According to (Nishida et al., 2011b), each fractal-like structure on two electrodes is referenced as a virtual coordinate $\xi \in [0, L_\xi]$ as marked by a red circle in Fig. 8.1b, and is represented by a distributed RC circuit illustrated in Fig. 8.2. For each structure, there are innumerable infinitesimal branches, where $R_1(\xi)$ represents the resistance density between two adjacent branches, and $R_2(\xi)$ and $C_2(\xi)$ correspond to the resistive and capacitive impedance densities of each branch, respectively. By taking the variables: $f_1(\xi,t) = -\partial Q(\xi,t)/\partial t$, $e_1(\xi,t) = Q(\xi,t)/C_2(\xi) + R_2(\xi)\partial Q(\xi,t)/\partial t$,

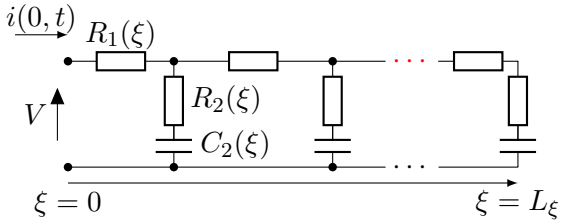

Figure 8.2: Infinite dimension electrical system.

$f_{r1}(\xi,t) = \partial/\partial\xi\,(Q(\xi,t)/C_2(\xi) + R_2(\xi)\partial Q(\xi,t)/\partial t)$, where $Q(\xi,t)$ is the charge density of each capacitor, one can express the dynamic function of the circuit in a PHS form: [1]

$$\begin{pmatrix} f_1 \\ f_{r1} \end{pmatrix} = \begin{pmatrix} 0 & \partial_\xi \\ \partial_\xi & 0 \end{pmatrix} \begin{pmatrix} e_1 \\ e_{r1} \end{pmatrix}, \text{with } e_{r1}(\xi,t) = -\frac{f_{r1}(\xi,t)}{R_1(\xi)}. \tag{8.1}$$

Assuming that the impedance is infinite, the current at the endpoint of each fractal structure is zero, namely $e_{r1}(L_\xi) = 0$.

[1] For the sake of compactness, $\partial/\partial\xi$ is denoted as ∂_ξ and the symbol t is omitted in the following context.

According to (Le Gorrec et al., 2005) and (Villegas, 2007), the boundary port variables of (8.1) can be expressed with respect to the physical boundary conditions:

$$\begin{aligned}\begin{pmatrix} f_{\partial\xi}^T & e_{\partial\xi}^T \end{pmatrix}^T &= \begin{pmatrix} e_1(0) & e_1(L_\xi) & -e_{r1}(0) & e_{r1}(L_\xi) \end{pmatrix}^T \\ &= \begin{pmatrix} V + V_c & e_1(L_\xi) & -I_e & 0 \end{pmatrix}^T, \end{aligned} \tag{8.2}$$

where V_c corresponds to the voltage coming from the gel, and I_e represents the output current. The Hamiltonian reads $H_{el} = \int_\xi Q^2/(2C_2)\mathrm{d}\xi$. The energy balance equation is given by:

$$\frac{\partial H_{el}}{\partial t} = \int_\xi \frac{\partial Q}{\partial t}^T \frac{Q}{C_2}\mathrm{d}\xi \leq f_{\partial\xi}^T e_{\partial\xi}, \tag{8.3}$$

where we have used the integration by parts, (8.2) and the dissipation arising from R_1 and R_2.

8.2.2. Electro-stress diffusion system

In this part we are interested into the electro-physical properties of the polymer and the associated electro-stress diffusion process occurring in the gel. The gel is composed of a solid and a liquid phase. The former contains the polymer network and fixed anions, and the latter includes cations and water molecules(Zhu et al., 2012). In the liquid phase, two coupled phenomena can be distinguished: the electro-osmosis and the water transport (Yamaue et al., 2005). This will later be modeled using P.G. de Gennes' method (De Gennes et al., 2000). The solid phase is assumed to be at a pseudo-equilibrium state, because the solvent dynamics is much slower compared to the mechanical dynamics of the polymer, hence forming a quasi-static electro-stress diffusion coupling model (Nishida et al., 2011b; Yamaue et al., 2005).

This assumption makes the mechanical dynamics of the gel implicit, such that the radius of curvature of the gel is addressed with the help of the rotational angle of the patch deformation along the x coordinate, i.e. $1/R(x) = -\partial\theta(x)/\partial x$, which leads to **algebraic constraints** in the coupling between the electro-stress diffusion system and the mechanical system associated with the patch deformation.

Here we explain both the solid phase and the liquid phase modelings in details. The deformation of the solid phase is assumed to be symmetric (right graph in Fig. 8.1b). The curvature $R(x)$ is assumed to be *locally homogeneous* along the x direction. Stress tensors are formulated by the curvature $R(x)$ and the swelling ratio $f_s(z,x)$:

$$\begin{aligned}\sigma_{xx}(z,x) &= \left(K - \frac{2}{3}G\right) f_s(z,x) + \frac{2G}{R(x)}z, \\ \sigma_{zz}(z,x) &= \left(K + \frac{4}{3}G\right) f_s(z,x) - \frac{4G}{R(x)}z,\end{aligned}$$

where K and G are the bulk and shear modulus of the gel, respectively (Yamaue et al., 2005). The pseudo-equilibrium state of the gel gives the pressure p as

$$p = \sigma_{zz}. \tag{8.4}$$

In the liquid phase, it is supposed that the gel goes only in the z direction. This is consistent with the hypothesis of local homogeneity of $R(x)$ in the solid phase. The conservation law on the volume leads to(Yamaue et al., 2005):

$$\frac{\partial f_s(z,x)}{\partial t} = -\frac{\partial \mathbf{j}_s(z,x)}{\partial z}, \tag{8.5}$$

where $\mathbf{j}_s(z,x)$ is the flux of solvent.

Different physical models dealing with the coupling between the ion and water transport have been studied, among which are the ones developed by Nemat-Nasser (Nemat-Nasser and Li, 2000) and by P.G. de Gennes (De Gennes et al., 2000). The former one(Nemat-Nasser and Li, 2000) emphasizes the importance of the electrostatic force over the hydraulic force and the latter (De Gennes et al., 2000) considers that the hydraulic force prevails in the coupling. Both models are consistent with the experimental results. In this work we use the P.G. de Gennes' model because it is based on irreversible thermodynamics and is well suited for the PH formulation, leading to a natural definition of the power conjugated flow and effort variables. The model is formulated as follows:

$$\mathbf{j}_e = -\sigma_e \nabla\psi - \lambda\nabla p,\ \mathbf{j}_s = -\phi\frac{d^2}{\eta}\nabla p - \lambda\nabla\psi, \tag{8.6}$$

where $\mathbf{j}_e$ represents the electrical current density. σ_e is the conductance, λ stands for the Onsager's coupling constant and ψ is the electric field. ϕ, d and η denote the water volume fraction, the effective pore size and the water viscosity, respectively, whose product $\phi d^2/\eta$ forms the constant of the Darcy's permeability (De Gennes et al., 2000).
By combining (8.4) and (8.6), one gets:

$$\begin{aligned}\mathbf{j}_s(z) &= \frac{\lambda}{\sigma_e}\mathbf{j}_e + \left(\frac{\lambda^2}{\sigma_e} - \phi\frac{d^2}{\eta}\right)\frac{\partial p}{\partial z} \\ &= -\mathcal{R}_g\frac{\partial}{\partial z}\left(\mathcal{R}_f f_s\left(z,x\right)\right) + \mathbb{1}_Z\frac{\lambda}{\sigma_e}\mathbf{j}_e + \mathbb{1}_Z\Phi(x),\end{aligned} \tag{8.7}$$

with $\mathcal{R}_g = d\left(\phi/\eta - \lambda^2/\left(d^2\sigma_e\right)\right)$, $\mathcal{R}_f = d\left(K + 4/3G\right)$, and $\Phi(x) = \left(\phi d^2/\eta - \lambda^2/\sigma_e\right)4G/R(x)$. $\mathcal{R}_f f_s$ can be seen analogous to a compression force. $\mathbb{1}_Z$ is firstly proposed in (Nishida et al., 2011b) and serves for the multiscale coupling. It stands for the characteristic function of domain z, and distributes uniformly the boundary values $\frac{\lambda}{\sigma_e}\mathbf{j}_e$ and $\Phi(x)$ into the z domain.
Similar to the electrical system, by defining $f_2 = -\partial_t f_s$, $f_{r2} = \mathcal{R}_f\partial_z f_s$, $e_2 = \mathcal{R}_f f_s$ and $e_{r2} = -\mathcal{R}_g\partial_z\left(\mathcal{R}_f f_s\right)$, (8.5) and (8.7) can then be reformulated in the PH framework as:

$$\begin{pmatrix} f_2 \\ f_{r2}\end{pmatrix} = \begin{pmatrix} 0 & \partial_z \\ \partial_z & 0\end{pmatrix}\begin{pmatrix} e_2 \\ e_{r2}\end{pmatrix}, \text{with } e_{r2} = -\mathcal{R}_g f_{r2}. \tag{8.8}$$

The boundary variables are:

$$\begin{pmatrix} f_{\partial z} \\ e_{\partial z}\end{pmatrix} = \begin{pmatrix} e_{r2}\left(-\frac{h}{2}\right) & e_{r2}\left(\frac{h}{2}\right) & -e_2\left(-\frac{h}{2}\right) & e_2\left(\frac{h}{2}\right)\end{pmatrix}^T. \tag{8.9}$$

Boundary conditions come from the impermeable assumption that $\mathbf{j}_s(\pm h/2) = 0$ (Nishida et al., 2011b). The Hamiltonian associated with the electro-stress diffusion system is $H_{em} = \int_z \mathcal{R}_f f_s^2/2\mathrm{d}z$. The energy balance equation is formulated as $\partial_t H_{em} = \int_z\left(\partial_t f_s\cdot\mathcal{R}_f f_s\right)\mathrm{d}z \le f_{\partial z}^T e_{\partial z}$, which is similar to the energy balance equation (8.3).
Considering that the swelling and shrinking are visualized at a macro scale, the gel generates locally a bending moment in the x direction,:

$$\begin{aligned}M(x) &= \int_z\left(\sigma_{xx} - p\right)bz\mathrm{d}z \\ &= \int_z B_a\mathcal{R}_f f_s(z,x)\mathrm{d}z + \frac{Gbh^3}{2R(x)},\end{aligned} \tag{8.10}$$

with $B_a(z) = -2Gbz/\mathcal{R}_f$. This bending moment can later be divided into two parts, M_{x1} and M_{x2}, reading:

$$M_{x1}(x) = \int_z B_a\mathcal{R}_f f_s(z,x)\mathrm{d}z,\ M_{x2}(x) = \frac{Gbh^3}{2R(x)}.$$

8.2.3. Mechanical system

A slightly deformed IPMC actuator can be modeled as a Timoshenko beam with $x \in [0, L]$ under the PH framework (Macchelli and Melchiorri, 2004):

$$\begin{pmatrix} f_3 \\ f_4 \\ f_5 \\ f_6 \end{pmatrix} = \begin{pmatrix} 0 & \partial_x & 0 & -1 \\ \partial_x & 0 & 0 & 0 \\ 0 & 0 & 0 & \partial_x \\ 1 & 0 & \partial_x & 0 \end{pmatrix} \begin{pmatrix} e_3 \\ e_4 \\ e_5 \\ e_6 \end{pmatrix} + \begin{pmatrix} 0 \\ 0 \\ 0 \\ 1 \end{pmatrix} \frac{M}{L}(x,t), \tag{8.11}$$

where [2] $f_3 = -(\partial_{tx}\omega - \partial_t\theta)$, $f_4 = \rho A \partial_{tt}\omega$, $f_5 = -\partial_{tx}\theta$, $f_6 = \rho I \partial_{tt}\theta$, $e_3 = GA(\partial_x\omega - \theta)$, $e_4 = -\partial_t\omega$, $e_5 = EI\partial_x\theta$ and $e_6 = -\partial_t\theta$. ω denotes the longitudinal displacement, ρ is the beam density, E represents the Young's modulus, A stands for the cross section area of the beam, I is the moment of inertia, and $M(x,t)$ is the distributed bending moment coming from the gel, formulated by (8.10).
The boundary port variables are calculated as:

$$\begin{pmatrix} f_{\partial x} \\ e_{\partial x} \end{pmatrix} = \begin{pmatrix} \begin{pmatrix} e_4(0) & e_3(L) & e_6(0) & e_5(L) \end{pmatrix}^T \\ \begin{pmatrix} -e_3(0) & e_4(L) & -e_5(0) & e_6(L) \end{pmatrix}^T \end{pmatrix}. \tag{8.12}$$

The Hamiltonian of the beam is $H_m = \frac{1}{2}\int_x \left(GA(\partial_x\omega - \theta)^2 + EI\partial_x^2\theta + \rho A \partial_t^2\omega + \rho I \partial_t^2\theta \right) \mathrm{d}x$.

Remark 8.2.1. *Differently from (Nishida et al., 2011b) the quasi-static behavior of the polymer is made explicit in the electro-stress diffusion system and the contribution of the polymer on the mechanical structure stemming from the modeling of the patch bending is considered as a distributed source term.* ◊

8.2.4. Coupling between the different subsystems

Electrical / electro-stress diffusion systems

According to (8.7), the interconnection between the electrical system and the electro-stress diffusion system is made through the boundary variables $e_1(0)$, $e_{r1}(0)$, and $\mathbf{j}_s(\pm h/2)$. Given that these boundary variables are of different scales and are defined in different independent domains ξ and z, a coupling element, named boundary multiscale coupling (BMS), has been introduced in (Nishida et al., 2011b) to proceed with the interconnection. As depicted in the bond graph in Fig. 8.3, the

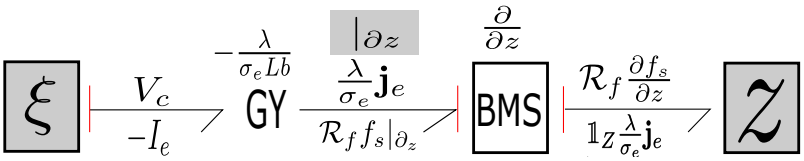

Figure 8.3: Bond graph of the coupling between ξ and z, with $\mathcal{R}_f f_s|_{\partial z} = \mathcal{R}_f\left(f_s\left(\frac{h}{2}\right) - f_s\left(-\frac{h}{2}\right)\right)$.

BMS element works as a differential gyrator. By crossing it, $\frac{\lambda}{\sigma_e}\mathbf{j}_e$ is multiplied by the characteristic function $\mathbb{1}_Z$, which represents a uniform distributed input in the domain z. Conversely, the effort variable $\partial(\mathcal{R}_f f_s)/\partial z$ in the z domain goes through the BMS in order to be integrated over z and become $\mathcal{R}_f\left(f_s\left(\frac{h}{2}\right) - f_s\left(-\frac{h}{2}\right)\right)$. The current density $\mathbf{j}_e$ is related to the current I_e by

$$\mathbf{j}_e = \frac{I_e}{Lb}. \tag{8.13}$$

[2] The second-order derivative operator $\partial^2/(\partial x \partial y)$ is denoted by ∂_{xy}.

Based on the power conservation, $\mathcal{R}_f f_s|_{\partial z}$ is transformed into the voltage V_c via the gyrator GY:

$$V_c = -\frac{\lambda}{\sigma_e L b}\mathcal{R}_f \left(f_s\left(\frac{h}{2}\right) - f_s\left(-\frac{h}{2}\right)\right). \tag{8.14}$$

Electro-stress diffusion system / mechanical system

At the macro-scale, the electro-stress diffusion model connects with the mechanical model through two bending moments (M_{x1} and M_{x2}) and the angular velocity $\partial\theta(x,t)/\partial t$.
The bond graph of the interconnection through $M_{x1}(x)$ is shown in Fig. 8.4 (left column). An additional term $\frac{B_a}{L}\mathbb{1}_Z\frac{\partial\theta}{\partial t}$ is added into (8.5) to match the power conservation. This term is considered in the electro-stress diffusion system as a source term coming from the mechanical level:

$$\frac{\partial f_s(z,x)}{\partial t} = -\frac{\partial \mathbf{j}_s(z)}{\partial z} - \frac{B_a}{L}\mathbb{1}_Z\frac{\partial\theta(x)}{\partial t}.$$

The coupling through $M_{x2}(x)$ and $\Phi(x)$ aims at describing the aforementioned algebraic constraints. From the bond graph in Fig. 8.4, since $\Phi(x)$ acts as a flow source for the electro-stress diffusion system and $M_{x2}(x)$ is the output of this system, with the linear relation

$$M_{x2}(x) = \Phi(x)B_p, \text{with } B_p = \frac{bh^3}{4}\left(\phi\frac{d^2}{\eta} - \frac{\lambda^2}{\sigma_e}\right)^{-1}, \tag{8.15}$$

a Lagrange multiplier $\lambda_{\mathbf{L}}$ is added to express the associated constraint and to guarantee the causality of the system, as presented on the right column of Fig. 8.4. One gets:

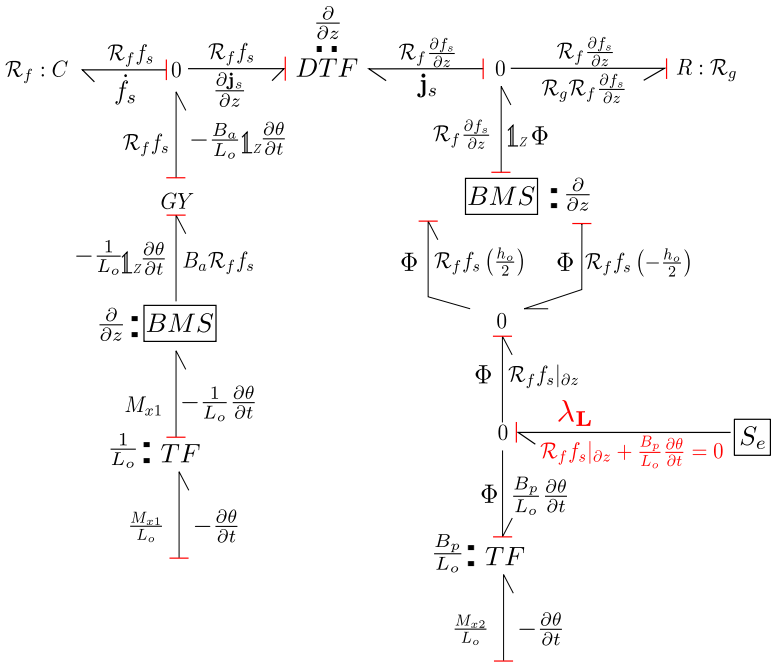

Figure 8.4: Bond graph of the coupling between z and x, through M_{x1} (left column), M_{x2} (right column) and $\partial\theta/\partial t$.

$$\begin{pmatrix} 1 & \frac{B_p}{L}\end{pmatrix}^T \lambda_{\mathbf{L}} = \begin{pmatrix}\Phi & \frac{M_{x2}}{L}\end{pmatrix}^T. \tag{8.16}$$

Furthermore, the physical constraint associated with the Lagrange multiplier $\lambda_{\mathbf{L}}$ is given by:

$$\begin{pmatrix} 1 & \frac{B_p}{L}\end{pmatrix}\begin{pmatrix}\mathcal{R}_f f_s|_{\partial z} \\ \frac{\partial\theta}{\partial t}\end{pmatrix} = \mathcal{R}_f f_s|_{\partial z} + \frac{B_p}{L}\frac{\partial\theta}{\partial t} = 0. \tag{8.17}$$

It reveals that the arrow associated with the Lagrange multiplier in the bond graph (shown in Fig. 8.4) is an effort source with zero flow, such that by passing the '0' junction, the effort variable Φ remains unchanged, while the flow variables $\mathcal{R}_f f_s|_{\partial z}$ and $\frac{B_p}{L}\frac{\partial\theta}{\partial t}$ sum to zero, ensuring the power conservation. This is analogous to an interconnection of two glued mass-spring systems, where the two masses have the same velocity and inverse reaction forces. Accordingly, (8.8) changes to:

$$\begin{pmatrix} f_2 \\ f_{r2} \end{pmatrix} = \begin{pmatrix} 0 & \partial_z \\ \partial_z & 0 \end{pmatrix} \begin{pmatrix} e_2 \\ e_{r2} \end{pmatrix} + \begin{pmatrix} \frac{B_a}{L}\mathbb{1}_Z \frac{\partial\theta}{\partial t} + \partial_z \mathbb{1}_Z \lambda_{\mathbf{L}} \\ 0 \end{pmatrix}, \tag{8.18}$$

closed with $e_{r2} = -\mathcal{R}_g f_{r2}$, boundary variables (8.9), and interconnections (8.16) and (8.17).

8.2.5. The overall system

The three above subsystems (8.1), (8.18) and (8.11), as well as their boundary variables (8.2), (8.9), and (8.12), can be coupled through the relations (8.13), (8.14) and the Lagrange multiplier (8.16) and (8.17), to get the global system:

$$f = \mathcal{J} e + \mathbf{A_L} \lambda_{\mathbf{L}}, \tag{8.19}$$

with $f = \begin{pmatrix} f_1 & f_{r1} & f_2 & f_{r2} & f_3 & f_4 & f_5 & f_6 \end{pmatrix}^T$, $e = \begin{pmatrix} e_1 & e_{r1} & e_2 & e_{r2} & e_3 & e_4 & e_5 & e_6 \end{pmatrix}^T$,

$$\mathcal{J} = \begin{pmatrix} 0 & \partial_\xi & 0 & 0 & 0 & 0 & 0 & 0 \\ \partial_\xi & 0 & 0 & 0 & 0 & 0 & 0 & 0 \\ 0 & 0 & 0 & \partial_z & 0 & 0 & 0 & -\frac{B_a}{L}\mathbb{1}_Z \\ 0 & 0 & \partial_z & 0 & 0 & 0 & 0 & 0 \\ 0 & 0 & 0 & 0 & 0 & \partial_x & 0 & -1 \\ 0 & 0 & 0 & 0 & \partial_x & 0 & 0 & 0 \\ 0 & 0 & 0 & 0 & 0 & 0 & 0 & \partial_x \\ 0 & 0 & \int_Z \frac{B_a}{L}(\,\cdot\,)dz & 0 & 1 & 0 & \partial_x & 0 \end{pmatrix}$$

, and $\mathbf{A_L}^* = \begin{pmatrix} 0 & 0 & (\,\cdot\,)|_{\frac{h}{2}} - (\,\cdot\,)|_{-\frac{h}{2}} & 0 & 0 & 0 & 0 & -\frac{B_p}{L} \end{pmatrix}$, such that

$$\mathbf{A_L}^* e = e_2\left(\frac{h}{2}\right) - e_2\left(-\frac{h}{2}\right) - \frac{B_p}{L} e_6 = 0, \tag{8.20}$$

which is similar to the constraint (8.17). The *extended space of flow variables* is defined as $\bar{\mathscr{F}} = \mathscr{F} \times \mathscr{F}_\partial$, with:

$$\begin{aligned} \mathscr{F} &= \mathscr{F}_{(0,L_\xi)} \times \mathscr{F}_{(-\frac{h}{2},\frac{h}{2})} \times \mathscr{F}_{(0,L)} \\ &= L_2\left([0,L_\xi]\times[0,L],\mathbb{R}^2\right) \times L_2\left([-\frac{h}{2},\frac{h}{2}]\times[0,L],\mathbb{R}^2\right) \times L_2\left([0,L],\mathbb{R}^4\right), \end{aligned}$$

$$\mathscr{F}_\partial = \mathscr{F}_{\partial\xi} \times \mathscr{F}_{\partial z} \times \mathscr{F}_{\partial x} = \mathbb{R}^2 \times \mathbb{R}^2 \times \mathbb{R}^4.$$

Let $H^N((a,b);R^n)$ denote the Sobolev space on the interval (a,b). The *extended space of effort variables* is $\bar{\mathscr{E}} = \mathscr{E} \times \mathscr{E}_\partial$, with:

$$\begin{aligned} \mathscr{E} &= \mathscr{E}_{(0,L_\xi)} \times \mathscr{E}_{(-\frac{h}{2},\frac{h}{2})} \times \mathscr{E}_{(0,L)} \\ &= H^1\left([0,L_\xi]\times[0,L],\mathbb{R}^2\right) \times H^1\left([-\frac{h}{2},\frac{h}{2}]\times[0,L],\mathbb{R}^2\right) \times H^1\left([0,L],\mathbb{R}^4\right), \end{aligned}$$

$$\mathscr{E}_\partial = \mathscr{E}_{\partial\xi} \times \mathscr{E}_{\partial z} \times \mathscr{E}_{\partial x} = \mathbb{R}^2 \times \mathbb{R}^2 \times \mathbb{R}^4.$$

Proposition 7. *The linear subset $\mathscr{D} \in \bar{\mathscr{F}} \times \bar{\mathscr{E}}$ defined by*

$$\mathscr{D} = \left\{ \begin{pmatrix} f \\ f_\partial \\ e \\ e_\partial \end{pmatrix} \middle| f \in \mathscr{F}, e \in \mathscr{E}, \begin{pmatrix} f_\partial \\ e_\partial \end{pmatrix} \in \mathscr{F}_\partial \times \mathscr{E}_\partial, \right.$$
$$f = \mathcal{J}e + \mathbf{A_L}\lambda_\mathbf{L}, \mathbf{A_L}^* e = 0, \lambda_\mathbf{L} \in H^1([0,L],\mathbb{R}),$$
$$e_1(0) + \frac{\lambda}{\sigma_e L b}\left(e_2\left(\frac{h}{2}\right) + e_2\left(-\frac{h}{2}\right)\right) = V,$$
$$e_{r2}\left(\pm\frac{h}{2}\right) + \frac{\lambda}{\sigma_e L b} e_{r1}(0) + \lambda_\mathbf{L} = 0,$$
$$\left. e_{r1}(L_\xi) = e_3(L) = e_4(0) = e_5(L) = e_6(0) = 0 \right\}$$

is a modulated Stokes-Dirac structure.

Proof: Equation (8.19) together with (8.20) can be reformulated as :

$$\begin{pmatrix} f \\ 0 \end{pmatrix} = \underbrace{\begin{pmatrix} \mathcal{J} & \mathbf{A_L} \\ \mathbf{A_L}^* & 0 \end{pmatrix}}_{\mathcal{J}_e} \begin{pmatrix} e \\ \lambda_\mathbf{L} \end{pmatrix},$$

The modulated Stokes-Dirac structure is inherent to the skew symmetry of $\mathcal{J}_e$. The skew symmetry of $\mathcal{J}_e$ lies in the equality between $\langle e^1, \mathcal{J}_e e^2 \rangle$ and $\langle -\mathcal{J}_e e^1, e^2 \rangle$ with the input, where $\langle \cdot, \cdot \rangle$ denotes the inner product in the Hilbert space. e^1 and e^2 are two pairs of effort variables in $\mathscr{E}$. Using integration by parts, relations of interconnection and boundary conditions 7 defined in $\mathscr{D}$, we have

$$\langle e^1, \mathcal{J}_e e^2 \rangle = \langle -\mathcal{J}_e e^1, e^2 \rangle - V \int_x \left(e^2_{r1}(0) + e^1_{r1}(0)\right) \mathrm{d}x,$$

where $-\int_x e^2_{r1}(0)dx$ is the output current I_{total} along the IPMC electrodes. ■

8.3. Multiscale discretization of the IPMC actuator

We consider now the discretization of the IPMC actuator model (8.19). To preserve the PH structure of the system, which is important for both analysis and control design, the structure preserving finite difference method on staggered grids (Trenchant et al., 2018) is applied for the discretization in space. In what follows, ξ and z are local coordinates, while x is the global coordinate, which rises the assumption that each point in x possesses one corresponding ξ and z. As a result, there are $N_e\,(= N_\xi \times N_b)$ elements for the electrical system, $N_g\,(= N_z \times N_b)$ elements for the electro-stress diffusion system, and N_b elements for the mechanical system.

8.3.1. Discretization of the electrical system

Before starting the discretization, (8.1) has to be reformulated in order to handle its algebraic linear expression in e_1. Therefore, (8.1) is rewritten as:

$$\begin{pmatrix} f_1 \\ f_{r1} \\ f_1 \end{pmatrix} = \begin{pmatrix} 0 & \partial_\xi & 0 \\ \partial_\xi & 0 & \partial_\xi \\ 0 & \partial_\xi & 0 \end{pmatrix} \begin{pmatrix} e_{1c} \\ e_{r1} \\ e_{1R} \end{pmatrix}, \tag{8.21}$$

with $e_{1c} = Q/C_2$ and $e_{1R} = R_2\partial_t Q = -R_2 f_1$.
The discretization scheme is shown in Fig. 8.5, where $j \in \{1, \cdots, N_b\}$ represents the jth element in the x coordinate, and h_1 is the discretization step along the ξ direction. With boundary condition

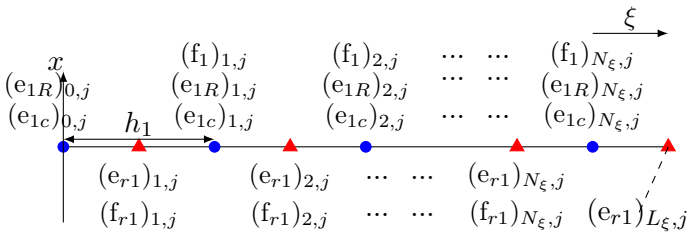

Figure 8.5: Discretization schema of (8.21).

$e_{r1}(L_\xi) = 0$, (8.21) is discretized into:

$$\begin{pmatrix} f_{1d} \\ f_{r1d} \\ f_{1d} \end{pmatrix} = \begin{pmatrix} \mathbf{0} & D_1 & \mathbf{0} \\ -D_1^T & \mathbf{0} & -D_1^T \\ \mathbf{0} & D_1 & \mathbf{0} \end{pmatrix} \begin{pmatrix} e_{1cd} \\ e_{r1d} \\ e_{1Rd} \end{pmatrix} + \begin{pmatrix} \mathbf{0} \\ g_1 \\ \mathbf{0} \end{pmatrix} e_{1b}, \tag{8.22}$$

with $f_{1d} = \begin{pmatrix} (f_1)_{1,1} & \cdots & (f_1)_{1,N_b} & \cdots & (f_1)_{N_\xi,N_b} \end{pmatrix}^T$, $f_{r1d} = \begin{pmatrix} (f_{r1})_{1,1} & \cdots & (f_{r1})_{1,N_b} & \cdots & (f_{r1})_{N_\xi,N_b} \end{pmatrix}^T$,
$e_{1cd} = \begin{pmatrix} (e_{1c})_{1,1} & \cdots & (e_{1c})_{1,N_b} & \cdots & (e_{1c})_{N_\xi,N_b} \end{pmatrix}^T$, $e_{1Rd} = \begin{pmatrix} (e_{1R})_{1,1} & \cdots & (e_{1R})_{1,N_b} & \cdots & (e_{1R})_{N_\xi,N_b} \end{pmatrix}^T$,
$e_{1b} = e_{1c}(0) + e_{1Rd}(0)$ and the matrices

$$D_1 = \begin{pmatrix} -\frac{\mathbf{1}}{\mathbf{h_1}} & \frac{\mathbf{1}}{\mathbf{h_1}} & & \\ & \ddots & \ddots & \\ & & \ddots & \frac{\mathbf{1}}{\mathbf{h_1}} \\ & & & -\frac{\mathbf{1}}{\mathbf{h_1}} \end{pmatrix}, g_1 = \begin{pmatrix} -\frac{\mathbf{1}}{\mathbf{h_1}} \\ \mathbf{0} \\ \vdots \\ \mathbf{0} \end{pmatrix},$$

where $R^{N_b \times N_b} \ni \frac{\mathbf{1}}{\mathbf{h_1}} = diag\left(\frac{1}{h_1}\right)$ and $\mathbf{0}$ is zero matrix of appropriate size.
The closure equations $e_{r1} = -f_{r1}/R_1$ and $e_{1R} = -R_2 f_1$ are discretized into:

$$e_{r1d} = L_{r1} f_{r1d}, \text{ and } e_{1Rd} = L_{r2} f_{1d}, \tag{8.23}$$

with $L_{r1} = diag(-1/R_1)$ and $L_{r2} = diag(-R_2)$.

8.3.2. Discretization of the electro-stress diffusion system

Similar to 8.3.1, (8.18) is recast into:

$$\begin{pmatrix} f_{2d} \\ f_{r2d} \end{pmatrix} = \begin{pmatrix} \mathbf{0} & D_2 \\ -D_2^T & \mathbf{0} \end{pmatrix} \begin{pmatrix} e_{2d} \\ e_{r2d} \end{pmatrix} + \begin{pmatrix} D_{26} & g_2 \\ \mathbf{0} & \mathbf{0} \end{pmatrix} \begin{pmatrix} e_{6d} \\ e_{2b} \end{pmatrix}, \tag{8.24}$$

where $f_{2d} = \begin{pmatrix} (f_2)_{1,1} & \cdots & (f_2)_{1,N_b} & \cdots & (f_2)_{N_z,N_b} \end{pmatrix}^T$, $f_{r2d} = \begin{pmatrix} (f_{r2})_{1,1} & \cdots & (f_{r2})_{1,N_b} & \cdots & (f_{r2})_{N_z-1,N_b} \end{pmatrix}^T$,
$D_{26} = \begin{pmatrix} -M_1 & \cdots & -M_m & \cdots & -M_{Ng} \end{pmatrix}^T$, $R^{N_b \times N_b} \ni M_m = diag\left(-\frac{2Gb}{\mathcal{R}_f L}\left(-\frac{h_2}{2} + \frac{(2m-1)h_2}{2}\right)\right)$,

$e_{2b} = \left(-\frac{\lambda}{\sigma_e}\mathbf{j}_e - \lambda_{\mathbf{L}d}\right)$, $\lambda_{\mathbf{L}d} = \begin{pmatrix}\lambda_{\mathbf{L}}{}^1 & \cdots & \lambda_{\mathbf{L}}{}^{N_b}\end{pmatrix}^T$, and matrices

$$D_2 = \begin{pmatrix} \frac{\mathbf{1}}{\mathbf{h_2}} & & \\ -\frac{\mathbf{1}}{\mathbf{h_2}} & \ddots & \\ & \ddots & \frac{\mathbf{1}}{\mathbf{h_2}} \\ & & -\frac{\mathbf{1}}{\mathbf{h_2}} \end{pmatrix}, g_2 = \begin{pmatrix} -\frac{\mathbf{1}}{\mathbf{h_2}} \\ \mathbf{0} \\ \vdots \\ \mathbf{0} \\ \frac{\mathbf{1}}{\mathbf{h_2}} \end{pmatrix}.$$

The closure equation $e_{r2} = -\mathcal{R}_g f_{r2}$ is discretized into

$$e_{r2d} = L_{r3} f_{r2d}, \text{ with } L_{r3} = diag(-\mathcal{R}_g). \tag{8.25}$$

8.3.3. Discretization of the mechanical system

For a clamped-free cantilever beam model, with boundary condition $e_3(L) = e_4(0) = e_5(L) = e_6(0) = 0$, (8.11) is discretized into:

$$\begin{pmatrix} f_{3d} \\ f_{4d} \\ f_{5d} \\ f_{6d} \end{pmatrix} = \underbrace{\begin{pmatrix} \mathbf{0} & D_3 & \mathbf{0} & S_1 \\ -D_3^T & \mathbf{0} & \mathbf{0} & \mathbf{0} \\ \mathbf{0} & \mathbf{0} & \mathbf{0} & D_3 \\ -S_1^T & \mathbf{0} & -D_3^T & \mathbf{0} \end{pmatrix}}_{J_{md}} \begin{pmatrix} e_{3d} \\ e_{4d} \\ e_{5d} \\ e_{6d} \end{pmatrix} + \underbrace{\begin{pmatrix} \mathbf{0} \\ \mathbf{0} \\ \mathbf{0} \\ -D_{26}^T \end{pmatrix}}_{S_2} e_{2d} + \underbrace{\begin{pmatrix} \mathbf{0} \\ \mathbf{0} \\ \mathbf{0} \\ \text{diag}(\frac{B_p}{L}) \end{pmatrix}}_{S_\lambda} \lambda_{\mathbf{L}d}, \tag{8.26}$$

where $f_{id} = \begin{pmatrix} f_i^1 & \cdots & f_i^{N_b} \end{pmatrix}^T$, $e_{id} = \begin{pmatrix} e_i^1 & \cdots & e_i^{N_b} \end{pmatrix}^T$, $i = \{3,4,5,6\}$, and matrices

$$D_3 = \begin{pmatrix} \frac{1}{h_3} & & \\ -\frac{1}{h_3} & \ddots & \\ & \ddots & \ddots \\ & & -\frac{1}{h_3} \quad \frac{1}{h_3} \end{pmatrix}, S_1 = -\begin{pmatrix} \frac{1}{2} & & \\ \frac{1}{2} & \ddots & \\ & \ddots & \ddots \\ & & \frac{1}{2} \quad \frac{1}{2} \end{pmatrix}.$$

With the coupling relations (8.13) and (8.14), closure equations (8.23) and (8.25), the discretized subsystems (8.22), (8.24) and (8.26) lead to the global discretized system:

$$\underbrace{\begin{pmatrix}\dot{x}_{1d}\\ \dot{x}_{2d}\\ \dot{x}_{md}\end{pmatrix}}_{\dot{x}_d} = \underbrace{\begin{pmatrix} M_2 D_1^T & P_1 & \mathbf{0} \\ M_1 D_1^T \left(\mathbf{I} - L_{r2} M_2 D_1^T\right) & P_2 & -S_2^T \\ \mathbf{0} & S_2 & J_{md}\end{pmatrix}}_{J_r} \underbrace{\begin{pmatrix} e_{1d}\\ e_{2d}\\ e_{md}\end{pmatrix}}_{e_d} + \underbrace{\begin{pmatrix}\mathbf{0}\\ g_2\\ S_\lambda\end{pmatrix}}_{g_c} \lambda_{\mathbf{L}d} + \underbrace{\begin{pmatrix} -M_2 g_1 \\ M_1 \left(D_1^T L_{r2} M_2 - \mathbf{I}\right) g_1 \\ \mathbf{0}\end{pmatrix}}_{B} V, \tag{8.27}$$

with $\mathbf{I}$ the identity matrix of appropriate size,

$$\begin{aligned}
&x_{1d} = Q_d, x_{2d} = f_{sd},\\
&x_{md} = \begin{pmatrix}\partial_x \omega_d - \theta_d & \rho A \partial_t \omega_d & \partial_x \theta_d & \rho I \partial_t \theta_d\end{pmatrix}^T,\\
&e_d = L_d x_d, L_d = diag\left(1/C_2, \mathcal{R}_f, GA, 1/\left(\rho A\right), EI, 1/\left(\rho I\right)\right),\\
&M_1 = g_2 \frac{\lambda}{\sigma_e L b} g_1^T L_{r1}, P_1 = M_2 g_1 \frac{\lambda}{\sigma_e L b} g_2^T,\\
&M_2 = -\left(\mathbf{I} + D_1 L_{r1} D_1^T L_{r2}\right)^{-1} D_1 L_{r1}, \text{ and}\\
&P_2 = -D_2 L_{r3} D_2 - M_1 \left(D_1^T L_{r2} M_2 + \mathbf{I}\right) g_1 \frac{\lambda}{\sigma_e L b} g_2^T.
\end{aligned}$$

The geometric constraint in (8.20) becomes $g_c^T e_d = 0$.

8.3.4. Elimination of the Lagrange multiplier

The Lagrange multiplier $\lambda_{\mathbf{L}d}$ in (8.27) has to be eliminated in order to perform the simulation and apply the control strategies afterwards. The proposed method is based on the coordinate projection in (A.J. van der Schaft and Maschke, 1994) that preserves the PH structure of the system. This projection approach has later been improved in (Wu et al., 2014b) to get a descriptor formulation in the linear case, which finally leads to:

$$\begin{pmatrix}\mathbf{I} & \mathbf{0}\\ \mathbf{0} & \mathbf{0}\end{pmatrix}\begin{pmatrix}\dot{\tilde{X}}_1\\ \dot{\tilde{X}}_2\end{pmatrix} = \begin{pmatrix}\tilde{J}_{11} & \tilde{J}_{12}\\ g_c^T \tilde{M}^T\end{pmatrix} \tilde{L}_d \begin{pmatrix}\tilde{X}_1\\ \tilde{X}_2\end{pmatrix} + \tilde{M} B V, \tag{8.28}$$

where $\tilde{M}$ is the coordinate transformation matrix such that $\tilde{M} = \begin{pmatrix} S \\ \left(g_c^T g_c\right)^{-1} g_c^T\end{pmatrix}$ with S satisfying $S \cdot g_c = 0$. $\tilde{X}_1 = \tilde{M}\begin{pmatrix}x_{1d}^T & x_{2d}^T & x_{3d}^T & x_{4d}^T & x_{5d}^T\end{pmatrix}^T$, $\tilde{X}_2 = \tilde{M} x_{6d}^T$, $\tilde{J} = \begin{pmatrix}\tilde{J}_{11} & \tilde{J}_{12}\\ \tilde{J}_{21} & \tilde{J}_{22}\end{pmatrix} = \tilde{M} J_r \tilde{M}^T$, and $\tilde{L}_d = \tilde{M}^{-T} L_d \tilde{M}^{-1}$.

8.4. Simulation results and experimental validation

The experimental set-up is shown in Fig. 8.6. The IPMC patch is controlled through a computer equipped with a dSPACE controller board in order to generate different types of input voltages. The

amplifier is used to regulate the input voltage. The laser position sensor and current sensor are dedicated to the measure of the tip displacement of the IPMC and to the measure of the output current, respectively. The dimension of the considered Nafion-based IPMC actuator is $45\text{mm} \times 5\text{mm} \times 0.2\text{mm}$, with a density of $1.633 \times 10^3 \text{kg/m}^3$, Young's modulus of $9 \times 10^7 \text{Pa}$ and Poisson ratio of 0.3. According to (Paquette et al., 2003), $\phi = 0.34$ and $\eta = 0.010 \text{Pa} \cdot \text{s}$. Identified parameters are listed in Table 8.1, where $R_{1\text{total}}$, $R_{2\text{total}}$ and $C_{2\text{total}}$ are the identified resistances and capacitance of the electrodes.

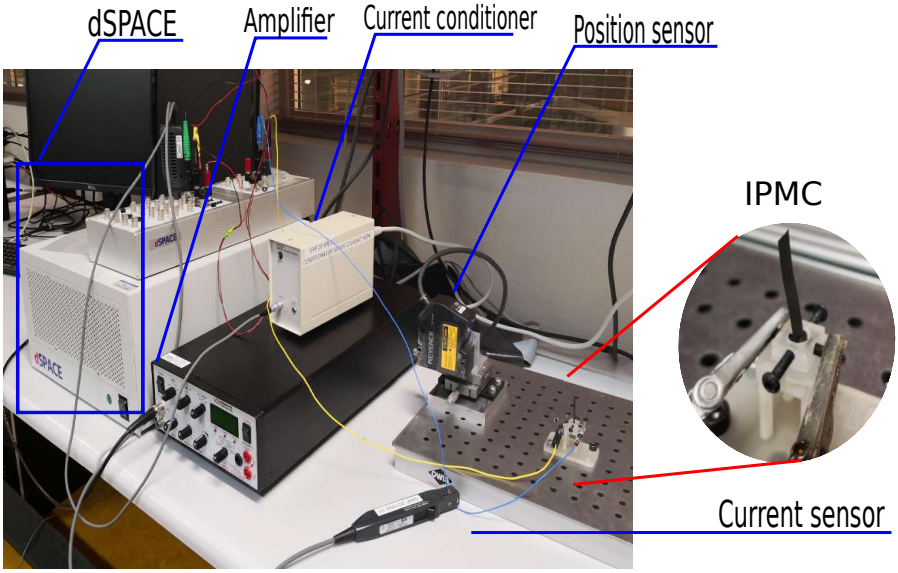

Figure 8.6: Experimental setup of IPMC.

Table 8.1: Identified parameters.

$R_{1\text{total}}$	460.54	Ω	λ	16.6×10^{-9}	$\text{m}^2/(\text{V s})$
$R_{2\text{total}}$	3	Ω	σ_e	13.10	$1/(\Omega\text{m})$
$C_{2\text{total}}$	0.021	F	d	10	nm

The temporal evolution of the current obtained in the simulation with a step voltage of 1V are depicted and compared to the experimental one in Fig. 8.7. The simulations correspond to four values of N_ξ (10, 50, 100 and 200), while both N_z and N_b fixed to 10. As N_ξ increases, the peak response obtained in simulation approaches gradually the experimental one (marked by black solid line), while the settling time remains similar. This evolution is in accordance with the frequency responses of the transfer functions associated to different values of N_ξ.
From the Bode diagram in Fig. 8.8, the transfer functions have a similar shape at low frequencies but are slightly different for the high frequencies. This difference tends to zero when N_ξ tends to infinity. However, one can notice that for the considered example, the difference is minor for N_ξ greater than 50. The influence of N_z and N_b on the current has also been investigated but omitted in this work for the sake of brevity. Actually, these parameters have a minor effect on the current responses compared to that of N_ξ.
We consider now the consistency between the simulation and experimental results for the tip deflection of the IPMC strip. Preliminary works suggest that the deflection does not change with N_z. Meanwhile, its variation is negligible as soon as N_ξ is greater than 20. As a consequence, the influence of the discretization number N_b on the mechanical deformation is demonstrated for : $N_\xi = 50$ and $N_z = 10$. As shown in Fig. 8.9, N_b has a significant influence on the predicted response: the simulation results of the tip deflection approach to the experimental ones with the increase of the

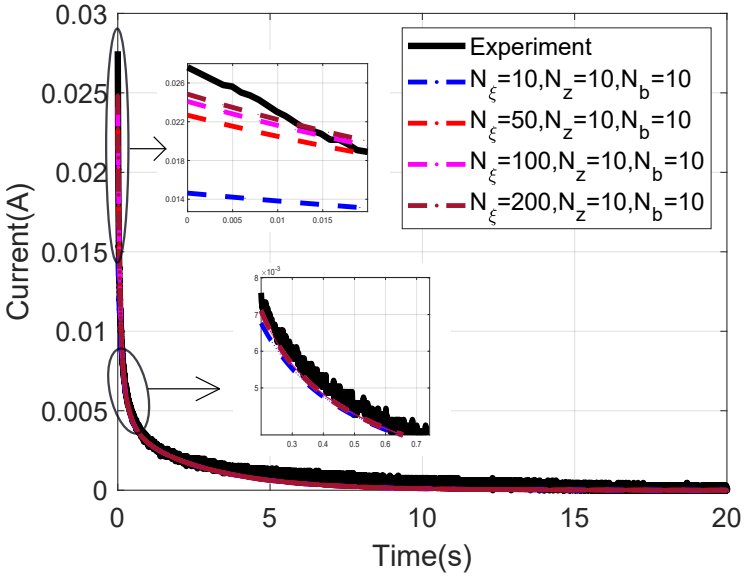

Figure 8.7: Variation of the output current according to different discretization numbers N_ξ, compared with experimental data.

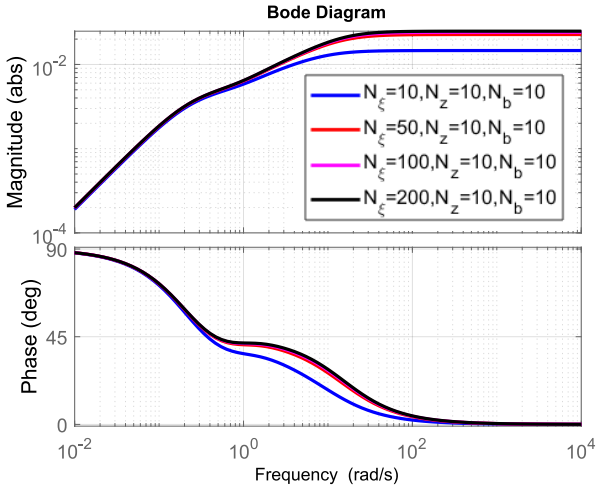

Figure 8.8: Bode diagrams for different discretization configurations of the electrical system.

discretization number N_b. One can see that $N_b = 100$ leads to a very good approximation of the system behavior. This demand of a large discretization number is mainly due to the applied finite differences method, because this method is a direct approximation of the PDEs, and one needs a great number of elements to approximate the analytic solutions.

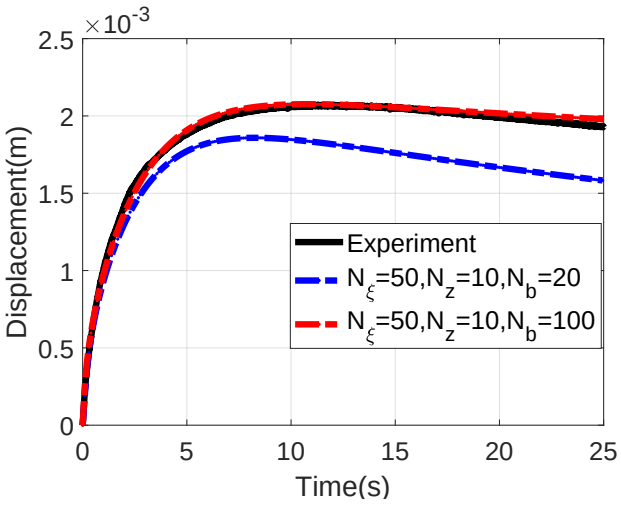

Figure 8.9: Tip deflection of IPMC strip according to different discretization numbers N_b, compared with experimental data.

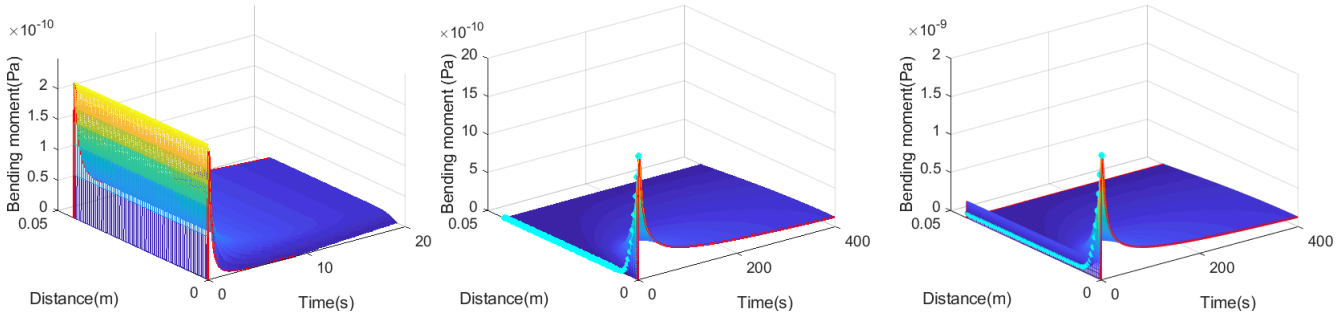

(a) M_{x1} (b) M_{x2} (c) M_{ext}

Figure 8.10: Simulation results for M_{x1}, M_{x2} and M_{ext} along x-axis and the time ($N_\xi = 50, N_z = 10$ and $N_b = 100$).

The two bending moments generated by the gel are simulated in Fig. 8.10 for $N_\xi = 50$, $N_z = 10$ and $N_b = 100$. Fig. 8.10a shows the distribution along the beam and the temporal evolution of the bending moment M_{x1}, while Fig. 8.10b shows those related to M_{x2}. At each time, the bending moments M_{x1} are the same whatever the points along the beam. Nevertheless, as illustrated by the dashed light blue line in Fig. 8.10b, M_{x2} has a larger value at the clamped point and is equal to zero at the free end point, which is in accordance with the considered boundary conditions for the cantilever.

The sum of the M_{x1} and M_{x2} forms the total bending moment that applies to the beam model, whose simulation result is given in Fig. 8.10c. One can notice a diffusion phenomenon in Fig. 8.10, as illustrated by the red solid lines. This diffusion effect of the bending moment explains the back-relaxation of the displacement in our model, as shown in Fig. 8.9. Considered as the main drawback of such actuators, this back relaxation exists in almost all Nafion-based IPMCs. More thorough studies on this phenomenon are referred to some recent references, e.g. (Porfiri et al., 2018).

A comparison between the experimental and simulation results in the case of a sinusoidal input voltage of amplitude 1V and frequency of 1Hz is also given in Fig. 8.11. One can see the simulation results are consistent with the experimental ones. It also illustrates that the proposed model copes with the hysteretic behavior of the actuator.

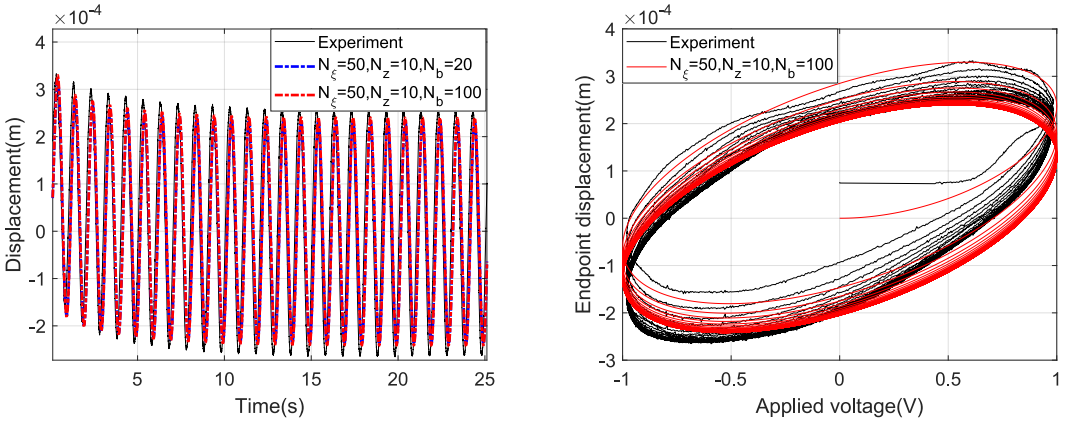

Figure 8.11: Tip deflection of IPMC strip with a sinusoidal input voltage.

Remark 8.4.1. *Comparisons have also been carried out between homogeneous and irregular meshing. The results show that one can reduce the number of elements near the clamped side without modifying significantly the behavior of the system. Furthermore, the order of the overall system can be drastically reduced using finite elements methods (Wu et al., 2014b) rather than finite differences.* ◊

8.5. Summary

In this chapter, we establish a comprehensive model of an IPMC patch within the framework of constrained PH theory. We employ the Lagrange multiplier method to address the geometric constraints that arise due to the connection between the gel and the actuator electrode. The resulting global system exhibits a Stokes–Dirac structure, derived from the energy balance expressions. To facilitate numerical simulations while preserving the system's geometric properties, we discretize it using the finite differences method on staggered grids. Subsequently, we reduce it to a set of differential algebraic equations.

We conduct experiments and simulations involving step and sinusoidal input cases. These investigations provide insights into selecting appropriate discretization parameters, ensuring that the simulated output current and displacement at the endpoint of the IPMC patch closely match experimental data.

Chapter 9

Modeling and control of IPMC actuated flexible beam

9.1. Introduction

This chapter proposes a 1D physically based model and control strategy for an IPMC actuated flexible structure representative of the mechanical properties of a flexible endoscope suitable for medical applications. To this end, we use the port Hamiltonian (PH) approach. PH systems (Maschke and van der Schaft, 1992) have proven to be powerful for the modelling and control of complex physical systems (Duindam et al., 2009), such as multi-physical (Doria-Cerezo et al., 2010) and non-linear (Ramirez et al., 2016). This approach has been generalized to distributed parameter systems described by partial differential equations (van der Schaft and Maschke, 2002; Le Gorrec et al., 2005; Ramirez et al., 2014) and irreversible thermodynamic systems (Ramirez et al., 2013). PHS modelling is based on the characterization of energy exchanges between the different components of a system. This framework is particularly adapted for the modular modelling of multi-physical systems. Hence, it is well suited for the modelling of flexible structure actuated with IPMC patches. A precise PH model of IPMC actuators accounting for multi-scale phenomena has been proposed in (Nishida et al., 2011a) but we shall consider in this work a simplified equivalent lumped electrical circuit coping with the main dynamics of the actuator. On the other hand, the PHS approach is well suited for the application of passivity based control tools with clear physical interpretation, such as energy shaping and control by interconnection and damping assignment (IDA-PBC).
The main contributions of this Chapter are the proposition of a lumped scalable model suitable for the modelling of flexible actuated structures, different control strategies which take into account the electro-mechanical coupling and the experimental validation of the approach. Firstly, a simple but realistic approximation model of the IPMC actuated medical endoscope (Chikhaoui et al., 2014) using the PHS formalism is proposed. For this purpose, we consider the model composed of IPMC patches glued on a flexible structure. A 1-D lumped model based on interconnected links is considered to model the flexible structure as shown in Figure 9.1. We consider that the bending of the flexible structure is due to the torques generated by the IPMC patches when a voltage is applied on the actuators as shown in Figure 9.2. Both the 1-D finite dimensional structure and the IPMC actuators are modelled using PHS and interconnected in a power preserving manner. The final model is non-trivial because of the electro-mechanical/mecano-electrical coupling between the flexible structure and the IPMC actuator. Then, two passivity based control strategies, IDA-PBC and the Control by Interconnection-Proportional Integral control are used to achieve a desired equilibrium position of the flexible structure with guaranteed performances. Because of the inter-domain coupling, the closed-loop Lyapunov function has to contain cross terms between electrical and actuated mechanical variables which is also studied in (Delgado and Kotyczka, 2014). In order to properly select the cross terms while guaranteeing the overall stability, a set of auxiliary design parameters are defined and used to solve the matching conditions associated with the control design problem. Finally an experimental

set-up which reproduces the endoscope's behavior is used to validate the proposed model and to test the effectiveness of the control design method.
The chapter is organized as follows: Section 9.2 presents the PH formulation of the IPMC actuated flexible structure. In Section 9.3, different passivity based control designs to achieve desired closed loop performances are proposed. The identification of parameters and the model validation on an experimental set-up are presented in Section 9.4. The simulation and the experimental results are shown in Section 9.5 to show the effectiveness of the proposed control laws. Some final remarks are given in Section 9.6.

9.2. PHS modelling of IPMC actuated flexible structure

The flexible structure is approximated by a mechanical structure composed of n inertia interconnected through flexible joints made up with springs and dampers as shown in Figure 9.1. We assume a planar model, and so all the links are allowed to move only in the x-y plane.

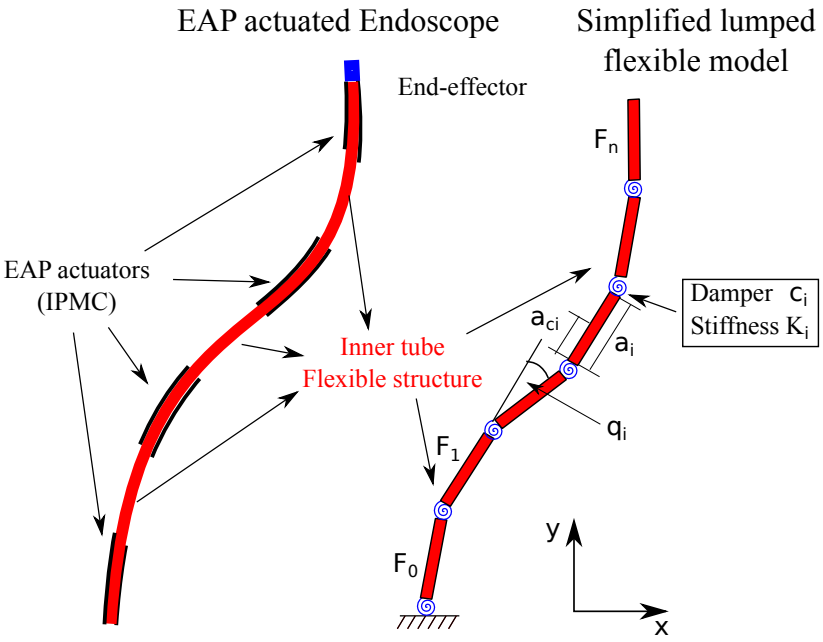

Figure 9.1: Lumped parameters flexible structure

We suppose that the flexible structure is under-actuated and that there are $m \leq n$ IPMC actuators inducing torques on $m \leq n$ joints as shown in Figure 9.2. Each (actuated or non-actuated) joint of the flexible structure contains a spring and a damper, as shown in Figure 9.1.

9.2.1. PHS formulation of a flexible structure

In this subsection, we introduce the PH model of the IPMC actuated flexible structure shown in Figure 9.1. The parameters of the n-degrees of freedom mechanism ($i = 1, 2, ..., n$) are:

- q_i the i-th joint angular;
- m_i the i-th link's mass;
- I_i the moment of inertia about the axe passing through the Center of Mass (CoM) of the i-th link;
- a_i length of the i-th link;
- a_{Ci} distance between the i-th Joint and the CoM of the i-th link;
- τ_i applied torque on the i-th joint;
- $\tilde{K}_i$ stiffness of the i-th joint;

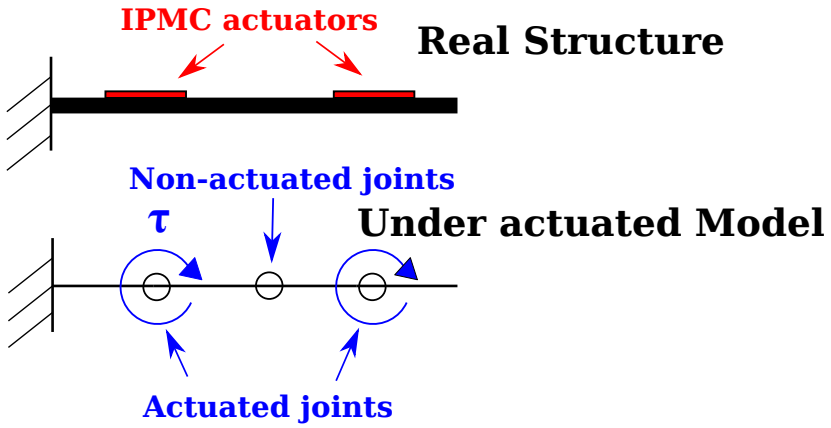

Figure 9.2: Flexible structure modelling with the actuators

- c_i viscous damping at the i-th joint;
- P_i E_i Potential and Kinetic energy of the i-th link.
- F_0 is the inertial frame;
- F_i is the reference frame attached to the CoM and with axe parallel to the principal axe of inertia of the i-th link .

The Hamiltonian function

In this subsection we derive the Hamiltonian function of the flexible structure with respect to the chosen coordinate frame. The Hamiltonian corresponds to the total mechanical energy which is the sum of the kinetic and potential energies. The kinetic energy of the i-th link has the form

$$E_i = \frac{1}{2} m_i v_{Ci}^T v_{Ci} + \frac{1}{2} \omega_i^T I_i \omega_i, \tag{9.1}$$

where v_{Ci} is the velocity of the center of mass (CoM) of the i-th link, ω_i is the angular velocity of the i-th link with respect to F_0, I_i is the inertia matrix of the i-th link with respect to F_i. The goal is to express the kinetic energy of every link only with respect to the joint angular velocities $\dot{q}_i$ (derivatives of every joint angular). Thanks to the rigidity of the links, it is possible to relate both the velocities of the CoM v_{Ci} and the angular velocities ω_i to the joint angular velocities $\dot{q}_i$. The relation that links joint angular velocities to angular velocities is trivial

$$\omega_i = \dot{q}_1 + \dot{q}_2 + \cdots + \dot{q}_i. \tag{9.2}$$

This relation can be expressed through the use of the so called angular Jacobian,

$$\omega_i = J_\omega^i \dot{q}, \tag{9.3}$$

where $q = [q_1, \cdots, q_i]^T$ and $\dot{q} = [\dot{q}_1, \cdots, \dot{q}_i]^T$. In this case, the angular Jacobian does not depend on the angular displacements. This is not the case for the Jacobian related to the velocities of the center of mass. The velocity Jacobian of the i-th link is obtained by differentiating the position of the i-th center of mass with respect to time in the F_0 frame,

$$q_{Ci} = \begin{bmatrix} x_{Ci} \\ y_{Ci} \end{bmatrix} = \begin{bmatrix} f_{xi}(q) \\ f_{yi}(q) \end{bmatrix} = f_i(q), \tag{9.4}$$

where,

$$f_{xi}(q) = \sum_{k=1}^{i-1} a_k \cos\left(\sum_{j=1}^{k} q_j\right) + a_{Ci}\cos\left(\sum_{k=1}^{i} q_k\right),$$
$$f_{yi}(q) = \sum_{k=1}^{i-1} a_k \sin\left(\sum_{j=1}^{k} q_j\right) + a_{Ci}\sin\left(\sum_{k=1}^{i} q_k\right).$$

Differentiating q_{Ci} with respect to time, we obtain $\dot{q}_{Ci} = v_{Ci} = \frac{\partial f_i(q)}{\partial q}\dot{q}$, hence the velocity Jacobian is

$$J_v^i = \frac{\partial f_i(q)}{\partial q}. \tag{9.5}$$

Now it is possible to express the kinetic energy of every link with respect to the derivative of the displacement vector

$$E_i = \frac{1}{2}\dot{q}^T \left(m_i J_v^{iT}(q) J_v^i(q) + J_\omega^{iT} I_i J_\omega^i\right)\dot{q}. \tag{9.6}$$

The total kinetic energy of the flexible structure is then

$$E = \frac{1}{2}\dot{q}^T M(q)\dot{q}, \tag{9.7}$$

where $M(q)$ is the mass matrix of the system, given by

$$M(q) = \sum_{i=1}^{n} \left(m_i J_v^{iT}(q) J_v^i(q) + J_\omega^{iT} I_i J_\omega^i\right). \tag{9.8}$$

The mass matrix allows to relate the generalized velocity with the momentum of the mechanical system

$$p = M(q)\dot{q}, \tag{9.9}$$

where $p = \begin{bmatrix} p_1 & p_2 & \cdots & p_n \end{bmatrix}^T$. The kinetic energy expressed as a function of the momentum is then

$$E(q,p) = \frac{1}{2}p^T M^{-1}(q) p. \tag{9.10}$$

In our framework we are supposing that the work plane is parallel to the ground, therefore we ignore the effect of the gravity on the dynamics of the system. Then, the potential energy is only due to the springs deformation. To find the potential energy we first define the stiffness matrix of the system

$$K = \text{diag}\begin{bmatrix} \tilde{K}_1, & \tilde{K}_2, & \cdots, & \tilde{K}_n \end{bmatrix}. \tag{9.11}$$

The constitutive relation between elastic torques and springs deformation is given by $\tau_e = Kq$, hence the total potential energy is

$$P(q) = \frac{1}{2}q^T K q. \tag{9.12}$$

Finally, the Hamiltonian, *i.e.*, the total energy of the flexible structure, is given by

$$H_b(q,p) = E(q,p) + P(q) = \frac{1}{2}p^T M^{-1}(q) p + \frac{1}{2}q^T K q. \tag{9.13}$$

9.2.2. The PH model of the flexible structure

By choosing as state vector of the flexible structure $x_b = [q, p]^T$, we can write the PH representation (Maschke and van der Schaft, 1992) of the system

$$\begin{cases} \dot{x}_b &= (J_b - R_b)\frac{\partial H_b(x_b)}{\partial x_b} + g_b u_b \\ y_b &= g_b^T \frac{\partial H_b(x_b)}{\partial x_b} \end{cases} \tag{9.14}$$

with

$$J_b = \begin{bmatrix} 0 & I_n \\ -I_n & 0 \end{bmatrix}, \quad R_b = \begin{bmatrix} 0 & 0 \\ 0 & C_n \end{bmatrix}, \quad g_b = \begin{bmatrix} 0 \\ g_m \end{bmatrix}$$

with $C_n = \text{diag}\begin{bmatrix} c_1, & c_2, & \cdots, & c_n \end{bmatrix}$, a positive diagonal matrix containing the viscous friction coefficients of the dampers associated with the respective joints. The structural matrix $J_b = -J_b^T$ represents the energy exchanges in the system, while the damping matrix $R_b = R_b^T \geq 0$ captures the internal dissipation of the system. The flexible structure is under-actuated on $m \leq n$ joints, thus the input vector of external torques $u_b = [\tau_1, \tau_2, \cdots \tau_m]^T \in \mathbb{R}^m$ and $g_m \in \mathbb{R}^{n \times m}$. The power conjugate output $y_b \in \mathbb{R}^m$ is the set of angular velocities on the actuated joints. The system is passive. In fact, the Hamiltonian is such that $H_b > 0$ and $H(0) = 0$, moreover its time derivative satisfies:

$$\dot{H}_b = -\frac{\partial H_b}{\partial x_b}^T R_b \frac{\partial H_b}{\partial x_B} + y_b^T u_b \leq y_b^T u_b. \tag{9.15}$$

9.2.3. The IPMC actuator model

The bending of the IPMC with respect to the applied voltage is mainly attributed to the cations flux and polar solvents in the polymer membrane diffusion between the electrodes (see left side in Figure 9.3) (Shahinpoor, 2016). A multiscale model of an IPMC actuator has been proposed in (Nishida et al., 2011b). It details the main physical phenomena involved in this multiphysical actuator. In this work, since we assume perfect interconnection between the actuator and the beam, the mechanical contribution of the IPMC actuator is considered as part of the flexible structure. Therefore, we use a simplified and control oriented model for the IPMC'S electric dynamics. This model is based on the lumped RLC equivalent circuit that has been proposed in (Yim et al., 2006; Gutta et al., 2009) (right side of Figure 9.3). The output torque of the IPMC is proportional to the voltage across the capacitor. The interconnection ports are placed across the capacitor.

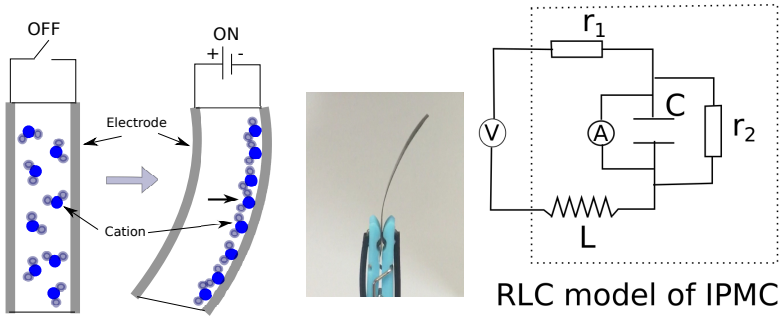

Figure 9.3: IPMC bending principle and its electrical model

The electrical model of the IPMC actuator can be written as

$$\begin{cases} \begin{bmatrix} \dot{\varphi} \\ \dot{Q} \end{bmatrix} = \begin{bmatrix} -r_1 & -1 \\ +1 & -\frac{1}{r_2} \end{bmatrix} \begin{bmatrix} \frac{\partial H_a}{\partial \varphi} \\ \frac{\partial H_a}{\partial Q} \end{bmatrix} + \begin{bmatrix} 1 \\ 0 \end{bmatrix} u(t) + \begin{bmatrix} 0 \\ 1 \end{bmatrix} u_a(t) \\ y = \begin{bmatrix} 1 & 0 \end{bmatrix} \begin{bmatrix} \frac{\partial H_a}{\partial \varphi} \\ \frac{\partial H_a}{\partial Q} \end{bmatrix}, \quad y_a = \begin{bmatrix} 0 & 1 \end{bmatrix} \begin{bmatrix} \frac{\partial H_a}{\partial \varphi} \\ \frac{\partial H_a}{\partial Q} \end{bmatrix} \end{cases} \tag{9.16}$$

where the total energy of the system is defined as the sum of the magnetic and electric energies

$$H_a = \frac{1}{2}\frac{Q^2}{C} + \frac{1}{2}\frac{\varphi^2}{L}. \tag{9.17}$$

and where the state vector is $x_a = [\varphi, Q]^T$ with φ the flux and Q the charge of the capacitor, r_1 and r_2 are the resistances, u is the applied voltage on the IPMC actuator and y is the current in the inductance and y_a is the voltage across the capacitor. Furthermore the torque applied on the flexible structure is generated by y_a with a constant coefficient $[k] = \frac{\mathsf{N \cdot m}}{\mathsf{V}}$, *i.e.*, $u_b = \tau = k y_a$. From the power conserving interconnection, u_a is the current applied on the capacitor due to the mechanical movement of the structure, *i.e.*, $u_a = i_a = -k y_b$. The interconnection relation is defined by

$$\begin{bmatrix} u_b \\ u_a \end{bmatrix} = \begin{bmatrix} 0 & k \\ -k & 0 \end{bmatrix} \begin{bmatrix} y_b \\ y_a \end{bmatrix}. \tag{9.18}$$

As mentioned before, we consider an under-actuated system, *i.e.*, $m < n$. We shall split the configuration coordinates into actuated and non-actuated ones, *i.e.*, $q = [q_1, q_2]^T$ and $p = [p_1, p_2]^T$ with $q_1, p_1 \in \mathbb{R}^m$ and $q_2, p_2 \in \mathbb{R}^{n-m}$. Thus the interconnected model of the flexible structure and the IPMC actuators can be written as

$$\begin{aligned} \begin{bmatrix} \dot{q} \\ \dot{p} \\ \dot{\varphi} \\ \dot{Q} \end{bmatrix} &= \begin{bmatrix} 0 & I_n & 0 & 0 \\ -I_n & -C_n & 0 & K_c \\ 0 & 0 & -R_{1m} & -I_m \\ 0 & -K_c^T & I_m & -R_{2m} \end{bmatrix} \begin{bmatrix} \frac{\partial H}{\partial q} \\ \frac{\partial H}{\partial p} \\ \frac{\partial H}{\partial \varphi} \\ \frac{\partial H}{\partial Q} \end{bmatrix} + \begin{bmatrix} 0 \\ 0 \\ I_m \\ 0 \end{bmatrix} u \\ y &= \begin{bmatrix} 0 & 0 & I_m & 0 \end{bmatrix} \begin{bmatrix} \frac{\partial H}{\partial q} \\ \frac{\partial H}{\partial p} \\ \frac{\partial H}{\partial \varphi} \\ \frac{\partial H}{\partial Q} \end{bmatrix}, \end{aligned} \tag{9.19}$$

where $u, y \in \mathbb{R}^m$ and 0 are zero matrices of appropriate dimensions, $R_{1m} = \mathsf{diag}[r_1, r_1, \cdots, r_1] \in \mathbb{R}^{m \times m}$, $R_{2m} = \mathsf{diag}[1/r_2, 1/r_2, \cdots, 1/r_2] \in \mathbb{R}^{m \times m}$ are the resistance matrices and the coupling matrix K_c is

$$K_c = \begin{bmatrix} K_m \\ 0 \end{bmatrix} \in \mathbb{R}^{n \times m} \tag{9.20}$$

with $K_m = \mathsf{diag}[k_1, k_2, \cdots, k_m] \in \mathbb{R}^{m \times m}$.
The total Hamiltonian of the interconnected system is:

$$\begin{aligned} H &= H_a + H_b \\ &= H^Q(x) + H^\varphi(x) + E(x) + P(x) \\ &= \tfrac{1}{2} Q^T C^{-1} Q + \tfrac{1}{2} \varphi^T L^{-1} \varphi + \tfrac{1}{2} p^T M^{-1} p + \tfrac{1}{2} q^T K q. \end{aligned} \tag{9.21}$$

with the capacitance matrix $C = \mathsf{diag}[C_1, C_2, \cdots, C_m]$ and the inductance matrix $L = \mathsf{diag}[L_1, L_2, \cdots, L_m]$.

9.3. Control design

For the current application the control objective is to change the equilibrium position of the IPMC actuated beam and assign a desired performance in terms of settling time and overshoot. Due to the fact that, unlike classical electro-mechanical systems, such as DC-motors, the equivalent electrical circuit has a pervasive dissipative term, at first both charge and magnetic flux equilibria have to be changed. Secondly, from an energy balance perspective the dissipation obstacle (van der Schaft, 2000) does not allow to use control by interconnection techniques for the control synthesis. As a consequence we use interconnection and damping assignment passivity based control (IDA-PBC) (Ortega et al., 2001, 2002; Ortega and Garcia-Canseco, 2004). The main idea is to match the open-loop system with a target system by using state feedback control law.

Proposition 8. *(Ortega et al., 2002) Consider the open loop system:*

$$\dot{x} = (J - R)\frac{\partial H}{\partial x} + g(x)u. \tag{9.22}$$

Define an asymptotically stable PHS target system

$$\dot{x} = (J_d - R_d)\frac{\partial H_d}{\partial x} \tag{9.23}$$

with matrices $J_d(x) = -J_d(x)^T$, $R_d(x) = R_d^T(x) \geq 0$ *and function* H_d *that verifies the PDE:*

$$g^{\perp}(J_d - R_d)\frac{\partial H_d}{\partial x} = g^{\perp}(J - R)\frac{\partial H}{\partial x}, \tag{9.24}$$

with $g^{\perp}$ *a full rank left annihilator of* g*, i.e.,* $g^{\perp}g = 0$ *and the Hamiltonian function* $H_d(x)$ *such that*

$$x^* = arg\min H_d(x). \tag{9.25}$$

with x^* *the equilibrium to be stabilized. The closed-loop system (9.22) with the feedback law* $u = \beta(x)$*, where*

$$\beta(x) = \left(g^T g\right)^{-1} g^T \left((J_d - R_d)\frac{\partial H_d}{\partial x} - (J - R)\frac{\partial H}{\partial x}\right) \tag{9.26}$$

behaves as the target system (9.23) with x^* *(asymptotically) stable.*

Remark 9.3.1 (Anti damping injection)**.** *The choice of the new damping matrix* R_d *affects the rise time of the closed loop system response. To speed up the system it is possible to choose* $0 \leq R_d \leq R$*. This scenario corresponds to an anti-damping injection: the parameter of the resulting damping injection is negative.* ◊

In our application we perform energy shaping on the position, charge and magnetic flux, which are coupled through a dissipative electrical circuit. This implies that the closed-loop energy/Lyapunov function will present cross terms between these variables. Hence in the following Proposition we present a non-trivial solution to the control problem.

Proposition 9. *Consider the open loop system* (9.19) *and define an asymptotically stable PHS target system:*

$$\dot{x} = (J_d - R_d)\frac{\partial H_d}{\partial x} \tag{9.27}$$

with the desired structure matrix $J_d = J$ *and the desired damping matrix defined as*

$$R_d = R + R_c \;\; with \;\; R_c = diag\begin{bmatrix}0, & 0, & r_c, & 0\end{bmatrix}. \tag{9.28}$$

with $r_c > -R_{1m}$. *The desired closed-loop Hamiltonian is defined as*

$$H_d(x) = \frac{1}{2} x_d^T Q_d x_d \tag{9.29}$$

where $x_d = \left[(q_1 - q_1^*), \quad q_2, \quad p, \quad (\varphi - \varphi^*), \quad (Q - Q^*)\right]^T$ *and the symmetric matrix* Q_d *is defined as:*

$$Q_d = \begin{bmatrix} K_1' & 0 & 0 & K_m R_{2m} \tilde{C} & K_m \tilde{C} \\ * & K_2 & 0 & 0 & 0 \\ * & * & M^1 & 0 & 0 \\ * & * & * & L'^{-1} & R_{2m} \tilde{C} \\ * & * & * & * & C'^{-1} \end{bmatrix} \tag{9.30}$$

with $\tilde{C} = \left(C'^{-1} - C^{-1}\right)$, $K_1' = K_1 + K_m^2 \tilde{C}$ *and* $L'^{-1} = L^{-1} + R_{2m}^2 \tilde{C}$. *The desired equilibrium position of the system is* $x^* = [q_1^*, 0, 0, \varphi^*, Q^*]$ *with*

$$Q^* = \frac{K_1 C}{K_m} q_1^*, \quad \varphi^* = \frac{R_{2m} L K_1}{K_m} q_1^*, \tag{9.31}$$

and $x^* = arg\min H_d(x)$. *Then the system* (9.19) *with feedback law* $u = \beta(x)$, *where*

$$\begin{aligned} \beta(x) = \quad & -\left(R_{1m} L'^{-1} + R_{2m} \tilde{C}\right)(\varphi - \varphi^*) \\ & -\left(R_{1m} R_{2m} + I_m\right) K_m \tilde{C} (q_1 - q_1^*) \\ & -\left(R_{1m} R_{2m} \tilde{C} + C'^{-1}\right)(Q - Q^*) \\ & +R_{1m} L^{-1} \varphi + C^{-1} Q - r_c L'^{-1} \varphi \end{aligned} \tag{9.32}$$

behaves as the target system (9.27) *with* x^* *(asymptotically) stable.*

Proof. In order to get the control law shown in (9.32), we first define a full rank annihilator $g^\perp$ is

$$g^\perp = \begin{bmatrix} I_m & 0 & 0 & 0 & 0 & 0 \\ 0 & I_{n-m} & 0 & 0 & 0 & 0 \\ 0 & 0 & I_m & 0 & 0 & 0 \\ 0 & 0 & 0 & I_{n-m} & 0 & 0 \\ 0 & 0 & 0 & 0 & 0 & I_m \end{bmatrix}. \tag{9.33}$$

We will not modify the closed-loop interconnection matrix *i.e.*, $J_d = J$. By observing the open-loop system (9.19) and the fact that the fifth column of the annihilator $g^\perp$ defined in (9.33) is zero, one find that the matching conditions do not depend on the φ coordinates. The desired damping matrix can then be defined as

$$R_d = R + R_c \text{ with } R_c = \text{diag}\left[0, \quad 0, \quad r_c, \quad 0\right]. \tag{9.34}$$

This choice of damping matrix leads to the damping injection effect in the closed-loop system without changing any matching condition. We can use a negative damping injection to increase the response time *i.e.* $r_c < 0$. However, in order to guarantee the stability in the closed-loop system, this negative damping injection has a lower bound $r_c > -R_{1m}$.

By setting $H_d(x) = H(x) + H_c(x)$ the matching condition (9.24) leads to the following matching equations

$$\frac{\partial H_c}{\partial p} = \frac{\partial H_c}{\partial q_2} = 0, \tag{9.35}$$

$$-\frac{\partial H_c}{\partial q_1} + K_m \frac{\partial H_c}{\partial Q} = 0, \tag{9.36}$$

$$\frac{\partial H_c}{\partial \varphi} - R_{2m} \frac{\partial H_c}{\partial Q} = 0, \tag{9.37}$$

where $q_1 \in \mathbb{R}^m$, $q_2 \in \mathbb{R}^{n-m}$, $p \in \mathbb{R}^n$, $Q, \varphi \in \mathbb{R}^m$, $K_m = \text{diag}[k_1, k_2, \cdots, k_m] \in \mathbb{R}^{m \times m}$ and $R_{2m} = \text{diag}[1/r_2, 1/r_2, \cdots, 1/r_2] \in \mathbb{R}^{m \times m}$.
We define the desired Hamiltonian as the composition of the desired mechanical potential energy, the desired mechanical kinetic energy and the desired electrical energy

$$H_d(x) = E_d(x) + P_d(x) + H_d^{\varphi}(x) + H_d^{Q}(x). \tag{9.38}$$

From the matching condition (9.35), we find that H_c cannot depend on the momentum variables p. Hence, we define the closed-loop kinetic energy as $E_d(x) = E(x)$. Hence, the only part of the energy that can be modified is $P_d(x)$, $H_d^Q(x)$ and $H_d^{\varphi}(x)$, and more precisely the part that depends on Q, φ and q_1. From the matching conditions (9.36) and (9.37), the desired energy has cross terms between q_1, Q and φ. Hence, we propose the following solution

$$\begin{aligned}
\frac{\partial H_d}{\partial q_1} &= K_1' (q_1 - q_1^*) + \kappa_1 (Q - Q^*) + \kappa_3 (\varphi - \varphi^*) \\
\frac{\partial H_d}{\partial Q} &= C'^{-1} (Q - Q^*) + \kappa_1 (q_1 - q_1^*) + \kappa_2 (\varphi - \varphi^*) \\
\frac{\partial H_d}{\partial \varphi} &= L'^{-1} (\varphi - \varphi^*) + \kappa_2 (Q - Q^*) + \kappa_3 (q_1 - q_1^*)
\end{aligned} \tag{9.39}$$

with K_1', C' and L' the desired stiffness, capacitance and inductance of the closed-system. The constants q_1^*, Q^* and φ^* are the equilibrium position of the closed loop system and κ_i, $i = \{1, 2, 3\}$ are constant cross terms. Now we shall compute the above design parameters such that the desired Hamiltonian satisfies the matching condition (9.36) and (9.37).
Taking (9.39) and the gradient of the open-loop Hamiltonian $\frac{\partial H}{\partial q_1} = K_1 q_1$, $\frac{\partial H}{\partial Q} = C^{-1} Q$ and $\frac{\partial H}{\partial \varphi} = L^{-1} \varphi$ into account, we have that

$$\begin{aligned}
\frac{\partial H_c}{\partial q_1} &= (K_1' - K_1) q_1 - K_1' q_1^* + \kappa_1 (Q - Q^*) + \kappa_3 (\varphi - \varphi^*) \\
\frac{\partial H_c}{\partial Q} &= (C'^{-1} - C^{-1}) Q - C'^{-1} Q^* + \kappa_1 (q_1 - q_1^*) + \kappa_2 (\varphi - \varphi^*) \\
\frac{\partial H_c}{\partial \varphi} &= (L'^{-1} - L^{-1}) \varphi - L'^{-1} \varphi^* + \kappa_2 (Q - Q^*) + \kappa_3 (q_1 - q_1^*)
\end{aligned} \tag{9.40}$$

To find a solution for H_c satisfying (9.40), we select

$$K_1' = K_1 + K_m^2 \tilde{C} \tag{9.41}$$

$$L'^{-1} = L^{-1} + R_{2m}^2 \tilde{C} \tag{9.42}$$

$$\kappa_1 = K_m \tilde{C} \tag{9.43}$$

$$\kappa_2 = R_{2m} \tilde{C} \tag{9.44}$$

$$\kappa_3 = K_m R_{2m} \tilde{C} \tag{9.45}$$

where the matrix $\tilde{C} = \left(C'^{-1} - C^{-1}\right)$ With the above choice, the matching conditions (9.36) and (9.37) are satisfied.

Now we compute the constants K_1', C' and L' such that the closed-loop system is asymptotically stable at the desired equilibrium $\left[q_1^{*T}, Q^{*T}, \varphi^{*T}\right]^T$. From (9.25) it should be verified that

$$\frac{\partial H_d}{\partial x}(x^*) = 0, \quad \frac{\partial^2 H_d}{\partial x^2}(x^*) > 0. \tag{9.46}$$

From the first equation of (9.46), $q_1 = q_1^*$,$Q = Q^*$ and $\varphi = \varphi^*$ satisfy the following relations

$$\begin{aligned} K_1'\left(q_1 - q_1^*\right) + K_m\tilde{C}\left(Q - Q^*\right) + K_m R_{2m}\tilde{C}\left(\varphi - \varphi^*\right) &= 0 \\ C'^{-1}\left(Q - Q^*\right) + K_m\tilde{C}\left(q_1 - q_1^*\right) + R_{2m}\tilde{C}\left(\varphi - \varphi^*\right) &= 0 \\ L'^{-1}\left(\varphi - \varphi^*\right) + R_{2m}\tilde{C}\left(Q - Q^*\right) + K_m R_{2m}\tilde{C}\left(q_1 - q_1^*\right) &= 0 \end{aligned} \tag{9.47}$$

From the open-loop dynamic (9.19), by computing $\dot{x}(x^*, u^*) = 0$, we find that the equilibrium q_1^*, Q^* and φ^* are related as follows

$$Q^* = \frac{K_1 C}{K_m} q_1^*, \quad \varphi^* = \frac{R_{2m} L K_1}{K_m} q_1^*. \tag{9.48}$$

Finally, to guarantee the equilibrium x^* be the strict minimum of the closed-loop Hamiltonian, the Hessian of H_d should be positive definite at the desired equilibrium. Thus the right inequality of (9.46) yields the following condition on the control design parameter C':

$$\begin{aligned} C'^{-1} &\geq C^{-1} - \frac{K_1}{K_m^2}, \quad C'^{-1} \geq \frac{K_m^2 C^{-2}}{K_1 + K_m C^{-1}}, \\ C'^{-1} &\geq \frac{\left(K_m^2 L^{-1} + R_m^2 K_1\right) C^{-2}}{K_1 L^{-1} + K_m^2 L^{-1} C^{-1} + R_m^2 K_1 C^{-1}}. \end{aligned} \tag{9.49}$$

From (9.41) and (9.42) we see that K_1', L' and C' are related. Hence once we choose the parameter C' satisfying the conditions (9.49), the two other parameters are fixed. The proof of the asymptotic stability is straightforward once it is noticed that the desired closed-loop dissipation matrix is equal to the open-loop dissipation matrix, and in particular that the dissipation sub-matrix of the electrical part is full rank. Hence, the asymptotic stability follows in an analog manner as the asymptotic stability of a mass-spring-damper systems (van der Schaft, 2000) by using LaSalle's invariance principle.
Finally from Proposition 8 and the damping injection (9.34), the following control law is obtained:

$$\begin{aligned} \beta(x) = \quad & -\left(R_{1m}L'^{-1} + R_{2m}\tilde{C}\right)\left(\varphi - \varphi^*\right) \\ & -\left(R_{1m}R_{2m} + I_m\right) K_m\tilde{C}\left(q_1 - q_1^*\right) \\ & -\left(R_{1m}R_{2m}\tilde{C} + C'^{-1}\right)\left(Q - Q^*\right) \\ & +R_{1m}L^{-1}\varphi + C^{-1}Q - r_c L'^{-1}\varphi \end{aligned} \tag{9.50}$$

□

The control law (9.32) that corresponds to the general solution of the control problem stated in Proposition 9 is a state feedback. As a consequence its implementation requires the use of an observer. A possible solution consists in choosing the control parameters such that (9.32) can be implemented as an output feedback. Indeed since the output of the PHS model is the electrical current of the actuator *i.e.*, $i = L'^{-1}\varphi$, an appropriate choice of the control parameters leads to an output feedback rather than a state feedback, simplifying its experimental implementation while guaranteeing the global stability.

Proposition 10. *Consider the control law* (9.32) *and assume* R_{2m} *negligible since the resistance in parallel to the capacitor* r_2 *is large enough. Then* (9.32) *becomes a Proportional integral control:*

$$u = -\tilde{C}\int_0^t i(s)ds + \left(K_m\tilde{C} + \frac{K_1 C}{K_m C'}\right) q_1^* - r_c i. \tag{9.51}$$

where $i \in \mathbb{R}^m$ is the measured current.

Proof. We assume the dissipation matrix R_{2m} is negligible then the control law (9.32) becomes:

$$\begin{aligned} u_c &= -R_{1m}L'^{-1}(\varphi - \varphi^*) - K_m\tilde{C}(q_1 - q_1^*) \\ &\quad -C'^{-1}(Q - Q^*) + R_{1m}L^{-1}\varphi + C^{-1}Q \\ &= -R_{1m}\left(L'^{-1} - L^{-1}\right)\varphi - K_m\tilde{C}q_1 - \tilde{C}Q \\ &\quad +K_m\tilde{C}q_1^* + C'^{-1}Q^* \end{aligned} \tag{9.52}$$

Because $L'^{-1} = L^{-1} + R_{2m}^2\tilde{C}$, then $L'^{-1} = L^{-1}$ with $R_{2m} \approx 0$. The above control law becomes

$$\begin{aligned} u_c &= -K_m\tilde{C}q_1 - \tilde{C}Q + K_m\tilde{C}q_1^* + C'^{-1}Q^* \\ &= -\tilde{C}(K_m q_1 + Q) + K_m\tilde{C}q_1^* + C'^{-1}Q^* \end{aligned} \tag{9.53}$$

where q_1, Q and $\varphi \in \mathbb{R}^m$, and is completed by damping injection through

$$u = u_c - r_c\frac{\varphi}{L'} = u^* - r_c i. \tag{9.54}$$

By taking into account the last equation of the complete system (9.19) and $R_{2m} = 0$, one can get:

$$i = y = k_1\dot{q}_1 + \dot{Q} \tag{9.55}$$

and since $Q^* = \frac{K_1 C}{K_m}q_1^*$, the control law (9.53) becomes:

$$u_c = -\tilde{C}\int_0^t i(s)ds + + \left(K_m\tilde{C} + \frac{K_1 C}{K_m C'}\right)q_1^* \tag{9.56}$$

Substituting the former equation in (9.54), we obtain equation (9.51). □

9.4. Identification and experimental validation

For the identification and experimental validation we consider a polyethylene flexible structure equipped with one IPMC actuator. The complete experimental set-up is shown in Figure 9.4.
A dSPACE board and a computer (with Matlab Simulink) is used to generate the control signals $U \in [0, 7\text{V}]$ on the IPMC, to get the measurements and to implement the controller. The measurements are the displacement of the flexible structure and the applied voltage to the IPMC actuator. The displacement is measured by a laser displacement sensor from KEYENCE company (LK-G152).

9.4.1. Identification of the flexible-structure parameters

In this section, we identify the parameters used for the finite dimensional modelling of the flexible structure. The physical parameters related to the considered polyethylene beam are summarized in Table 9.1. It is considered that the flexible structure is composed of four links ($n = 4$) and actuated at the first joint with an IPMC actuator ($m = 1$). The known parameters of the PHS lumped parameter model (9.14) are shown in Table 9.2.
The unknown parameters are the stiffness and the damping coefficients of every joint. We shall assume a uniform beam, hence we assume identical stiffness K_i and damping C_i coefficients. In order to identify these parameters, we measure the displacement at the end of the beam with the laser sensor. The positioning of the laser sensor is at 5 mm from the tip of the flexible structure in equilibrium position.

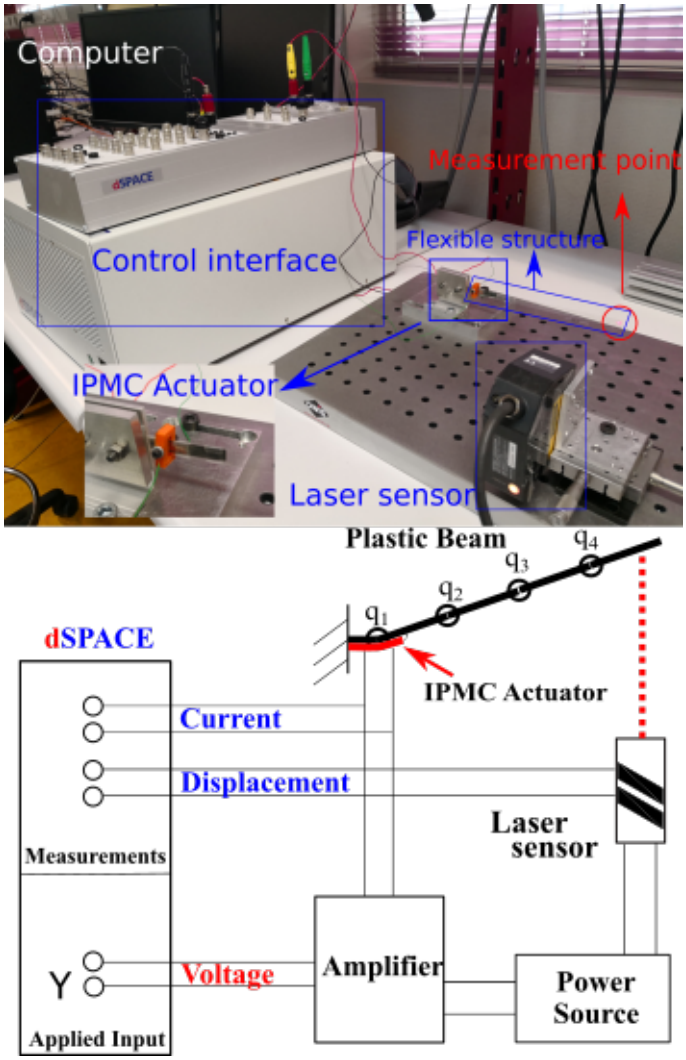

Figure 9.4: Experimental set-up

L	Length	0.16 m
W	Width	7×10^{-3} m
T	Thickness	0.22×10^{-3} m
ρ	mass density	936 kg/m^3

Table 9.1: Physical parameters of the flexible beam

a_i	Length of the $i-$link	4×10^{-3} m
m_i	Mass of the $i-$link	0.58×10^{-4} kg
I_i	Inertia of CoM of the $i-$link	0.77×10^{-8} kg$\cdot$ m^3

Table 9.2: Fixed parameters of the Lumped parameter model

In the current experimental set-up, $n = 4$ and the a_i are given in Table 9.2. The experimental data used to identify the parameters is the displacement, taken at $x_s = 15.5$ cm.
The identification procedure is performed using Sequential Quadratic Programming (SQP) and trust-region-reflective algorithms ('*fmincon*'). These optimal algorithms for non-linear model identification ('*nlgreyest*') are implemented in the Matlab Identification Toolbox®.
The identification result is shown in Figure 9.5 (lhs). The curve fitting of the model simulation with optimally identified parameters (black dashed line) and the experimental data (red solid line) is satisfying, with a fitting percentage of 88.39%. The identified stiffness and damping coefficients are shown in Table 9.3.

K_i	Stiffness of the $i-$joint	10.4×10^{-4} N/m
c_i	Damping of the $i-$joint	7.682×10^{-6} Pa $\cdot$ s

Table 9.3: Identified stiffness and damping coefficients

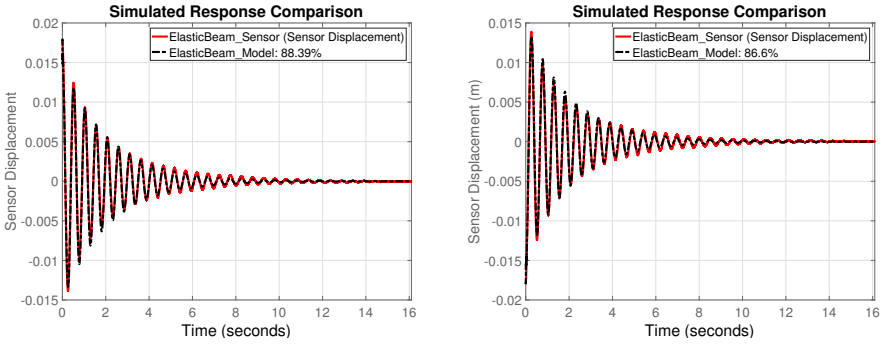

Figure 9.5: (lhs) Parameter estimation with linear stiffness for every joints. The displacement measurement is taken at $x_s = 15.5$ cm. (rhs) Model validation with $x_s = 14$ cm.

To validate the identified model, we measure the displacement at a different point, $x_s = 14$ cm with the different initial position, and compare the measurements with the simulation. The results are shown in Figure 9.5 (rhs). The fitting percentage is 86.6%.

9.4.2. Identification of the IPMC parameters

The physical parameters of the RLC model of the IPMC are given in Table 9.4 (Nishida et al., 2011b; Yim et al., 2006; Gutta et al., 2009).

C	5.8×10^{-2} F
r_1	29.75 Ω
r_2	700 Ω

Table 9.4: Parameters of the IPMC actuator

The movement of the flexible structure is due to the bending of the IPMC when applying a voltage. Two voltages step inputs are applied, first $U_1 = 2$ V at 5 s, and then $U_2 = 4$ V at 20 s. The measure is the displacement at $x_s = 15.5$ cm. An average of several experimental tests is has been performed in order to avoid environmental perturbations as much as possible. The experimental response is

shown in Figure 9.6. One can observe that the flexible structure displaces 6.5 mm and 13.8 mm when applying 2 V and 4 V respectively.

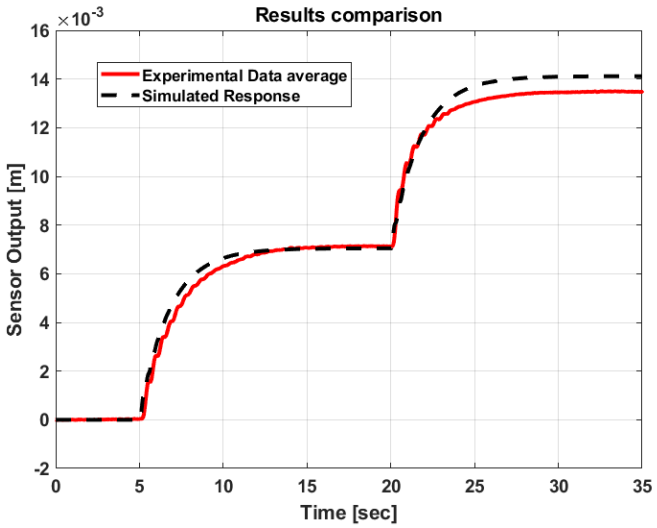

Figure 9.6: IPMC actuation identification for $U_1 = 2$ V and $U_2 = 4$ V.

Using the same identification procedure as in the previous subsection, the coupling parameter is identified as

$$k = 0.98 \times 10^{-5} \mathrm{N \cdot m/V} \tag{9.57}$$

The simulation result is given in Figure 9.6 in red solid line and the experimental data in black dashed line.

Remark 9.4.1. *In the proposed model, the dynamics of the IPMC actuator are simplified to a RLC circuit and the coupling between the actuator and the flexible structure is also simplified to a constant coefficient k. However, the IPMC actuator has a nonlinear electro-stress diffusion dynamic which is not addressed in this chapter. This is why in Figure 9.6, the simulation curve (black dashed line) is slightly different from the experimental data (red solid line) at second 22 s.* ♢

9.5. Control implementation by experimental validation

9.5.1. Flexible structure with one IPMC patch

In this subsection the control strategy of Section 9.3 is applied and experimentally validated on the flexible structure controlled by using one IPMC actuator. The control law (9.51) is cast in the single patch actuation case, and implemented using the voltage as control input to the IPMC. Instead of plotting the angular displacement of the joints, the displacement y_s is plotted since it is the quantity that is experimentally measured by the laser sensor, as explained in the previous section. The reference position is given in terms of y_s. The desired angular position q^* can be computed as

$$q^* = \tan^{-1}\left(\frac{y_s}{x_s - \frac{L}{n+1}}\right) \tag{9.58}$$

where in this case, $y_s^* = 5$ mm, $x_s = 15.5$ cm, $L = 16$ cm and $n = 4$.
The experimental results are shown in Figure 9.7. It is shown that without any damping term the raising time can be drastically reduced up to 1 second. However, in this case, since the response of the controlled system is faster, the high frequency modes of the flexible structure are excited

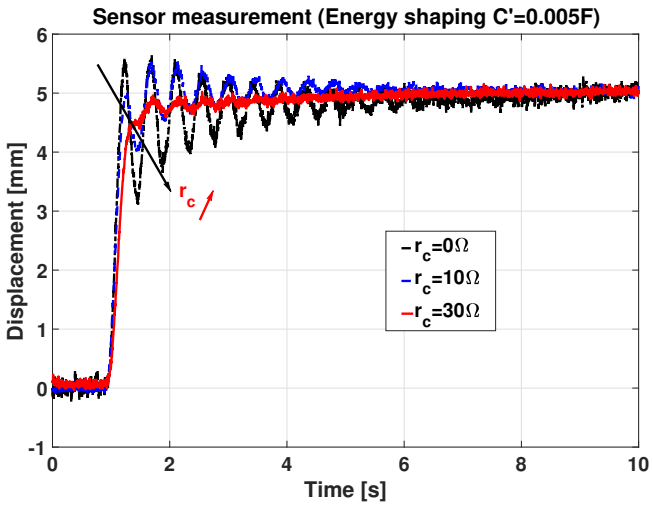

Figure 9.7: Controlled response with energy shaping $C' = 0.005$ F. Response time $\nearrow$ and oscillation $\searrow$ when $r_c \nearrow$

and have a significant oscillatory contribution to the time response (black dashed-dotted line with $r_c = 0\Omega$). The use of damping injection allows to damps this oscillation. In Figure 9.7 one can see that by using the damping term $r_c = 10\Omega$ the step response is less oscillatory (blue dashed line). Finally, a good compromise between oscillations and time response (around 1 second) can be found by choosing $r_c = 30\Omega$ (red solid line).

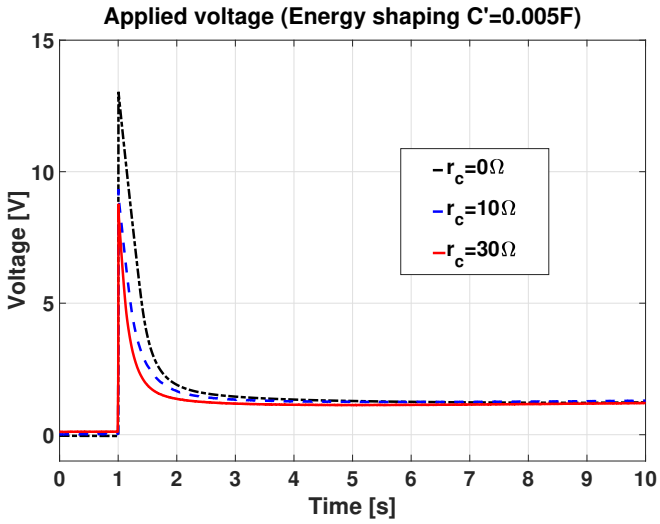

Figure 9.8: Applied voltage with energy shaping $C' = 0.01$ F.

In Figure 9.8, the applied voltage to the IPMC actuator when using control by energy shaping is shown. The controller sends a peak voltage to the IPMC and then decreases until converging to the the steady state position.

9.5.2. Flexible structure with two IPMC patches

In this subsection, we investigate the actuation through two IPMC patches. One patch is placed at the clamped side of the beam as in the previous subsection and the second actuator is placed at the middle of the flexible structure as shown in Figure 9.9.
The control objective of the multi-actuated flexible structure is to reach a desired shape for the structure (as shown at the bottom of Figure 9.9) with guaranteed performances in terms of settling

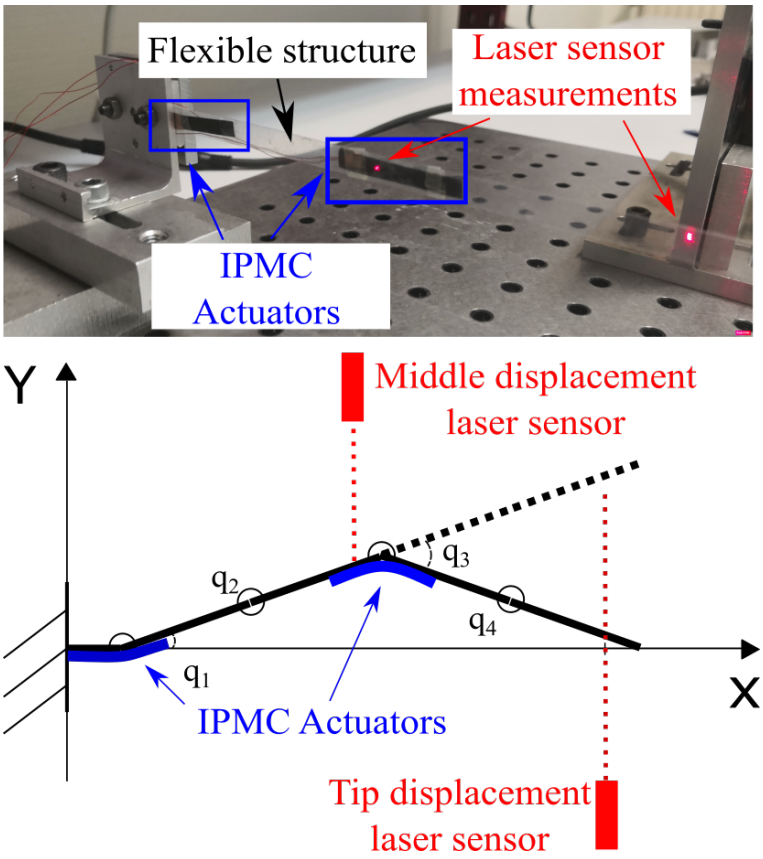

Figure 9.9: Multi-actuation experimental set-up.

time and overshoot. In this case, we propose to use the four links structure to design the controller as it provides a good compromise between acurracy and complexity. The actuation is applied to the the first and the third joint of the structure respectively. Two KEYENCE laser sensors are used to measure the tip displacement and the middle displacement of the flexible structure.
We first move the free end of the structure to the desired position $y_s^* = 5$ mm as in the previous subsection. Then, the desired angular position q_1^* is computed from (9.58) using $y_s^* = 5$ mm. In a second instance, we bring the free end of the structure to the original position $i.e,\ y_s = 0$ by the second IPMC actuator placed at the middle of the structure (third joint). It applies the angular position $q_3^* = -2q_1^*$. Hence the desired angular positions corresponding to the desired shape of the structure are $q^* = \begin{bmatrix} q_1^* & 0 & -2q_1^* & 0 \end{bmatrix}^T$. The control design parameters are $C' = 0.05$ F and $r_c = 30\Omega$ for both actuators.
In Figure 9.10, the tip and middle displacement measurements are shown. The red dashed curve is the tip displacement and the blue solid curve is the measurement from the middle laser sensor. First the control law (9.51) is used to drive the clamped side IPMC actuator such that the tip of the structure moves to the desired position 5 mm and then at 6 seconds, we control the second IPMC actuator placed at the middle of the structure to drive the tip to its original place. One can observe that the tip displacement (red dashed curve) first goes to the desired position and then goes back to 0 at 6 seconds. The middle of the flexible structure (blue solid line) first goes to 2.5 mm and does not move anymore apart from a small oscillation at 6 seconds when the second IPMC is actuated.

9.6. Summary

This Chapter presents a lumped model and control strategy for a class of 1-D IPMC actuated flexible structure using the PHS framework. The developed model effectively replicates the primary behavior

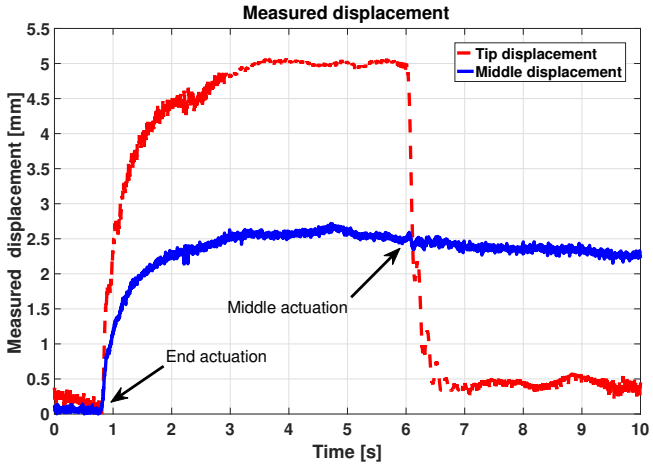

Figure 9.10: Tip and middle displacements.

of IPMC actuated endoscopes, with a notable feature of being easily scalable. The control strategy is rooted on IDA-PBC, and takes into account the electro-mechanical coupling in the design of the closed-loop Hamiltonian function. The cross terms result in non-trivial matching conditions which are solved by using a set of auxiliary control design parameters. The resulting controller allows to modify the closed-loop equilibrium and shape the closed-loop Hamiltonian.
An experimental set-up has been employed to test and validate the proposed model and control strategy. This experimental set-up replicates the main properties of a compliant bio-medical endoscope process. The comparison between the simulations and the experimental data demonstrates that the model replicates the experimental response in a satisfactory way. Two control strategies are implemented, one which only changes the closed-loop equilibrium and a second one which also shapes the closed-loop energy function. Both controllers asymptotically stabilize the system. It has been shown by means of simulations and experimental tests that by modifying the closed-loop Hamiltonian function the closed-loop response can be effectively tuned and rendered faster. Furthermore, the flexible structure is actuated by two IPMC patches which allow to get a desired configuration of the structure.

Chapter 10

Modeling and control of HASEL actuator

10.1. Introduction

In the recent years, the Hydraulically Amplified Self-Healing Electrostatic (HASEL) actuator has provided a new road-map for the design of soft actuators (Acome et al., 2018). By combining the design concept of dielectric elastomer actuators and fluidic-driven soft actuators, more desirable features of HASEL actuators are indicated (Rothemund et al., 2020a) including self-sensing and self-healing capabilities and great potential for many applications, such as: HASEL artificial muscles made from elastomers, elastomeric donuts, quadrant donuts and curling HASEL actuators (Rothemund et al., 2020b), soft grippers (Acome et al., 2018) and soft-actuated joints created based on the hydraulic mechanism used in spider legs (Kellaris et al., 2021). One of the advantages of the HASEL actuator is that it is easy to manufacture, low cost, and open to many potential design based on its working principle (Kellaris et al., 2018). The authors of (Mitchell et al., 2019) present an easy to implement toolkit to design and fabricate multiple HASEL actuators incorporating electrostatic zipping mechanisms and reducing operating voltages. Several attempts to model and control the HASEL actuator have recently been proposed. In (Kellaris et al., 2019), the geometrical analysis of HASEL is investigated. In (Johnson et al., 2020), an identification of a nonlinear HASEL actuator model has been presented and the controller design using the self-sensing strain is addressed with a basic control approach. In (Liu et al., 2021a), the planar HASEL actuator model is investigated to describe the relationship between the output force and the applied voltage. These works reveal that the modeling and control of complex mechanical structure with fluid structure interaction is very hard and challenging. Only few studies on control-oriented modeling and control design has been proposed in the literature (Johnson et al., 2020).

To overcome these constraints, this work proposes a physically based dynamic model and a control strategy for HASEL actuators using the port Hamiltonian (PH) approach. This approach (Maschke and van der Schaft, 1992) has proven to be powerful for the modeling and control of complex multi-physical systems. PH modeling is based on the characterization of energy exchanges between the different components of the system. This approach is particularly adapted for the modular modeling of multi-physical systems. On the other hand, the PH approach is well suited passivity based control design with clear physical interpretation, such as energy shaping and control by interconnection and damping assignment (IDA-PBC) (Ortega et al., 2002).

The main contributions of this work are the proposition of a PH model to describe the dynamics of the HASEL actuator and the position control strategy based on the IDA-PBC method. The geometry of the HASEL pouch is investigated and based on this analysis, a PH dynamic model is established using a non linear spring-damper system to approximate the mechanical behavior of the flowing liquid in the pouches. A control law based on IDA-PBC method is employed to achieve the desired equilibrium position. Furthermore an integral action is added to the previous controller to

cope with the uncertainties in the load mass. The proposed PH model is identified and validated by an experimental setup and the proposed control method is also validated by the same experimental setup which is described in Fig. 10.4.
This Chapter is organized as follow: Section 10.2 presents the geometry analysis and the PH modeling of the HASEL actuator. The IDA-PBC based position control and integral action are proposed in Section 10.3. In Section 10.4, the experimental setup and the parameters identification are presented. The proposed control laws is experimentally validated and the results are discussed in Section 10.5. The summary of this chapter is given in Section 10.6.

10.2. Port Hamiltonian modeling of HASEL actuator

In the following sections, the geometric constraints of the system are introduced. All the geometric variables can be interpreted as function of the endpoint displacement q (the geometry of HASEL actuator is shown in Fig 10.1b), the partial derivative of these variables are naturally derived and which is essential for the PH model.

10.2.1. Geometry description of HASEL actuator

We first introduce the HASEL unit, which is a simplified geometric model to approximate the real actuator. Unlike an ellipse geometric shape presented in (Rothemund et al., 2020b), we use a diamond shape to describe the unit pouch of the HASEL actuator as shown in Fig. 10.1a.

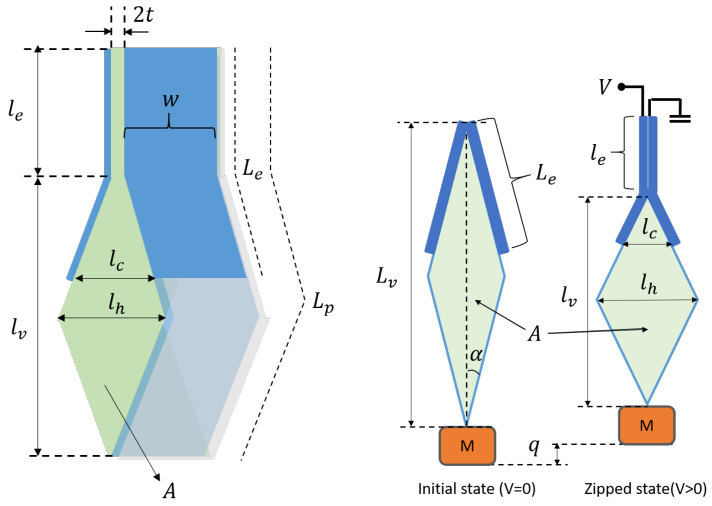

(a) (b)

Figure 10.1: (a) The geometry of HASEL unit; (b) Deformation description of the actuator

The HASEL unit is composed of a pouches filled with dielectric liquid, and equiped with a pair of electrodes covering the two polymer films. The parameters of the actuator include:

- L_p the length of pouches;
- w the width of pouches and electrodes;
- L_e the length of paired electrodes;
- L_v the initial length of actuator;
- A the cross-sectional area of pouches;
- t the thickness of dielectric film.

When we apply the voltage to the actuator, the Maxwell force zips the pair of electrodes which leads to the deformation of actuator. We define the geometric variables due to the deformation as follows:

- l_e the length of the zipped electrodes;
- l_h the height of the pouches;
- l_v the length of the unzipped pouches;
- l_c the distance between the endpoints of the paired electrodes.

In this work, we make two assumptions for the actuator during its deformation: 1) the cross-section area A is constant because the dielectric liquid is incompressible, and 2) the length of the pouch L_p is constant because the membrane is inextensible. The objective is to find how the displacement q relates to the geometry of the HASEL unit. From the deformation of the actuator, we can write the geometrical relationship to achieve the different variables. The actuator endpoint displacement is defined as:

$$q = L_v - (l_e + l_v) = \Omega(l_e) \tag{10.1}$$

Since the cross-sectional area is assigned to a diamond shape, the following geometry relationship holds:

$$\begin{aligned} A &= \frac{l_v l_h}{2} \\ (L_p - l_e)^2 &= l_v^2 + l_h^2 \end{aligned} \tag{10.2}$$

By substituting the first equation of (2) to the second one, we can present the height l_h and the width l_v as the function of l_e as following:

$$l_h = \sqrt{\frac{(L_p - l_e)^2}{2} - \sqrt{\frac{(L_p - l_e)^4}{4} - 4A^2}} \tag{10.3}$$

$$l_v = \sqrt{\frac{(L_p - l_e)^2}{2} + \sqrt{\frac{(L_p - l_e)^4}{4} - 4A^2}} \tag{10.4}$$

Then we can substitute the above equation to Eq. (10.1) and the length of the zipped electrodes l_e can be presented as a function of the actuator endpoint displacement q:

$$l_e(q) = \Omega^{-1}(q) \tag{10.5}$$

Finally, the geometric constraints of the actuator can written as a function of the displacement q. The more precise geometric analysis of the actuator has been made based on the ellipse shape in (Kellaris et al., 2019; Moretti et al., 2018). In this work, we have chosen the the diamond shape for the dynamic modeling, because it is a good compromise between the accuracy of the model and its simplicity of the geometric analysis. All the geometric variables can be expressed in the function of q with the diamond shape assumption. However, in the ellipse shape case, it is not easy to present or compute all the geometric variables in the function of q.

10.2.2. PH Formulation of HASEL

In this part, we derive a dynamic model of the HASEL actuator by using the PH framework. The main idea is the use of spring damper systems to describe the mechanical properties of the dielectric liquid in pouch. The motivation is from the observation of the physical properties during the actuator deformation: 1) the displacement of the liquid and the constraints on the structure cause the resistance to the deformation, and 2) the actuator returns to its initial state (position) when the voltage is switched off. These properties imply that the mechanical properties of the flowing

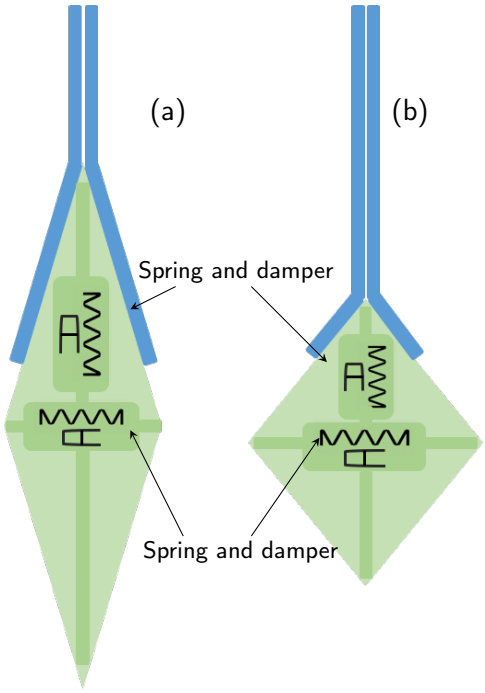

Figure 10.2: (a) Initial state when load is placed at the end; (b) The deformed state with zipped part of electrodes.

dielectric liquid can be described by a spring-damper system. In this work, we propose two spring-damper systems places in the vertical and horizontal directions of the actuator, as shown in Fig. 10.2.

To model the dynamics of the actuator, we first introduce its Hamiltonian function (energy function) which is composed by the mechanical energy and the electric energy. The total mechanical energy is the sum of the kinetic and the potential energy. The potential energy of the spring system is written as

$$H_s(q) = \frac{1}{2}k_v(q)\Delta\xi_v(q)^2 + \frac{1}{2}k_h(q)\Delta\xi_h(q)^2 \tag{10.6}$$

where $\Delta\xi_v(q)$, $\Delta\xi_h(q)$ are the deformation of the springs in the vertical and horizontal directions, and $k_v(q)$, $k_h(q)$ are the coefficients of the nonlinear springs. The deformation of the springs are defined as

$$\begin{aligned} \Delta\xi_v(q) &= l_v(q) - \xi_v(m) \\ \Delta\xi_h(q) &= l_h(q) - \xi_h(m) \end{aligned} \tag{10.7}$$

where ξ_v, ξ_h are the original length of the springs. In this work, the original length of the springs are designed as nonlinear functions depending on the load mass m. Because the geometry constrains limit initial states of the actuator, no matter how heavy the load is applied to the actuator, the initial states should remain the same. From a physical point of view, it can be explained by the fact that the uncompressible dielectric liquid generates an equivalent inner pressure to resist to the external force from the load and maintains the actuator in the initial geometry.

The electric energy of the capacitance between the paired electrodes is

$$H_c(q, Q) = \frac{1}{2}\frac{Q^2}{C(q)} \tag{10.8}$$

where Q is the charge of the capacitor and C is the capacitance value. While C depends on q, its computation can be split into two parts: the zipped region and unzipped region. The capacitance in the zipped region can be described by

$$C_z(q) = \frac{\epsilon_r\epsilon_0 w}{2t}l_e(q) \tag{10.9}$$

For the unzipped region, it is approximated by the capacitance between two unparalleled plates

$$C_{uz}(q) = \int_0^{(L_e - l_e)\cos(\alpha)} \frac{\epsilon_r \epsilon_0 w \tan(\alpha)}{2t + 2x\tan(\alpha)} dx \tag{10.10}$$

As a result, the total capacitance is

$$C(q) = C_z(q) + C_{uz}(q) \tag{10.11}$$

Then including the kinetic energy of the load and the potential energy related to the gravity, the Hamiltonian function, *i.e.* the total energy of the system can be described as:

$$H(q,p,Q) = H_s(q) + H_c(q,Q) + \frac{1}{2}\frac{p^2}{m} + mgq \tag{10.12}$$

where the p is the momentum of the load and g is the gravity constant. By choosing the energy variables as the state variables $x = [q,p,Q]^T$. The co-energy variables e are:

$$e = \begin{bmatrix} \frac{\partial H}{\partial q} \\ \frac{\partial H}{\partial p} \\ \frac{\partial H}{\partial Q} \end{bmatrix} = \begin{bmatrix} \frac{\partial H_c}{\partial q} + \frac{\partial H_s}{\partial q} + mg \\ \frac{p}{m} \\ \frac{Q}{C(q)} \end{bmatrix} \tag{10.13}$$

where $\frac{\partial H}{\partial q}$ stands for the total force working on the load in the q direction, resulting from the sum of the spring force working on the load $\frac{\partial H_s}{\partial q}$, the force from capacitance $\frac{\partial H_s}{\partial q}$ and the gravity force mg.
With the above variables, the dynamics of the actuator can be presented by the following PH formulation:

$$\begin{bmatrix} \dot{q} \\ \dot{p} \\ \dot{Q} \end{bmatrix} = \underbrace{\begin{bmatrix} 0 & 1 & 0 \\ -1 & -b(q) & 0 \\ 0 & 0 & -1/r \end{bmatrix}}_{(J-R)} \begin{bmatrix} \frac{\partial H}{\partial q} \\ \frac{\partial H}{\partial p} \\ \frac{\partial H}{\partial Q} \end{bmatrix} + \underbrace{\begin{bmatrix} 0 \\ 0 \\ 1/r \end{bmatrix}}_{g} V \tag{10.14}$$

where the interconnection matrix $J = -J^T$ represents the energy exchanges in the system, while the damping matrix $R = R^T = \text{diag}\begin{bmatrix} 0 & b(q) & 1/r \end{bmatrix} \geq 0$ describes the internal dissipation of the system with $b(q)$ the nonlinear damping coefficient depending on the vertical and horizontal damper and r the resistance of the actuator. Let choose the current, the power conjugate variable of the input, as the output $y = g^T \frac{\partial H}{\partial x} = i$, the system is passive, since the Hamiltonian is such that $H > 0$ and $H(0) = 0$, moreover its time derivative satisfies:

$$\dot{H} = -\frac{\partial H}{\partial x}^T R \frac{\partial H}{\partial x} + y^T u \leq y^T u. \tag{10.15}$$

10.3. Position control design

In this work, the objective is to control the end position of the HASEL in closed loop. Based on the PH model proposed in the previous section, the IDA-PBC method (Theorem 8) will be investigated to control the position of the actuator. The IDA-PBC method provides several degrees of freedom to assign the closed-loop equilibrium position and performance with clear physical interpretation from energy point of view (Ortega et al., 2002). Furthermore, a structure preserving integral action will be added to improve the robustness of the control law while guaranteeing the closed-loop stability.

10.3.1. Application to HASEL actuator position control

To apply the IDA-PBC design procedure on the HASEL actuator position control, we firstly consider the open loop system (10.14) and define the desired closed-loop Hamiltonian function

$$H_d(p,q,Q) = \frac{k_p}{2}(q-q^*)^2 + \frac{1}{2}\frac{p^2}{m} + \frac{k_Q}{2}(Q-Q^*)^2 \tag{10.16}$$

where q^* and Q^* are the desired equilibrium position and charge of capacitance, and the asymptotically stable PH target system corresponds to (9.23) with

$$J_d = \begin{bmatrix} 0 & J_{12} & \alpha_1 \\ -J_{12} & 0 & \alpha_2 \\ -\alpha_1 & -\alpha_2 & 0 \end{bmatrix}, R_d = \begin{bmatrix} 0 & 0 & 0 \\ 0 & r_1 & 0 \\ 0 & 0 & \frac{1}{r} \end{bmatrix}$$

where α_1, α_2 are the frees variable to be designed. By defining the full rank left annihilator $g^\perp = \begin{bmatrix} -1 & 0 & 0 \\ 0 & 1 & 0 \end{bmatrix}$, the matching equation (9.24) leads to

$$\begin{aligned} J_{12}(q,p,Q) &= 1 - \alpha_1 \frac{m}{p} k_Q (Q-Q^*) \\ r_1(q,p,Q) &= b + \frac{m}{p}\left(\frac{\partial H}{\partial q} - J_{12} k_p (q-q^*) - \right. \\ &\qquad \left. - \alpha_2 k_Q (Q-Q^*)\right) \end{aligned} \tag{10.17}$$

which are the variable depending on the state variables q, p, Q. The desired equilibrium of the system is $x^* = \left[q^*, 0, Q^*\right]$. To make sure the closed loop system is asymptotically stable, the parameter $r_1 \geq 0$ which implies

$$Q^* \geq \frac{\alpha_2 k_Q Q - \kappa}{\alpha_2 k_Q} \tag{10.18}$$

where $\kappa = b + \frac{m}{p}(\frac{\partial H}{\partial q} - J_{12} k_d (q-q^*))$ According to equation (9.26), the control law of closed-loop system is

$$\beta(x) = -\alpha_1 r k_p (q-q^*) - k_Q (Q-Q^*) + \frac{Q}{C(q)} - \alpha_2 r \frac{p}{m} \tag{10.19}$$

10.3.2. Integral Action (IA) for robustness

The main drawback of the controller proposed in the previous section is the lack of robustness to overcome the steady state error due to the external disturbance or the unmatched mass of load. To improve the robustness, the integral action control (Ferguson et al., 2017) based on the IDA-PBC method is applied in this subsection.

The uncertainties of the load can be interpreted as external force applied on the system. Hence, the closed-loop system in the previous section can be expressed as

$$\begin{bmatrix} \dot{Q} \\ \dot{p} \\ \dot{q} \end{bmatrix} = \left[J_d(x) - R_d(x)\right] \begin{bmatrix} \frac{\partial H}{\partial Q} \\ \frac{\partial H}{\partial p} \\ \frac{\partial H}{\partial q} \end{bmatrix} + \begin{bmatrix} 0 \\ d \\ 0 \end{bmatrix} \tag{10.20}$$

where the matrices $J_d(x)$ and $R_d(x)$ are defined as

$$J_d(x) := \left[\begin{array}{c|c} J_{aa}(x) & J_{au}(x) \\ \hline -J_{au}^T(x) & J_{uu}(x) \end{array}\right] = \left[\begin{array}{c|cc} 0 & -\alpha_1 & -\alpha_2 \\ \hline \alpha_1 & 0 & -J_{12} \\ \alpha_2 & J_{12} & 0 \end{array}\right]$$

$$R_d(x) := \left[\begin{array}{c|c} R_{aa}(x) & R_{au}(x) \\ \hline -R_{au}^T(x) & R_{uu}(x) \end{array}\right] = \left[\begin{array}{c|cc} \frac{1}{r} & 0 & 0 \\ \hline 0 & 0 & 0 \\ 0 & 0 & r_1 \end{array}\right]$$

and d is a unknown constant external force (disturbance) to the system that depends on the unknown load. According to (Ferguson et al., 2017), if we choose the new closed-loop Hamiltonian function H_{cl}

$$H_{cl} = H_d + \frac{K_i}{2}\|Q - x_c\|^2, \tag{10.21}$$

we can derive the new closed-loop Hamiltonian system

$$\left[\begin{array}{c} \dot{x}_a \\ \hline \dot{x}_u \\ \hline \dot{x}_c \end{array}\right] = \Big[J_{cl}(x) - R_{cl}(x)\Big] \left[\begin{array}{c} \frac{\partial H_{cl}}{\partial x_a} \\ \hline \frac{\partial H_{cl}}{\partial x_u} \\ \hline \frac{\partial H_{cl}}{\partial x_c} \end{array}\right] + \left[\begin{array}{c} 0 \\ \hline d \\ \hline 0 \\ \hline 0 \end{array}\right]. \tag{10.22}$$

Thus the control law of the integral action is

$$\begin{aligned} u_i = &\Big[-J_{aa} + R_{aa} + J_{c_1} - R_{c_1} - R_{c_2}\Big]\frac{\partial H_d}{\partial x_a} \\ &+ \Big[J_{c_1} - R_{c_1}\Big] K_i(x_a - x_c) + 2R_{au}\frac{\partial H_d}{\partial x_u} \end{aligned} \tag{10.23}$$

$$\dot{x}_c = -R_{c_2}\frac{\partial H_d}{\partial x_a} + (J_{au} + R_{au})\frac{\partial H_d}{\partial x_u} \tag{10.24}$$

where x_c is the state of integral action. In this work, we choose the following design of matrices:

$$J_{c_1} = 0,\ R_{c_1} = \frac{1}{r},\ R_{c_2} = 0 \tag{10.25}$$

and the interconnection and damping matrices given by

$$\begin{aligned} J_{cl} &:= \begin{bmatrix} 0 & J_{au}(x) + R_{au}(x) & 0 \\ -(J_{au}^T(x) + R_{au}^T(x)) & J_{uu}(x) & 0 \\ 0 & 0 & 0 \end{bmatrix} \\ R_{cl} &:= \begin{bmatrix} 1/r & 0 & 1/r \\ 0 & R_{uu}(x) & 0 \\ 1/r & 0 & 1/r \end{bmatrix}. \end{aligned} \tag{10.26}$$

Then the following integral control law and the controller state can be derived:

$$u_i = \frac{1}{r}K_i(Q - x_c) \tag{10.27}$$

$$\dot{x}_c = -\alpha_1 k_p(q - q^*) - \alpha_2\frac{p}{m} \tag{10.28}$$

where K_i is the gain of the integral action need to be designed. Combining the IDA-PBC (10.19) and Integral action (10.27), we can implement the controller as the block diagram in Fig. 10.3.

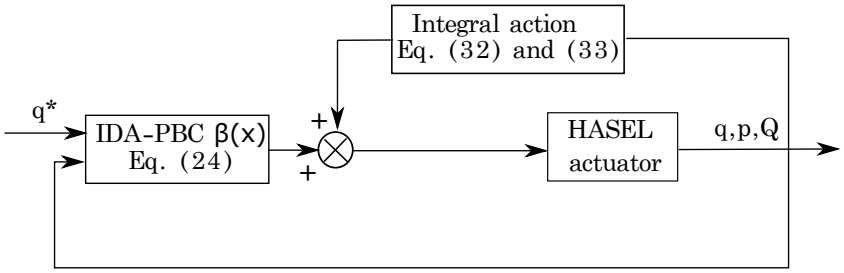

Figure 10.3: Block diagram of closed-loop control with integral action

10.4. Experiment Description and Identification

10.4.1. Experiment Setup

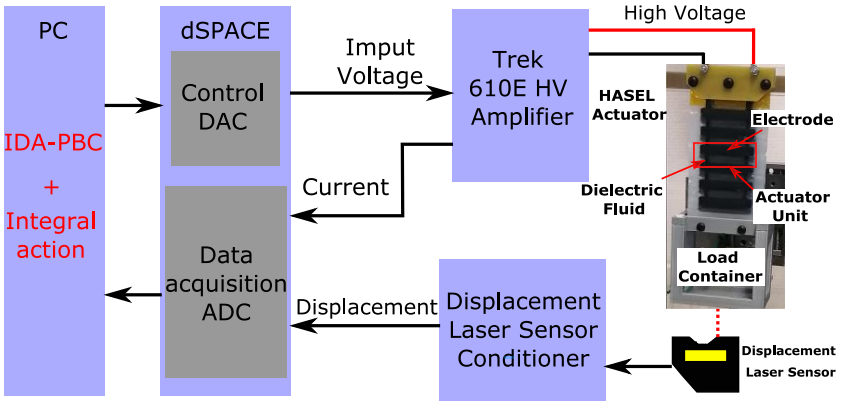

Figure 10.4: Experimental setup description

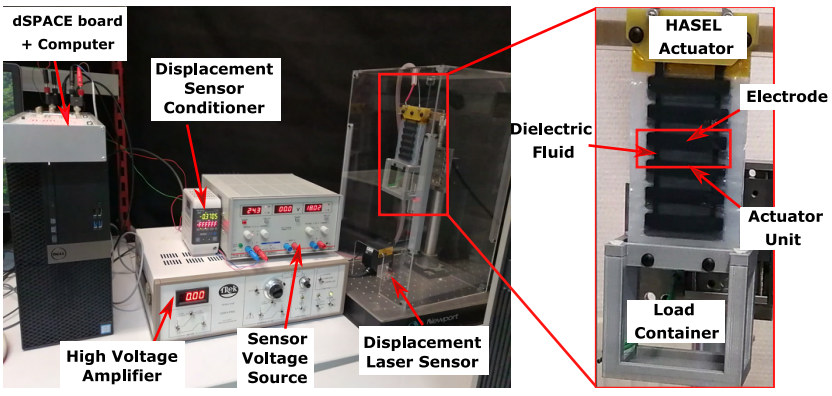

Figure 10.5: Experimental setup

The real-life experimental setup is shown in Fig. 10.5 and can be presented by the scheme shown in Fig. 10.4. This experimental setup is composed of the following elements:

- The actuator used in this study is composed of 5 C-5015 HASEL actuators that were manufactured by *Artimus Robotic*®. A 3-D printed load container is attached to the bottom of the actuator to simplify the load change during the manipulation.

- A $Trek^{®}610E$ high voltage amplifier is used to linearly amplify $0-10V$ input signal to $0-10KV$ output voltage with guaranteeing the current up to $2mA$ which provides sufficient driven power for the actuator motion. This amplifier can also return the current measurement in real-time during the manipulation.
- A $Kenyence^{®}$LK-G152 laser sensor is used to measure the actuator displacement. The sensor is tuned to have $10kHz$ of bandwidth and $\pm 4cm$ measurement range which are large enough to track the dynamics of the actuator and to validate the proposed control law.
- A computer with $Matlab\ Simulink^{®}$is used to generate the reference signals, to implement the proposed controller and to get the measurement data.
- A $dSPACE\ board\ (dS1104)$ serves the signals converters interface such as DAC (digital analogic converter) between the computer and the actuator and the ADC (analogic digital converter) between experimental sensor measurement (displacement and current) and the computer.

10.4.2. Model Identification and Validation

For the model identification and the experimental validation, we conduct experiments with different loads ($m = 150g,\ 200g,\ 250g$) and different applied voltages ($V = 4kV,\ 5kV,\ 6kV$) to obtain the experimental data of the displacement q and the electrical charge Q. The objective of identification is to find the proper coefficients of the spring-damper systems which approximate the dynamics of dielectric liquid of the HASEL actuator. From the system (10.14), we can obtain the mechanical force of the HASEL actuator as $F_m = \frac{\partial H_s}{\partial q} + F_d = \dot{p} - \frac{\partial H_c}{\partial q} - mg$ with $F_d = b(q)\frac{p}{m}$. Thus the identification problem becomes to find the optimal solution for the original length, the stiffness of the springs and the damper coefficients such that the difference between the mechanical force F_m and the measured force F_e is minimum.

Table 10.1: HASEL actuator's parameters

Parameter	**Value**	**Units**
L_p	0.012	m
L_e	0.06	m
w	0.05	m
t	18×10^{-6}	m
ϵ_0	8.85×10^{-12}	F/m
ϵ_r	2.2	F/m
r	8000	Ω

The coefficients are nonlinear and defined as the first order polynomial form:

$$\begin{aligned} \xi_i(m) &= \phi_1^j m + \phi_0^j \\ k_i(q) &= \theta_1^j q + \theta_0^j \\ b_i(q) &= \lambda_1^j l_i(q) + \lambda_0^j \end{aligned} \tag{10.29}$$

where $j = v, h$ stands for the vertical and horizontal directions. The length of the springs is the function of the load m with coefficients ϕ_n^j, the stiffness and the damper are the function of deformation with coefficients θ_n^j and λ_n^j. The identification problem is solved by the nonlinear

model identification ('*nlgreyest*') and the trust-region-reflective algorithm ('*fmincon*') which are implemented in Matlab Identification Toolbox®.

The experimental data of the mechanical force used for the parameters identification are shown by the blue curve in Fig. 10.6. Using the identification toolbox as mentioned before, one can get the identified parameters. Then the model simulation result with the identified parameters is compared to the experimental data in Fig. 10.6. The curve fitting has a very high percentage (fit $= 94\%$) where fit $= \left[100\left(1 - \frac{\|y_{exp} - y_{sim}\|}{\|y_{exp} - mean(y_{exp})\|}\right)\right]$ % with the experimental data y_{exp} and the model simulation result y_{sim}.

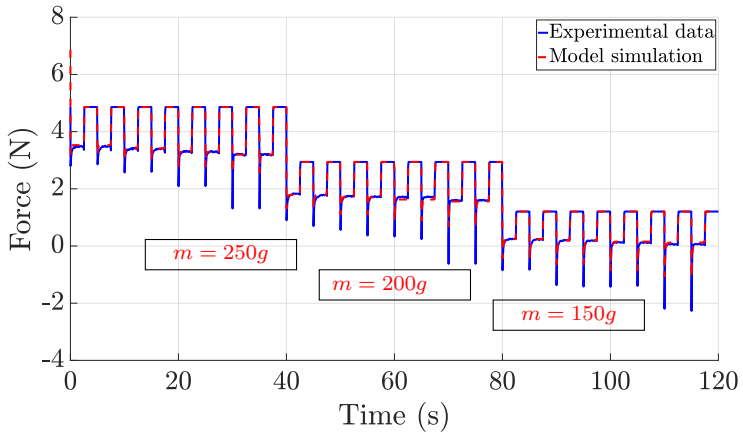

Figure 10.6: Mechanical force identification (Fitness: 94%)

In order to verify the previous identified parameters, the actuator position response in the simulation is also compared to the experimental position data as shown in Fig. 10.7 with high fitness (88%). Meanwhile, the model with the identified parameters provides high fitness both in position and force response in the case of the different loads and the different applied voltages. These results suggest that the proposed model is able to describe the dynamics of the HASEL actuator.

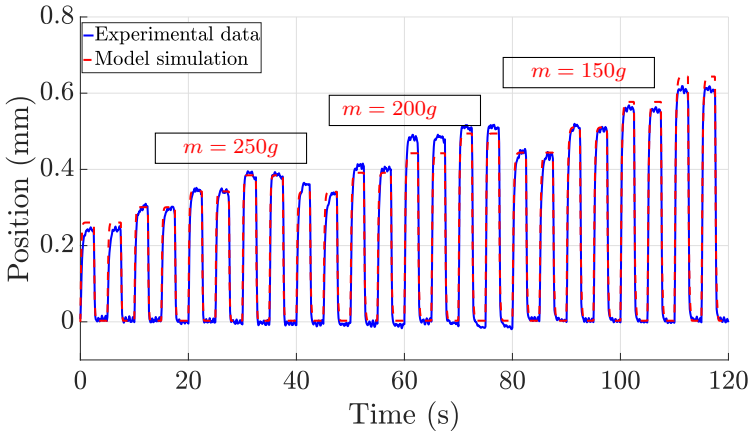

Figure 10.7: Position identification (Fitness: 88%)

10.5. Control implementation

In this section, we implement the proposed IDA-PBC controller (10.19) and the Integrate action (10.27) to the actuator with identified parameters to get the desired positions. Fig. 10.8 shows the closed loop responses with IDA-PBC controller with $k_p = 4$, $k_Q = 2$ and $\alpha_2 = 0.1$ (blue dashed line) and IDA-PBC + IA controller with $K_i = 1$ (red solid line) which follow the desired position defined as the successive ramp reference between $[0.5\text{mm}, 3, 5\text{mm}]$ (black dotted line). From Fig. 10.8, the closed loop responses with and without IA controller both follow the reference in a satisfactory way and the the difference is not easy to see. The relative error ($e_r = \frac{\text{absolute error}}{\text{reference}}$) of the closed-loop responses are 3% to 5% with and without IA controller.

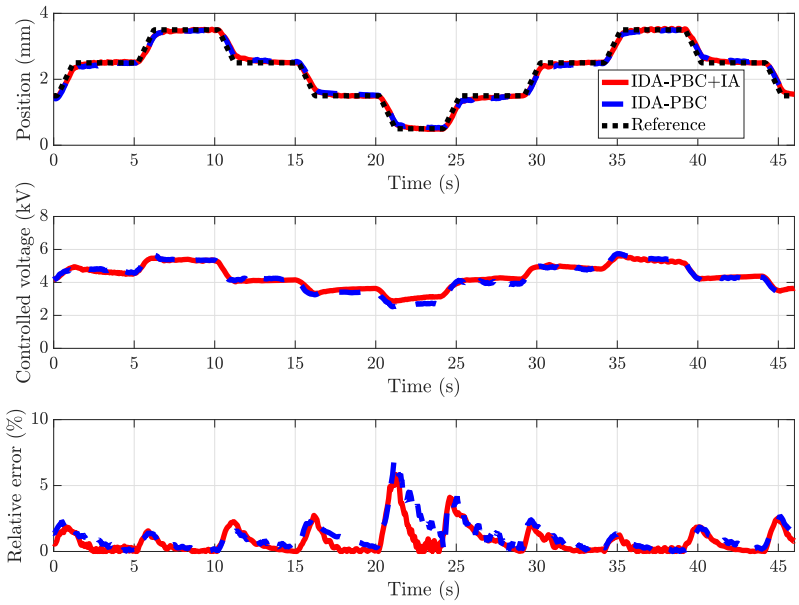

Figure 10.8: Position control with the successive ramp reference signal (Upper figure); Control voltage (Middle figure); Relative error e_r (Bottom figure)

In Fig 10.9, we use a sinusoidal reference signal to define the desired position. The signal frequency is 0.2Hz and the signal range is $[0.5\text{mm}, 2\text{mm}]$ (black dotted line). In this case, we only use the IDA-PBC + IA controller to control the actuator. The experimental result shows the closed loop response (red solid line) follows well the reference (upper figure). The maximal error of the signal tracking is around 0.1mm and with 4% relative error.

In Figure 10.10, we show the effectiveness of the proposed IDA-PBC+IA controller to the frequency position assignment. The desired position is defined by the sinusoidal reference with 1 Hz, 3 Hz, 5 Hz, 7 Hz. We can see the proposed controller can guarantee the position assignment with different frequencies.

From Fig. 10.8, one can observe that the IA does not significantly improve the closed loop performance. But as mentioned before, the purpose of using IA is to improve the robustness of the controller to the unknown load disturbance. In Fig. 10.11, we show the robustness improvement with the IA (red solid line) compared to the IDA-PBC controller without IA (blue dotted line). We assign the desired position to 2mm and 0.5mm. A 100g load mass is added in the load container when the actuator position at 2mm and removed when the position at 0.5mm. we can see that the closed loop position is disturbed when we add or remove the load mass for both controllers. The

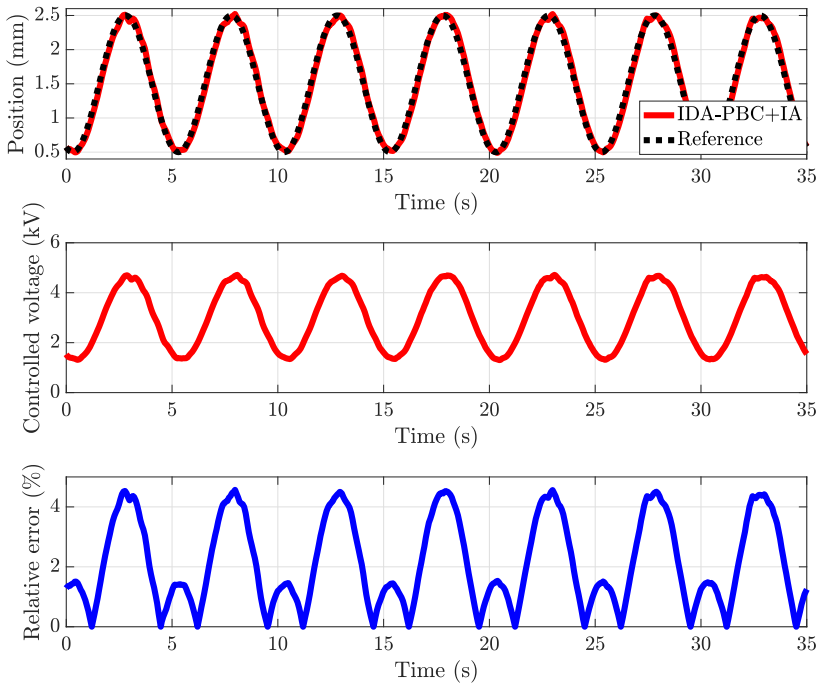

Figure 10.9: Position control with the sinusoidal signal (Upper figure); Control voltage (Middle figure); Relative error e_r (Bottom figure)

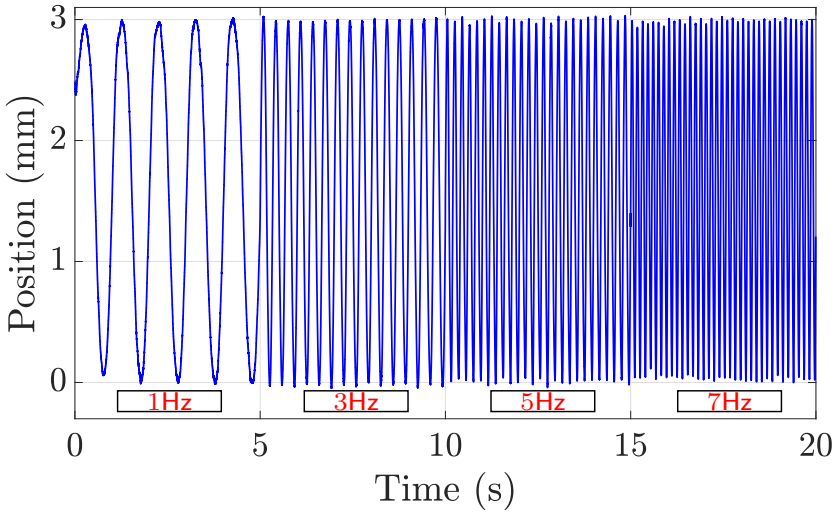

Figure 10.10: Position responses of the sinusoidal signal with 1 Hz, 3 Hz, 5 Hz, 7 Hz, respectively.)

IDA-PBC can not reject this external disturbance while the closed loop response with IDA-PBC+IA controller goes back to the desired position as expected.

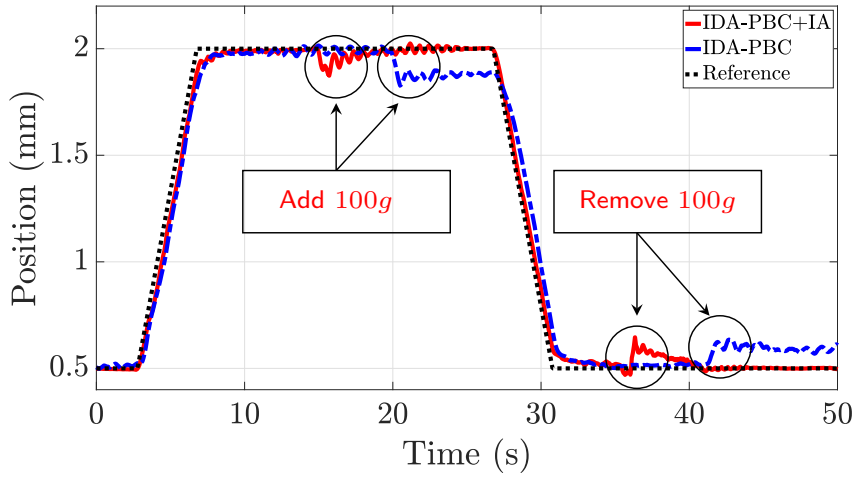

Figure 10.11: Disturbance rejection with Integral Action on the IDA-PBC controller

10.6. Summary

In this Chapter, we propose a dynamic model of an HASEL actuator via the PH approach. The mechanical behavior of the actuator is approximated by two perpendicular nonlinear spring-damper systems. The proposed model reproduces the main dynamic behavior of the actuator. The experimental results show that the proposed model is sufficiently accurate to cope with the main system dynamics (up to 94% fitness). Based on the proposed model, the IDA-PBC method is investigated for the positioning control of the actuator. Further integral action is added to cope with load uncertainties. The experimental closed loop responses validate the proposed control laws to different desired position references with the relative error less than 5%. This work is the first attempt to the control-oriented modeling and control design of the HASEL actuator taking the advantage of the PH approach. In the future, the dynamic modeling and control design for more complex structures based on the HASEL actuator will be investigated. The high speed position control design and the controller parameters tuning problem will be considered in the future.

Chapter 11

Conclusion of Part II

In Part II, I have presented my contributions to the modeling and control of soft actuators using the port Hamiltonian (PH) framework.
Firstly, in Chapter 8, a distributed PH model of IPMCs actuators is presented. This research encompasses a comprehensive IPMC model composed of three subsystems, each addressing a different scale of the device: the distributed electric model for the electrode/polymer interface subsystem, the electro-stress diffusion model for the polymer subsystem, and the beam model for the mechanical structural deformation subsystem. These subsystems within different scales are interconnected using boundary multi-scale coupling (BMS) operators in the proposed model. For the purpose of simulation and experimental validation, the proposed distributed PH IPMC model is discretized while preserving the power structure. The physical parameters of the model are then determined through experimentation, and the model's accuracy is verified using various sets of data.
Secondly, the control of flexible structure by IPMCs are investigated in Chapter 9. In this study, the flexible structure is described by a nonlinear lumped parameter PH model, with flexibility represented through rotational springs. The flexible structure is actuated by IPMCs actuators, which are modeled using a simplified RC circuit system within the PH framework. These two systems are interconnected in a power preserving manner, ensuring the conservation of the PH structure in the coupled systems. A control strategy based on IDA-PBC is subsequently introduced to achieve the desired shape of the flexible structure using IPMC actuators. The proposed model has been identified on an experimental set-up. Additionally, the effectiveness of the proposed control law is validated using the experimental setup in various actuation scenarios, including both single and multiple actuators.
Finally, Chapter 10 delves into the modeling and control of HASEL actuators. Through reasonable geometric and mechanical assumptions, a PH model is presented for the HASEL actuator, effectively reproducing its primary dynamic characteristics. Subsequently, the study explores position control of the HASEL actuator using the IDA-PBC method. Additionally, a structure-preserving integral action is incorporated to enhance robustness while ensuring closed-loop stability. An experimental set-up is build to test the proposed model and control laws. The experimental closed loop responses validate the proposed control laws to different desired position references in a satisfactory way.

Publication list

1. Ning Liu, **Yongxin Wu**, Yann Le Gorrec, *Energy based modeling of ionic polymer metal composite actuators dedicated to the control of flexible structures*, IEEE/ASME Transaction on Mechatronics, vol. 26, no. 6, pp. 3139-3150, Dec. 2021, DOI: 10.1109/TMECH.2021.3053609.

2. Andrea Mattioni, **Yongxin Wu**, Hector Ramirez, Yann Le Gorrec, Alessandro Macchelli, *Modelling and control of an IPMC actuated flexible structure: A port-Hamiltonian approach*, Control Engineering Practice, Volume 101, August 2020, https://doi.org/10.1016/j.conengprac.2020.104498.

3. Ye Yuh, Nelson Cisneros, **Yongxin Wu**, Kanty Rabenorosoa, Yann Le Gorrec, *Modeling and Position Control of the HASEL Actuator via port-Hamiltonian Approach,* IEEE Robotics and Automation Letters, Volume: 7, Issue: 3, July 2022, DOI: 10.1109/LRA.2022.3181365

Chapter 12

General conclusion and future research

12.1. General conclusion

In this manuscript, I summarize the main results I obtained since my recruitment at Supmicrotech-ENSMM and FEMTO-ST institute in 2016. My research can be orgnized around two main research lines that have been presented in two parts of this manuscript.

The first Part (Part I) is focused on control of distributed port Hamiltonian (PH) systems in 1D and mixed (PDEs-ODEs) PH systems. Two scenarios are considered, when the control action is applied at the boundary or within the spatial domain. In both scenarios, the early lumped approach is employed, which means the distributed PH system is first discretized and the controller is designed from this discretized model. In the first case, in Chapter 3 the finite dimensional (reduced order) observer-based controllers are investigated. The conditions for the observer and controller gains are given such that the derived observer-based controllers are also PH systems. Hence, the closed loop stability can be guaranteed and the spillover effect can be avoided when the finite dimensional controller is implemented on the infinite dimensional PH systems.

Chapter 4 presents the control design when the actuation is located along the spatial domain. In this case, we show how dynamic extensions and structural invariants can be used to change the internal properties of the system when the system is fully actuated, and how it can be done in an approximate way when the system is actuated using piece-wise continuous actuators stemming from the use of actuator patches. Asymptotic stability is achieved using damping injection.

In Chapter 5, we develop a control strategy that allows to stabilize a class of mixed ODE-PDE systems with actuation on the ODE part. The control law consists of proportional and derivative parts with a "strong dissipation" term. With the help of this term, we can guarantee the exponential stability for the closed loop system without position control and the asymptotic stability when the position control is considered.

Part II is dedicated to the modeling and control of a class of soft actuators, such as electro-active polymers based actuators (IPMCs) and HASEL actuators, employing the PH approach.

In Chapter 8, a new model of IPMCs actuators is proposed with the help of the PH framework. The three components of the IPMC (Ionic Polymer-Metal Composite) actuators are introduced within three infinite-dimensional PH sub-systems, incorporating a multi-scale approach and linked through boundary multi-scale operators (BMS). These subsystems are a distributed electrical system for the electrode, an electro-diffusion systems for the polymer gel, and a Timoshenko beam model representing the flexible structure of the actuator. The model has been identified and validated through experimental results.

In Chapter 9, the control of a flexible structure using IPMCs actuators is investigated. In this study, the dynamics of the actuators are modeled as RLC circuits, interconnected with a lumped model of the flexible structure in a power-preserving manner. The IDA-PBC method is utilized, enabling the IPMC-actuated flexible structure to reach the desired shape. The validity of the proposed model and controller has been confirmed through experimentation on a benchmark system.

Chapter 10 introduces some preliminary results on modeling and position control of a novel class of soft actuators, namely HASEL (Hydraulically Amplified Self-Healing Electrostatic) actuators. Based on reasonable mechanical and geometric assumptions, a PH representation of the HASEL actuator is derived, comprising an interconnected system with electrical and mechanical components. The IDA-PBC method is employed for the position control of the actuator, and a structure-preserving integral action is incorporated to enhance the closed-loop system's robustness against external force disturbances. The proposed model and controller are validated through an experimental setup.

The results presented in this manuscript are the fruit of of four Ph.D. thesis, including one under progress, and four Master thesis. Apart from the work presented in this manuscript, I also have contributed to the observer design for 1D distributed PH systems using a late lumped approach (Toledo-Zucco et al., 2023), the modeling and control of an optic fiber using a piezo tube under a mixed nonlinear PDE-ODE system within the PH framework (Ayala et al., 2023), the structure preserving discretization for acoustic propagation tube presented by 2D wave equation in an acoustic tube (Liu et al., 2020) . As a result, I have co-authored 18 journal papers and 28 conference papers in the past years.

Another significant aspect of my work has been dedicated to advancing experimental platforms for validating controllers for various types of soft actuators. The experimental setup designed for IPMC actuators is detailed in Chapter 9 and illustrated in Fig 9.4. Additionally, another platform tailored for HASEL actuators is introduced in Chapter 10, as depicted in Fig 10.5. Apart from the two aforementioned platforms, two other different experimental setups have been constructed to validate the proposed control laws for various purposes. The first platform is designed for controlling boundary-controlled distributed parameter systems, consisting of an optic fiber using a piezo tube, as illustrated in Figure 12.1. This experimental platform will serve as a benchmark for validating the 3D motion control of nonlinear distributed parameter systems, which can be described by the Cosserat Rod model (Ayala et al., 2023). The other platform has been built for the flexible beam

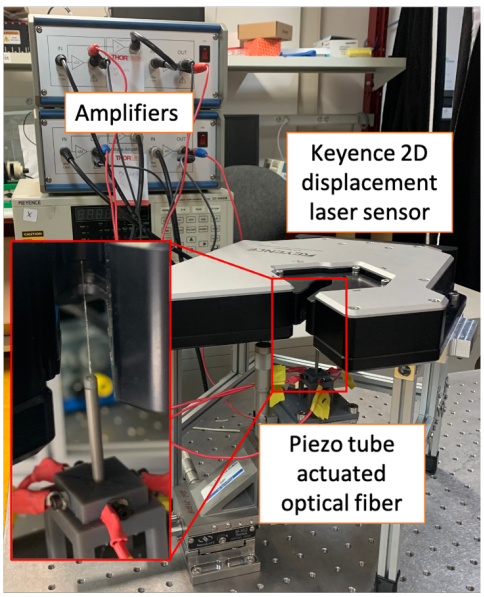

Figure 12.1: Experimental setup for piezotube actuated optical fiber

(carbon fiber plate) actuated by the HASEL actuators in a distributed manner, as shown in Fig 12.2. The distributed shape control method (Ponce et al., 2023) will be validated in this platform.

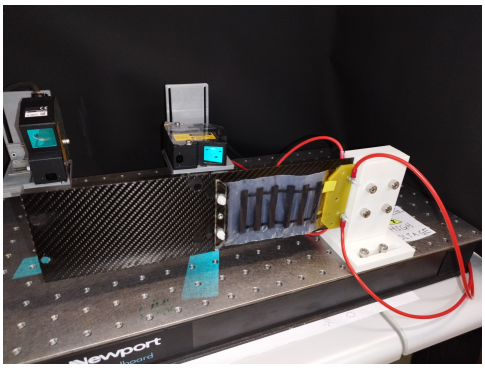

Figure 12.2: Experimental setup for Shape control using HASEL

12.2. Ongoing and future research

The aforementioned results offer a brief overview of the contributions made to implementable control design for distributed PH systems and some classes of soft actuators. However, there are still several critical aspects related to these topics that have not been thoroughly explored, sparking my interest for potential investigation in my future research.

12.2.1. Robust control design for the PH systems

The first research direction in the future will be the robust control design for PH systems. Modeling complex physical systems presents challenges in precisely capturing all the system's dynamics, and uncertainties remain in both physical parameters and external potential disturbances. For example, in the early lumped approach, neglecting high-frequency modes in discretizing the distributed parameter system may lead to closed-loop instability. When using an IPMC soft actuator, its dynamics are notably influenced by humidity, and its capabilities diminish significantly when the actuator is dry. On the other hand, Mechatronic systems are susceptible to external noises, such as vibrations or collision forces at the micro-scale.

Unexpected dynamic uncertainties, varying parameters, and external disturbances can significantly impact systems' performances and reliability, posing notable challenges in maintaining precision and stability. Addressing these issues through robust control strategies is essential for ensuring systems' dependable operation despite the complexities and uncertainties inherent in real-world applications.

This research direction targets a breakthrough in robust control and its numerical and experimental implementation on complex multi-physical systems obtained by considering the uncertainties of modeling the soft and compliant actuators. First, the varying physical parameters of the soft actuators will be characterized as a sub-model with bounded uncertainty at the modeling stage, which has not been considered in the literature. Secondly, some structure-preserving approximation schemes developed for the considered class of distributed PH systems will be investigated while the neglected part (high-frequency residue) shall be quantified as an error model. Furthermore, control design will be studied, and the robustness will be considered regarding these two bounded uncertainty models using the passivity propriety of the PH formulation which has been proven to be very useful for the stability analysis. The objective is to expand upon control design methodologies that rely on the Riccati equation, specifically those exemplified by the LQG control design presented in (Wu et al., 2020)extending them to encompass robust H_∞ control scenarios while preserving the passivity of the closed-loop system. The assessment of the proposed control method will include a thorough analysis of the closed-loop system's well-posedness and stability. Leveraging the passivity property inherent in the PH structure will enhance this evaluation. Additionally, the study will incorporate considerations for robustness, incorporating principles associated with H_∞ control.

12.2.2. Control of nonlinear distributed PH systems

The second axis of my future research focuses on control design for nonlinear distributed PH systems. Until now, my investigations on distributed PH systems have considered linear PH systems only. Nevertheless, the nonlinear characteristics of multi-physical systems frequently appear, especially when dealing with soft actuators like piezoelectric actuators and HASEL actuators. The inherent nonlinearity observed in these actuators can be attributed to various factors. One source of nonlinearity stems from geometric considerations during large deformations (e.g., nonlinear strain-displacement formulation). Moreover, nonlinearities stem from material behavior characteristics, such as the hyperelastic strain-stress relation. The presence of hysteresis phenomena in various actuators, including piezoelectric actuators or shape memory alloys (SMAs), also contributes to the overall nonlinearity. One of the essential difficulties of the control design for nonlinear distributed parameter systems is showing the existence of the solution of closed-loop systems. In the first instance of my research, I will assume the solution of the closed-loop nonlinear distributed system exists. Then, we will investigate the closed-loop stability using the Lyapunov theory arguments. The preliminary work on control design for nonlinear distributed PH systems has been done in (Ayala et al., 2023). In this study, the modeling and control of a optic fiber actuated by a piezoelectric tube have been investigated. The 1D nonlinear Cosserat rod PDE model is used to represent the large deformations of the optic fiber in two directions under the PH framework. The main dynamics of the piezoelectric tube has been considered as a linear second order mechanical system which is also presented in the PH framework. The two sub-systems are interconnected in a power preserving manner. Then, the finite dimensional control design method is proposed based on the approximation of the original system in the finite dimensional space.

Building on these previous results, the upcoming work will encompass several aspects. Firstly, an exploration into the control design for the nonlinear distributed PH system will be conducted, considering both late and early lumped approaches. To this end, the energy shaping method using control by interconnection and structural invariant Casmir function initially presented for linear distributed control system (Liu et al., 2024) (*cf.* Chapter 4) will be generalized to non linear distributed systems. Meanwhile, we will address the control problem of flexible structures incorporating nonlinearity in the actuators, such as hysteresis or creep. This approach aims to enhance the applicability and precision of the control design.

12.2.3. Modeling and control of HASEL actuators based soft robots

The third research axis concentrates on developing the modeling and control methodology for soft robots driven by HASEL actuators. The demonstrated capacity of the HASEL actuator to construct soft robots marks a significant breakthrough in robotics. However, the study of modeling HASEL actuators and the soft robots built upon such actuators still needs to be solved in the current literature.

Throughout Nelson Cisneros's ongoing Ph.D. thesis, one focus has been to explore the fabrication of HASEL actuators. Importantly, we have achieved the capability to produce complex structures based on HASEL actuators with diverse designs tailored for specific purposes. In this context, my next focus involves utilizing PH methods to model the intricate structures obtained from the HASEL actuators. The intention is to leverage these models to design control methods using the passivity property. This approach enables us to achieve control strategies for different purposes, such as position, trajectory, force control, etc. By integrating the passivity property into the control design, we aim to enhance the efficiency and adaptability of the HASEL actuators in diverse applications, contributing to the advancement of soft robotics.

The HASEL actuator has demonstrated its capability to propel the 1D flexible structure in the experimental platform depicted in Figure 12.2. Nevertheless, their size remains impractical for multi-dimensional actuation. Another aspect of this research direction centers on standardizing HASEL actuator fabrication technology and strives to miniaturize these actuators. This perspective is in

harmony with the research scope of the FEMTO-ST Institute and is motivated by the actuation needs for shaping control of 2D flexible structures.

Bibliography

E. Acome, S. K. Mitchell, T. G. Morrissey, M. B. Emmett, C. Benjamin, M. King, M. Radakovitz, and C. Keplinger. Hydraulically amplified self-healing electrostatic actuators with muscle-like performance. *Science*, 359(6371):61–65, 2018. ISSN 0036-8075. doi: 10.1126/science.aao6139.

A.J. van der Schaft and B. Maschke. On the Hamiltonian formulation of nonholonomic mechanical systems. *Reports on Mathematical Physics*, 34(2):225 – 233, 1994. ISSN 0034-4877.

B. D. Anderson and J. B. Moore. *Optimal control: linear quadratic methods*. Courier Corporation, 2007.

A. Andry, E. Shapiro, and J. Chung. Eigenstructure assignment for linear systems. *IEEE transactions on aerospace and electronic systems*, (5):711–729, 1983.

S. Aoues, D. Eberard, and W. Marquis-Favre. Canonical interconnection of discrete linear port-Hamiltonian systems. In *2nd IEEE Conference on Decision and Control*, pages 3166–3171, 2013.

S. Aoues, F. L. Cardoso-Ribeiro, D. Matignon, and D. Alazard. Modeling and control of a rotating flexible spacecraft: a port-hamiltonian approach. *IEEE Transactions on Control Systems Technology*, 27(1):355–362, 2017.

B. Augner. *Stabilisation of infinite-dimensional port-Hamiltonian systems via dissipative boundary feedback*. PhD thesis, Universität Wuppertal, Fakultät für Mathematik und Naturwissenschaften . . . , 2018.

E. P. Ayala, Y. Wu, K. Rabenorosoa, and Y. Le Gorrec. Energy-based modeling and control of a piezotube actuated optical fiber. *IEEE/ASME Transactions on Mechatronics*, 28(1):385–395, 2023. doi: 10.1109/TMECH.2022.3199566.

M. Balas. Toward a more practical control, theory for distributed parameter systems. *in Control and Dynamic Systems*, 361, 1982.

M. J. Balas. Active control of flexible systems. *Journal of Optimization theory and Applications*, 25 (3):415–436, 1978.

R. Banavar and B. Dey. Stabilizing a flexible beam on a cart: A distributed port-hamiltonian approach. *Journal of nonlinear science*, 20:131–151, 2010.

J. Bontsema and R. F. Curtain. A note on spillover and robustness for flexible systems. *IEEE Transactions on Automatic Control*, 33(6):567–569, 1988.

P. C. Branco and J. Dente. Derivation of a continuum model and its electric equivalent-circuit representation for ionic polymer–metal composite (IPMC) electromechanics. *Smart Materials and Structures*, 15(2):378, 2006.

F. Brasch and J. Pearson. Pole placement using dynamic compensators. *IEEE Transactions on Automatic Control*, 15(1):34–43, 1970.

Z. Chen and X. Tan. A control-oriented and physics-based model for ionic polymer–metal composite actuators. *IEEE/ASME Transactions on Mechatronics*, 13(5):519–529, 2008.

M. T. Chikhaoui, K. Rabenorosoa, and N. Andreff. Kinematic Modeling of an EAP Actuated Continuum Robot for Active Micro-endoscopy. In *Advances in Robot Kinematics*, pages 457–465. Springer International Publishing, Cham, 2014. doi: 10.1007/978-3-319-06698-1_47. URL http://link.springer.com/10.1007/978-3-319-06698-1{_}47.

A. H. Committee. *Properties and Selection: Nonferrous Alloys and Special-Purpose Materials*. ASM International, 01 1990. ISBN 978-1-62708-162-7. doi: 10.31399/asm.hb.v02.9781627081627. URL https://doi.org/10.31399/asm.hb.v02.9781627081627.

F. Conrad and O. Morgül. On the stabilization of a flexible beam with a tip mass. *SIAM Journal on Control and Optimization*, 36(6):1962–1986, 1998.

R. F. Curtain and H. Zwart. *An introduction to infinite-dimensional linear systems theory*, volume 21. Springer Science & Business Media, 2012.

R. F. Curtain and H. Zwart. *An Introduction to Infinite-Dimensional Systems, A State Space Approach*. Springer Verlag, New York, 2020.

P. De Gennes, K. Okumura, M. Shahinpoor, and K. J. Kim. Mechanoelectric effects in ionic gels. *EPL (Europhysics Letters)*, 50(4):513, 2000.

M. de Queiroz, D. Dawson, and F. Zhang. Boundary control of a rotating flexible body-beam system. *Proceedings of the 1997 IEEE International Conference on Control Applications*, pages 812–817, 1997.

M. S. de Queiroz, D. M. Dawson, M. Agarwal, and F. Zhang. Adaptive nonlinear boundary control of a flexible link robot arm. *IEEE Transactions on Robotics and Automation*, 15(4):779–787, 1999.

S. Delgado and P. Kotyczka. Overcoming the dissipation condition in passivity-based control for a class of mechanical systems. *IFAC Proceedings Volumes*, 47(3):11189 – 11194, 2014. ISSN 1474-6670. 19th IFAC World Congress.

J. Deutscher. A backstepping approach to the output regulation of boundary controlled parabolic PDEs. *Automatica*, 57:56–64, 2015.

J. Deutscher, N. Gehring, and R. Kern. Output feedback control of general linear heterodirectional hyperbolic ODE-PDE-ODE systems. *Automatica*, 95:472–480, 2018.

J. Deutscher, N. Gehring, and R. Kern. Output feedback control of general linear heterodirectional hyperbolic PDE-ODE systems with spatially-varying coefficients. *International Journal of Control*, 92(10):2274–2290, 2019.

A. Doria-Cerezo, C. Batlle, and G. Espinosa-Perez. Passivity-based Control of a Wound-rotor Synchronous Motor. *IET Control Theory Applications*, 4(10):2049–2057, 2010.

V. Dos Santos Martins, Y. Wu, and M. Rodrigues. Design of a proportional integral control using operator theory for infinite dimensional hyperbolic systems. *IEEE Transactions on Control Systems Technology*, 22(5):2024–2030, 2014. doi: 10.1109/TCST.2014.2299407.

V. Duindam, A. Macchelli, S. Stramigioli, and H. Bruyninckx. *Modeling and control of complex physical systems: the port-Hamiltonian approach*. Springer Science & Business Media, 2009.

B. d' Andréa-Novel and J. Coron. Exponential stabilization of an overhead crane with flexible cable via a back-stepping approach. *Automatica*, 36(4):587–593, 2000.

N. El-Atab, R. B. Mishra, F. Al-Modaf, L. Joharji, A. A. Alsharif, H. Alamoudi, M. Diaz, N. Qaiser, and M. M. Hussain. Soft actuators for soft robotic applications: A review. *Advanced Intelligent Systems*, 2(10):2000128, 2020. doi: https://doi.org/10.1002/aisy.202000128. URL https://onlinelibrary.wiley.com/doi/abs/10.1002/aisy.202000128.

T. Endo, M. Sasaki, F. Matsuno, and Y. Jia. Contact-force control of a flexible Timoshenko arm in rigid/soft environment. *IEEE Transactions on Automatic Control*, 62(5):2546–2553, 2017.

J. Ferguson, A. Donaire, R. Ortega, and R. H. Middleton. New results on disturbance rejection for energy-shaping controlled port-Hamiltonian systems, 2017.

G. Golo, V. Talasila, A. van Der Schaft, and B. Maschke. Hamiltonian discretization of boundary control systems. *Automatica*, 40(5):757–771, 2004.

G.-Y. Gu, J. Zhu, L.-M. Zhu, and X. Zhu. A survey on dielectric elastomer actuators for soft robots. *Bioinspiration & Biomimetics*, 12(1):011003, jan 2017. doi: 10.1088/1748-3190/12/1/011003. URL https://dx.doi.org/10.1088/1748-3190/12/1/011003.

S. Gutta, J. S. Lee, M. B. Trabia, and W. Yim. Modeling of Ionic Polymer Metal Composite Actuator Dynamics Using a Large Deflection Beam Model. *Smart Materials and Structures*, 18(11), 2009.

N. Higham. Computing a nearest symmetric positive definite matrix. *Linear Algebra and its Applications*, 103:103–118, 1988.

B. Jacob and H. J. Zwart. *Linear port-Hamiltonian systems on infinite-dimensional spaces*, volume 223. Springer Science & Business Media, 2012.

J. Jiang. Design of reconfigurable control systems using eigenstructure assignments. *International Journal of Control*, 59(2):395–410, 1994.

F. John. On linear partial differential equations with analytic coefficients unique continuation of data. *Communications on Pure and Applied Mathematics*, 2(2-3):209–253, 1949.

B. K. Johnson, V. Sundaram, M. Naris, E. Acome, K. Ly, N. Correll, C. Keplinger, J. S. Humbert, and M. E. Rentschler. Identification and control of a nonlinear soft actuator and sensor system. *IEEE Robotics and Automation Letters*, 5(3):3783–3790, 2020.

R. E. Kalman, P. L. Falb, and M. A. Arbib. *Topics in mathematical system theory*, volume 1. McGraw-Hill New York, 1969.

R. Kanno, S. Tadokoro, T. Takamori, M. Hattori, and K. Oguro. Modeling of icpf (ionic conducting polymer film) actuator-modeling of electrical characteristics. In *Industrial Electronics, Control, and Instrumentation, 1995., Proceedings of the 1995 IEEE IECON 21st International Conference on*, volume 2, pages 913–918. IEEE, 1995.

N. Kellaris, V. Gopaluni Venkata, G. M. Smith, S. K. Mitchell, and C. Keplinger. Peano-hasel actuators: Muscle-mimetic, electrohydraulic transducers that linearly contract on activation. *Science Robotics*, 3(14), 2018. doi: 10.1126/scirobotics.aar3276.

N. Kellaris, V. G. Venkata, P. Rothemund, and C. Keplinger. An analytical model for the design of peano-hasel actuators with drastically improved performance. *Extreme Mechanics Letters*, 29: 100449, 2019. ISSN 2352-4316. doi: https://doi.org/10.1016/j.eml.2019.100449.

N. Kellaris, P. Rothemund, Y. Zeng, S. K. Mitchell, G. M. Smith, K. Jayaram, and C. Keplinger. Spider-inspired electrohydraulic actuators for fast, soft-actuated joints. *Advanced Science*, 8(14): 2100916, 2021.

J. Khawwaf, J. Zheng, R. Chai, R. Lu, and Z. Man. Adaptive microtracking control for an underwater IPMC actuator using new hyperplane-based sliding mode. *IEEE/ASME Transactions on Mechatronics*, 24(5):2108–2117, 2019.

O. I. Kosmidou. Generalized Riccati equations associated with guaranteed cost control: An overview of solutions and features. *Applied Mathematics and Computation*, 191(2):511–520, 2007.

P. Kotyczka, B. Maschke, and L. Lefèvre. Weak form of stokes–dirac structures and geometric discretization of port-hamiltonian systems. *Journal of Computational Physics*, 361:442–476, 2018.

A. Lanzon, Y. Feng, B. D. Anderson, and M. Rotkowitz. Computing the positive stabilizing solution to algebraic Riccati equations with an indefinite quadratic term via a recursive method. *IEEE Transactions on Automatic Control*, 53(10):2280–2291, 2008.

Y. Le Gorrec, H. Zwart, and B. Maschke. Dirac structures and boundary control systems associated with skew-symmetric differential operators. *SIAM journal on control and optimization*, 44(5): 1864–1892, 2005.

Y. Le Gorrec, H. Ramirez, Y. Wu, N. Liu, and A. Macchelli. *Energy Shaping Control of 1D Distributed Parameter Systems*, pages 3–26. Springer International Publishing, Cham, 2022. ISBN 978-3-030-94766-8. doi: 10.1007/978-3-030-94766-8_1. URL https://doi.org/10.1007/978-3-030-94766-8_1.

C. Liu, H. Qin, and P. T. Mather. Review of progress in shape-memory polymers. *J. Mater. Chem.*, 17:1543–1558, 2007. doi: 10.1039/B615954K. URL http://dx.doi.org/10.1039/B615954K.

D.-X. Liu, J. Bao, D. Liu, Y. Lu, and J. Xu. Modeling of planar hydraulically amplified self-healing electrostatic actuators. *IEEE Robotics and Automation Letters*, 6(4):7533–7540, 2021a. doi: 10.1109/LRA.2021.3098916.

N. Liu. *Modélisation Hamiltonienne à ports et commande distribuée de structures flexibles : application aux endoscopes biomédicaux à actionneurs à base de polymère électro-actif*. PhD thesis, 2020. URL http://www.theses.fr/2020UBFCD054. Thèse de doctorat dirigée par Le Gorrec, Yann et Wu, Yongxin Automatique Bourgogne Franche-Comté 2020.

N. Liu, Y. Wu, Y. Le Gorrec, H. Ramirez, and L. Lefèvre. Structure-preserving discretization and control of a two-dimensional vibro-acoustic tube. *IMA Journal of Mathematical Control and Information*, 38(2):417–439, 11 2020. ISSN 1471-6887. doi: 10.1093/imamci/dnaa028. URL https://doi.org/10.1093/imamci/dnaa028.

N. Liu, Y. Wu, and Y. Le Gorrec. Energy based modeling of ionic polymer metal composite actuators dedicated to the control of flexible structures. *IEEE/ASME Transactions on Mechatronics*, pages 1–1, 2021b. doi: 10.1109/TMECH.2021.3053609.

N. Liu, Y. Wu, Y. Le Gorrec, L. Lefèvre, and H. Ramirez. In-domain finite dimensional control of distributed parameter port-Hamiltonian systems via energy shaping. In *2021 Proceedings of the Conference on Control and its Applications*, pages 70–77. Society for Industrial and Applied Mathematics, Philadelphia, PA, jan 2021c. doi: 10.1137/1.9781611976847.10. URL https://epubs.siam.org/doi/10.1137/1.9781611976847.10.

N. Liu, Y. Wu, Y. Le Gorrec, L. Lefevre, and H. Ramirez. Reduced order in domain control of distributed parameter port-hamiltonian systems via energy shaping. *Automatica*, 161:111500, 2024. ISSN 0005-1098.

Z. Liu and S. Zheng. *Semigroups associated with dissipative systems*, volume 398. CRC Press, 1999.

D. G. Luenberger. Observing the state of a linear system. *IEEE transactions on military electronics*, 8(2):74–80, 1964.

Z.-H. Luo, B.-Z. Guo, and Ö. Morgül. *Stability and stabilization of infinite dimensional systems with applications*. Springer Science & Business Media, 2012.

A. Macchelli and C. Melchiorri. Modeling and control of the Timoshenko beam. The distributed port Hamiltonian approach. *SIAM Journal on Control and Optimization*, 43(2):743–767, 2004.

A. Macchelli and C. Melchiorri. Control by interconnection of mixed port hamiltonian systems. *IEEE Transactions on Automatic Control*, 50(11):1839–1844, 2005.

A. Macchelli, Y. Le Gorrec, H. Ramirez, and H. Zwart. On the synthesis of boundary control laws for distributed port-Hamiltonian systems. *IEEE Transactions on Automatic Control*, 62(4): 1700–1713, April 2017. ISSN 0018-9286. doi: 10.1109/TAC.2016.2595263.

A. Macchelli, Y. Le Gorrec, and H. Ramírez. Exponential stabilization of port-hamiltonian boundary control systems via energy shaping. *IEEE Transactions on Automatic Control*, 65(10):4440–4447, 2020.

C. Majidi. Soft robotics: A perspective—current trends and prospects for the future. *Soft Robotics*, 1(1):5–11, 2014. doi: 10.1089/soro.2013.0001. URL https://doi.org/10.1089/soro.2013.0001.

T. Malzer, H. Rams, and M. Schöberl. Energy-based in-domain control of a piezo-actuated euler-bernoulli beam. *IFAC-PapersOnLine*, 52(2):144–149, 2019. ISSN 2405-8963. 3rd IFAC Workshop on Control of Systems Governed by Partial Differential Equations CPDE 2019.

T. Malzer, H. Rams, B. Kolar, and M. Schöberl. Stability analysis of the observer error of an in-domain actuated vibrating string. *IEEE Control Systems Letters*, 5(4):1237–1242, 2020a.

T. Malzer, H. Rams, and M. Schöberl. On structural invariants in the energy-based in-domain control of infinite-dimensional port-hamiltonian systems. *Systems & Control Letters*, 145:104778, 2020b. ISSN 0167-6911.

T. Malzer, J. Toledo, Y. L. Gorrec, and M. Schöberl. Energy-based in-domain control and observer design for infinite-dimensional port-hamiltonian systems. *arXiv preprint arXiv:2002.01717*, 2020c.

B. Maschke and A. van der Schaft. Port Controlled Hamiltonian Systems: Modeling Origins and System Theoretic Properties. In *Proceedings of the 3rd IFAC Symposium on Nonlinear Control Systems, NOLCOS'92*, pages 282–288, Bordeaux, France, 1992.

B. Maschke, A. Van Der Schaft, and P. Breedveld. An intrinsic hamiltonian formulation of network dynamics: non-standard poisson structures and gyrators. *Journal of the Franklin Institute*, 329 (5):923–966, 1992. ISSN 0016-0032.

A. Mattioni. *Modelling and stability analysis of flexible robots : a distributed parameter port-Hamiltonian approach*. PhD thesis, 2021. URL http://www.theses.fr/2021UBFCD030. Thèse de doctorat dirigée par Le Gorrec, Yann et Wu, Yongxin Automatique Bourgogne Franche-Comté 2021.

A. Mattioni, Y. Wu, H. Ramirez, Y. Le Gorrec, and A. Macchelli. Modelling and control of an ipmc actuated flexible structure: A lumped port hamiltonian approach. *Control Engineering Practice*, 101:104498, 2020. ISSN 0967-0661. doi: https://doi.org/10.1016/j.conengprac.2020.104498. URL https://www.sciencedirect.com/science/article/pii/S0967066120301192.

A. Mattioni, Y. Wu, Y. Le Gorrec, and H. Zwart. Stabilization of a class of mixed ode–pde port-hamiltonian systems with strong dissipation feedback. *Automatica*, 142:110284, 2022. ISSN 0005-1098. doi: https://doi.org/10.1016/j.automatica.2022.110284. URL https://www.sciencedirect.com/science/article/pii/S0005109822001303.

F. D. Meglio, F. B. Argomedo, L. Hu, and M. Krstic. Stabilization of coupled linear heterodirectional hyperbolic PDE-ODE systems. *Automatica*, 87:281–289, 2018.

S. K. Mitchell, X. Wang, E. Acome, T. Martin, K. Ly, N. Kellaris, V. G. Venkata, and C. Keplinger. An easy-to-implement toolkit to create versatile and high-performance hasel actuators for untethered soft robots. *Advanced Science*, 6(14):1900178, 2019.

G. Moretti, M. Duranti, M. Righi, R. Vertechy, and M. Fontana. Analysis of dielectric fluid transducers. In Y. Bar-Cohen, editor, *Electroactive Polymer Actuators and Devices (EAPAD) XX*, volume 10594, pages 142 – 154. International Society for Optics and Photonics, SPIE, 2018.

Ö. Morgül. A dynamic control law for the wave equation. *Automatica*, 30(11):1785–1792, 1994.

O. Morgul. Stabilization and disturbance rejection for the wave equation. *IEEE Transactions on Automatic Control*, 43(1):89–95, 1998.

O. Morgül, B. P. Rao, and F. Conrad. On the stabilization of a cable with a tip mass. *IEEE Transactions on Automatic Control*, 39(10):2140–2145, 1994.

R. Moulla, L. Lefévre, and B. Maschke. Pseudo-spectral methods for the spatial symplectic reduction of open systems of conservation laws. *Journal of Computational Physics*, 231(4):1272–1292, feb 2012. ISSN 00219991.

A. Naylor and G. Sell. *Linear Operator Theory in Engineering and Science*. Applied mathematical sciences. Holt, Rinehart and Winston, 1971. ISBN 9780030793905. URL https://books.google.fr/books?id=wvJQAAAAMAAJ.

S. Nemat-Nasser and J. Y. Li. Electromechanical response of ionic polymer-metal composites. *Journal of Applied Physics*, 87(7):3321–3331, 2000.

K. M. Newbury and D. J. Leo. Electromechanical modeling and characterization of ionic polymer benders. *Journal of Intelligent Material Systems and Structures*, 13(1):51–60, 2002.

K. M. Newbury and D. J. Leo. Linear electromechanical model of ionic polymer transducers-part i: Model development. *Journal of Intelligent Material Systems and Structures*, 14(6):333–342, 2003.

G. Nishida, K. Takagi, B. Maschke, and T. Osada. Multi-scale distributed parameter modeling of ionic polymer-metal composite soft actuator. *Control Engineering Practice*, 19(4):321–334, 2011a.

G. Nishida, K. Takagi, B. Maschke, and T. Osada. Multi-scale distributed parameter modeling of ionic polymer-metal composite soft actuator. *Control Engineering Practice*, 19(4):321–334, 2011b.

R. Ortega and E. Garcia-Canseco. Interconnection and damping assignment passivity-based control: A survey. *European Journal of control*, 10(5):432–450, 2004.

R. Ortega, A. Van Der Schaft, I. Mareels, and B. Maschke. Putting energy back in control. *IEEE Control Systems Magazine*, 21(2):18–33, 2001. doi: 10.1109/37.915398.

R. Ortega, A. van der Schaft, B. Maschke, and G. Escobar. Interconnection and damping assignment passivity-based control of port-controlled hamiltonian systems. *Automatica*, 38(4):585–596, 2002.

R. Ortega, A. van Der Schaft, F. Castanos, and A. Astolfi. Control by interconnection and standard passivity-based control of port-hamiltonian systems. *IEEE Transactions on Automatic control*, 53 (11):2527–2542, 2008.

A. Pagoli, F. Chapelle, J.-A. Corrales-Ramon, Y. Mezouar, and Y. Lapusta. Review of soft fluidic actuators: classification and materials modeling analysis. *Smart Materials and Structures*, 31 (1):013001, dec 2021. doi: 10.1088/1361-665X/ac383a. URL https://dx.doi.org/10.1088/1361-665X/ac383a.

M. Pan, C. Yuan, X. Liang, T. Dong, T. Liu, J. Zhang, J. Zou, H. Yang, and C. Bowen. Soft actuators and robotic devices for rehabilitation and assistance. *Advanced Intelligent Systems*, 4(4):2100140, 2022. doi: https://doi.org/10.1002/aisy.202100140. URL https://onlinelibrary.wiley.com/doi/abs/10.1002/aisy.202100140.

J. W. Paquette, K. J. Kim, J.-D. Nam, and Y. S. Tak. An equivalent circuit model for ionic polymer-metal composites and their performance improvement by a clay-based polymer nano-composite technique. *Journal of Intelligent Material Systems and Structures*, 14(10):633–642, 2003.

K. Park, M.-K. Yoon, S. Lee, J. Choi, and M. Thubrikar. Effects of electrode degradation and solvent evaporation on the performance of ionic-polymer–metal composite sensors. *Smart Materials and Structures*, 19(7):075002, 2010.

R. Pelrine, R. Kornbluh, Q. Pei, and J. Joseph. High-speed electrically actuated elastomers with strain greater than 100%. *Science*, 287(5454):836–839, 2000. doi: 10.1126/science.287.5454.836. URL https://www.science.org/doi/abs/10.1126/science.287.5454.836.

C. Ponce, H. Ramirez, and Y. L. Gorrec. Finite dimensional shape control design of linear port-hamiltonian systems with in-domain pointwise inputs. *IFAC-PapersOnLine*, 56(2):6777–6782, 2023. ISSN 2405-8963. doi: https://doi.org/10.1016/j.ifacol.2023.10.385. URL https://www.sciencedirect.com/science/article/pii/S2405896323007528. 22nd IFAC World Congress.

M. Porfiri, H. Sharghi, and P. Zhang. Modeling back-relaxation in ionic polymer metal composites: The role of steric effects and composite layers. *Journal of Applied Physics*, 123(1):014901, 2018.

S. Prajna, A. van der Schaft, and G. Meinsma. An LMI approach to stabilization of linear port-controlled Hamiltonian systems. *Systems & control letters*, 45(5):371–385, 2002.

H. Ramirez, B. Maschke, and D. Sbarbaro. Irreversible port-hamiltonian systems: A general formulation of irreversible processes with application to the cstr. *Chemical Engineering Science*, 89: 223–234, 2013.

H. Ramirez, Y. Le Gorrec, A. Macchelli, and H. Zwart. Exponential stabilization of boundary controlled port-Hamiltonian systems with dynamic feedback. *IEEE Transactions on Automatic Control*, 59(10):2849–2855, Oct 2014. ISSN 0018-9286. doi: 10.1109/TAC.2014.2315754.

H. Ramirez, Y. Le Gorrec, B. Maschke, and F. Couenne. On the passivity based control of irreversible processes: A port-hamiltonian approach. *Automatica*, 64:105–111, 2016.

H. Ramirez, H. Zwart, and Y. Le Gorrec. Stabilization of infinite dimensional port-Hamiltonian systems by nonlinear dynamic boundary control. *Automatica*, 85:61 – 69, 2017. ISSN 0005-1098. doi: https://doi.org/10.1016/j.automatica.2017.07.045.

B. Rao. Uniform stabilization of a hybrid system of elasticity. *SIAM Journal on Control and Optimization*, 33(2):440–454, 1995.

R. Rashad, F. Califano, A. J. van der Schaft, and S. Stramigioli. Twenty years of distributed port-hamiltonian systems: a literature review. *IMA Journal of Mathematical Control and Information*, 2020.

P. Rothemund, N. Kellaris, S. K. Mitchell, E. Acome, and C. Keplinger. Hasel artificial muscles for a new generation of lifelike robots-recent progress and future opportunities. *Advanced materials*, 2020a.

P. Rothemund, S. Kirkman, and C. Keplinger. Dynamics of electrohydraulic soft actuators. *Proceedings of the National Academy of Sciences*, 117(28):16207–16213, 2020b. ISSN 0027-8424. doi: 10.1073/pnas.2006596117.

D. Rus and M. T. Tolley. Design, fabrication and control of soft robots. *Nature*, 521:467–475, 2015. URL https://api.semanticscholar.org/CorpusID:217952627.

S. Seok, C. D. Onal, K.-J. Cho, R. J. Wood, D. Rus, and S. Kim. Meshworm: A peristaltic soft robot with antagonistic nickel titanium coil actuators. *IEEE/ASME Transactions on Mechatronics*, 18 (5):1485–1497, 2013. doi: 10.1109/TMECH.2012.2204070.

M. Shahinpoor. Micro-electro-mechanics of ionic polymeric gels as electrically controllable artificial muscles. *Journal of Intelligent Material Systems and Structures*, 6(3):307–314, 1995.

M. Shahinpoor, editor. *Ionic Polymer Metal Composites (IPMCs)*, volume 1 of *Smart Materials Series*. The Royal Society of Chemistry, 2016. ISBN 978-1-78262-077-8.

M. Shahinpoor and K. J. Kim. Ionic polymer–metal composites: IV. Industrial and medical applications. *Smart Materials and Structures*, 14(1):197–214, feb 2004. ISSN 0964-1726. doi: 10.1088/0964-1726/14/1/020. URL https://iopscience.iop.org/article/10.1088/0964-1726/14/1/020.

T. Shores. *Applied linear algebra and matrix analysis*, volume 2541. Springer, 2007.

J. Toledo, Y. Wu, H. Ramirez, and Y. Le Gorrec. Observer-based boundary control of distributed port-hamiltonian systems. *Automatica*, 120:109130, 2020. doi: 10.1016/j.automatica.2020.109130. URL https://doi.org/10.1016/j.automatica.2020.109130.

J. Toledo, H. Ramirez, Y. Wu, and Y. Le Gorrec. Linear matrix inequality design of exponentially stabilizing observer-based state feedback port-hamiltonian controllers. *IEEE Transactions on Automatic Control*, pages 1–8, 2022. doi: 10.1109/TAC.2022.3227927.

J. P. Toledo Zucco. *Synthèse de lois de commande à base d'observateurs pour les systèmes à paramètres distribués : une approche Hamiltonienne à ports*. PhD thesis, 2021. URL http://www.theses.fr/2021UBFCD032. Thèse de doctorat dirigée par Le Gorrec, YannRamirez Estay, Hector et Wu, Yongxin Automatique Bourgogne Franche-Comté 2021.

J.-P. Toledo-Zucco, Y. Wu, H. Ramirez, and Y. Le Gorrec. Infinite-dimensional observers for high-order boundary-controlled port-hamiltonian systems. *IEEE Control Systems Letters*, 7:1676–1681, 2023. doi: 10.1109/LCSYS.2023.3278252.

M. T. Tolley, R. F. Shepherd, B. Mosadegh, K. C. Galloway, M. Wehner, M. Karpelson, R. J. Wood, and G. M. Whitesides. A resilient, untethered soft robot. *Soft Robotics*, 1(3):213–223, 2014. doi: 10.1089/soro.2014.0008. URL https://doi.org/10.1089/soro.2014.0008.

V. Trenchant, T. Vu, H. Ramirez, L. Lefèvre, and Y. Le Gorrec. On the use of structural invariants for the distributed control of infinite dimensional port-Hamitonian systems. In *2017 IEEE 56th Annual Conference on Decision and Control (CDC)*, pages 47–52, Dec 2017. doi: 10.1109/CDC.2017.8263641.

V. Trenchant, H. Ramirez, P. Kotyczka, and Y. Le Gorrec. Finite differences on staggered grids preserving the port-Hamiltonian structure with application to an acoustic duct. *Journal of Computational Physics*, 373:673–697, November 2018.

A. van der Schaft. *L_2-gain and passivity techniques in nonlinear control*, volume 2. Springer, 2000.

A. van der Schaft and B. M. Maschke. Hamiltonian formulation of distributed-parameter systems with boundary energy flow. *Journal of Geometry and Physics*, 42(1-2):166–194, 2002.

J. Villegas. *A Port-Hamiltonian Approach to Distributed Parameter Systems*. PhD thesis, University of Twente, Netherlands, 2007.

J. Villegas, H. Zwart, Y. Le Gorrec, B. Maschke, and A. Van Der Schaft. Stability and stabilization of a class of boundary control systems. In *Proceedings of the 44th IEEE Conference on Decision and Control*, pages 3850–3855. IEEE, 2005.

J. A. Villegas, H. Zwart, Y. Le Gorrec, and B. Maschke. Exponential stability of a class of boundary control systems. *IEEE Transactions on Automatic Control*, 54(1):142–147, 2009.

J. Wang and M. Krstic. Output feedback boundary control of a heat PDE sandwiched between two ODEs. *IEEE Transactions on Automatic Control*, 64(11):4653–4660, 2019.

J. Wang, A. J. McDaid, C. Z. Lu, and K. C. Aw. A compact ionic polymer-metal composite (IPMC) actuated valveless pump for drug delivery. *IEEE/ASME Transactions on Mechatronics*, 22(1): 196–205, 2017.

R. Weldegiorgis, P. Krishna, and K. Gangadharan. Vibration control of smart cantilever beam using strain rate feedback. *Procedia Materials Science*, 5:113–122, 2014.

Y. Wu. *Passivity preserving balanced reduction for the finite and infinite dimensional port Hamiltonian systems*. PhD thesis, 2015. URL `http://www.theses.fr/2015LYO10278`. Thèse de doctorat dirigée par Maschke, Bernhard, Le Gorrec, Yann et Hamroun, Boussad Automatique Lyon 1, 2015.

Y. Wu, B. Hamroun, Y. Le Gorrec, and B. Maschke. Structure preserving reduction of port hamiltonian system using a modified LQG method. In *Proceedings of the 33rd Chinese Control Conference*, pages 3528–3533, 2014a. doi: $10.1109/\mathrm{ChiCC}.2014.6895525$.

Y. Wu, B. Hamroun, Y. Le Gorrec, and B. Maschke. Port Hamiltonian system in descriptor form for balanced reduction: Application to a nanotweezer. *IFAC Proceedings Volumes*, 47(3):11404–11409, 2014b.

Y. Wu, B. Hamroun, Y. Le Gorrec, and B. Maschke. Reduced order LQG control design for port Hamiltonian systems. *Automatica*, 95:86–92, 2018.

Y. Wu, B. Hamroun, Y. Le Gorrec, and B. Maschke. Reduced order lqg control design for infinite dimensional port hamiltonian systems. *IEEE Transactions on Automatic Control*, 2020.

Y. Xiao and K. Bhattacharya. Modeling electromechanical properties of ionic polymers. In *Smart Structures and Materials 2001: Electroactive Polymer Actuators and Devices*, volume 4329, pages 292–301. International Society for Optics and Photonics, 2001.

T. Yamaue, H. Mukai, K. Asaka, and M. Doi. Electrostress diffusion coupling model for polyelectrolyte gels. *Macromolecules*, 38(4):1349–1356, 2005.

K.-J. Yang, K.-S. Hong, and F. Matsuno. Robust boundary control of an axially moving string by using a pr transfer function. *IEEE Transactions on Automatic Control*, 50(12):2053–2058, 2005.

Y. Yeh, N. Cisneros, Y. Wu, K. Rabenorosoa, and Y. L. Gorrec. Modeling and position control of the hasel actuator via port-hamiltonian approach. *IEEE Robotics and Automation Letters*, 7(3): 7100–7107, 2022. doi: 10.1109/LRA.2022.3181365.

W. Yim, M. B. Trabia, J. M. Renno, J. Lee, and K. J. Kim. Dynamic Modeling of Segmented Ionic Polymer Metal Composite (IPMC) Actuator. In *2006 IEEE/RSJ International Conference on Intelligent Robots and Systems*, pages 5459–5464, 2006.

Z. Zhu, H. Chen, Y. Wang, and B. Li. Multi-physical modeling for electro-transport and deformation of ionic polymer metal composites. In *Electroactive Polymer Actuators and Devices (EAPAD) 2012*, volume 8340, page 83400Q. International Society for Optics and Photonics, 2012.